

1 **Alpacas in Space - An Autobiography**
2

3 By
4

5 JOSEPH LEVINE
6 DISSERTATION
7

8 Submitted in partial satisfaction of the requirements for the degree of
9
10 DOCTOR OF PHILOSOPHY

11 in
12

13 Physics
14

15 in the
16

17 OFFICE OF GRADUATE STUDIES
18
19 of the
20

21 UNIVERSITY OF CALIFORNIA
22

23 DAVIS
24

25 Approved:
26

27 J. Anthony Tyson, Chair
28

30 S. Mani Tripathi
31

33 Brian Kolner
34

36 Committee in Charge
37

38 2025

39

Abstract

40 comment: This is my qual write up and is here only as a place holder. Don't edit this
41 yet It is believed that a large majority of the mass in the universe comes from an as yet
42 undetermined source. This claim stems originally from work performed in 1933 by Fritz
43 Zwicky who noticed a discrepancy between measured velocities of galaxies within the Coma
44 Cluster and velocities predicted by applying the virial theorem. He wrote

45 *If this [experimental result] would be confirmed we would get the surprising result
46 that dark matter is present in much greater amount than luminous matter [1].*

47 Vera Rubin furthered this work by measuring velocities of stars rotating in the M31 galaxy
48 and concluded there must be additional non-luminous mass (originally published in [2],
49 and shown in Fig.0.1). Studies of other phenomena, such as lensing (see [**lensing2**]) have
50 confirmed the existence of this dark matter, and it is currently one of the major mysteries
51 in modern physics.

52 Since the 1980's, the leading theories have consisted of an unknown species of elementary
53 particle. The search for weakly interacting massive particles (WIMPs) have dominated
54 the budgets and schedules of the dark matter search effort but have yet to provide any
55 experimental evidence.

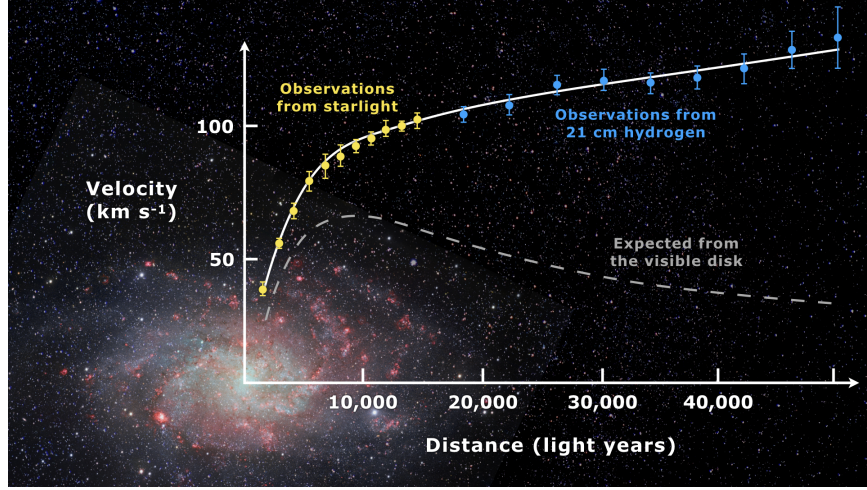


Figure 0.1: Expected vs observed velocity distributions of M33

56 In light of this, the 2017 community report on dark matter [3] highlights a need for a multi-
 57 experiment program in which many small scale experiments (< \$10M) split up to cover the
 58 vast landscape of potential dark matter candidates (see Fig. 0.2). Since very little is known
 59 about the dark matter, it is a playground for theoretical physicists to invent candidates.

60 This overwhelming search should be narrowed down.

61 The enormous mass range splits nicely into two regimes; waves and particles. At a mass of
 62 order 1eV the inter-particle spacing \approx wavelength. Lighter than this it is more convenient
 63 to think of dark matter as a wave. Alternatively, dark matter candidates heavier than this
 64 are more conveniently modeled as exhibiting particle-like behavior. The Dark E-Field Radio
 65 experiment searches for dark photons in the nano- to milli-eV mass range where dark matter
 66 is best described as a wave. This property means one would search for a dark photon using
 67 wave-like detectors, e.g. antennas.

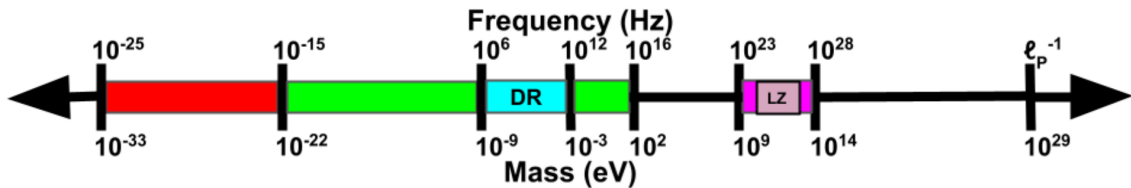


Figure 0.2: Cartoon depicting the mass scales over which dark matter may be found. Corresponding frequencies shown above. At heavy mass scales $> \mathcal{O}(1\text{ eV})$ the dark matter would behave like a particle, while on the lighter end it would behave like a wave. The Dark Radio Experiment searches at radio/microwave frequencies (blue) for a hidden photon using an antenna and spectrum analyzer. LUX-ZEPLIN Experiment (LZ) also shown.

68 comment: Discussion from paper. Good to pull from

69 This experiment extends the earlier results of our pilot experiment [4], which was designed to
 70 demonstrate feasibility of the Dark E-field Radio technique. The pilot experiment was run
 71 over the same frequency range as the experiment reported here, but did not make use of the
 72 calibration techniques to approximate statistical uniformity, nor did it fully account for the
 73 resonant enhancement of the cavity. In this paper we describe how we randomize antenna
 74 positions by moving it many times during the run. In addition, we detail EM simulations
 75 which give the average relation between the E-field at the antenna and the voltage into
 76 the LNA, accounting for resonant enhancement of the cavity. A 2^{24} -point FFT produces a
 77 spectrum dominated by background thermal noise which varies gradually with frequency.

78 We then searched over the full 50-300 MHz frequency span for any narrow-band dark photon
 79 signal of at least 5% global significance. Optimally filtering the resulting spectrum, we detect
 80 a single candidate which we are able to identify as interference, likely from our electronics.

81 Rejecting this candidate, we obtain a null result for any signal which could be attributed
82 to the dark photon in our frequency range. The resulting 95% exclusion limit for the dark
83 photon kinetic coupling ϵ is then obtained over this mass range of 0.2-1.2 μeV . Our null result
84 is a factor of ≈ 100 more sensitive than current astrophysical limits.

85 Ultimately, we can apply this detection technique at higher frequencies, ultimately going up
86 to the sub-THz band. This will require new antennas and microwave electronics. Cryogenic
87 cavities and LNAs could improve our sensitivity by an order of magnitude.

88 **Contents**

89	Contents	vi
90	List of Figures	x
91	List of Tables	xiv
92	1 The Dark Matter Story	1
93	1.1 The History of Dark Matter	2
94	1.1.1 Early ideas in dark matter	2
95	1.1.2 Into the modern era	2
96	1.1.2.1 Galactic rotation curves	2
97	1.1.3 Local dark matter density measurements	2
98	1.2 From “History” to “Current Events”	2
99	1.2.1 Modern evidence and observations of dark matter	2
100	1.2.1.1 The cosmic microwave background	2
101	1.2.1.2 Gravitational lensing	2
102	1.2.1.3 MOND and the bullet cluster	2
103	1.3 MACHOs, WIMPs and WISPs, oh my!	3
104	1.3.1 WISPs	3
105	1.3.1.1 Axions	3
106	1.4 Dark Photon Physics	3
107	1.5 Detection Strategy: a Resource Allocation Problem	4
108	2 Experiment Overview and Design	5
109	2.1 Sources of Power in Measured Spectrum	8
110	2.1.1 Thermal noise	8
111	2.1.1.1 Blackbody electric field density	8
112	2.1.1.2 Antenna noise	11
113	2.1.1.3 Dicke radiometer equation	14
114	2.1.2 Dark photon signal	19
115	2.1.3 Radio frequency interference	21
116	2.1.4 Amplifier chain noise	22
117	2.1.5 ADC effects	26

118	2.1.5.1	Spurious signals	27
119	2.1.5.2	ADC noise	28
120	2.2	Toy Analysis	28
121	2.2.1	Signal significance	30
122	2.2.1.1	Computing an exclusion limit	32
123	2.2.2	Predicted time to detection	36
124	2.3	Thermal Noise in a cavity: Thermal Wiggles	38
125	2.3.1	Theory of thermal radiation in a cavity	38
126	2.3.2	Inspection of thermal noise spectra	42
127	2.3.3	A simple resonator: shorted coax cable	43
128	2.3.3.1	RF circulators	46
129	2.3.4	A simpler resonator: shorted coax cable and circulator	49
130	2.3.5	A more complex resonator: antenna in room	51
131	2.3.6	Effective temperature of amplifier	53
132	2.3.7	Intentional breaking of thermal equilibrium	56
133	2.3.8	Relation of antenna S_{11} to thermal noise without a circulator	63
134	2.3.9	Discussion of Thermal Wiggles	66
135	2.4	Reverberation Chambers and Statistical Uniformity	67
136	2.4.1	Deterministic solutions to electromagnetic waves in cavities	69
137	2.4.2	Statistical approach to electromagnetic waves in cavities	73
138	2.5	System Design	74
139	2.5.1	Shielded room	77
140	2.5.2	Antenna	78
141	2.5.3	Terminator and fiber-optic switch control	82
142	2.5.4	Signal conditioning	82
143	2.5.4.1	Low noise amplifier	83
144	2.5.4.2	Secondary amplifier	84
145	2.5.4.3	Band pass filter	84
146	2.5.4.4	Assembling a signal conditioning chain	86
147	2.5.5	Veto antenna	89
148	2.5.6	12 V power system	89
149	2.5.7	GPU-Based Real-Time Spectrum Analyzer	92
150	3	System Characterization and Data Acquisition System	96
151	3.1	Measurement of Amplifier Chain Performance	97
152	3.1.1	Y-factor method	97
153	3.1.2	Confirming gain with tracking generator measurement	105
154	3.1.3	System stability over a run period	106
155	3.2	Measurement of shielding effectiveness and radio frequency interference	110
156	3.3	Spectrum Analyzer Characterization	116
157	3.3.1	Spectrum analyzer calibration	116
158	3.3.2	Spurious signal performance of the ADC	117
159	3.3.3	ADC clock performance	119

160	3.3.4 Real-time data collection efficiency	120
161	4 Data Acquisition, Data Analysis and Calibration	122
162	4.1 Data Acquisition	124
163	4.1.1 Raw data, S_o	125
164	4.2 Data Analysis	128
165	4.2.1 Fit background, $\hat{B}(\nu)$	130
166	4.2.2 Normalized spectrum, S_o^{norm}	132
167	4.2.3 Signal-matched filter	133
168	4.2.4 Monte Carlo: pseudo experiments	136
169	4.2.5 Rejection of a single candidate	141
170	4.3 Calibration	142
171	4.3.1 Average effective aperture, $\langle A_e(\nu) \rangle$	143
172	4.3.2 Simulation of $\langle \tilde{Q} A_e \rangle$	144
173	4.3.3 Correction and uncertainty of $\langle \tilde{Q} A_e \rangle$	147
174	4.4 Hardware Injection Test	150
175	4.4.1 Injection test prerequisites	151
176	4.4.1.1 Determination of required injected power	151
177	4.4.1.2 Proxy dark photon signal injection	154
178	4.4.2 Performing the injection test	156
179	4.4.3 Inspection of Data	161
180	5 Results	165
181	5.1 Discussion of Uncertainties	166
182	5.2 Exclusion Limit	167
183	6 Beyond 300 MHz	170
184	6.1 A First Attempt at Run 1B	174
185	6.1.1 Run 1B upgrades	174
186	6.1.1.1 Run 1B spectrum analyzer	174
187	6.1.1.2 Run 1B signal conditioning	175
188	6.1.1.3 Vivalid antenna stand	175
189	6.1.1.4 Mode stirrer and statistical uniformity	175
190	6.1.2 Run 1B: data run and analysis	177
191	6.2 Mixer System: Run 2	181
192	6.2.1 Frequency mixing	182
193	6.2.1.1 The superheterodyne receiver	185
194	6.2.2 Design requirements	188
195	6.2.3 The dual-conversion superheterodyne receiver	189
196	6.2.3.1 Run 2A mixer system design	195
197	6.2.3.2 Additional considerations	198
198	6.2.3.3 Comments on Run 2B	203
199	6.3 Possible Future Upgrades	204

200	6.3.1	Detector design principles to maximize the signal-to-noise ratio	204
201	6.3.1.1	Maximize the signal	205
202	6.3.1.2	Reduce noise	205
203	6.3.1.3	Filtering	206
204	6.4	Leveraging Axion experiments for Dark Photon searches	207
205	6.4.1	Reanalysis of axion haloscope data	207
206	6.4.2	Design and operation of axion experiments for dark photons	208
207	A	Overview of RTSA code base	209
208	A	Tips for using the RTSA system	211
209	B	Data structure and processing	212
210	B.1	Writing data	212
211	B.2	Reading and averaging data	216
212	Bibliography		219

²¹³ List of Figures

214	0.1	Expected vs observed velocity distributions of M33	iii
215	0.2	Dark matter mass regimes	iv
216	2.1	Overview of the Dark E-field Radio experiment	7
217	2.2	Blackbody electric field spectral density from radio to UV frequencies	10
218	2.3	An antenna and matched resistor in cavities which are in thermal equilibrium.	13
219	2.4	Simulated antenna noise voltage at room temperature in the time domain	15
220	2.5	Simulated antenna noise power spectral density at room temperature in the frequency domain	16
221	2.6	Effect of averaging on simulated antenna noise power spectral density at room temperature in the frequency domain	18
222	2.7	Schematic of LNA adding input referred noise	22
223	2.8	Schematic of cascade of amplifiers and their added noise	24
224	2.9	Cascaded noise temperature for system with two amplifiers	25
225	2.10	Input-referred power spectral density from simplified simulation	30
226	2.11	Noise spectrum containing sub-detection-threshold signal	34
227	2.12	Noise spectrum containing sub-detection-threshold signal, various number of averages	35
228	2.13	Predicted time to detection for the toy analysis spectra	37
229	2.14	Two cavities in thermal equilibrium of arbitrary shape, material and physical contents contain equivalent radiation fields	39
230	2.15	A cavity with a small hole behaves like a black body as long as the probability of absorption << 1. The probability of absorption at each reflection is given by the emissivity, so the total probability of <i>reflection</i> is the emissivity raised to the power of the average number of bounces. Figure from Wikipedia.	41
231	2.16	Output-referred Vivaldi antenna and terminator spectra as measured through Run 1A amplifier chain	43
232	2.17	A coax cable with a short on the end and a matched measurement device on the other behaves like a “closed-open” resonator. Replacing the short termination with an open (not shown here) produces a similar resonator, though with a 180-degree phase shift.	45
233	2.18	Power spectrum of short and open terminations at the end of 1.85 m of RG400 coax cable	45
234	2.19	Schematic symbol of a circulator	46

247	2.20 Photo of Teledyne C-0S03A-3M RF circulator	47
248	2.21 3-port, frequency-dependent S-parameter data for Teledyne C-0S03A-3M circulator	48
249	2.22 A coax cable with a short on one end and a circulator isolating the system from the amplifier.	50
251	2.23 Power spectrum of 185 cm coax resonator as measured through circulator.	50
252	2.24 Schematic of experimental set-up using circulator to isolate antenna from ampli- fier effects	52
254	2.25 Normalized power spectrum for Vivaldi antenna in the room with and without circulator	52
256	2.26 Schematic of set-up to measure the noise emerging <i>out</i> of an amplifiers input . .	55
257	2.27 Power spectrum of noise emerging <i>out</i> of the input of an amplifier's input . . .	55
258	2.28 Setup to create hot and cold terminator	57
259	2.29 Spectra resulting from the antenna and circulator set up at a variety of temper- atures above room temperature	59
261	2.30 Spectra resulting from the antenna and circulator set up with the terminator 210 K above and below room temperature	61
263	2.31 Sum of normalized spectra shown in Fig. 2.30	62
264	2.32 $1 - S_{11} ^2$ and the normalized antenna spectrum over plotted	64
265	2.33 Correlation of $1 - S_{11} ^2$ and the normalized antenna spectrum	65
266	2.34 Modal density for an electromagnetic cavity with dimensions of the shielding room	71
267	2.35 Pictures of conductor configurations in shielded room	72
268	2.36 Measured S_{11} with different conductors in shielded room	72
269	2.37 Schematic of the RF receiver system	75
270	2.38 Photo of dark radio lab	76
271	2.39 AB-900A biconical antenna free space effective aperture, simulated, measured and theoretical	80
273	2.40 simulated AB-900A biconical antenna free space complex input impedance, vs measured biconical data	81
275	2.41 Measured through gain (S_{21}) of the Run 1A band-pass filter	87
276	2.42 Schematic of Run 1A Amplifier chain	88
277	2.43 Schematic of Interlock board	90
278	2.44 Photo of lead-acid battery and slow turn on circuit	91
279	2.45 Real time DAQ data stream.	94
280	3.1 Cartoon showing Y-factor data	98
281	3.2 Raw output power spectra used to compute the gain and noise temperature for the Run 1A amplifier chain using the Y-factor method	100
283	3.3 Y-factor data from the Run 1A amplifier chain at a single frequency (625 MHz)	101
284	3.4 Frequency dependent noise temperature of the Run 1A amplifier chain, measured using the Y-factor method	102
286	3.5 Frequency-dependent gain of the Run 1A amplifier chain, measured using the Y-factor method	103
288	3.6 Run 1A terminator, input-referred power spectral density	104

289	3.7	Gain vs. frequency of the Run 1A amplifier chain	105
290	3.8	Gain vs. LNA voltage of the Run 1A amplifier chain	107
291	3.9	Voltage at LNA vs. time with Run 1A setup	108
292	3.10	Frequency-averaged power spectral density vs. time of the terminator from Run 293 1A	109
294	3.11	Photo of setup to measure Shielding effectiveness of shielded room	112
295	3.12	Shielding effectiveness of shielded room, 50-300 MHz	113
296	3.13	Shielding effectiveness of shielded room, 125-3000 MHz	114
297	3.14	Spectrum from veto antenna during 300 MHz data run	115
298	3.15	Scan of terminated input of Teledyne spectrum analyzer system to measure spur 299 performance	118
300	3.16	Acquisition efficiency for GPU-based Real-time spectrum analyzer	121
301	4.1	Run 1A averaged, output-referred antenna power spectrum S_o	126
302	4.2	Logarithmic scaled Run 1A averaged, output-referred, antenna and terminator 303 power spectra	127
304	4.3	Flow chart outlining the logic of signal processing in the detection algorithm of 305 sections 4.2.1 through 4.2.3	129
306	4.4	Fitting background \hat{B} in the presence of a synthetic signal	132
307	4.5	Normalized, output-referred power spectrum S_o^{norm}	134
308	4.6	S_o^{norm} after it has been passed through a matched filter	136
309	4.7	Result of Monte Carlo pseudo experiments on signal detection	139
310	4.8	Limit on output-referred total integrated signal power, P_o^{lim}	140
311	4.9	Screenshot of COMSOL simulation GUI for two-antenna validation	146
312	4.10	Simulated vs measured $\langle S_{21} \rangle$	147
313	4.11	Corrected average effective aperture	149
314	4.12	Schematic of hardware injection test	152
315	4.13	Average S-parameters of hardware injection test	153
316	4.14	Histogram of frequencies used for hardware injection test	156
317	4.15	Output-referred power spectral density from the hardware injection test	158
318	4.16	Standard deviation of normalized, output-referred power spectral density from 319 the hardware injection test	159
320	4.17	Standard deviation of normalized, output-referred power spectral density from 321 the hardware injection test, computed with median absolute deviation	160
322	4.18	Output-referred power spectrum from hardware injection test, various levels of 323 zoom	162
324	4.19	Normalized, output-referred power spectrum from hardware injection test, various 325 levels of zoom	163
326	4.20	Matched filtered, output-referred power spectrum from hardware injection test, 327 various levels of zoom	164
328	5.1	Zoom of 95 % exclusion limit on ϵ from Dark E-field Radio run 1A	168
329	5.2	Dark photon limits of various experiments with this work shown in red	169

330	6.1	Picture of modified COMPOWER antenna stand holding Vivaldi antenna for Run 1B	176
332	6.2	Closeup picture of modified COMPOWER antenna stand holding Vivaldi antenna for Run 1B	177
334	6.3	Run 1B averaged, output-referred antenna power spectrum S_o	179
335	6.4	Run 1B S_o^{norm} after it has been passed through a matched filter.	180
336	6.5	9-day averaged veto spectrum and Run 1B S_o^{norm} after it has been passed through a matched filter	181
338	6.6	Overview of basic mixer operation in both upconversion and downconversion mode	184
339	6.7	Illustration of the problem of images in frequency mixing	185
340	6.8	Schematic of a basic superheterodyne receiver system	186
341	6.9	Power spectra along various points of a superheterodyne receiver	187
342	6.10	Block diagram of the mixer system to be used in Run 2	189
343	6.11	Schematic of simplified dual conversion superheterodyne receiver	191
344	6.12	Cartoon illustrating the first mixer stage of dual conversion superheterodyne receiver system	192
346	6.13	Simulated frequency response of dual conversion superheterodyne receiver with signals around 1 GHz	193
348	6.14	Simulated frequency response of dual conversion superheterodyne receiver with signals around 8 GHz	194
350	6.15	Schematic of Run 2A dual conversion superheterodyne receiver	196
351	6.16	Picture of dual-conversion mixer system	198
352	6.17	Spur web, calculated using Marki Microwave's online calculator	201
353	A.1	Real-time heads up window for data acquisition.	215

³⁵⁴ List of Tables

355	2.1	Statistics of simple Monte Carlo simulation for probability of signal detection in the toy analysis	36
356	2.2	Direction, coordinate, and length measurements of the shielded room in lab 314	78
358	2.3	Specifications for the Pasternack PE15A1012-E low noise amplifier	83
359	2.4	Specifications for the Mini-Circuits ZKL-1R5+ as measured with 9.05 V bias . .	84
360	2.5	Specifications for the custom, real-time spectrum analyzer used for Run 1A. . .	93
361	4.1	Run 1A details	124
362	4.2	Threshold parameters that are part of the detection algorithm and Monte Carlo	138
363	6.1	Overview of planned future runs	173
364	6.2	Run 1B details	178
365	6.3	Dual Conversion Mixer System Components	197
366	A.1	Example database file	213

367

Acknowledgments

368 Thank you to:

369 Self plagiarism statement <https://journals.aps.org/copyrightFAQ.html>

370 As the author of an APS-published article, may I include my article or a portion
371 of my article in my thesis or dissertation? Yes, the author has the right to use
372 the article or a portion of the article in a thesis or dissertation without requesting
373 permission from APS, provided the bibliographic citation and the APS copyright
374 credit line are given on the appropriate pages.

375 <https://grad.ucdavis.edu/preparing-filing-your-thesis-or-dissertation>

376 Published or publishing pending material may be used with permission from the
377 copyright owner, if not you, and the Graduate Chair, if you are not the first-
378 author. See the Copyright FAQ for information about permissions when using
379 published material.

380 Material you have authored, and which has been previously published or is pend-
381 ing publishing, may be used in its published format with three exceptions: 1)
382 Margins - You must maintain 1" margins on all sides throughout the paper. 2)
383 Pagination - page numbers must follow the UC Davis standards. 3) The title
384 page must follow UC Davis standards and you must include an overall abstract.

385 comment: Need to add note about github and where code comes from

³⁸⁶ Chapter 1

³⁸⁷ The Dark Matter Story

388

If we start making a list of things that aren't here, we could be here all night. You know, pens for instance. Let's stick with things we can see.

Wheatley

³⁸⁹ **1.1 The History of Dark Matter**

³⁹⁰ **1.1.1 Early ideas in dark matter**

³⁹¹ **1.1.2 Into the modern era**

³⁹² **1.1.2.1 Galactic rotation curves**

³⁹³ **1.1.3 Local dark matter density measurements**

³⁹⁴ **1.2 From “History” to “Current Events”**

³⁹⁵ **1.2.1 Modern evidence and observations of dark matter**

³⁹⁶ **1.2.1.1 The cosmic microwave background**

³⁹⁷ Billy and Ben’s thesis

³⁹⁸ **1.2.1.2 Gravitational lensing**

³⁹⁹ -ben thesis

⁴⁰⁰ -tony 92 article// -J. A. Tyson, G. P. Kochanski, and I. P. Dell’Antonio, Detailed mass map

⁴⁰¹ of CL0024+1654 from strong lensing

⁴⁰² **1.2.1.3 MOND and the bullet cluster**

⁴⁰³ -history of dark matter bertone

⁴⁰⁴ - billy and ben

405 - D. Clowe, M. Bradac, A. H. Gonzalez, M. Markevitch, S. W. Randall, et al., A direct
406 empirical proof of the existence of dark matter,

407 **1.3 MACHOs, WIMPs and WISPs, oh my!**

408 -Billy thesis sec 1.2

409 - G. Bertone, D. Hooper, and J. Silk, Particle dark matter: Evidence, candidates and con-
410 straints

411 **1.3.1 WISPs**

412 **1.3.1.1 Axions**

413 **1.4 Dark Photon Physics**

414 - Ben's thesis

415

$$|\mathbf{E}_{\text{ant}}| \approx \epsilon \sqrt{\frac{2}{\epsilon_0} \rho_{\text{DM}}}, \quad (1.1)$$

416 Tony says 9/23/25- Production mechanisms: fluctuation occurs early in inflation or mis-
417 alignment mechanism.

418

419 two scales cross, peter graham Point out that DP doesn't have a thermal origin like a
420 WIMP does

⁴²¹ **1.5 Detection Strategy: a Resource Allocation**

⁴²² **Problem**

⁴²³ - US Cosmic Visions 2017

⁴²⁴

⁴²⁵ Chapter 2

⁴²⁶ Experiment Overview and Design

⁴²⁷

A month in the laboratory can often save an hour in the library.

Frank Westheimer

428 Veljko Radeka said of detectors, “One would imagine that in each particular case the
429 best solution is arrived at by 1) the detector design to maximize the significant signal, 2)
430 reduction of noise at its physical source, and 3) optimum filtering of signal and noise.”
431 [5]. While he was referring to position-sensitive particle detectors, the same three principles
432 apply to this experiment. Put more directly, the goal is to maximize the signal-to-noise ratio.
433 The detector, in this case, is a low-noise, wide-band radio receiver system searching not for
434 discrete instances of particle-like interactions but for coherent waves that are constant over
435 long periods. The signal is a small RF-power excess received by an antenna in a cavity. The
436 dominant noise is due to the thermal background of the 300 K cavity walls. This noise is
437 nearly white, with small variations. See Sec. 2.1.1 for an overview and Sec. 2.3 for more
438 detail. An overview of the entire experiment is shown in Fig. 2.1.

439 This chapter begins with Sec. 2.1, devoted to exploring the sources of power in the mea-
440 sured spectrum. It walks through several back-of-the-envelope calculations to follow the
441 signals and noises as they progress from fields in free space through a simplified detector.
442 Section 2.2 takes the next step. It simulates these signals and noises and shows a framework
443 for statistical data analysis. These two sections serve to build up intuition about the experi-
444 ment which will explain design choices discussed in later chapters. Furthermore, this section
445 is useful because the actual experiment will report a null result, i.e. a lack of detection of a
446 signal. By following a signal *forward* through the system and toy data analysis, it will be
447 clearer how to infer an exclusion limit from a power spectrum and working *backward* through
448 the experiment. In the following two sections, 2.3 and 2.4, effects will be introduced that
449 were not apparent from the simplistic analysis of the first section. The final section, 2.5,

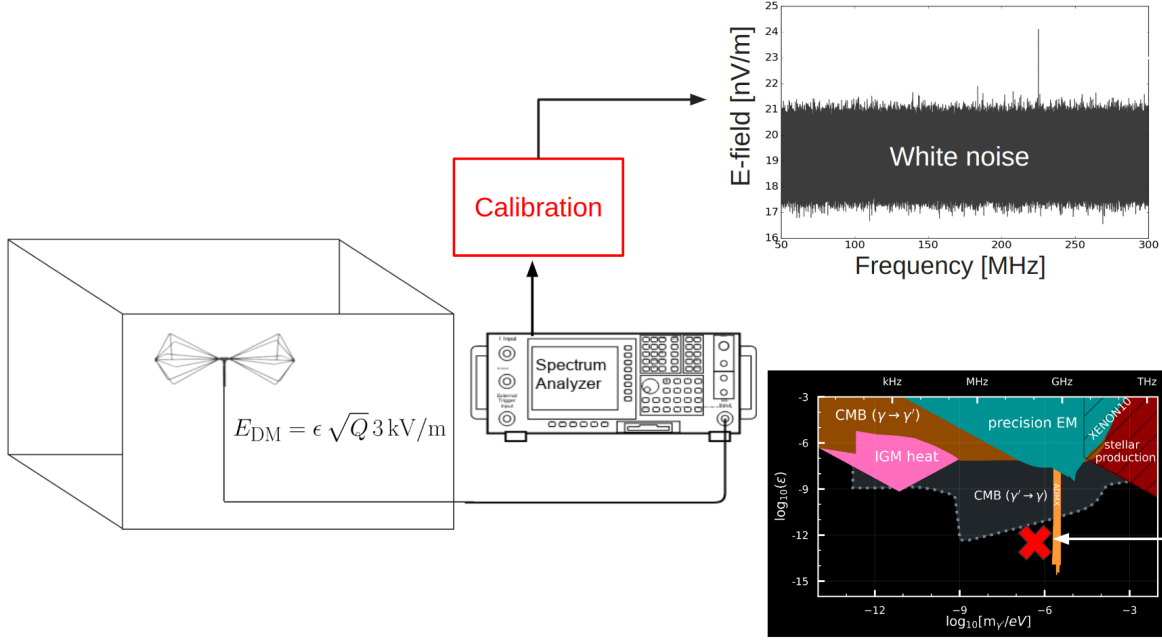


Figure 2.1: Overview of Dark E-field Radio experiment. The free space electric field strength was calculated in Sec. 1.4, and will be modified to include the Q of the cavity in Sec. 2.1.2. The design of the system is outlined in this chapter, while its performance is measured in Ch. 3. The use of the system, its calibration, and setting a limit are all discussed in Ch. 4. **comment: Remake this. Change E_{DM} to E_{ant} , 3kV to 4.5kV, change limit plot. Image from google slide called "schematic"**

450 details each piece of the system. Measurements of system performance are put off until Ch.
 451 3).

452 A note on experiment “run numbers”. Run 1A is the 50-300 MHz run (defined, along with
 453 future planned runs in Tab. 6.1). There have been four attempts at collecting Run 1A data.
 454 The final, published data run was collected between May 10 and May 19, 2023, and is called
 455 Run 1.4 or Run 1p4 throughout my power points and file names. In this thesis, this run will
 456 be referred to as Run 1A or as Run 1A.4 if it is necessary to distinguish between specific

457 runs.

458 2.1 Sources of Power in Measured Spectrum

459 This section will break down each term in the following equation for the input-referred power

$$P_i = \text{Thermal Noise} + \text{Dark Photon Signal} + \text{RFI} + \text{Amp Chain Noise} + \text{ADC Effects}/G, \quad (2.1)$$

460 where G is a gain factor. While convenient, this word equation is not rigorous and relies
461 on the following subsections 2.1.1 - 2.1.5 for definition.

462 2.1.1 Thermal noise

463 2.1.1.1 Blackbody electric field density

464 This subsection estimates the noise-like¹ electric field in free space due to black body ra-
465 diation. It assumes to be in *some* enclosure in that the ambient temperature is known to
466 be 300 K and not, for example, the 3.6 K of the sky. The enclosure considered is assumed
467 to be “black” in that all radiation impinging on its surface is absorbed. This assumption is
468 introduced in Sec. 2.1.1.2 and investigated further in Sec. 2.3.

469 Planck’s law gives the black body spectral energy density as

$$u_\nu(\nu, T) d\nu = \frac{8\pi h\nu^3}{c^3} \frac{1}{e^{h\nu/kT} - 1} d\nu \quad \left[\frac{J}{m^3} \right]. \quad (2.2)$$

¹“Noise-like” simply means that the power contained in a signal is proportional to the bandwidth measured. Noise-like signals are more conveniently described as a power spectral density (PSD) which we will describe with the symbol S . As we will see, coherent signals that have finite width in frequency space $\Delta\nu_{\text{sig}}$ can share this property if the measurement bandwidth $\Delta\nu_{\text{RF}} \lesssim \Delta\nu_{\text{sig}}$, even though one wouldn’t think of a coherent signal as being “noise-like”

470 This is frequently written in terms of spectral radiance,

$$B_\nu(\nu, T) d\nu = \frac{2h\nu^3}{c^2} \frac{1}{e^{h\nu/kT} - 1} d\nu d\Omega \quad \left[\frac{W}{m^2} \right]. \quad (2.3)$$

471 Integrating this isotropic radiance over a solid angle 4π sr as well as a small frequency

472 band $\Delta\nu$ gives the flux density $|\mathbf{S}|$ (AKA, the magnitude of the Poynting vector),

$$\begin{aligned} |\mathbf{S}| &= \int_0^{4\pi} \int_\nu^{\nu+\Delta\nu} B_\nu(\nu, T) d\nu d\Omega \\ &= \int_0^{4\pi} \int_\nu^{\nu+\Delta\nu} \frac{2h\nu^3}{c^2} \frac{1}{e^{h\nu/kT} - 1} d\nu d\Omega \quad \left[\frac{W}{m^2} \right]. \\ &\approx \frac{8\pi h\nu^3}{c^2} \frac{1}{e^{h\nu/kT} - 1} \Delta\nu \end{aligned} \quad (2.4)$$

473 Poynting's theorem relates this flux density to the RMS electric field

$$|\mathbf{S}| = \frac{|E_{rms}|^2}{\eta} \quad \left[\frac{W}{m^2} \right], \quad (2.5)$$

474 where η is the impedance of free space. Equating Eqs. 2.4 and 2.5 and solving for the

475 electric field gives

$$\frac{|E_{rms}|}{\sqrt{\Delta\nu}} = \sqrt{\eta \frac{8\pi h\nu^3}{c^2} \frac{1}{e^{h\nu/kT} - 1}} \quad \left[\frac{V}{m \cdot \sqrt{Hz}} \right], \quad (2.6)$$

476 and is plotted in Fig. 2.2.

477 Eq. 2.6 breaks up nicely into two regimes,

$$\frac{|E_{rms}|}{\sqrt{\Delta\nu}} = \begin{cases} \sqrt{\eta \frac{8\pi kT\nu^2}{c^2}} & \text{Rayleigh-Jeans regime } (h\nu \ll kT) \\ \sqrt{\eta \frac{8\pi h\nu^3}{c^2} e^{-h\nu/kT}} & \text{Wien approximation } (h\nu \gg kT) \end{cases} \quad \left[\frac{V}{m \cdot \sqrt{Hz}} \right]. \quad (2.7)$$

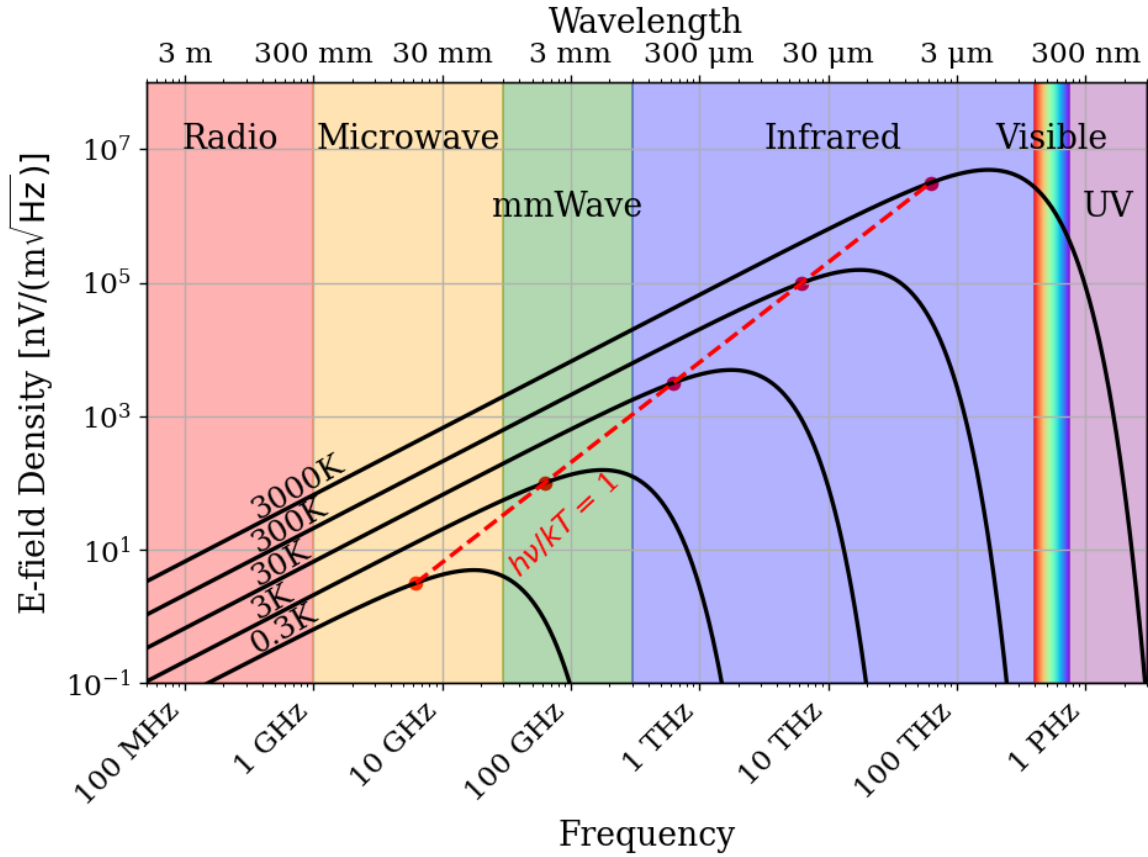


Figure 2.2: Blackbody electric field spectral density from radio to UV frequencies. A variety of temperatures are shown in black. The dashed red curve and red points indicate where along the black curves $h\nu = kT$, i.e. where Eq. 2.7 breaks up between the Rayleigh-Jeans regime to the Wien approximation. Note that these points are only a function of ν and T ; their vertical placement is chosen to lie on their respective curve but has no physical significance. The dark radio experiment is firmly in the Rayleigh-Jeans regime.

478 At frequencies and temperatures where the experiment is operated ($< 300 \text{ MHz}$ and
 479 300 K), $h\nu/kT \lesssim 5 \times 10^{-5}$ suggesting the Rayleigh-Jeans approximation is valid. At 300 K ,
 480 this yields electric field spectral densities of 1 and $6 \text{ nV}/(\text{m}\sqrt{\text{Hz}})$ at 50 and 300 MHz respec-
 481 tively.

482 It is interesting to note, however, that for cryogenic experiments operating at a few GHz

483 and in the sub K range (A common technique; see, for example, [6–8]), $h\nu/kT \approx 1$ and
 484 the full form of Eq. 2.6 must be used. This is shown at frequencies and temperatures to the
 485 right of the red dashed line in Fig. 2.2.

486 **2.1.1.2 Antenna noise**

487 An antenna's effective aperture, $A_e [\text{m}^2]$, represents the effective area that it has to collect
 488 power density or irradiance [W/m^2] from an incident Poynting vector,

$$P_A = |\mathbf{S}| A_e, \quad (2.8)$$

489 Where $|\mathbf{S}|$ is the magnitude of the incident Poynting vector, and P_r is the power received at
 490 the antenna, which is available at its terminals.

491 A_e is a directional quantity that varies with the antenna's directivity $D(\Omega)$, where Ω
 492 represents the solid angle around the antenna. It varies with frequency ν , though it is
 493 generally discussed in terms of wavelength λ . Three matching parameters are introduced to
 494 describe how much actual power the antenna is able to deliver to a transmission line; p the
 495 polarization match of the wave to the antenna, m the impedance match of the antenna to
 496 the transmission line and η_a the efficiency of the antenna which represents how much power
 497 is absorbed compared to that lost to Joule heating of the antenna. p , m and η_a are all real,
 498 dimensionless and vary between 0 and 1.

$$A_e \equiv \frac{\lambda^2}{4\pi} D(\Omega) p m \eta_a. \quad (2.9)$$

499 This definition follows [9], though some authors do not include p in the definition [10,
500 11].

501 A simple derivation of the direction-averaged effective aperture based on thermodynamics
502 will provide intuition. An isotropic antenna placed in a cavity at temperature T will be
503 illuminated by randomly polarized, isotropic radiation of the form given by the Rayleigh-
504 Jeans limit of Eq. 2.4, $|\mathbf{S}| = 8\pi kT\Delta\nu\nu^2/c^2$. The power received by the antenna can be found
505 by Eq. 2.8,

$$\begin{aligned} P_A &= \langle A_e \rangle \frac{1}{2} |\mathbf{S}| \\ &= \langle A_e \rangle \frac{4\pi kT\nu^2}{c^2} \Delta\nu, \end{aligned} \tag{2.10}$$

506 Where the factor of $1/2$ is introduced to account for the random polarization and the $\langle \rangle$
507 indicate an average aperture over all angles around the antenna. If a resistor is placed in a
508 second cavity, also at temperature T , it will deliver its Johnson-Nyquist noise power [12, 13]

$$P_R = kT\Delta\nu \tag{2.11}$$

509 into a matched transmission line. This is shown in Fig. 2.3. The second law of thermo-
510 dynamics makes a very powerful statement here: the net power flow between the antenna
511 and terminator must equal 0 if the two temperatures are indeed equivalent. This means
512 $P_R = P_A$ or Eq. 2.10 = Eq. 2.12,

$$\langle A_e \rangle \frac{4\pi kT\nu^2}{c^2} \Delta\nu = kT\Delta\nu \tag{2.12}$$

513 or,

$$\begin{aligned} \langle A_e \rangle &= \frac{c^2}{4\pi\nu^2} \quad [\text{m}^2] \\ &= \frac{\lambda^2}{4\pi} \end{aligned} \quad (2.13)$$

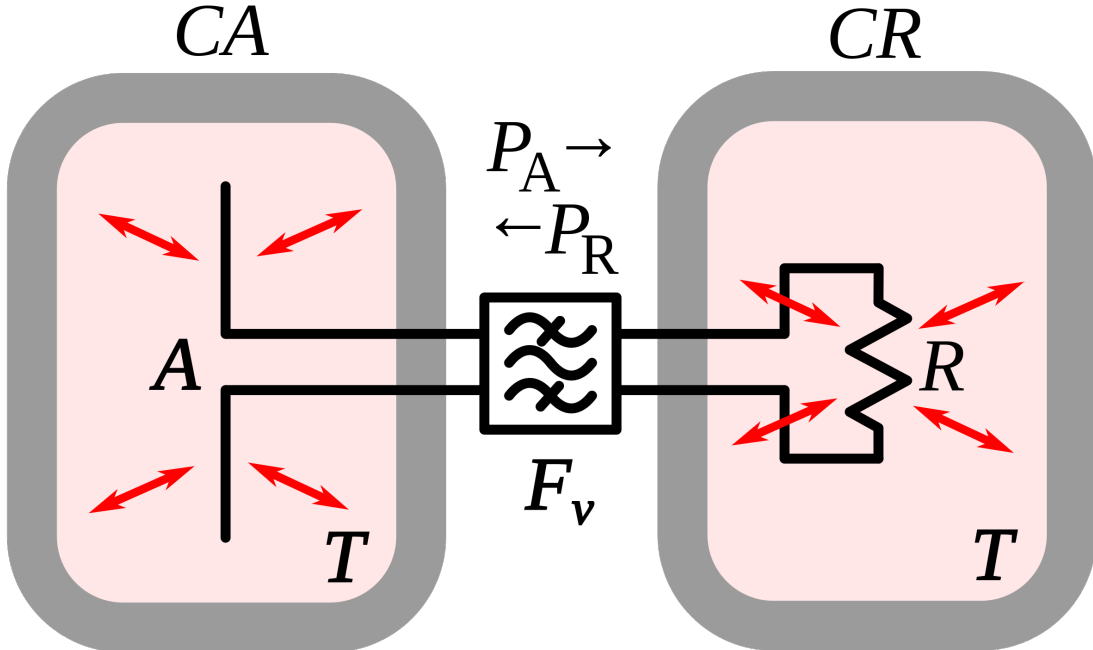


Figure 2.3: An antenna and matched resistor in cavities that are in thermal equilibrium. They are connected by a narrow filter permitting a narrow frequency band $\Delta\nu$. Image from Wikipedia, and is similar to the thought experiment proposed by Dicke [14].

514 This allows us to conclude that the power spectral density S_{ant} received by an antenna
 515 surrounded by an isotropic temperature is simply $kT\Delta\nu$ in the Rayleigh-Jeans limit of room
 516 temperatures and standard electronic frequencies. This result is independent of frequency,
 517 which can be understood by the reciprocal frequency dependence of the blackbody radiation
 518 (Eq. 2.4) and the average effective aperture (Eq. 2.13). The result is an antenna power which
 519 is equivalent to the well-known result for a resistor at 290 K,

$$S_{\text{ant}} = 3.9 \times 10^{-22} [\text{W}/\text{Hz}] = -174 [\text{dBm}/\text{Hz}]. \quad (2.14)$$

520 Note that S_{ant} indicates power spectral density and should not be confused with \mathbf{S} which
 521 indicates a Poynting vector.

522 **2.1.1.3 Dicke radiometer equation**

523 Equation 2.14 gave the mean of a power spectrum that is inherently noisy. We will now
 524 show the origin of this spectrum.

525 An enclosure whose electrically-lossy walls contain free charge carriers at a finite tem-
 526 perature will radiate incoherently by the fluctuation-dissipation theorem. This theorem is
 527 the underlying principle of phenomena such as Brownian motion [15] and Johnson-Nyquist
 528 noise [12, 13], but was not generally proven until 1951 by Callen and Welton [16]. The
 529 random thermal fluctuation of the charge carriers will radiate a black-body spectrum. Ob-
 530 serving the electric field in the time domain, one can imagine the radiation arriving at a
 531 detector at a wide variety of random frequencies and phases. This is incoherent noise in that
 532 at each time domain sample is independent of the one proceeding it ². The detector will
 533 produce a voltage that can be modeled as Gaussian with zero mean and standard deviation
 534 $\sigma = \sqrt{S_{\text{ant}} \Delta \nu_{\text{RF}} |Z|}$ where Z is the system impedance (here 50Ω). This is shown for a room
 535 temperature antenna (or equivalently a room temperature resistor, see Fig. 2.3) in Fig. 2.4.

²The hidden assumption here is that blackbody radiation is totally incoherent. It actually has a coherence time $\tau_c \approx 2 \times 10^{-14} \text{ s}$ at 300 K [17]. For this statement to hold, the sample time $\tau_s \gg \tau_c$. For Run 1A, $\tau_s = 1/800 \text{ MHz} = 1.25^{-9} \text{ s}$, 5 orders of magnitude more than τ_c

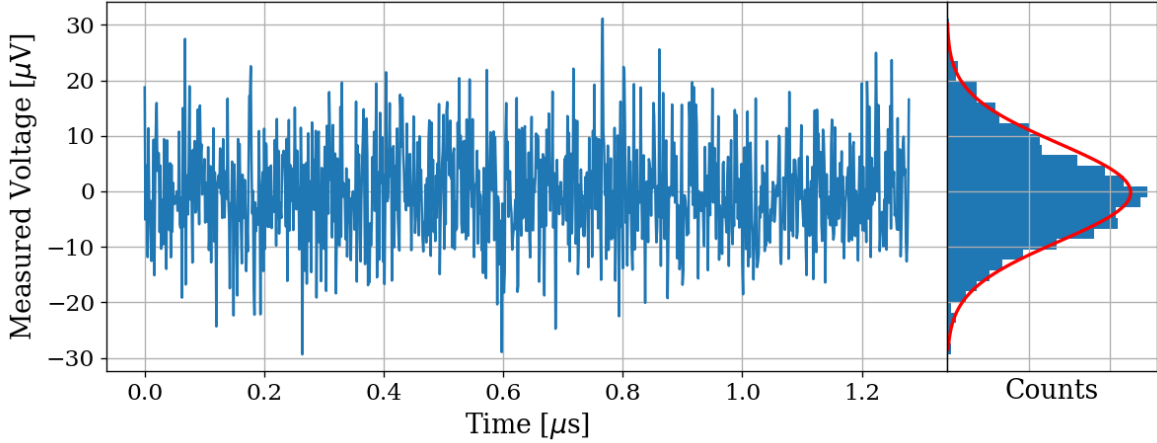


Figure 2.4: Simulated antenna noise voltage at room temperature in the time domain. Sample rate $\nu_s = 800\text{MHz}$ and number of samples $N = 2^{10} = 1024$. Bin width $\Delta\nu_{\text{RF}} = \nu_s/N \approx 800\text{ kHz}$. Data are binned and plotted as a histogram to the right. The best fit Gaussian is shown on the histogram in red with $\mu = -0.199\text{ }\mu\text{V}$ and $\sigma = 8.86\text{ }\mu\text{V}$. Counts have been normalized such that the bins add up to unity.

536 The next step is converting this time-domain voltage signal to a frequency-domain power
 537 spectral density (PSD). The first step is taking a discrete Fourier transform. This is usually
 538 implemented with an algorithm known as a fast Fourier transform (FFT), so that $\tilde{V} =$
 539 $\text{FFT}(V)$. In order to convert to a power spectrum, a non-trivial normalization prefactor
 540 must be included;

$$S = \frac{2}{N^2 |Z|} |\Re(\tilde{V})[:N//2]|^2, \quad (2.15)$$

541 where N is the number of samples, Z is the system impedance, and [:N//2] is Python notation
 542 for the second half of the samples contained in the \tilde{V} array. Performing this operation on
 543 the data in Fig. 2.4 yields the data in Fig. 2.5

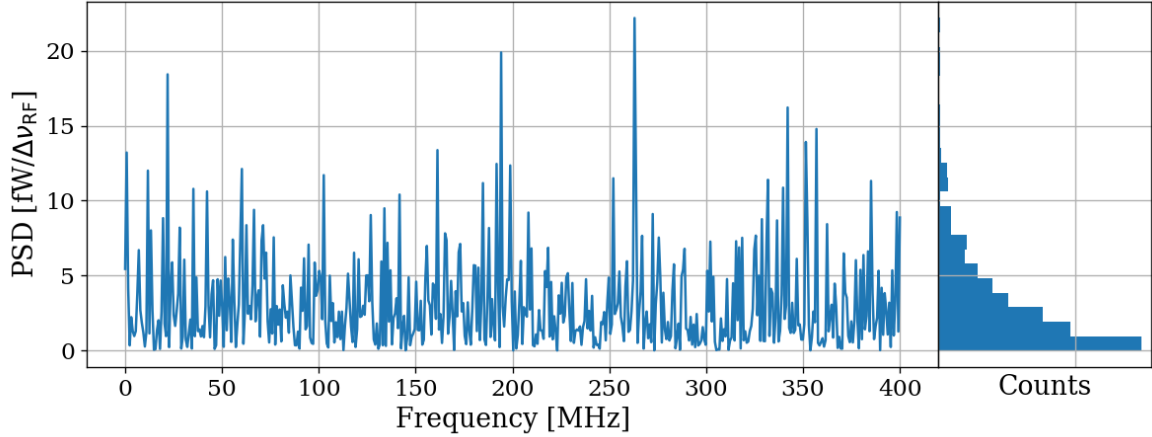


Figure 2.5: Simulated antenna noise power spectral density (PSD) at room temperature in the frequency domain. Sample rate $\nu_s = 800\text{MHz}$ and number of samples $N = 2^{10} = 1024$. Bin width $\Delta\nu_{\text{RF}} = \nu_s/N \approx 800\text{ kHz}$. Data are binned and plotted as a histogram to the right. Counts have been normalized such that the bins add up to unity.

544 The peculiar PDF of the histogram shown in Fig. 2.5 is known as a χ^2 distribution with
 545 1 degree of freedom and comes about because power is a positive-definite quantity and the
 546 standard deviation of the PSD is greater than it's mean.

547 However, by averaging many of these power spectra together, the central limit theorem
 548 dictates that we can expect the resulting PDF to be Gaussian. The transition from χ^2 to
 549 Gaussian distributed spectra is shown in Fig. 2.6.

550 Finally, this averaged power spectrum can be modeled with the Dicke radiometer equa-
 551 tion. The measured power (assuming only thermal noise) is given by

$$P_{\text{ant}} = kT\Delta\nu \left(1 \pm \frac{1}{\sqrt{\Delta\nu\tau}} \right) \quad [\text{W}]. \quad (2.16)$$

552 Here τ is the total acquisition time, and so $\Delta\nu\tau$ is equivalent to the number of spectra

553 that are averaged together. This can be nondimensionalized and written

$$\frac{P_{\text{ant}}}{kT\Delta\nu_{\text{RF}}} = 1 \pm \frac{1}{\sqrt{N}} \quad [\text{None}], \quad (2.17)$$

554 which will become important during data analysis which is the topic of Sec. 4.2.

555 For the remainder of this thesis, unless otherwise stated, it will be assumed enough

556 spectra have been averaged together that a PSD is Gaussian and scales with the square root

557 of total acquisition time according to Eq. 2.16.

558 Thus far the analysis has focused only on thermal noise, however there are other sources

559 of noise and interfering signals which must be considered, not to mention the actual dark

560 photon signal.

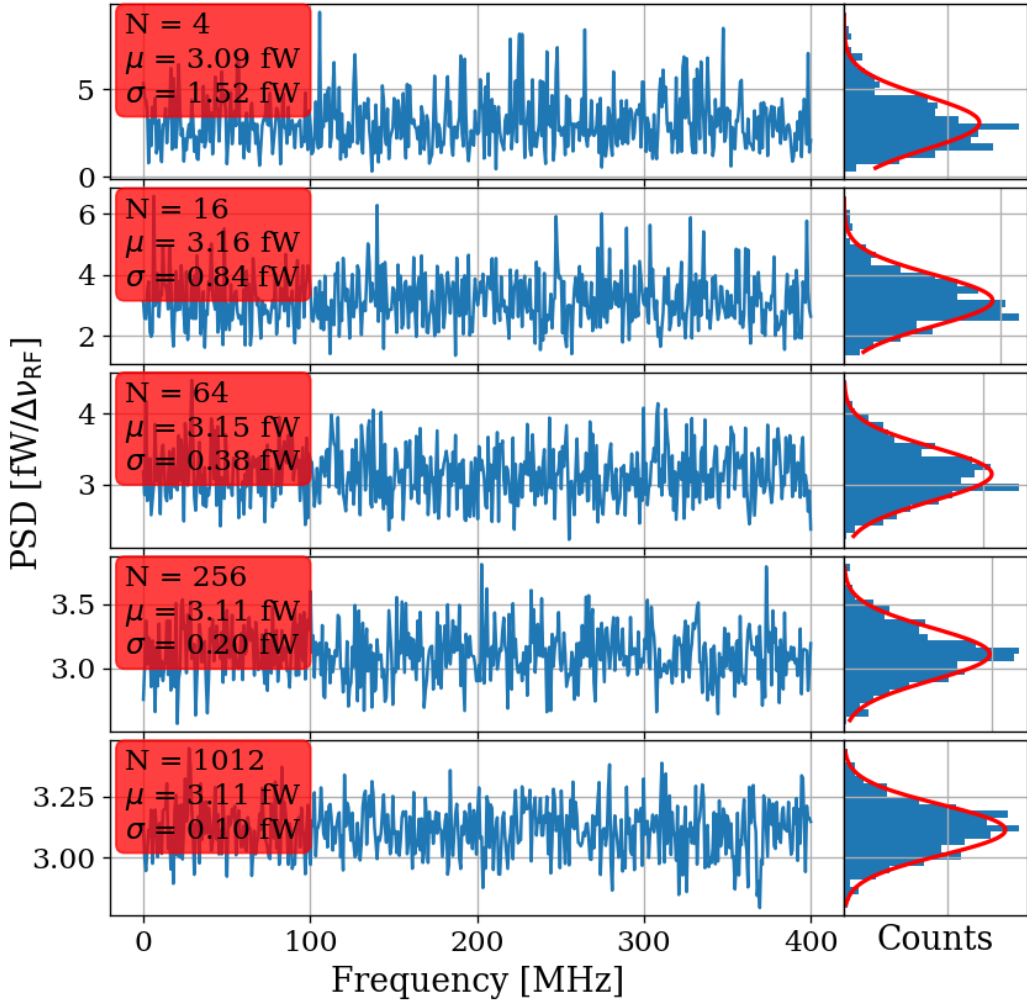


Figure 2.6: Effect of averaging on simulated antenna noise power spectral density (PSD) at room temperature in the frequency domain. Subplots show different numbers of averaged power spectra from $N = 4$ to 1024. Each subplot shows a factor of 4 times more averaging than the previous one. The Dicke radiometer equation predicts the standard deviation σ will scale like $N^{-1/2}$ once a large number of averages have been taken such that $\sigma \ll \mu$. Sample rate $\nu_s = 800\text{MHz}$ and number of samples $N = 2^{10} = 1024$. Bin width $\Delta\nu_{\text{RF}} = \nu_s/N \approx 800 \text{ kHz}$. Data are binned and plotted as a histogram to the right with a best-fit Gaussian shown in red. Counts have been normalized such that the bins add up to unity. Note that the Y-axis scale changes between subplots to show the improvement of the Gaussian fit. The standard deviation is indeed decreasing between plots.

561 **2.1.2 Dark photon signal**

562 The electric field of a kinetically mixed dark photon in free space $\mathbf{E}_{\text{ant}}^{\text{free space}}$ was shown in
 563 Eq. 1.1. In a cavity, the E-field will be enhanced by the quality factor Q of the cavity. This
 564 Q must be measured or simulated, but for this toy analysis, we will assume it to be known
 565 ³. The E-field inside the cavity then is

$$\mathbf{E}_{\text{ant}} = \mathbf{E}_{\text{ant}}^{\text{free space}} \sqrt{Q}, \quad (2.18)$$

566 since Q is proportional to power, i.e. \mathbf{E}^2 . This E-field will then need to be converted from
 567 a wave in the cavity to a wave in a 50Ω transmission line by an antenna. Similar to the
 568 thermal noise of the previous section, this electric field will be converted via the effective
 569 aperture of the antenna. Similar to Q , the aperture will be assumed to be known.

570 The total received power from a coherent signal inside the room then is

$$P = \frac{\mathbf{E}_{\text{ant}}^{\text{free space}^2}}{\eta} Q < A_e >, \quad (2.19)$$

571 where η is the impedance of free space.

572 The observed spread of the frequencies of the dark photon is an important effect that
 573 determines system design. In the following paragraphs of this section, several sections of
 574 Gramolin et al. [19] are summarized. Also note that the original calculation for the predicted
 575 line shape appears to be Michael Turner in 1990 [20].

576 A simple model of the dark photon line assumes it is monochromatic, i.e. its line shape
 577 is a delta function in the frequency-domain,

$$\nu_{\text{obs}} = \delta(\nu - \nu_{\text{DP}}). \quad (2.20)$$

³Typical values are in the ballpark of 100. Some experiments have ultra-high Q cavities $\approx 10^{10}$ [18]

578 This is consistent with its production add reference: misalignment mechanism/ch 1.

579 However, when observed in a frame other than its rest frame, the frequency of a (single)

580 dark photon will shift by an amount proportional to its kinetic energy

$$\nu_{\text{obs}} = \left(1 + \frac{v_n^2}{2c^2}\right) \nu_{\text{DP}}, \quad (2.21)$$

581 where ν_{obs} is the observed frequency of the n th dark photon, v_n is its velocity, c is the speed

582 of light, and ν_{DP} is its rest frequency. The end result will be a signal that has some spread

583 in frequency, $\nu_{\text{DP}}/(\Delta\nu) \equiv Q_{\text{DP}} \approx 10^6$, with a line shape given by 2.24.

584 By summing over an infinity of dark photons of random phases and velocities (sampled

585 from the relative velocity of the dark matter halo), each with a frequency given by Eq. 2.21,

586 one can construct a PSD of the dark photon signal as measured on earth, S [W/Hz].

587 When performing a measurement, one records the voltage V emerging from a detector

588 for a period of time greater than the coherence of the dark photon $\tau_{\text{FFT}} \gg \tau_c$. The Fourier

589 transform of $V(t)$ is denoted $\tilde{V}(\nu)$

590 The signal will have a total power

$$P_0 = \frac{1}{\tau_{\text{FFT}}} \int_0^{\tau_{\text{FFT}}} \frac{V(t)^2}{|Z|} dt = \int_0^{1/\tau_{\text{FFT}}} S(\nu)^2 d\nu, \quad (2.22)$$

591 which is a statement of Parseval's theorem.

592 The normalized line shape is defined by dividing by P_0 ; $\lambda(\nu) \equiv S(\nu)/P_0$. This has the

593 property of being normalized to unity,

$$\int_0^\infty \lambda(\nu) d\nu = 1. \quad (2.23)$$

594 Finally, the result for this normalized line shape is

$$\lambda(\nu) = \frac{2 c^2}{\sqrt{\pi} v_0 v_{\text{lab}} \nu_{\text{DP}}} \exp \left(-\frac{\beta^2 v_0^2}{4 v_{\text{lab}}^2} - \frac{v_{\text{lab}}^2}{v_0^2} \right) \sinh \beta \quad \left[\frac{1}{\text{Hz}} \right], \quad (2.24)$$

595 where $|v_0| \approx 220$ km/s is the circular rotation speed of the Galaxy at the radius of the sun

596 (approximately 8 kpc), $v_{\text{lab}} \approx 233$ km/s is the relative velocity of the Sun to the rest frame

597 of the Galaxy and

$$\beta \equiv \frac{2 c v_{\text{lab}}}{v_0^2} \sqrt{\frac{2 (\nu - \nu_{\text{DP}})}{\nu_{\text{DP}}}}.$$

598 Equation 2.24 is used to generate Fig. 4.14. Note the quality factor $Q_{\text{DP}} \approx 10^6$ as

599 mentioned above.

600 2.1.3 Radio frequency interference

601 Radio Frequency Interference (RFI) includes any coherent interfering signals which can be
602 detected by the experiment. While noise is better described as a power spectral *density*
603 [W/Hz] or electric field *density* [V/(m $\sqrt{\text{Hz}}$)], RFI is made up of more narrow lines and is
604 discussed in terms of power [W] or electric field [V/m]. In this experiment, RFI is mitigated
605 through the shielding effectiveness (SE) of the cavity. SE measurements and more details
606 about local RFI are discussed further in Sec. 2.5.1 and Sec. 3.2, and a plot of the local RFI
607 spectrum is shown in Fig. 3.14.

608 The peak RFI spike is at 186 MHz and approximately 100 $\mu\text{V}/\text{m}$, an energy density
609 of roughly 10^{-11} W/m². This will be reduced by the SE of the room (roughly 120 dB at
610 200MHz, see Fig. 3.11), but just like a coherent dark photon, it will be enhanced by the

611 Q/effective aperture. This will be right on the edge of detection, but in the actual data run,
 612 it was not detected.

613 **2.1.4 Amplifier chain noise⁴**

614 Any amplifier will have some noise which it adds to an incoming signal which will degrade
 615 the signal-to-noise ratio (SNR) of the measurement ⁵. A low noise amplifier (LNA) is an
 616 amplifier that has been specifically designed to minimize the noise contribution. This process
 617 is shown schematically in Fig. 2.7.

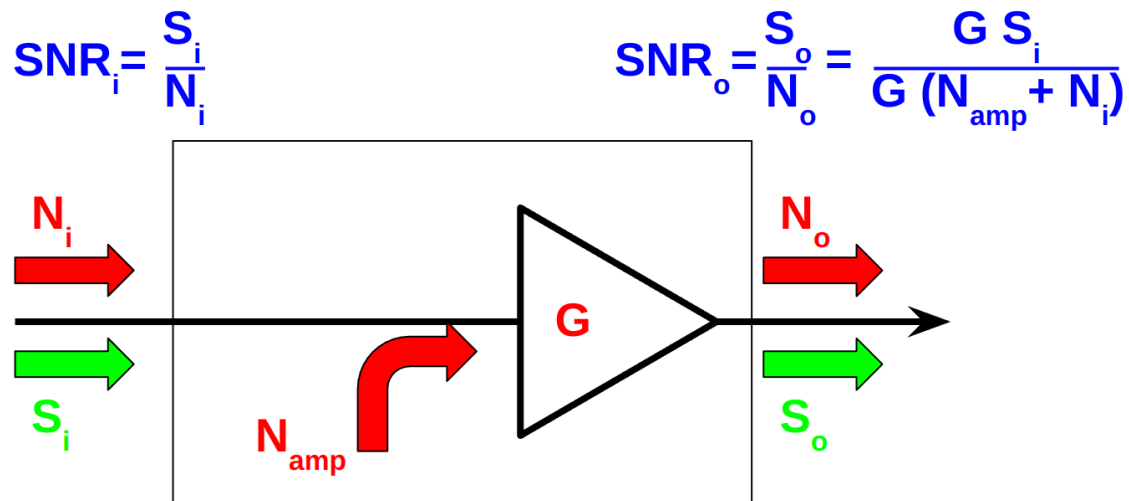


Figure 2.7: Schematic of LNA (with power gain G) adding input referred noise N_{amp} . Since N_{amp} is referred to the input, it can be directly added to the input noise which is itself input-referred. The ideal, noiseless amplifier is represented by the triangle, while the physical amplifier, including noise, is contained in the rectangle.

⁴Code for this section can be found at: <https://github.com/josephmlev/darkRadio/tree/master/thesis/ch2/CH2.ipynb>

⁵A great lecture on the subject by Prof. Greg Durgin can be found at [21]

618 The performance of an LNA is generally evaluated by its noise factor (F). F is defined
 619 to be the ratio of the SNR at the input of an LNA to that at its output.

$$\begin{aligned}
 F &\equiv \frac{\text{SNR}_i}{\text{SNR}_o} \\
 &= \frac{S/N}{[S G]/[(N + N_{\text{amp}})G]} \\
 &= \frac{1}{1/[1 + N_{\text{amp}}/N]} \\
 &= 1 + \frac{N_{\text{amp}}}{N},
 \end{aligned} \tag{2.25}$$

620 where S and N are the signal and noise [W] presented to the LNA respectively, N_{amp} is
 621 the input-referred noise added by the LNA, and G is the power gain. By factoring out the
 622 implicit $k \Delta\nu$ from $N = kT\Delta\nu$, we find

$$F = 1 + \frac{T_e}{T_0}, \tag{2.26}$$

623 where T_e is the noise temperature of a device and T_0 is the temperature of the system
 624 being measured by the LNA.

625 Note that following the same derivation as Eq. 2.25, it is simple to show that the noise
 626 figure of an attenuator at temperature T with loss L is given by

$$F_{\text{att}} = 1 + \frac{(L - 1)T}{T_0}, \tag{2.27}$$

627 where T_0 is the reference temperature defined above. If $T = T_0$, Eq. 2.27 simplifies to
 628 $F_{\text{att}} = L$

629 In order to standardize device specifications for across system applications, it is common
 630 to choose a reference temperature T_0 of 290K. If not specified, it is generally safe to assume
 631 this has been done.

632 Noise factor is simply defined in terms of noise figure,

$$\text{NF} \equiv 10\log_{10}(F). \quad (2.28)$$

633 When working with LNAs, all three measurements (T_e , F and NF) are frequently used,
 634 and one must use Eqs. 2.26 and 2.28 to convert between them.

635 One important generalization is that of a cascaded series of amplifiers, shown schemati-
 636 cally in Fig. 2.8.

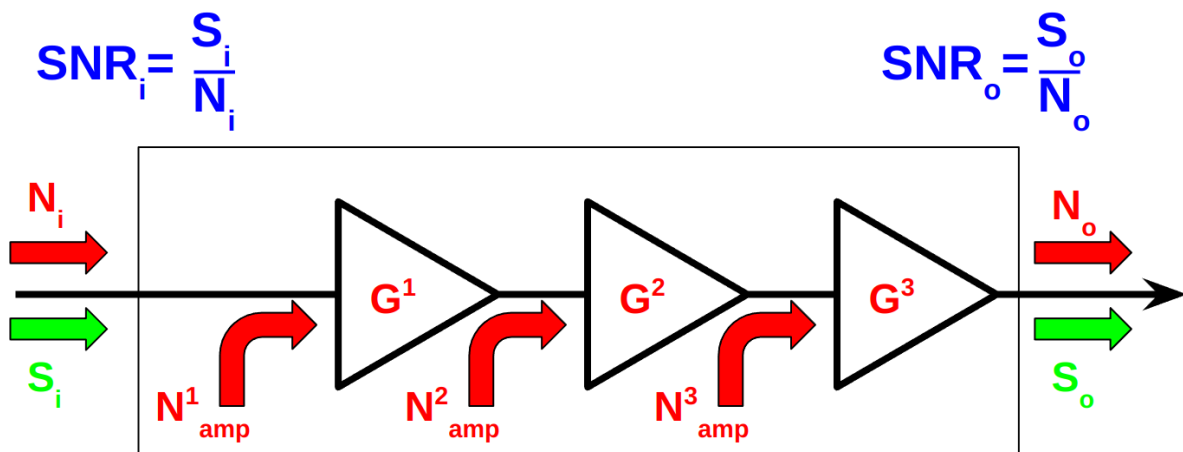


Figure 2.8: Schematic of cascade of $n = 3$ amplifiers and their added noise N_{amp}^n . Each amplifier has a gain of G^n . The SNR at the output is derived in Eq. 2.29. Note that superscripts in the figure and caption refer to the index of each component and are not exponents.

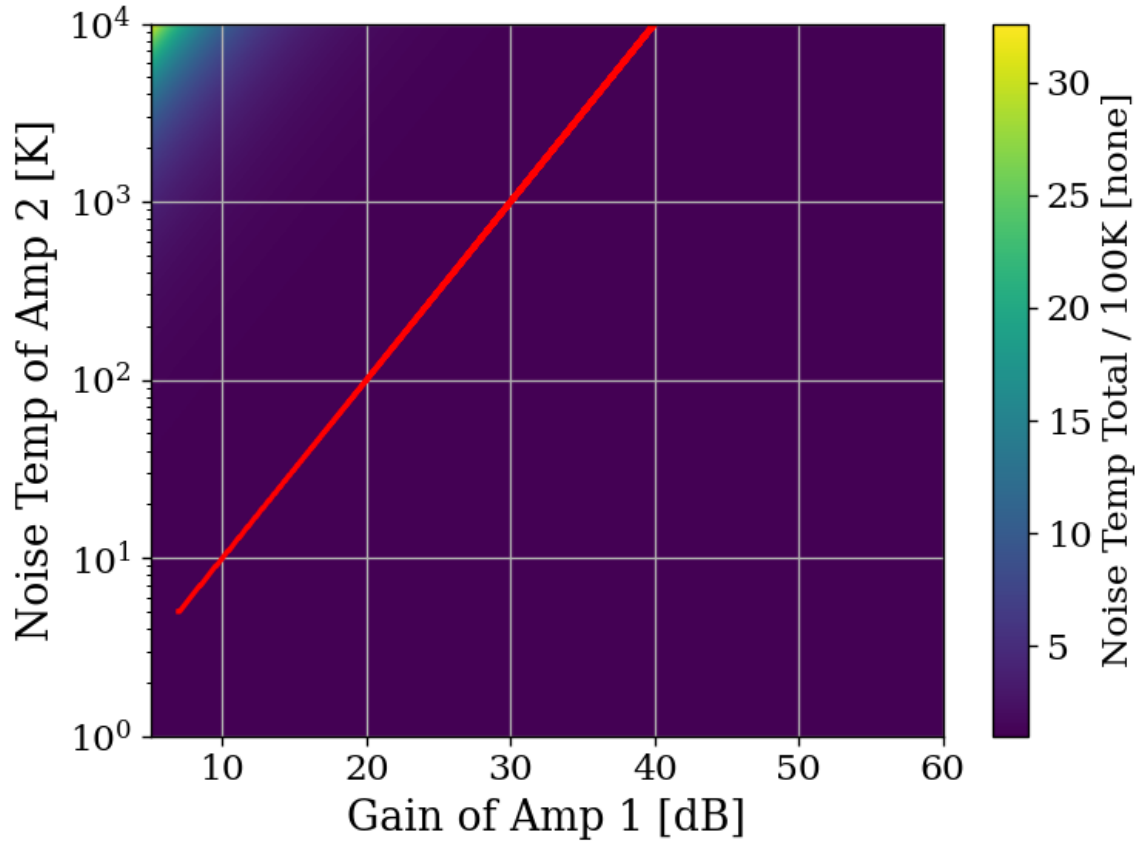


Figure 2.9: Cascaded noise temperature for a system with $n = 2$ amplifiers, normalized to noise temperature of amplifier 1 (the so-called LNA) = 100 K. Shown schematically (for $n = 3$) in Fig. 2.8. The first amplifier's noise temperature and gain (40 dB and 100 K, respectively) are roughly equivalent to the LNA used in phase 1A of the experiment[22]. The red curve shows where the system's noise temperature is 1% higher than LNA noise temperature. This shows that for a 40 dB, 100 K LNA, in order to change the system noise temperature by 1 K, a second-stage amplifier with a noise temperature of 10^4 would be required. Secondary amplifiers with noise temperatures closer to 500 K are realistic and inexpensive. Note that the red curve should continue but is cut off as a plotting artifact.

637 Here the total noise figure of n amplifiers can be shown to be

$$F_{\text{total}} = F_1 + \frac{F_2 - 1}{G_1} + \frac{F_3 - 1}{G_1 G_2} + \cdots + \frac{F_n - 1}{G_1 G_2 \cdots G_{n-1}}, \quad (2.29)$$

638 following the same derivation as Eq. 2.25. Since the noise temperature of a system depends

639 on the noise temperature a given amplifier divided by he gain which precedes it, a front-end
640 LNA with modest gain ensures the total noise figure of the the system is equal to it's noise
641 figure to very good approximation. This is shown in Fig. 2.9. We will use this approximation
642 and assert

$$\text{Amp Chain Noise} = \text{LNA Noise}, \quad (2.30)$$

643 where LNA here is taken to mean the first gain stage in the amplifier chain.

644 Noise figures are typically frequency dependent, though they vary slowly over frequency
645 and can be approximated as constant over narrow frequency bands. Noise figures are typically
646 given on the data sheet of the LNA [22], but can also be measured. Measurement of LNA
647 noise is covered in Sec. 3.1.1 and is shown in Fig. 3.4 (which is in good agreement with the
648 LNA's data sheet [22]).

649 The power contributed by the LNA's noise is simply given by

$$P_{\text{LNA}} = kT_e\Delta\nu \quad (2.31)$$

650 This is again the mean of a fluctuating power, just as 2.16.

651 2.1.5 ADC effects

652 “ADC effects” is a catch-all term that refers to power introduced by an analog-to-digital
653 converter. It contains are a three components, listed in order of importance;

$$\text{ADC Effects} = \text{Spurious Signals} + \text{ADC Noise Floor} \quad (2.32)$$

654 Equation 2.29 shows that (power) gain G introduced before a noisy element in the RF
655 chain reduces the relative contribution of that noise (power) by a factor of G . The same idea
656 applies to ADC effects, though one must be careful with the language used to describe this;
657 spurious *signals* are not noise, and the experiment's output *is* mostly noise.

658 **2.1.5.1 Spurious signals**

659 Spurious signals (also known as spurs) are coherent signals that are introduced into the signal
660 path at the ADC⁶. They are likely caused by candidates caused by RFI due to various clocks
661 in the PC in close proximity to the ADC. The coherence of spurs means they will pop up
662 above the noise with more averaging. Spurs don't degrade the SNR of the experiment in
663 the same way a noisy amplifier chain would; instead, they produce false positive candidates,
664 which must be excluded, similar to RFI discussed in Sec. 2.1.3. Similar to ADC noise,
665 they can be measured easily by terminating the input of the ADC and scanning. They
666 are investigated in Sec. 3.3.2 and shown in Fig. 3.15, where they are shown to be nearly
667 negligible, having been mitigated by the gain of the system. There is a single spur detected
668 after a few days in Run 1A (see Sec. 4.2.5), but for this simple analysis, we will assume spurs
669 are negligible.

⁶Note that these spurs described here are not the same as the spurs that are described by the ADC specification *spur free dynamic range* (SFDR). SFDR is measured in dBc, i.e. *relative* to a carrier. Since our “carrier” is broadband noise, each bin produces some spurs, which are -66 dBc [23] relative to itself. The aggregate of these spurs is also broadband and averages down with the experiment's noise. The SFDR spurs are negligible for an experiment that looks at a noise-like background.

670 **2.1.5.2 ADC noise**

671 ADC noise can simply be measured by terminating the input and taking a scan. This is the
672 same procedure used to measure spurs and can be seen in Fig. 3.15. The result is that ADC
673 noise is $\approx -130\text{dBm}/47.7\text{Hz}$; a factor of 10^5 lower than the thermal noise of the experiment
674 $\approx -81\text{dBm}/47.7\text{Hz}$, both output-referred⁷, which agrees with the ADC's data sheet [23].
675 Since ADC noise follows the same scaling as the experiment's thermal noise (Eq. 2.16), this
676 factor of 10^5 is independent of averaging, and ADC noise is totally negligible.

677 **2.2 Toy Analysis**⁸

678 With each of the terms of Eq. 2.1 defined in the previous section, we will now perform and
679 view several simulations of a simplified dark photon signal on a simplified background. This
680 section should provide intuition about the process of detecting a weak, narrow signal on a
681 background PSD of thermal noise. It is assumed the noise has been averaged a sufficient
682 number of times such that its PDF is Gaussian (discussed in Sec. 2.1.1.3). Furthermore,
683 following the discussion of Sec. 2.1, Eq. 2.1 can be simplified by setting RFI and ADC
684 Effects to zero and combining Thermal Noise (300 K) with Amp Chain Noise (100 K) into a
685 single term which represents the total of the noise in the whole system, $S_{\text{sys}} = P_{\text{sys}}/\Delta\nu_{\text{RF}} =$
686 $k(T_{\text{ant}} + T_{\text{LNA}})$. With these simplifications, the input-referred measured power of Eq. 2.1

⁷Technically it doesn't matter where they are referred since they are taken in ratio. As long as they are referred to the same point!

⁸Code for this section can be found at: <https://github.com/josephmlev/darkRadio/tree/master/thesis/ch2/toyAnalysis.ipynb>

687 reduces to

$$P_i = P_{DP} + kT_{sys}\Delta\nu_{RF} \left[1 \pm \frac{1}{\sqrt{N}} \right], \quad (2.33)$$

688 where $T_{sys} \equiv 400$ K, realistic for the experiment that is being simulated. Also, note that this
689 equation assumes the dark photon's line shape is much more narrow than $\Delta\nu_{RF}$ such that the
690 measured input-referred dark photon power is independent of $\Delta\nu_{RF}$. In the simulations, the
691 line shape will be modeled as a delta function as in Eq. 2.20. The signal will be introduced
692 simply by adding some power in a single bin to a Gaussian background in the frequency-
693 domain. Performing an FFT on a perfect (discretized) sine wave can cause it's power to
694 be split among adjacent bins depending on the ratio of the sample rate to the sine wave's
695 frequency. This can be minimized by windowing the time-domain data as is discussed in
696 Ch. 2 Sec. 2 of Ben Godfrey's thesis [24]. This effect is avoided by working in the frequency
697 domain and adding power to a single bin which is the method used here. A reminder that
698 throughout this thesis, code is available at github and is linked in the footnote of each section
699 title.

700 With a simple simulation framework in place, we can now begin to generate signal-
701 containing-spectra. Figure 2.10 qualitatively shows the 400 K system noise (input-referred
702 antenna plus LNA) averaging down, leaving a small signal visible. Further subsections in
703 this section will quantify this.

704 With a basic conceptual framework in place, it is now simpler to quantify signal detection
705 and the uncertainty on how many averages are required to detect a signal and have that
706 detection be significant in that it isn't a random fluctuation (false positive).

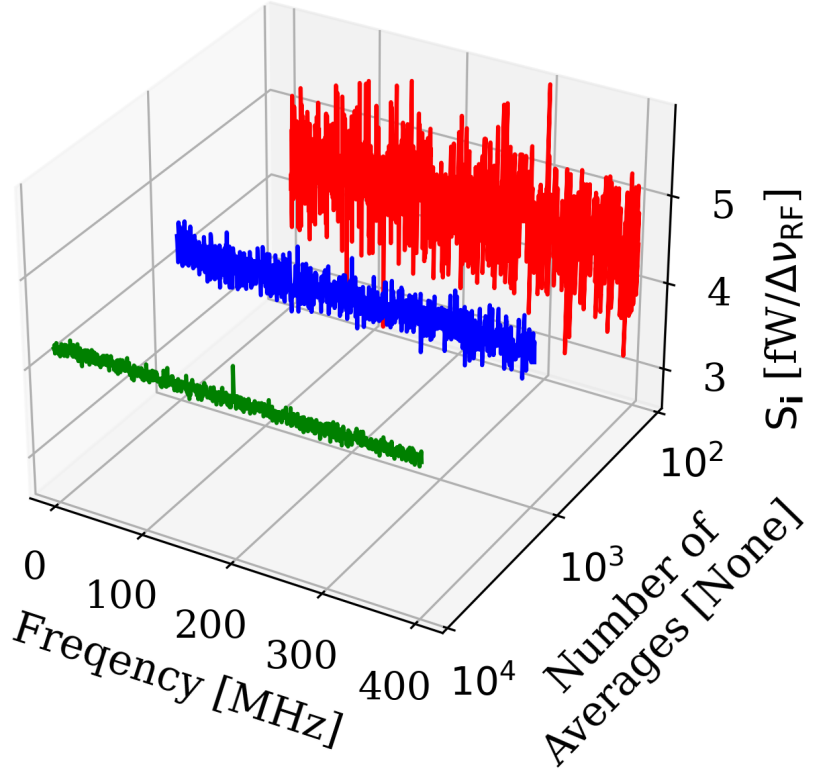


Figure 2.10: Input-referred power spectral density from simplified simulation illustrating noise averaging down to reveal a persistent, software-injected, dark photon proxy signal. The red, blue and green spectra represent 100, 1,000 and 10,000 averages, respectively. The power of the signal P_{DP} is set to 0.4 fW and it only occupies a single bin. The mean of the noise is $\approx 4.3 \text{ fW}/\Delta\nu_{RF}$ where $\Delta\nu_{RF} \approx 0.78 \text{ MHz}$. The standard deviation ranges between $0.41 \text{ fW}/\Delta\nu_{RF}$ and $0.041 \text{ fW}/\Delta\nu_{RF}$ for 100 and 10,000 averages respectively. Note that this factor of 10 reduction in noise is predicted by the Dicke radiometer equation Eq. 2.16 for a factor of 100 times more averaging, as is shown in the red and green curves. Noise represents a 300 K antenna into a 100 K LNA for a total system temperature of 400 K. Signal is in a single bin at 200 MHz with a delta function line shape, defined in Eq. 2.20.

707 2.2.1 Signal significance

708 The problem of the extraction of signal from noise is fundamentally a statistical one since,
 709 in general, both the signal and noise are random variables. A method for computing a

710 *significance threshold* (ST) must be established, such that any bin containing more power
711 than this threshold is X % significant. In this way, it is possible to have some known
712 confidence a given signal was not just a random fluctuation.

713 The probability that all N bins are less than z standard deviations $z\sigma$ for a standard
714 Gaussian distribution is given by

$$P(\max < z\sigma) = \left\{ \frac{1}{2} \left[1 + \operatorname{erf} \left(\frac{z}{\sqrt{2}} \right) \right] \right\}^N, \quad (2.34)$$

715 where P is the probability, $\operatorname{erf}(z)$ is the standard error function and z is real. Setting
716 this equal to 100%–X (where X is the *significance* or the desired probability a fluctua-
717 tion crosses the $z\sigma$ threshold assuming no signal), and inverting $\operatorname{erf}(z)$ yields a significance
718 threshold (ST). A convenient significance that was used in [25] is X = 5% corresponding to
719 a 5% probability that an observed fluctuation above this ST is due to chance rather than a
720 significant effect (i.e., a signal). A 5% ST for $2^{10}/2 = 512$ frequency bins⁹ works out to 3.9σ .

721 It should be noted that it is common in physics to discuss “ 5σ significance”. This means
722 that a given experiment has a $1 - \operatorname{erf}(5/\sqrt{2})$ probability (about 1 in 3×10^6) of a false positive.

723 The analysis of these normal spectra involves testing many independent frequency bins to see
724 if any one of them exceeds some threshold. It is helpful to view these bins as “independent
725 experiments”, each involving a random draw from the same parent Gaussian distribution.

726 In this context, we discuss global significance (all of the bins) in contrast to local significance
727 (a single bin). Setting a global 5% significance threshold is equivalent to setting a local

⁹Note that a real FFT produces half the number of frequency bins as an output compared to the time domain sample it received, hence the factor of 2 established in Fig. 2.4

728 threshold of 3.9σ given 512 bins.

729 One concept that can assist in choosing the significance is known as the *cost* of a decision.
730 If an experiment requires a facility that charges by the hour and where the schedule is
731 set years in advance, a false positive is quite expensive since it will lead to publicity and,
732 ultimately, humiliation. A follow-up experiment will have to take out more expensive time
733 to verify the results, and until that happens, theorists will spend their time rewriting physics
734 to explain the result of a random fluctuation. In this case, the global significance should
735 be quite low to avoid these high-cost outcomes, hence the 5σ discussed in the previous
736 paragraph.

737 In the case of the dark radio experiment, a false positive is quite inexpensive. If a signal
738 is detected, just repeat the experiment. For Run 1A, this is 9 days of averaging which is
739 mostly passive and is little more than an annoyance. If a signal is detected at the same
740 frequency, things become interesting. This concept of cost is discussed formally in Appendix
741 1 of Extraction of Signals From Noise by Wainstein and Zubakov [26].

742 For this reason, a significance of 5% (i.e. 5% chance of a false positive) is acceptable for
743 this experiment, where it is certainly not acceptable at the LHC.

744 2.2.1.1 Computing an exclusion limit

745 With the significance threshold (ST) defined for a spectrum containing a signal in the previ-
746 ous subsection, we turn briefly to the concept of an exclusion limit. In the actual experiment,
747 no signals were detected. In this case, the null result must be translated into an exclusion
748 limit, as in Fig. 5.2. While this section on toy analysis looks at small signals riding on noise

749 spectra, it can be easy to lose sight of the fact that no signal was observed.

750 It is tempting to draw a line above the spectrum, claim no signals were observed above
751 it, and cite that as the exclusion limit. This is the red dashed line in Fig. 2.11. However,
752 this line is riding on the thermal background and is actually significantly higher than the
753 true exclusion limit, which is shown in dashed green. The mean μ must be subtracted from
754 this upper (red) line to compute the exclusion limit. In Fig. 2.12, the exclusion limit is
755 pushed down with additional averaging, resulting in the detection of a small signal shown as
756 an orange dot. The frequency-dependent exclusion limit from the actual Run 1A data run
757 is shown in Fig. 4.8.

758 With the derivation of the significance threshold complete, the next subsection will focus
759 on predicting the amount of time.

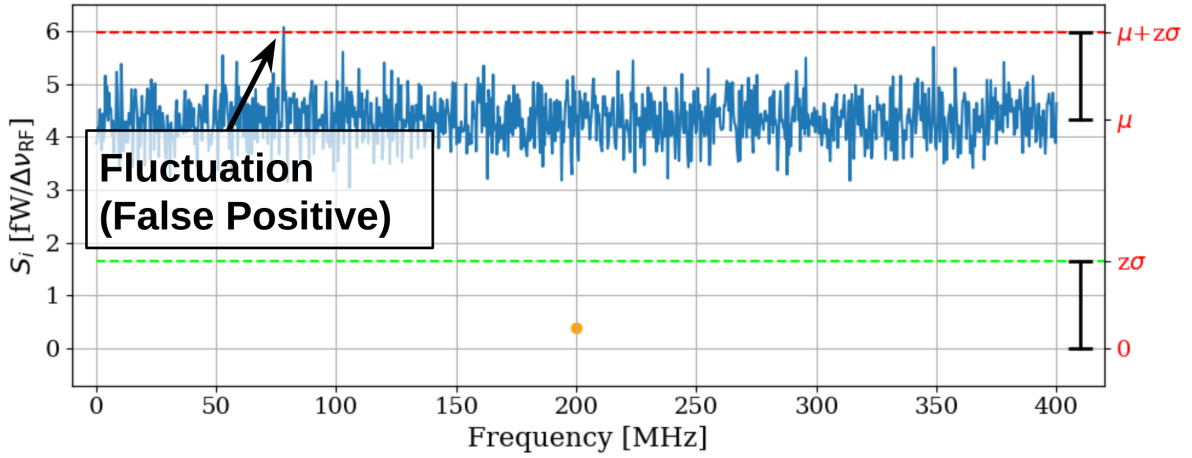


Figure 2.11: Simulated, input-referred noise spectrum containing small signal at 200MHz. The signal power = 0.4 fW, system temperature = 400 K and $N_{avg} = 100$; the same as is shown in the red spectrum of Fig. 2.10. The 0.4 fW signal is shown as an orange point. This power is added to the random background, so the measured power in the bin at 200 MHz is a Gaussian random variable given by Eq. 2.33; the mean is shifted up by the power contained in the signal. The dashed red line shows $\mu + z\sigma$, where z was derived in section 2.2.1. The detection threshold (dashed green line) is the red line minus the mean, $(\mu + z\sigma) - \mu = z\sigma$. This shows that the detection threshold is set by *fluctuations* of the measured power spectrum and not its mean. Note the detection at approximately 75 MHz; this is a random fluctuation and is expected to occur in 5 out of 100 simulations of these spectra since the significance used to calculate the ST was set at 5%.

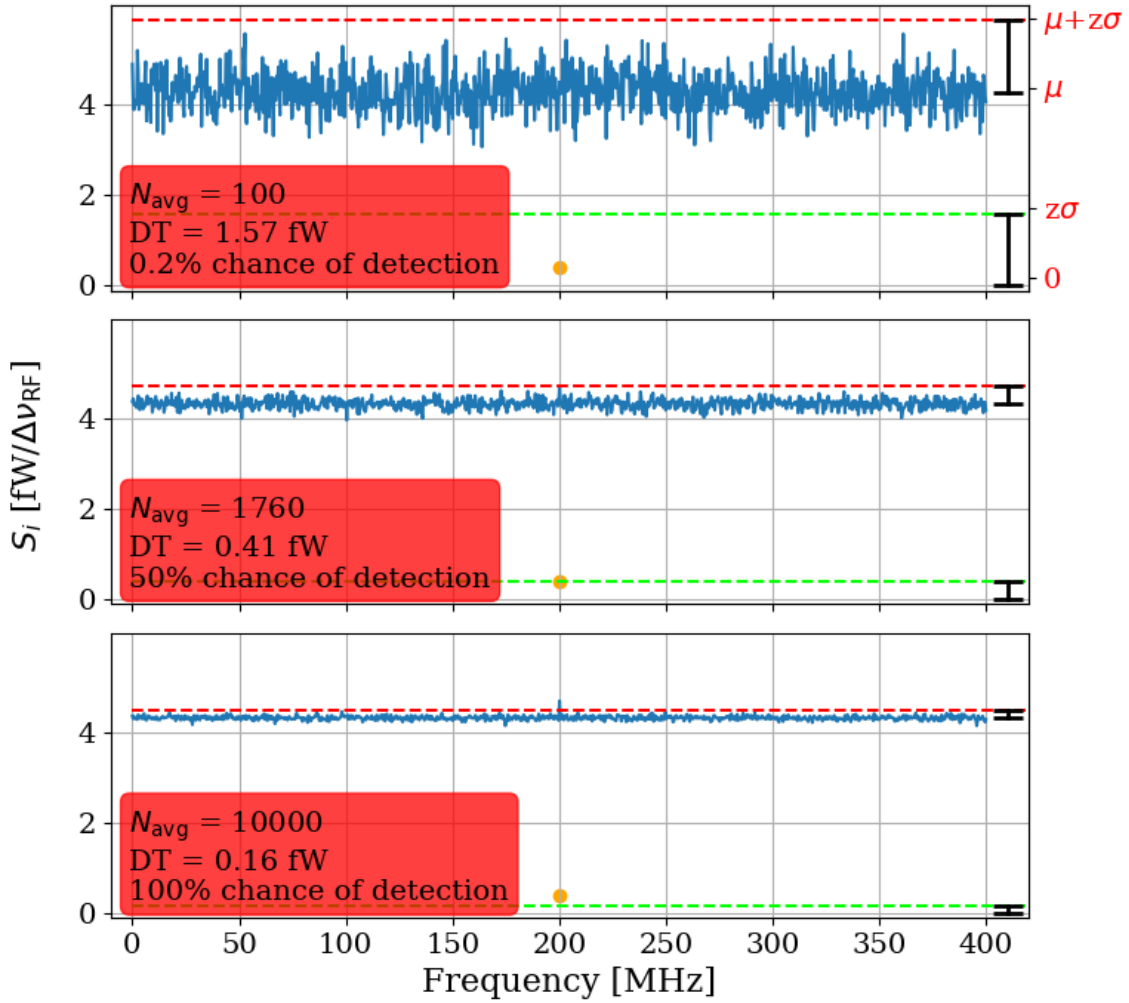


Figure 2.12: Simulated, input-referred noise spectrum containing small signal at 200MHz. The signal power = 0.4 fW, system temperature = 400 K and N_{avg} = 100, 1,760 and 10,000; the first and last are shown as the red and green spectra respectively in Fig. 2.10. The 0.4 fW signal is shown as an orange point. The chance of detection is computed via a simple Montie Carlo where 100,000 similar spectra containing noise and signal are generated, and the number of times the measured power at 200 MHz is greater than $\mu + z\sigma$ (red dashed line). The full set of statistics from this Montie Carlo is shown in Table 2.1. The detection threshold (DT, dashed green line) is $(\mu + z\sigma) - \mu = z\sigma$. Note that red labels on the right Y-axis are suppressed for the second and third subplots to prevent clutter, but they are the same as the first subplot

760 **2.2.2 Predicted time to detection**

761 To conclude this subsection, Fig. 2.13 fills in the gaps between the three sub-plots shown
762 in Fig. 2.12. The continuous detection threshold is shown to decrease following $1/\sqrt{N}$
763 shape given by Eq. 2.16. The intersections with this curve and the $1-\sigma$ uncertainty of the
764 background give the $1-\sigma$ uncertainty on the number of averages required for a known signal
765 and background. Table 2.1 summarizes the statistics for the probability of detection for a
766 few numbers of averages.

Number of Averages	True Pos. [%]	False Neg. [%]	False Pos. [%]	True Neg. [%]
100	0.2	99.8	5.7	94.3
971	16.3	83.7	5.5	94.5
1,760	49.8	50.2	5.7	94.3
2,782	83.8	16.2	5.7	94.3
10,000	100.0	0.0	5.6	94.4

Table 2.1: Statistics of simple Monte Carlo simulation for the probability of signal detection in the toy analysis. Number of averages chosen based on Fig. 2.13. 100 and 10,000 averages show extreme cases, 1760 is a 50% chance of detection, and the two remaining values show the $\pm 1\sigma$ uncertainty band (shaded red region in Fig. 2.13).

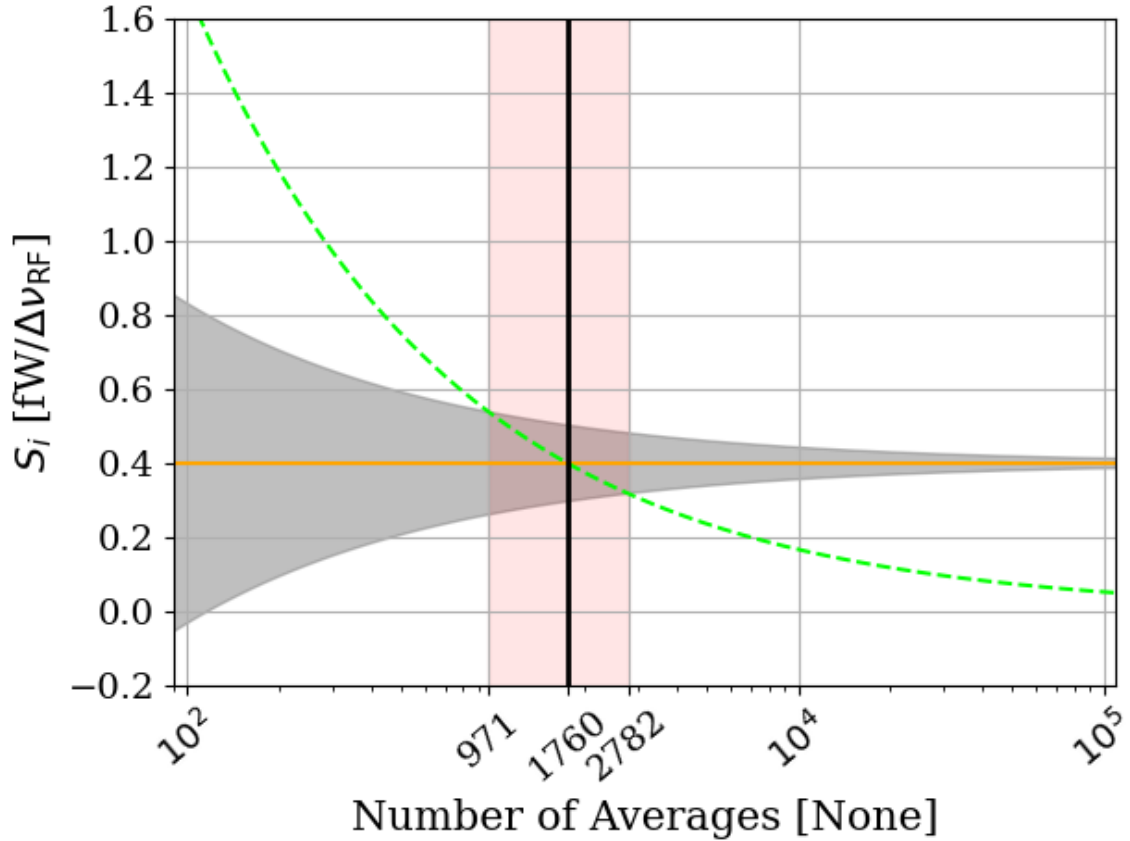


Figure 2.13: Predicted time to detection for the toy analysis spectra shown throughout this section. This is a companion to Fig. 2.12 and shows all numbers of averages between the three subplots shown in that figure, though only at a single frequency bin; 200 MHz in the case of the previous figures in this section. Orange line represents the known, injected signal, shown as orange points in Fig. 2.12. Gray shaded region shows the standard deviation of the noise σ , which is equivalent to the uncertainty on the measured power. It is given by Eq. 2.16, and scales with the square root of time. Dashed green curve is the exclusion limit defined in Sec. 2.2.1.1. It is also shown as a dashed green line in Fig. 2.12. Finally, the red shaded region shows the intersection of the exclusion limit (dashed green) with measurement uncertainty (shaded gray), which gives the $\pm 1\sigma$ uncertainty on the number of averages required to detect the signal. The detection statistics from a simple Monte Carlo simulation at a few points from this plot are shown in Tab. 2.1. This figure is a recreation of Fig. 3 in [4].

767 2.3 Thermal Noise in a cavity: Thermal Wiggles

768 This section is concerned with the topic of variations of thermal noise emerging from a cavity;
769 “Thermal Wiggles”. Throughout this experiment, this was a challenging concept since the
770 theory outlined in Sec. 2.3 predicts the experiment will measure a frequency-independent
771 noise spectrum, and it doesn’t. This theory will be expanded upon, the data that seem
772 not to conform to this theory will be presented, the reasons for this disagreement will be
773 discussed, and finally, an experiment that tests this understanding will be presented.

774 2.3.1 Theory of thermal radiation in a cavity

775 In his 1946 paper The Measurement of Thermal Radiation at Microwave Frequencies [14],
776 Robert Dickie presented a thought experiment to derive the aperture of a matched antenna
777 from thermodynamic arguments. This was previously discussed in Sec. 2.1.1.2.

778 To recap the argument; if an antenna (in a black cavity) and matched load are matched
779 to a transmission line and in thermal equilibrium (the situation presented in Fig. 2.3), the
780 net power flow in the line must be zero by the second law of thermodynamics. If there was
781 a power flow, one of the environments would warm up, resulting in spontaneous pumping of
782 heat. An interesting way to model this situation is by treating the antenna as an aperture
783 in the cavity, as pointed out in [27].

784 A simpler model removes the antenna and load altogether. Although removal of the
785 antenna also removes the ability to perform the measurement, this is a useful thought exper-
786 iment. In Fundamentals of Statistical and Thermal Physics [28], F. Reif uses four examples

787 to explore the radiation field $f_\alpha(\kappa, \mathbf{r})$ (wave vector κ at position \mathbf{r} with polarization α)
 788 within cavities connected by an aperture (see Fig. 2.14). All cavities and materiel contained
 789 within them are presumed to be in thermal equilibrium. As we shall see, this function is
 790 independent of position, direction, polarization and specifics of the cavity. It can be written
 791 simply as $f(|\kappa|)$, where the dependence on wave number is simply given by Eq. 2.6.

$$f_\alpha^{(1)}(\kappa) = f_\alpha^{(2)}(\kappa)$$

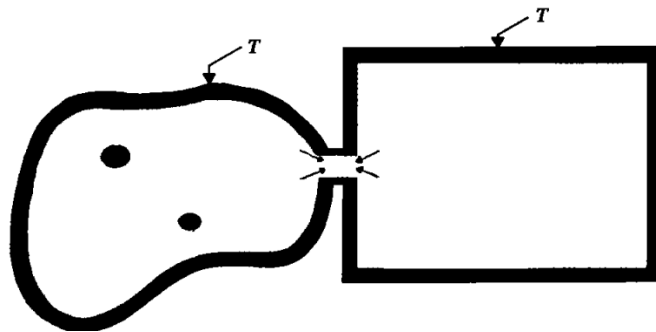


Figure 2.14: Two cavities in thermal equilibrium of arbitrary shape, material and physical contents contain equivalent radiation fields $f_\alpha(\kappa, \mathbf{r})$. Figure from Reif [28].

792 **1. Independence of Position:** The radiation field inside an enclosure is homogeneous,
 793 meaning $f_\alpha(\kappa, \mathbf{r}) = f_\alpha(\kappa)$, independent of position \mathbf{r} . If the radiation field depended
 794 on position, two identical bodies at temperature T placed at different points in the
 795 enclosure would absorb different amounts of radiation, leading to a temperature dif-
 796 ference.
 797 **2. Independence of Direction:** The radiation field is isotropic, meaning it depends
 798 only on $|\kappa|$ and not its direction. If this were not true, then bodies placed in the
 799 enclosure would absorb different amounts of energy based on orientation.

800 3. **Independence of Polarization:** The radiation field is unpolarized, meaning $f(|\kappa|)$
801 is independent of the polarization index α . If it depended on polarization, bodies
802 surrounded by polarizing filters would absorb different amounts of radiation depending
803 on the orientation, leading to temperature differences.

804 4. **Independence of Enclosure Shape and Contents:** The function $f(|\kappa|)$ is inde-
805 pendent of the shape, volume, and material of the enclosure, as well as the bodies
806 contained within. The argument is that if $f^{(1)}(|\kappa|)$ and $f^{(2)}(|\kappa|)$ were different for two
807 enclosures at the same temperature T , then connecting them would result in unequal
808 radiation transfer. Therefore, $f(|\kappa|)$ must be the same across different enclosures.

809 To further flush out argument four, picture a photon entering a metallic cavity (emissivity
810 < 1) through a small hole as in Fig. 2.15. At each bounce, the photon has a probability of
811 absorption given by the emissivity (a photon hitting a perfect black body has a 100% chance
812 of being absorbed). As long as the geometries of the cavity and aperture allow a photon to
813 bounce many times before it escapes, even a highly reflective cavity will behave like a black
814 body. This is because when a photon enters, it is likely to be absorbed and a new photon will
815 be emitted with a random wavelength drawn from the blackbody spectrum corresponding
816 to the temperature of the walls. (Fig. 2.2).

817 The conclusion is rather surprising; a cavity with a small aperture will behave as a
818 black body, and the spectrum emanating from a black body is a universal function that is
819 independent of the cavity and its modes. Therefore, **a well-matched antenna in a cavity**
820 **will not measure the modal structure of the cavity.** This seems to defy intuition.

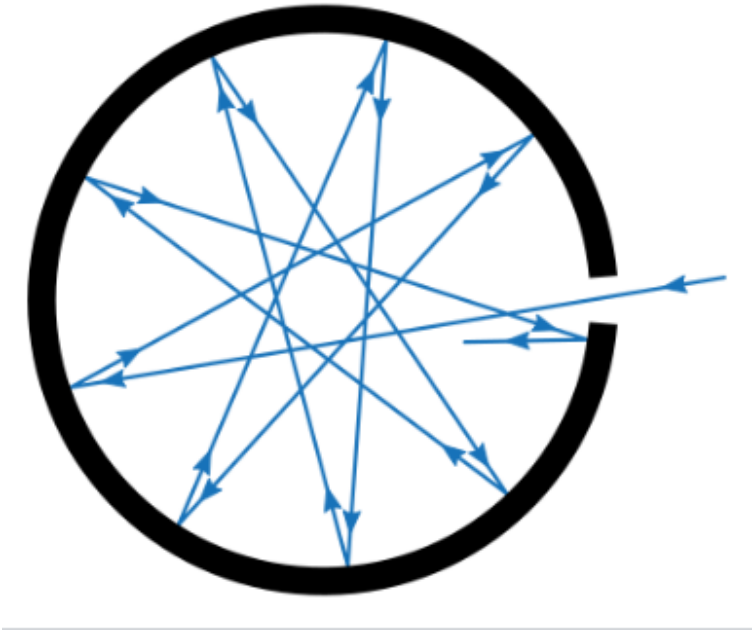


Figure 2.15: A cavity with a small hole behaves like a black body as long as the probability of absorption $\ll 1$. The probability of absorption at each reflection is given by the emissivity, so the total probability of *reflection* is the emissivity raised to the power of the average number of bounces. Figure from Wikipedia.

821 Cavities are resonators, and resonators... resonate?

822 The resolution to the seeming discrepancy is that this intuition only holds outside of
823 equilibrium, a situation that is nearly ubiquitous in engineering contexts. A resonant cavity
824 resonates because photons are pumped in faster than they can be absorbed by the walls and
825 remitted with a thermal distribution. In this out-of-equilibrium case, the photons interfere in
826 such a way as to excite cavity modes. Turn the amplitude of the source down to $\approx kT$, and
827 the modes vanish. This case, among others, will be investigated in the following subsections.

828 **2.3.2 Inspection of thermal noise spectra**¹⁰

829 The theory outlined above predicts the (input-referred) spectrum of an antenna in a cavity
830 should not vary with frequency if there is thermal equilibrium between the cavity and the
831 receiver system¹¹. A real measurement will take place after an amplifier (in other words,
832 will be output-referred), and will vary due to the gain and noise figure of the amplifier. A
833 simple way to correct for the amplifier is to compare the spectrum between an antenna and
834 a terminator since both will have identical gain and amplifier noise contributions. Since we
835 are more focused on the qualitative *shape* of the spectrum and not absolute input referred
836 power, this method is acceptable. A comparison of antenna and terminator data from an
837 identical amplifier chain is shown in Fig. 2.16.

838 The variations are unexpected in light of the theory presented in the previous subsection.

839 In the following subsection, the thermal spectrum emerging from a simple resonator will be
840 presented.

¹⁰Code for this section can be found at: https://github.com/josephmlev/darkRadio/tree/master/daqAnalysisAndExperiments/run1p4/thermalNoiseVsH/thermalWiggles_writeup.ipynb

¹¹this assumes $h\nu \ll kT$ (Rayleigh-Jeans limit), an ideal antenna aperture $\propto \lambda^2$, and an impedance match between the antenna and amplifier. The final assumption will be relaxed in Sec. 2.3.8.

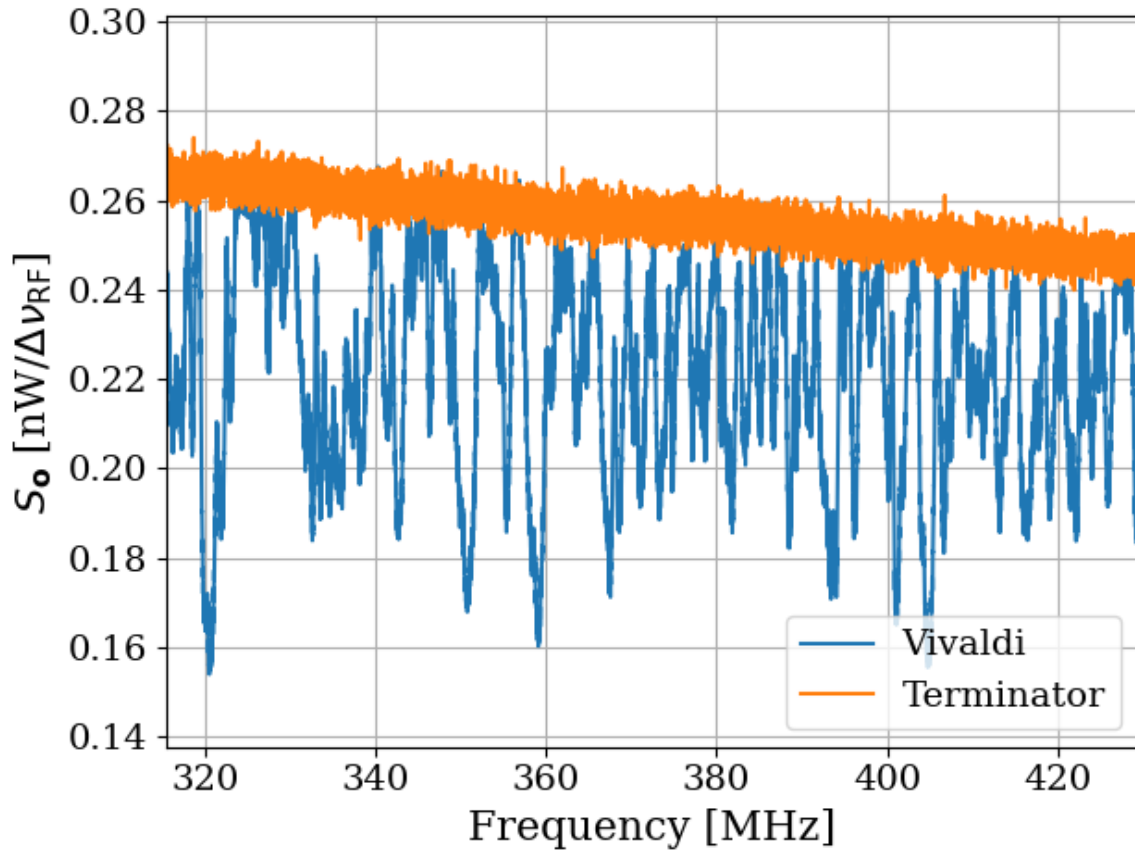


Figure 2.16: Output-referred Vivaldi antenna and terminator thermal spectra as measured through an amplifier chain ($G \sim 68$ dB, noise temperature ~ 120 K). The Vivaldi is inside the shielded room. Both spectra represent about 1 second of data, with $\Delta\nu_{\text{RF}} = 9.5$ kHz. The Vivaldi antenna is in a single position throughout all averaging, in contrast to the technique where it moves, outlined in later chapters.

2.3.3 A simple resonator: shorted coax cable

A coax cable that is shorted on one end and matched to a measurement device ¹² on the other

is a simple resonator. The short provides a boundary condition demanding the voltage goes

to zero¹³ while the measurement device, being matched, absorbs the wave. A “closed-open”

¹²In the entirety of this section, a Pasternack PE15A-1012 will be used as the front end amplifier.

¹³Similarly, an open termination will force the *current* to zero, resulting in a similar resonator, though with a 180-degree phase shift.

845 resonator such as this will resonate with frequency

$$\nu = \frac{v(2n - 1)}{4L}, \quad (2.35)$$

846 for integer $n > 0$, where v is the wave speed in the cable and L is the length. For a
847 185 cm cable with velocity factor = 69.5% (i.e. $v = 0.695 c$), this works out to a first mode
848 at 28.2 MHz and following modes every 56.4 MHz. A schematic of the setup is shown in
849 Fig. 2.17, and the output power spectrum is shown in ratio to a terminator in Fig. 2.18.
850 Also shown in Fig. 2.18 is an open termination at the end of the cable in place of the short.
851 Fitting the peaks ¹⁴ reveals the average spacing between peaks is 55.2 ± 2.4 MHz, in good
852 agreement with the prediction of 56.4 MHz of Eq. 2.35.

853 By the fluctuation-dissipation theorem, the loss of the cable will dissipate some thermal
854 noise into the system, which can excite the cable. As discussed in Sec 2.3.1, if the resonator
855 (cable) is in thermal equilibrium with the measurement device, a frequency-independent
856 power spectrum is expected. The deviation from this expectation is surprising because the
857 data seem to be in contradiction with thermodynamics. Now, a cable is not a particularly
858 good resonator ($Q \lesssim 10$), so the effects are rather small here, but the simplicity of the system
859 makes it one that is worth exploring.

860 One assumption which is critical to the above logic is that of equilibrium. The amplifier
861 is a likely culprit for breaking this equilibrium, so a test that can remove the amplifier's
862 ability to interact with the resonator is worth pursuing. Fortunately, such a test is quite
863 simple to implement using a circulator ¹⁵.

¹⁴Code for this section can be found at: https://github.com/josephmlev/darkRadio/tree/master/daqAnalysisAndExperiments/run1p4/thermalNoiseVsH/thermalWiggles_writeup.ipynb

¹⁵I got one for \$36 on Ebay!



Figure 2.17: A coax cable with a short on the end and a matched measurement device on the other behaves like a “closed-open” resonator. Replacing the short termination with an open (not shown here) produces a similar resonator, though with a 180-degree phase shift.

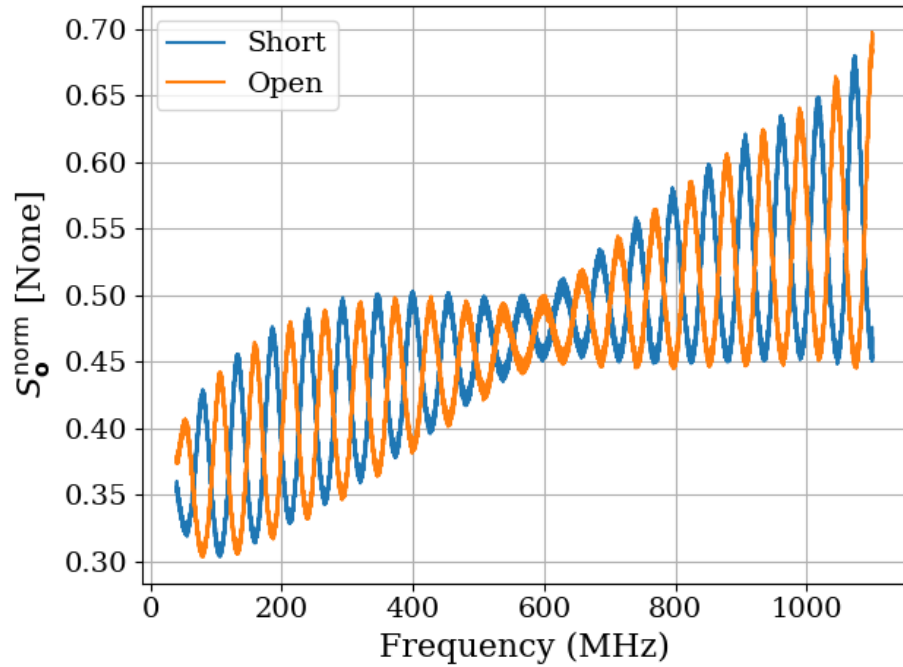


Figure 2.18: Power spectra of short (blue) and open (orange) terminations at the end of 1.85 m of RG400 coax cable (velocity factor = 69.5%). Schematic of this set-up is shown in Fig. 2.17. These spectra are normalized to the spectrum of a terminator, which was measured through the same amplifier chain. For example, when $S_o^{\text{norm}} = 0.5$, the power measured in this setup is half of the power measured by a terminator through the same amplifier chain. The average spacing between peaks is 55.2 ± 2.4 MHz, in good agreement with the prediction of 56.4 MHz of Eq. 2.35.

864 **2.3.3.1 RF circulators**¹⁶

865 A circulator is a three-port, non-reciprocal device that allows power to flow only in specific

866 ways between its ports¹⁷. A schematic symbol is shown in Fig. 2.19.

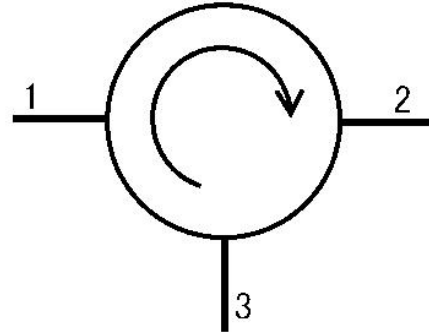


Figure 2.19: Schematic symbol of a circulator. Power can only flow from ports 1 to 2, 2 to 3 and 3 to 1. Image from Wikipedia.

867 The (linear) S-parameters [29, 30] of an ideal circulator are given by the matrix

$$S = \begin{pmatrix} 0 & 0 & 1 \\ 1 & 0 & 0 \\ 0 & 1 & 0 \end{pmatrix}. \quad (2.36)$$

868 In other words, in an ideal circulator, $S_{12} = 0$, so power can not flow from port 2 to port

869 1, while $S_{21} = 1$, so power can flow from 1 to 2. Also of note, the diagonal elements $S_{ii} = 0$,

870 meaning ports do not reflect power.

871 A Teledyne C-0S03A-3M RF circulator has an approximate bandwidth from 490-510 MHz

872 and was available inexpensively on eBay, so it is used for testing. A photo of it is shown in

¹⁶Code for this section can be found at: https://github.com/josephmlev/darkRadio/tree/master/thesis/ch2/circulatorData/SParameter_circulator/calc3portSPParam.ipynb

¹⁷See Ch. 9 of Pozar's *Microwave Engineering* for a detailed reference.

873 Fig. 2.20, and its S-parameter data are shown in Fig. 2.21. Note that a circulator with one
874 port terminated is sometimes known as an “isolator”, but I will refrain from using this term.



Figure 2.20: Photo of Teledyne C-0S03A-3M RF circulator. Lines in the background are collage-ruled lined paper (\approx 7mm spacing) for scale.

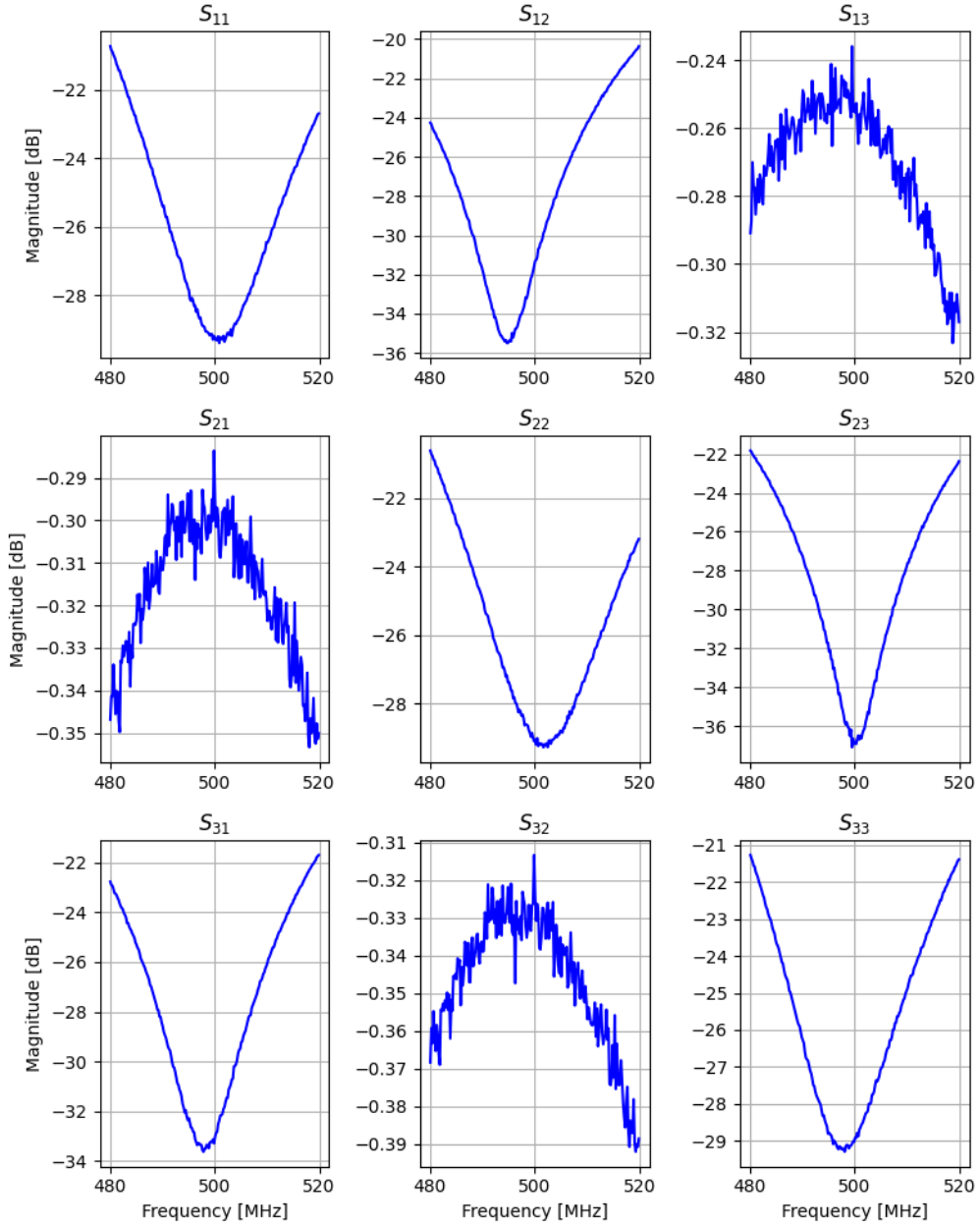


Figure 2.21: 3-port, frequency-dependent S-parameter data for Teledyne C-0S03A-3M circulator. Data taken by Ben Godfrey and Andrea Lopez Arguello with 2-port VNA with the circulator's unused port terminated. Circulator is rated for use between 490 and 510 MHz. These data show good agreement with Eq. 2.36. Note that magnitude is in dB, so these data are proportional to power, i.e. the square of linear S-parameters.

875 **2.3.4 A simpler resonator: shorted coax cable and circulator**

876 In light of the variations observed in Fig. 2.18, a similar measurement was made using
877 a circulator in order to isolate the coax resonator from any effects of the amplifier. The
878 schematic of this setup is shown in Fig. 2.22, and resulting the spectrum is shown in Fig. 2.23.
879 This is an interesting measurement because any net power flow from the amplifier will be
880 absorbed by the terminator on port three since it presents a good impedance match. This
881 net power flow has the potential to cause a temperature change in the terminator; however,
882 it is in a thermally-conductive metal can that is exposed to the air, which serves as a heat
883 bath and holds it very close to room temperature. The coax resonator will just see the
884 Johnson noise of the room temperature terminator in equilibrium with the Johnson noise
885 caused by its internal loss. The overall effect is a resonator that is in thermal equilibrium
886 yet is able to be measured by an extremely sensitive spectrum analyzer.

887 The result of introducing the circulator and matched load on port 3 is the removal of the
888 variations that were seen without the circulator (Fig. 2.23).

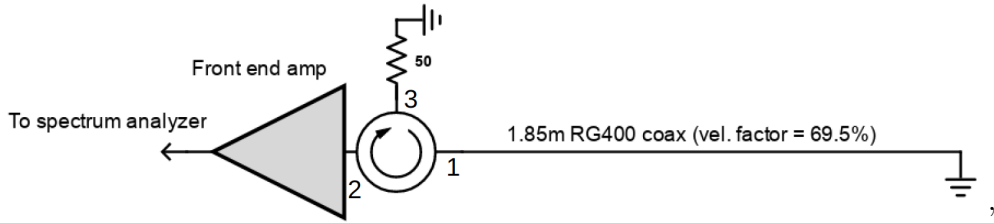


Figure 2.22: A coax cable with a short on one end and a circulator isolating the system from the amplifier.

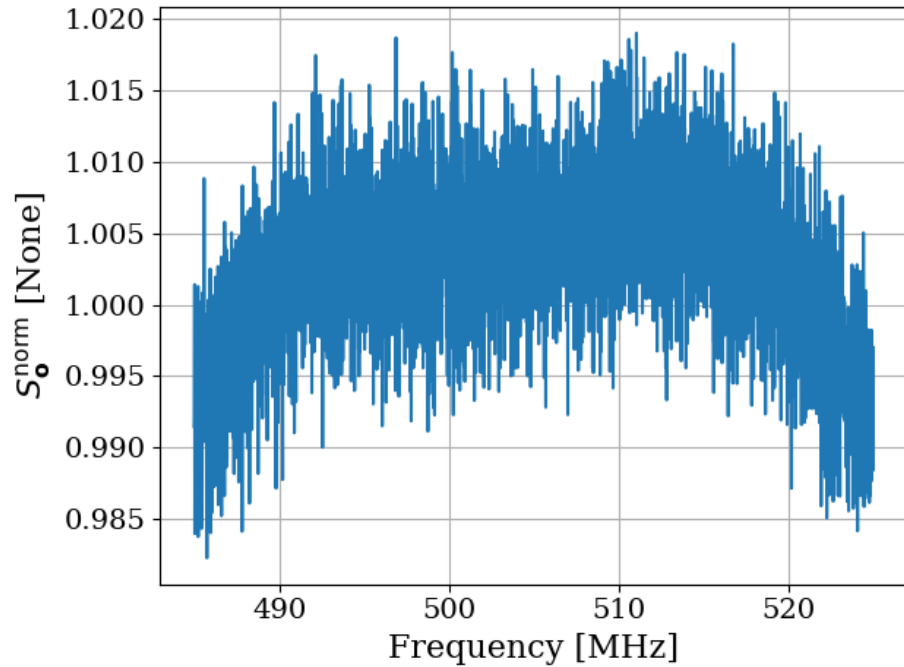


Figure 2.23: Power spectrum of 185 cm coax resonator as measured through a circulator. Short termination at the end of the cable as depicted in Fig. 2.22. The amplitude of the variations in this spectrum is on the order of half a percent and hardly visible under the noise. They are much smaller than those at the $\sim 15\%$ level without a circulator (Fig. 2.18). Also, note this spectrum is normalized to a terminator through the same amplifier chain and very close to 1. The normalized spectrum without the circulator shown in Fig. 2.18 was significantly lower, around 0.5. Note that the peak-to-peak frequency variations of the cable without a circulator (Fig. 2.18) are ≈ 55 MHz, and would be visible in the ≈ 30 MHz span shown here. This span is limited by the circulator.

889 **2.3.5 A more complex resonator: antenna in room**

890 Similar to the coax resonator shown in Fig. 2.17, the antenna data presented in Fig. 2.16
891 are of a resonator (antenna-room system) which is being measured by an amplifier. The
892 experiment in the previous section suggests that the amplifier seems to have an effect on
893 the delicate thermal equilibrium, which can be mitigated by including a circulator. The
894 experimental set-up for the antenna in the room is shown in Fig. 2.24, and the data from
895 this setup is shown in Fig. 2.25.

896 The result is striking. The theory outlined early in the chapter predicted the noise
897 power spectrum of an antenna in a cavity will look the same as a matched terminator;
898 -174 dBm/Hz, independent of frequency. The Dark E-Field Radio Experiment measures
899 just such a spectrum, but comparing a terminator and antenna in Fig. 2.16, they are remark-
900 ably different; the Vivaldi has large variations. However, introducing a circulator to the set
901 up such as in Fig. 2.24 removes these variations. Compare blue/orange curves in Fig. 2.25.

902 A nice test case would be to measure the thermal noise of an extremely high Q cavity
903 after carefully ensuring the radiation that is allowed to enter has a black body spectrum of
904 the same temperature of the cavity. This is nicely demonstrated in a few places, notably by
905 Cervantes et. al with a cavity of $Q = 10^{10}$ (!!!) [18]. When care is taken to create equilibrium
906 here, the resulting spectrum is flat, even on a frequency span that includes the resonance
907 (Fig. 2). When this equilibrium condition is broken, the cavity resonance becomes visible
908 (Fig. 10).

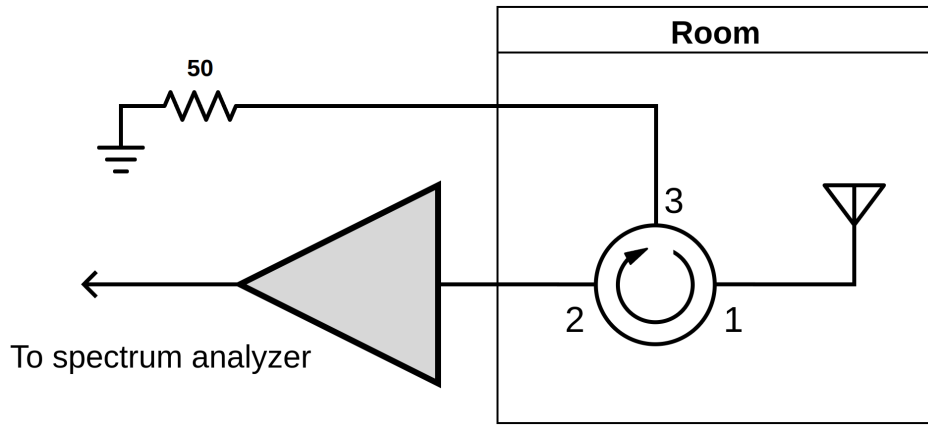


Figure 2.24: Schematic of experimental set-up using circulator to isolate the antenna from amplifier effects.

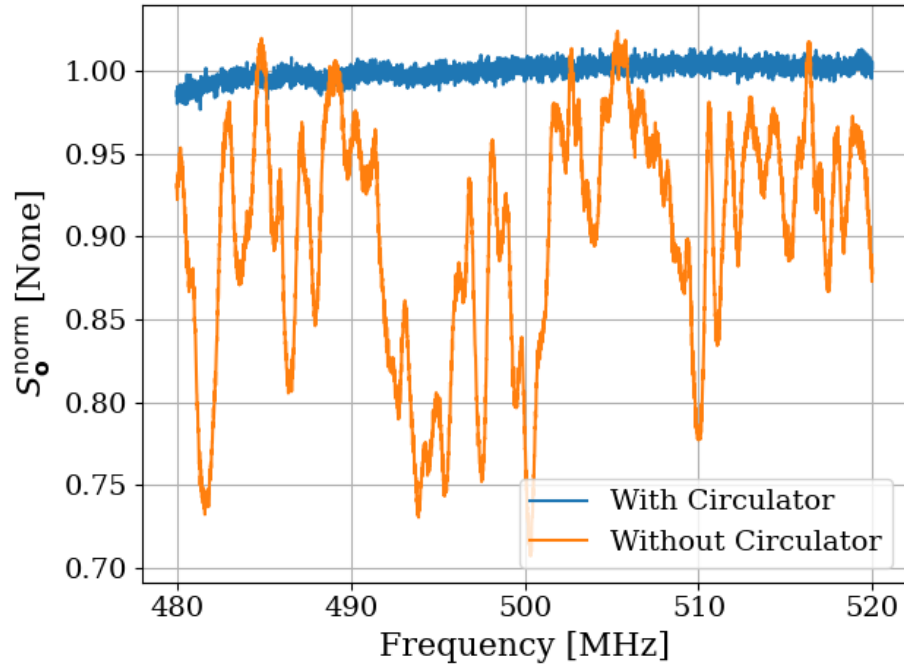


Figure 2.25: Normalized power spectrum for Vivaldi antenna in the room with/without circulator (blue/orange). This setup is shown schematically in Fig. 2.24. The normalized spectrum of the same antenna in the same position is shown with the circulator removed in orange for reference. This orange spectrum is the same as that shown in Fig. 2.16, but here it has been normalized to a terminator measured through the same amplifier chain. The terminator's spectrum is also shown in Fig. 2.16.

909 **2.3.6 Effective temperature of amplifier**

910 At this point, the seemingly obvious explanation is that the amplifier, being warm, is sourcing
911 more power than it's absorbing. To test this theory, two amplifiers can be placed input-to-
912 input as shown in Fig. 2.26. The noise power emerging *out* of the amp-under-test's input will
913 be measured by the front-end amplifier. This amplifier has a noise temperature $\sim 100\text{ K}$, so
914 it should be sensitive to very small variations in power. The data from the set-up is shown
915 in Fig. 2.27. Also shown in this figure are the spectra of the amp-under-test replaced by
916 both short and open terminations for reference.

917 An important number to keep in mind is the noise floor of this detector and what it looks
918 like in the dimensionless units shown. This is set by the noise temperature of the front end
919 amp, $\sim 100\text{ K}$. If the load-under-test were at 0 K , the power measured $S_{0\text{K}}^{\text{meas}}$ would be only
920 that of the front end amp. Taken in ratio to a 300 K matched terminator measured by the
921 same amp chain,

$$\frac{S_{0\text{K}}^{\text{meas}}}{S_{300\text{K}}^{\text{meas}}} \approx \frac{0 + 100\text{ K}}{300 + 100\text{ K}} \quad (2.37)$$

$$= 0.25, \quad (2.38)$$

922 where the factors of Boltzman's constant k and the measurement bandwidth $\Delta\nu_{\text{RF}}$ were
923 suppressed since they cancel immediately.

924 Thus, anything with an apparent noise temperature $\ll 100\text{ K}$ will appear with a dimen-
925 sionless power spectral density of ~ 0.25 in Fig. 2.27.

926 This phenomenon actually has been discussed in the literature[5].¹⁸, which I will provide
927 a brief summary of.

928 In this case, two amplifiers are placed back to back on either side of a transmission
929 line. When a particle interacts with the transmission line, a pulse is detected at each of the
930 amplifiers, and the difference in time provides a means to work out the position the particle
931 came in along the line. It is advantageous in this case to minimize the noise emanating out
932 of the inputs of these amplifiers. By tuning the reactance of the input of these amplifiers,
933 they can absorb a net power, putting them at an “effective temperature” lower than their
934 physical temperature.

935 In the case of off-the-shelf Pasternack RF amplifiers, this was likely not an intentional
936 effect. However, the data presented here seem to agree with the idea that the amplifiers have
937 an effective temperature $\ll 100\text{ K}$.

938 In the next subsection, I will demonstrate that by changing the temperature of the
939 matched load outside the shielded room (shown in Fig. 2.24), the amplitude of the thermal
940 wiggles can be controlled.

¹⁸I am very grateful to Greg Wright for pointing this out.

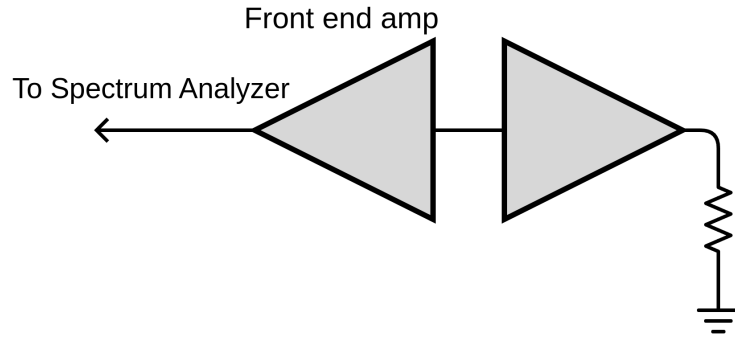


Figure 2.26: Schematic of set-up to measure the noise emerging *out* of an amplifier's input.

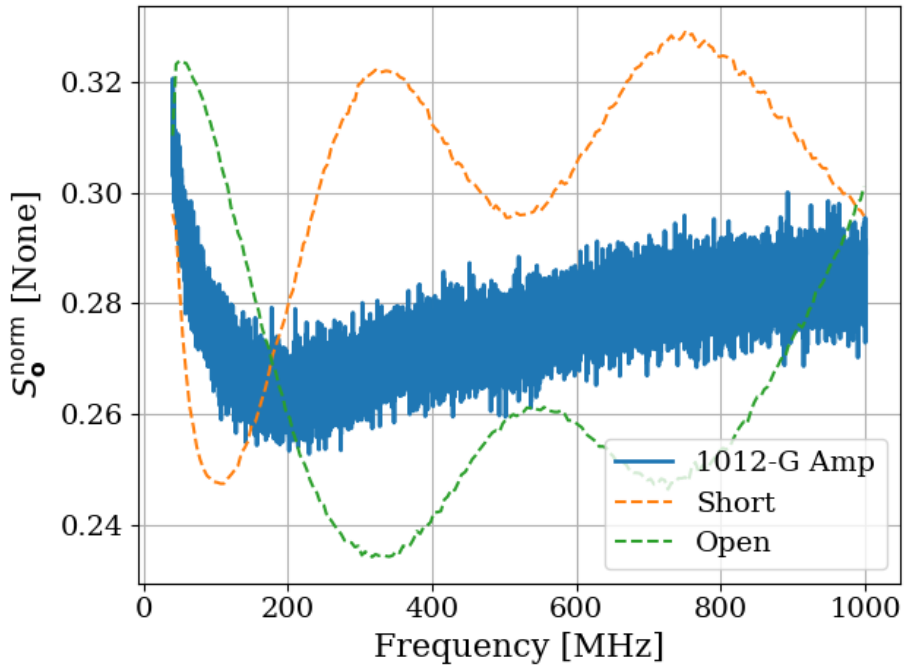


Figure 2.27: Power spectrum of noise emerging *out* of the input of an amplifier's (Paster-nack PE15A-1012-G) input, see Fig. 2.26. Normalized to a matched 50Ω terminator. Also shown as dashed curves are the spectra of a short and open termination. These spectra have a median fit applied to reduce visual clutter. Low-frequency behavior is due to the high noise figure of the amplifier at these frequencies; see Eq. 2.37.

941 **2.3.7 Intentional breaking of thermal equilibrium**

942 At this point, it has been demonstrated that an amplifier absorbs more thermal noise than
943 it emits, likely due to the electronic cooling effect described by Radeka [5]. This causes the
944 spectrum of a resonator, which is measured with such an amplifier, to exhibit wiggles, which
945 disappear when a circulator is used to isolate the system from the amplifier. An interesting
946 question naturally arises; what happens when the the thermal equilibrium is disturbed by
947 varying the temperature of the 50Ω terminator on port 3 of the circulator (Fig. 2.24)? Since
948 the terminator is outside the room, it is simple to conduct a highly controlled experiment
949 where the terminator's temperature is varied without entering the room and disturbing
950 sensitive boundary conditions.

951 The hot terminator is created by using a noise source (red device in the left panel of
952 Fig. 2.28). The noise source has an effective noise ratio (ENR) of approximately 16.1 dB
953 according to its calibration sheet. Noise temperature is related to ENR by the formula[31]

$$T_n = (10^{\text{ENR}/10} \times 290 K) + 290 K, \quad (2.39)$$

954 where ENR is measured in dB and a reference temperature of 290 K has been assumed.

955 Therefore, the noise source has a noise temperature of around 12,100 K ¹⁹.

956 The cold terminator is a standard Pasternack 50Ω (with the blue rubber case removed),
957 and the cable is semi-rigid and rated for cryogenic temperatures. This assembly is shown
958 immersed in liquid nitrogen in the right panel of Fig. 2.28.

¹⁹This testing was performed before the Y-factor measurements of Sec. 3.1.1. The noise source worked correctly here but failed before the Y-factor measurements.

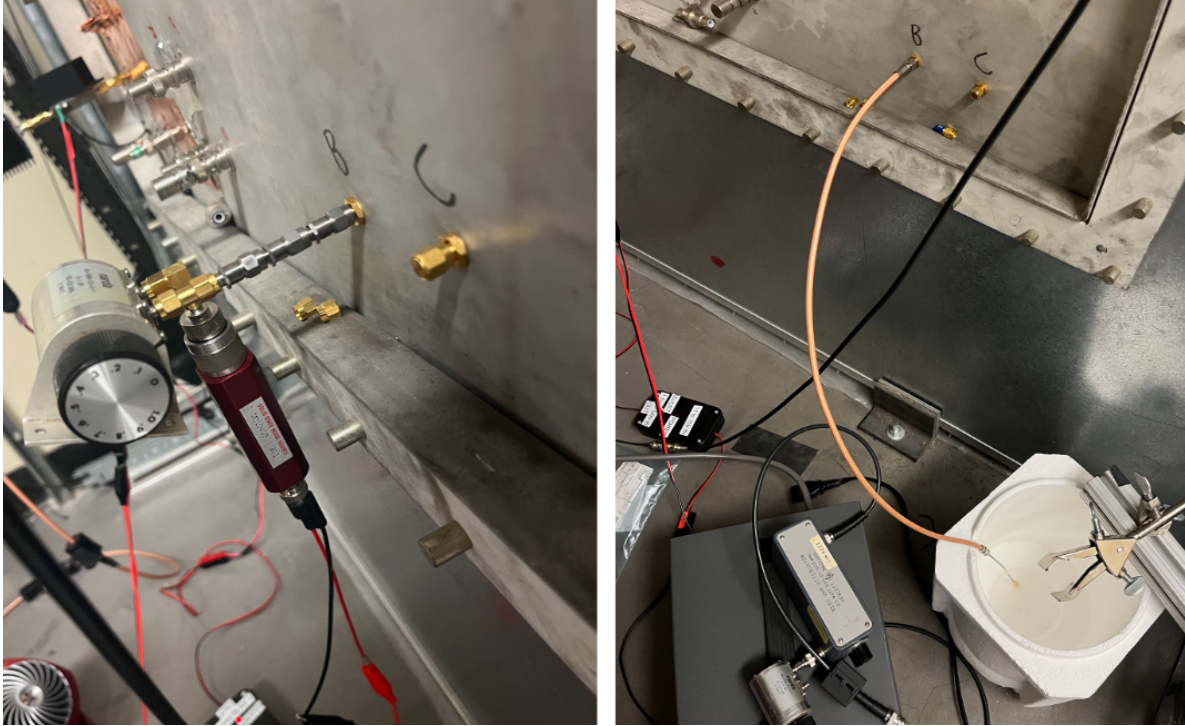


Figure 2.28: Setup to create hot and cold terminator. The hot/cold load is connected to port 3 of the circulator (as shown in Fig. 2.24). The circulator is in the room and not visible in this photo. The left panel shows the noise source ($16.1 \text{ dB ENR} \approx 12,000 \text{ K}$ noise temperature) and attenuators allowing the specific control of the hot temperature, see Eq. 2.40. Course attenuation is controlled by adding fixed attenuators, while fine control (0.1 dB steps) is provided by the step attenuator. Right panel shows the semi-rigid cryogenic-capable cable in liquid nitrogen to create a cold load.

959 In both the hot and cold measurements, the loads were shown to have a good impedance
 960 match to the 50Ω line using a VNA. The noise source is designed to have a good match,
 961 but the terminator is not rated for cryogenic temperatures, so this is an important test.
 962 The cryogenic test load (semi-rigid cable plus terminator) was measured to have $S_{11} <$
 963 -35 dB at both room temperature and at 77 K (by submerging in liquid nitrogen), confirming
 964 performance at cryogenic temperatures.

965 The noise source looks like a terminator, which is a factor of ~ 40 times hotter than room

966 temperature, while the cryogenic terminator is a factor of ~ 4 colder than room tempera-
967 ture. To account for this, room temperature attenuators can be added to bring the effective
968 temperature of the noise source down closer to room temperature. Therefore, the total noise
969 temperature T_{out} of a terminator at physical temperature T_{in} in series with an attenuator at
970 physical temperature T_{att} with (linear) loss L is a useful quantity. For brevity, the derivation
971 outlined in the white paper by Whitham D. Reeve [32] is skipped, and the result is provided;

$$T_{\text{out}} = \frac{T_{\text{in}}}{L} + T_{\text{att}}\left(1 - \frac{1}{L}\right). \quad (2.40)$$

972 Returning to the set-up in Fig. 2.24, replacing the terminator on port 3 with either a
973 noise source (including an attenuator chain) or a terminator in liquid nitrogen provides a
974 means to break thermal equilibrium in both the hot and cold direction by applying a matched
975 load at a very precise temperature to port 3 of the circulator. Equation 2.40 converts the
976 attenuation and noise source temperature into an output temperature.

977 Figure 2.29 shows the resulting spectra from the set-up shown in Fig. 2.24 using a noise
978 source/attenuator chain shown in the left panel of Fig. 2.28. The two panels show the spectra
979 from the same set-up, but for different ranges and resolutions of T_{out} as defined by Eq. 2.40.

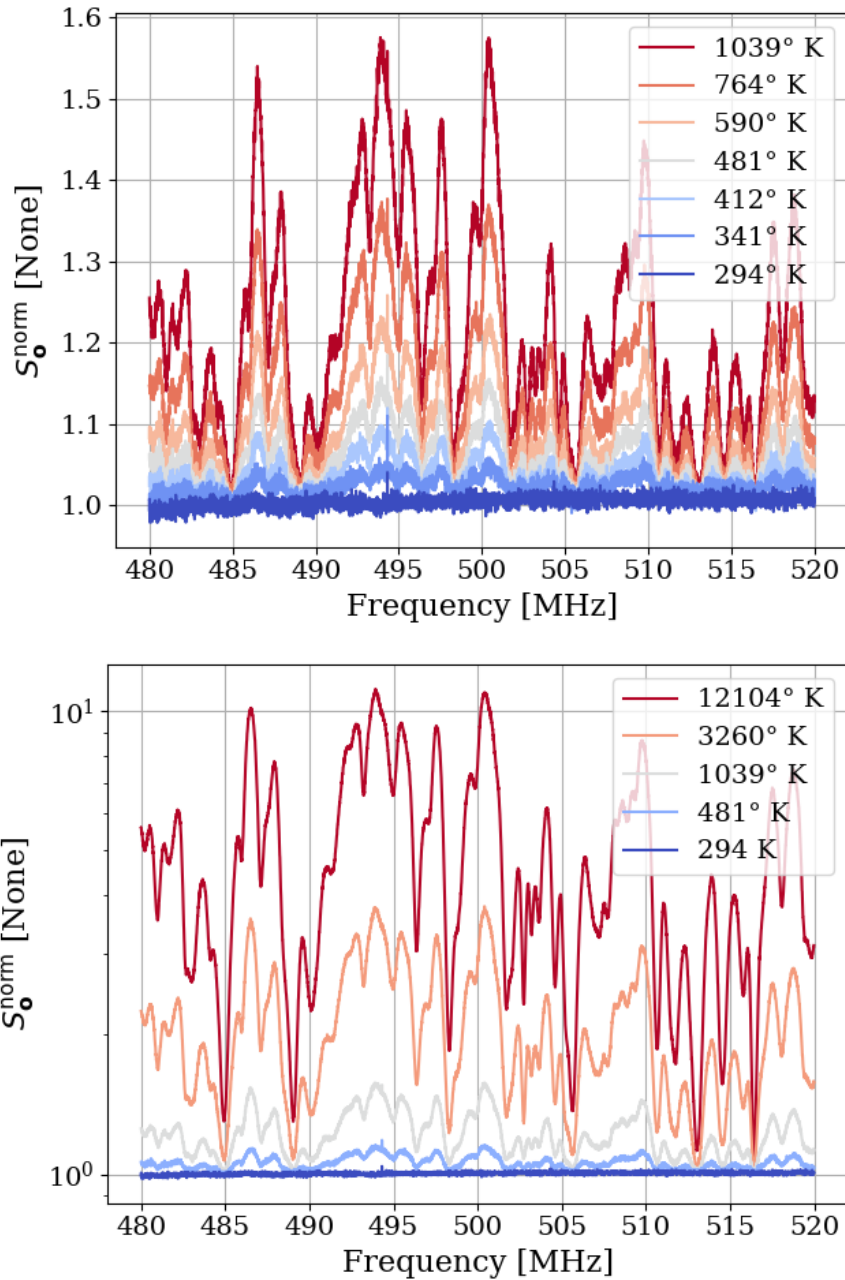


Figure 2.29: Spectra resulting from the antenna and circulator set up of Fig. 2.24 with the terminator on port 3 of the circulator at a variety of temperatures, as calculated by Eq. 2.40. Spectra are all normalized to a terminator through the same amplifier chain. The two panels show different ranges and resolutions of temperatures for clarity, but are the same setup.

980 Figure 2.29 showed spectra from the set-up shown in Fig. 2.24 for a hot terminator, but
981 a cold terminator can also be used by dunking a terminator into liquid nitrogen (Fig. 2.28).
982 Neglecting the small attenuation of the cable, the noise temperature is simply 77 K. An
983 interesting test case is to set the hot temperature such room temperature is halfway between
984 T_{hot} and T_{cold} . In other words, let

$$T_{\text{hot}} = (T_{\text{room}} - T_{\text{cold}}) + T_{\text{room}} \quad (2.41)$$

$$\approx 511 \text{ K}. \quad (2.42)$$

985 For $T_{\text{hot}} = 12,100 \text{ K}$, $T_{\text{att}} = 294 \text{ K}$ and $T_{\text{out}} = 511 \text{ K}$, inverting Eq. 2.40 we expect L to
986 be ~ 54.4 or 17.4 dB.

987 The two spectra with the terminator at 504 K (the closest temperature accessible with the
988 0.1dB step attenuator) and 77 K are shown in Fig. 2.30. Again, they have been normalized
989 to the spectrum of a room-temperature terminator.

990 The two spectra shown in Fig. 2.30 appear to be mirrored about $S_0^{\text{norm}} = 1$. In a test of
991 this reflection, these spectra are added, and the resulting sum spectrum is flat to about 1%
992 with another 1.5% offset from the expected value of 2. This is shown in Fig. 2.31. The offset
993 is likely due to the amplifier gain or ambient temperature drift between measurements.

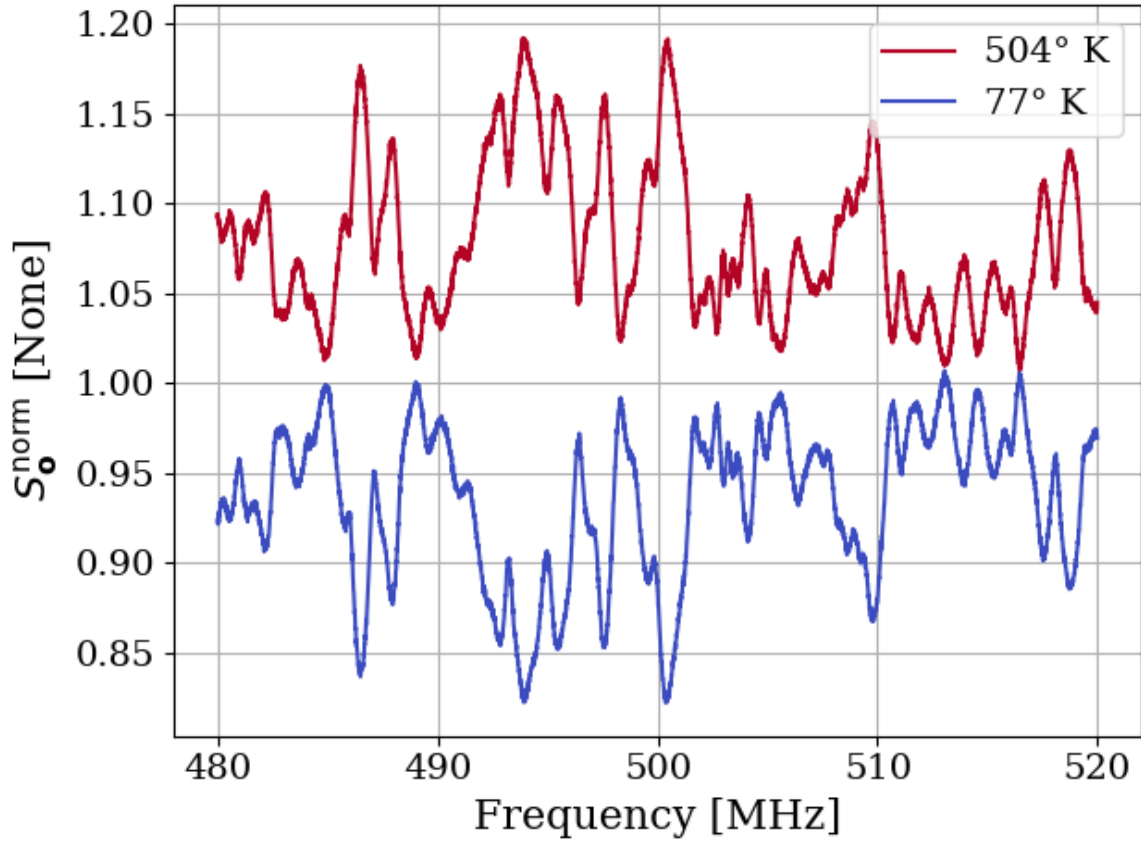


Figure 2.30: Spectra resulting from the antenna and circulator set up of Fig. 2.24 with the terminator on port 3 of the circulator $\approx 210\text{ K}$ above and below room temperature, as calculated by Eq. 2.40. Spectra are both normalized to a terminator through the same amplifier chain.

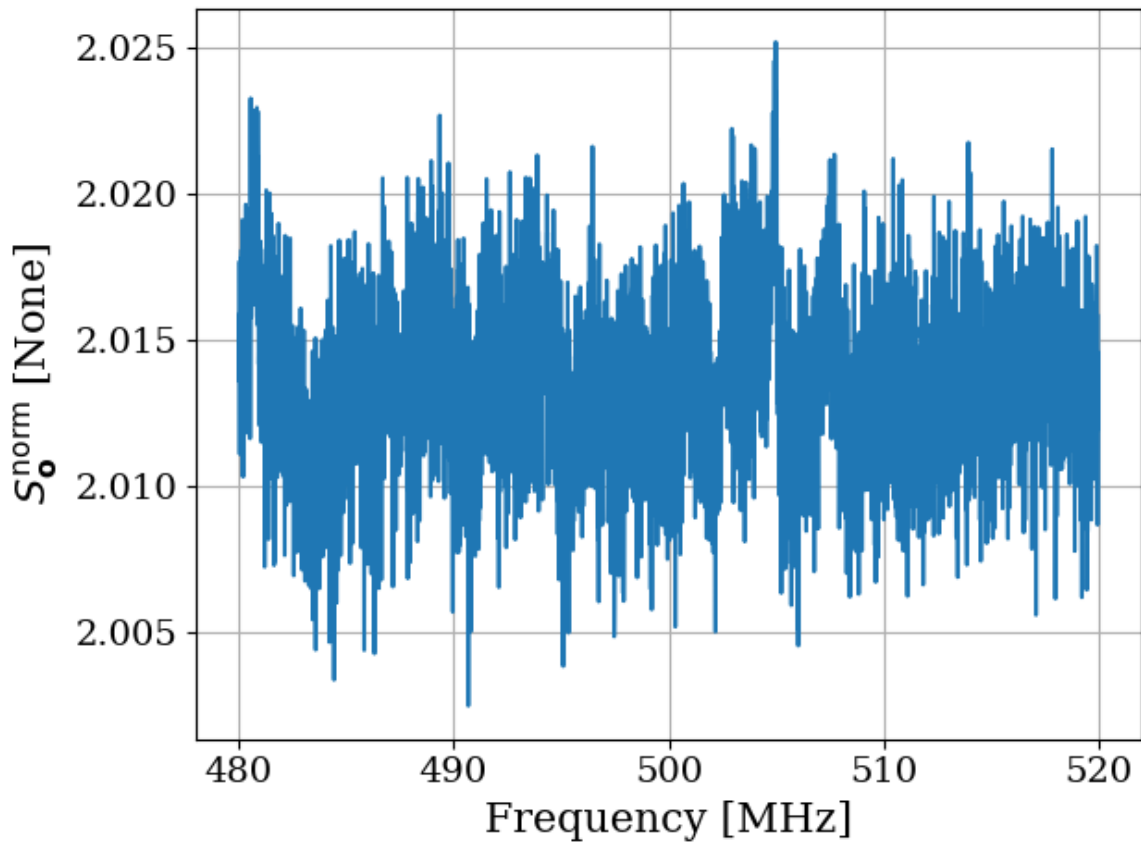


Figure 2.31: Sum of normalized spectra shown in Fig. 2.30. If the two normalized spectra in that figure were perfect reflections about 1, their sum would be a constant 2 in this figure. That is close to what is observed.

994 **2.3.8 Relation of antenna S_{11} to thermal noise without a**

995 **circulator**

996 As pointed out in [27], the antenna impedance determines how much power is transferred

997 from the cavity's electric field noise into the transmission line, and therefore what is mea-

998 sured by the amplifier²⁰. Indeed, impedance is a useful tool in understanding the situation

999 outside equilibrium. However, viewing from this perspective misses a subtle point when con-

1000 sidering equilibrium; while an impedance mismatch will prevent the antenna's noise power

1001 from entering the transmission line, it will also prevent the noise in the line from leaving!

1002 This power will reflect off of the mismatch at the antenna and be absorbed by the matched

1003 amplifier, resulting in a flat spectrum. This can be seen in the coax resonator when mea-

1004 sured with the circulator in Sec. 2.3.4, specifically Figs. 2.22 and 2.23. Figure 2.32 shows a

1005 comparison of $1 - |S_{11}|^2$ and the noise spectrum of an antenna measured with a Pasternack

1006 low noise amplifier (LNA). There is no circulator in the setup, so variations are observed.

1007 Figure 2.33 shows the strong correlation between the curves in Fig. 2.32.

²⁰The amplifier has a small impedance mismatch as well ($S_{11} \lesssim -15$ dB), but this is a small effect and is neglected.

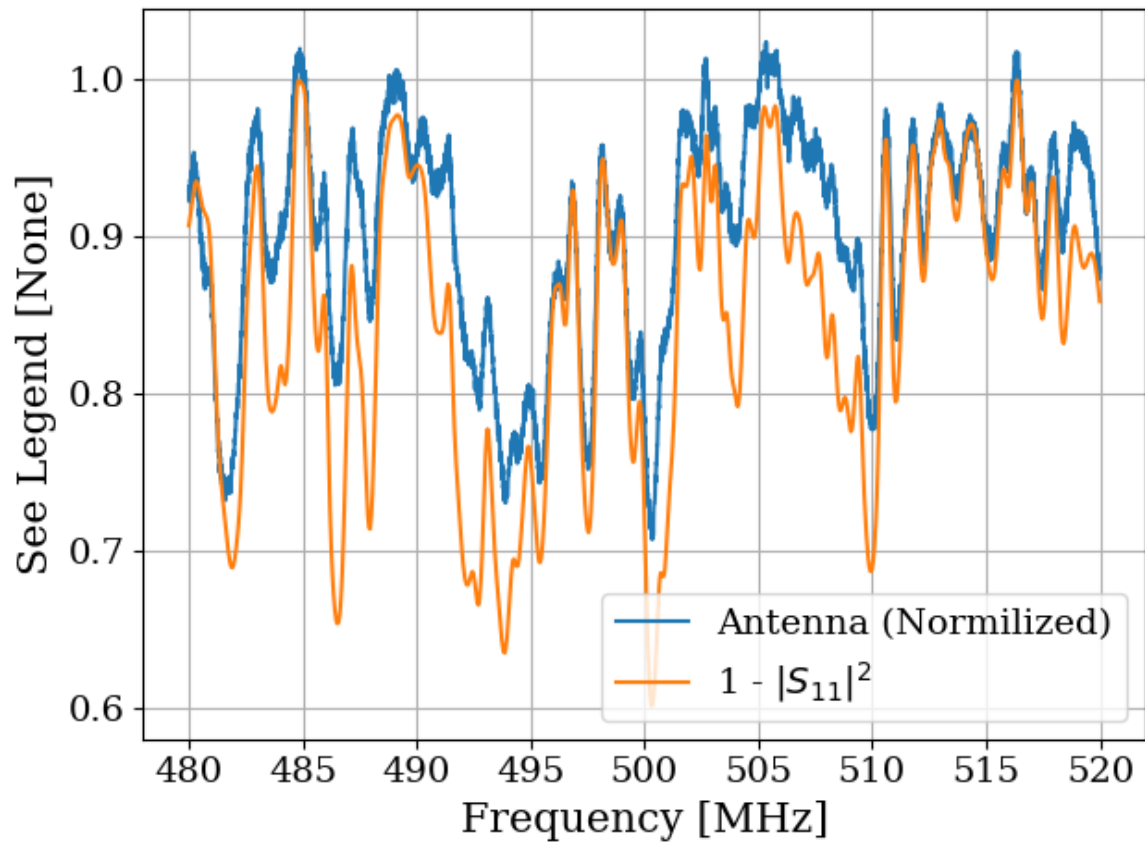


Figure 2.32: $1 - |S_{11}|^2$ and the normalized antenna spectrum without circulator. Shown at significant zoom to show detail. A much wider span is used to generate the correlation shown in Fig. 2.33.

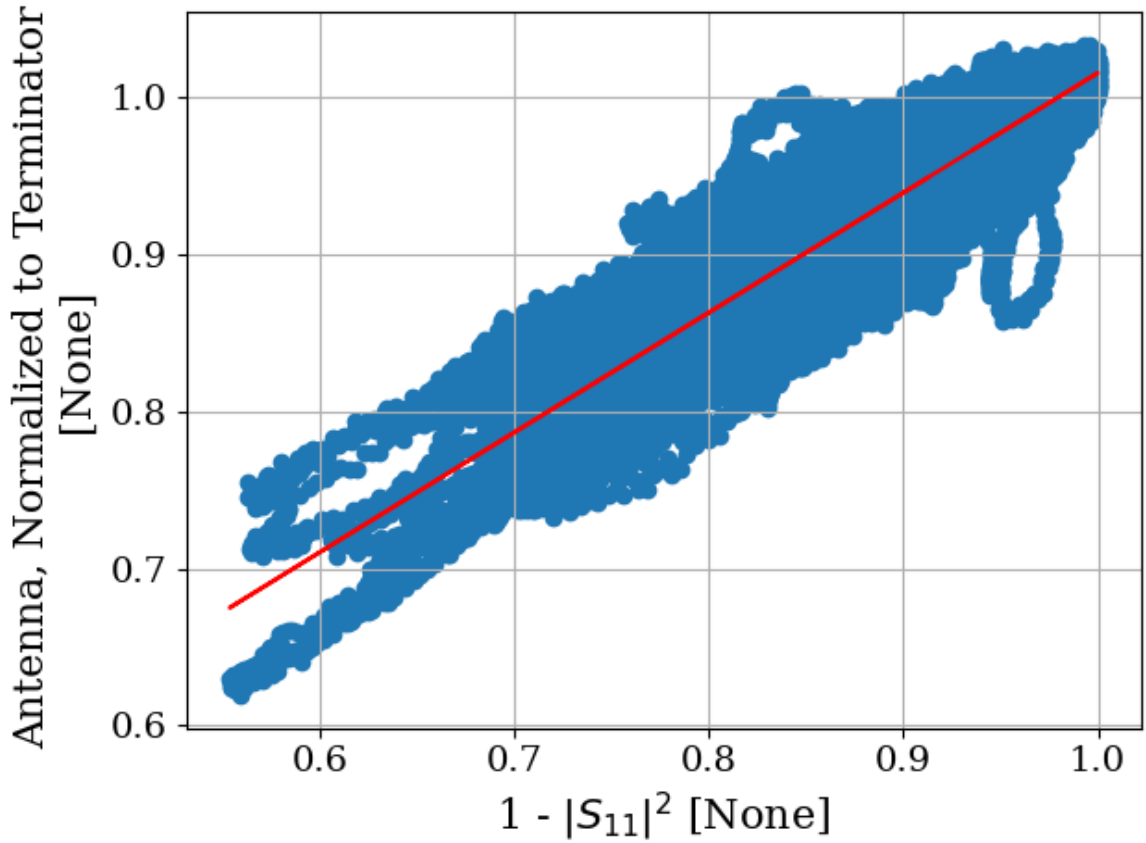


Figure 2.33: Correlation of $1 - |S_{11}|^2$ and the normalized antenna spectrum without the circulator. The data are taken between 300 and 800 MHz, a much wider span than shown in Fig. 2.32. The antenna is connected directly to the low noise amplifier (LNA), i.e. with the circulator shown in Fig. 2.19 removed. The line of best fit is shown in red. The Pearson correlation coefficient is 0.92.

1008 2.3.9 Discussion of Thermal Wiggles

1009 Inspection of the output of the experiment (S_o , Fig. 2.16) reveals small variations in PSD
1010 (power spectral density) over spans of tens of kHz. Given an antenna in a cavity in thermal
1011 equilibrium with the input of an LNA, whose input is assumed to be real and matched,
1012 one would expect an output PSD which is constant with respect to frequency (up to small
1013 variations in system gain and noise temperature). The theory for this is outlined in Sec 2.3.1.
1014 These observed variations are not noise; for a given antenna position, the same shape is
1015 repeatedly measured (though the noise riding on these variations *is* random). The origin of
1016 the observed small variations lies in the effective temperature difference between the room
1017 and the LNA, causing a net power flow from the antenna into the LNA (Fig. 2.26). This
1018 effective temperature difference partially excites modes of the antenna/cavity system, causing
1019 the observed variations. This effect likely originates from a small reactive component of the
1020 LNA's input causing the electronic cooling described originally by Radeka [5]. This effect
1021 can be eliminated by adding a circulator between the antenna and LNA [33, 34] though for
1022 this experiment, it is impractical to get an isolator that covers such a wide band at relatively
1023 low frequency. Furthermore, the relatively wide (tens of kHz) variations can be handled by
1024 fitting to them, which is discussed in Sec. 4.2. Finally, a topic which was not described here
1025 but may be fruitful for future inquiry into this topic is the analysis of noise waves. See [35]
1026 or Sec. 9.12 of [36].

1027 **2.4 Reverberation Chambers and Statistical**

1028 **Uniformity**

1029 The Dark E-Field Radio experiment consists of an antenna in a cavity. An averaged noise
1030 power spectrum is measured and an exclusion limit is set on the amount of power excess
1031 that would have been detected if it were there. In order to convert this limit on power into
1032 a limit on kinetic mixing ϵ , the antenna/cavity detector system must be calibrated.

1033 In many situations, an electromagnetic cavity can be treated with a "spherical cow"
1034 approach; they contain one mode with a few simple properties that can be analytically
1035 computed. This works well enough for a smooth, empty cavity that resonates near its
1036 first mode, but for complex cavities, this treatment turns out to be insufficient. At high
1037 frequencies (where the wavelength is much smaller than the cavity), many modes, each with
1038 a finite spread in frequency, overlap. Each of these modes depends on very specific boundary
1039 conditions of the cavity and everything within it. The configuration of the cavity and its
1040 contents simply cannot be known to a level of precision that would allow for an analytic or
1041 simulated solution. Qualitatively, placing a small conducting object²¹ in a cavity greatly
1042 impacts the cavity's resonances as measured by its S-parameters (Fig. 2.36).

²¹This is a point made by Hill [37], with the example of placing a soda can in a reverb chamber. Ben Godfrey and I independently discovered this by measuring S_{21} of an antenna in our shielding room with and without a small SMA terminator on the ground with surprisingly different results.

1043 The problem is summarized nicely by Price et al. [38];

1044 The solution cannot depend in detail on such things as whether a small metallic
1045 can has been set down somewhere inside the test article, or the position of the
1046 pilot's arms, or whether some mechanical widget has moved from position A
1047 to position B, changing the mode structure. If the answer did depend on those
1048 things, all of the measurements would be useless, defeated by the minutiae present
1049 in all systems.

1050 The answer to this dilemma is found in the study of mode-stirred reverberation chambers,
1051 such as those studied by Price, whose quote appears directly above. These are electromag-
1052 netic or acoustic cavities in which a large volume is occupied by an object that is highly
1053 reflective and designed to move, a so-called *mode stirrer*. Making the geometry more com-
1054 plex seems counter-intuitive. However, the payoff is in the transition from a deterministic
1055 theory to a statistical one. The fields in the cavity at any given configuration are complex
1056 and are not known, but the statistics of the fields subject to the stirring can be rather simple.

1057 This section provides a mostly qualitative overview of the subject. The de facto reference
1058 is David Hill's 2009 book [37] which consolidates his many papers spanning his ~ 30 -year
1059 career. There is little I can do to explain the theory of electromagnetic reverberation cham-
1060 bers, which is not in this book, so I will focus on their application to the experiment and
1061 cite Hill where appropriate. The reader is encouraged to consult this book and its references
1062 for a more detailed exploration of the subject.

1063 **2.4.1 Deterministic solutions to electromagnetic waves in cavities**

1064 The electromagnetic fields within a cavity can be modeled by applying Maxwell's equations
1065 with the appropriate boundary conditions. In principle, with enough knowledge about the
1066 contents of the cavity, this treatment could calculate fields in any cavity. Unfortunately,
1067 it quickly becomes untenable for all but the simplest cases. Therefore, we will restrict
1068 ourselves to an empty cavity with perfectly conducting surfaces. The resulting fields have
1069 simple analytic solutions which vary sinusoidally in both space and time. They are derived
1070 in many places. See for example [37, 39]. While this treatment will not solve the problem
1071 at hand, it is a good starting point and will illustrate important features leading to the
1072 statistical treatment in the following subsection.

1073 For a rectangular cavity of linear dimensions a , b and d , the frequencies of resonance are
1074 given by

$$\nu_{mnp} = \frac{c}{2} \sqrt{\left(\frac{m}{a}\right)^2 + \left(\frac{n}{b}\right)^2 + \left(\frac{p}{d}\right)^2}, \quad (2.43)$$

1075 for integer mode numbers m , n and $p \geq 0$ and wave speed c . The lowest frequency of
1076 resonance requires at least two non-zero mode numbers. Thus, for $a < b < d$ the lowest
1077 frequency is at TE_{011} . For an ideal cavity with dimensions equal to that of the shielded
1078 room in this experiment ($8 \times 10 \times 12$ feet), the lowest mode is 63.6 MHz. An important
1079 consideration is the degeneracy of electric and magnetic fields for any mode where all three
1080 mode numbers are non-zero. For example, TE_{111} and TM_{111} occur at the same frequency,
1081 and both of these modes must be counted in the following section. See page 28 of Hill [37]
1082 for a discussion.

1083 A quantity of interest is the functional form of the cumulative number of modes at
 1084 frequencies below a given frequency $N(\nu)$. This is rather simple by brute force computer
 1085 counting²², though an analytic solution can be computed by looking at the volume enclosed
 1086 in a sphere of k -space [40], where k is the wave vector²³. This analytic form is given by

$$N_s = \frac{8\pi}{3} abd \frac{\nu^3}{c^3} - (a + b + d) \frac{\nu}{c} + \frac{1}{2}. \quad (2.44)$$

1087 Differentiation of Eq. 2.44 results in a functional form for the mode density, i.e. the
 1088 number of modes contained in a frequency band,

$$\frac{dN_s}{d\nu} = 8\pi abd \frac{\nu^2}{c^3} - \frac{a + b + d}{c}. \quad (2.45)$$

1089 Equations 2.44 and 2.45 are plotted in Fig. 2.34

1090 This is useful because as the mode density becomes high, modes in a cavity of finite
 1091 conductivity begin to overlap. The modification of modal structure by conductors is demon-
 1092 strated in Figs. 2.35 and 2.36 by placing different conductors in the room and measuring
 1093 S_{11} .

1094 From these measurements it can be seen that modes can be pulled around, even by
 1095 conductors occupying a small percentage of room volume. This is especially true for high
 1096 frequencies. However, by using a large volume of conductors such as a mode-stirrer (sim-
 1097 ulated here with scrap metal), high-frequency modes are pulled around so much that they
 1098 overlap. This is the intuition behind reverb chambers and the idea of statistical uniformity.

²²As long as you don't forget the degeneracy!

²³This whole business of mode counting is directly analogous to the calculation of density of states in statistical mechanics. It shouldn't come as a surprise that the calculation is carried out in the same way.

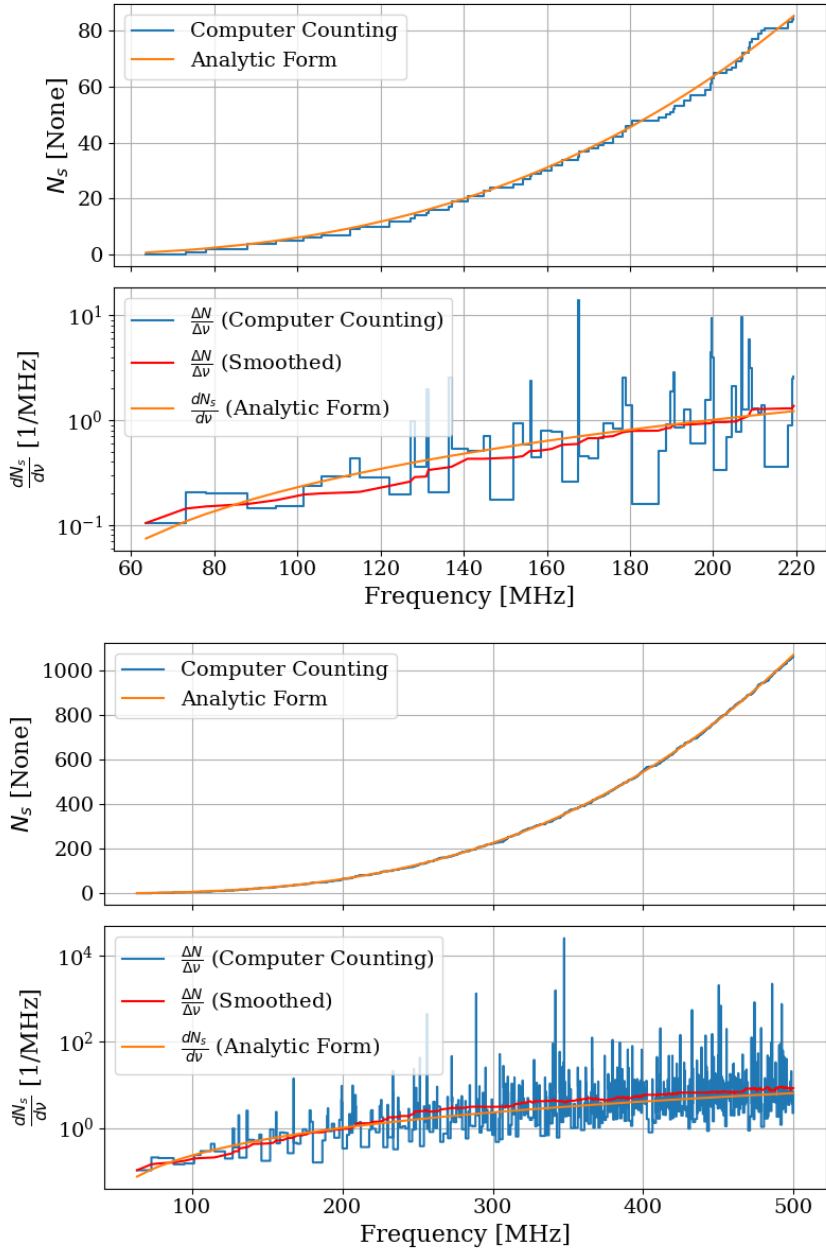


Figure 2.34: Modal density for an electromagnetic cavity with dimensions of the shielding room (nominally $8 \times 10 \times 12$ ft, see table 2.2). The upper sub-plot shows $N_s(\nu)$, the cumulative number of modes below a given frequency. The lower sub-plot shows the derivative of $N_s(\nu)$. The upper and lower panels show the same data at two different frequency spans. These plots are a recreation of Figs. 3, 4 and 5 from [40] for a cavity with dimensions of the shielding room. Note that large spikes in $\Delta N/\Delta\nu$ should be interpreted as binning artifacts and are only shown for reference. The analytic derivative is more useful.



Figure 2.35: Pictures of conductor configurations in the shielded room. The antenna is in the same position between photos. The left panel shows a tin foil hat, and the right shows a random placement of scrap metal. Hat and scrap metal courtesy of Tyler Erjavec.

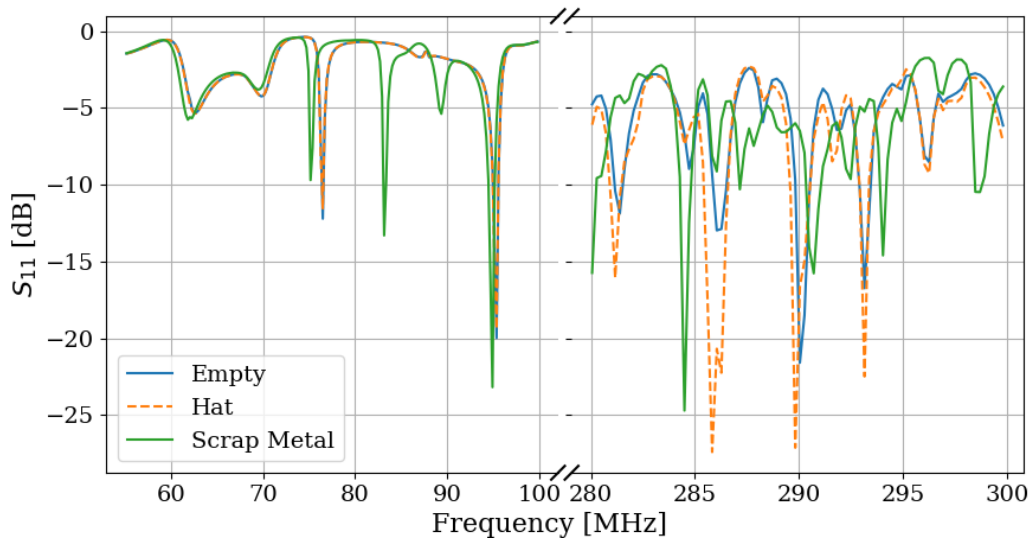


Figure 2.36: Measured S_{11} with different conductors in shielded room, as pictured in Fig. 2.35. Modes visible at low frequency agree nicely with the predictions of Eq. 2.43, though they are pulled around by the scrap metal. Note, the scale changes slightly after the X-axis break.

1099 **2.4.2 Statistical approach to electromagnetic waves in cavities**

1100 By using a mode stirrer, modes are intentionally pulled around in frequency, and the average
1101 response of the cavity begins to converge to be relatively flat. The regime where this occurs is
1102 known as being well-stirred. It requires the stirrer to be large enough and obey some design
1103 principles and that the frequency to be above a threshold. This lowest usable frequency
1104 (LUF) is determined by a minimum modal density since the modes must be close enough
1105 together in order to overlap. For a room-sized reverberation chamber with a lowest resonance
1106 of around 60 MHz (~ 3 or 4 meters per side), the rule of thumb cited by Hill, among others,
1107 is the LUF is close to where the modal density is about 1 mode/MHz. Therefore, according
1108 to Fig. 2.34, the LUF of our shielded room is about 200 MHz.

1109 A simple alternative to using a purpose-built mode stirrer is moving a receive antenna
1110 around in the room. Instead of moving the spatial structure of the modes around the antenna,
1111 the antenna is moved through the modes. While not as effective, it is simpler to implement,
1112 so this was the method used in Run 1A. Note that Run 1A does not rely on statistical
1113 uniformity. Simulations provide a means to calibrate the system as discussed in Sec. 4.3.
1114 However, using these statistical ideas provides a much more stable simulation with a much
1115 better agreement with measurement.

1116 One final remark that is relevant to the experiment is the concept of composite Q . This
1117 parameter represents a resonant enhancement factor that corresponds to the antenna/room
1118 system's tendency to "ring up" in the same way any resonator will. It is referred to as *com-*
1119 *posite Q* and represented as \tilde{Q} . It is analogous to the standard quality factor of a resonator

1120 with one important modification; the experiment is operated across a wide frequency range,
1121 so \tilde{Q} is defined across the continuum of these resonances, not only on classical eigenmodes
1122 of the system.

1123 2.5 System Design

1124 This section outlines the subsystems which make up the experiment. While specifics and
1125 basic calculations are provided as they apply to design choices of subsystems, testing and
1126 characterization of the system as a whole is left to Ch. 3. A simplified schematic of the
1127 entire experiment is shown in Fig. 2.37 and a photo of the lab is shown in Fig. 2.38.

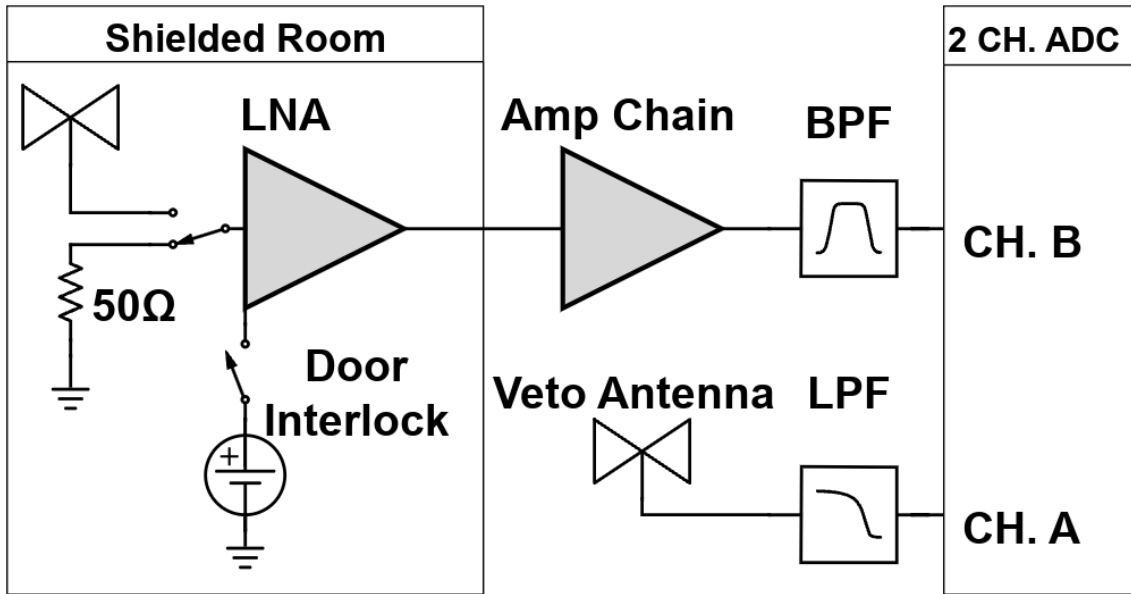


Figure 2.37: Schematic of the RF receiver system. An RF coax switch allows the PC to control the source (antenna or terminator). The amplifier chain is shown with more detail in Fig. 2.42. The switch is controlled by optical fiber to maintain the isolation of the room. The LNA (Pasternack PE15A1012) has a nominal gain and noise temperature of 40dB and 100K (measurements shown in Sec. 3.1.1). It is interlocked (Fig. 2.43) to the door to protect amp B and the ADC from large signals when the door is open. The secondary amplifier is a Mini-Circuits (MC) ZKL-1R5+ and has a nominal gain of 38dB. Not pictured after this amplifier is a fixed 4dB of attenuation. The band pass filter (BPF) defines the experiment's bandwidth, $-3 \text{ dB} \approx 40 - 320 \text{ MHz}$ and is discussed in Sec. 2.5.4. The veto antenna is outside of the room and interference is not reduced by the $\approx 100 \text{ dB}$ SE of the room, so no gain is required. The low pass filter (LPF) on the veto is for anti-aliasing.



Figure 2.38: Photo of dark radio lab. The shielded room contains the main antenna as well as the LNA and power supply (not visible). The veto antenna can be seen hanging outside of the shielded room. Photo taken looking south.

1128 **2.5.1 Shielded room**

1129 The shielding room [41] serves two purposes. The first is straightforward; to shield the
1130 antenna, keeping radio frequency interference (RFI) *out*. The second purpose is a bit more
1131 subtle; to keep any converted dark photons *in*. This second point is addressed further as an
1132 aspect of system calibration in Ch. 4, but roughly can be described by the loaded quality
1133 factor [42–44] of the antenna/room system. Namely, a more resonant system will be more
1134 sensitive to coherent signals. This subsection will focus on the first point, keeping RFI out.

1135 Shielding effectiveness SE is a measurement of a shielding enclosure’s ability to attenuate
1136 electromagnetic waves from entering,

$$\text{SE} \equiv 10 \log_{10} \left(\frac{P_{\text{open}}}{P_{\text{closed}}} \right) = P_{\text{open}, \text{dB}} - P_{\text{closed}, \text{dB}} \quad (2.46)$$

1137 where $P_{\text{open}}/P_{\text{closed}}$ are powers received with the door open/closed. The ratio of powers
1138 allows all the specifics of antenna matching to cancel, allowing for a very simple differential
1139 measurement. The results of this are described in Sec. 3.2.

1140 Another important measurement are the dimensions, shown in table 2.2. I carefully
1141 measured the room with a laser range finder. I checked the rangefinder against a measuring
1142 tape, and it gives good agreement to 1 mm²⁴. The room is out of square by a few mm,
1143 especially the height measured in the south-west corner compared to the height measured
1144 everywhere else. This is the most extreme deviation and is about 5 mm.

²⁴After a year, I dropped it and it now gives crazy readings which jump around by 10s of cm. Be careful!

Direction	Coordinate	Nominal Length [ft]	Measured Length [m]
West-East	x	10	3.070
Vertical	y	8	2.457
North-South	z	12	3.684

Table 2.2: Direction, coordinate, and length measurements of the shielded room in lab 314. Note that Fig. 2.38 is looking south, so x is right-left, and z is into the page. Note that these are the mean values of several measurements. The room was found to be about 5 mm out of square, so these should be interpreted as \pm 5 mm.

2.5.2 Antenna

The antenna plays an important role in the experiment as the matching device between electromagnetic waves in the cavity and the 50Ω receiver system. For a broadband search such as the 50-300 MHz run (a 6:1 bandwidth), a broadband antenna must be used. The chosen antenna must provide a good impedance match and high efficiency since an inefficient antenna would convert a substantial amount of the converted dark photon's power into heat within the antenna's structure. The antenna is connected to the RF switch via a low loss (0.45dB at 300 MHz) 21 ft. LMR400 cable. This contributes about 31.6 K to the ≈ 400 K antenna noise, see Eq. 2.27. Note that the final limit on epsilon scales with the square root of system temperature, so this is only a few percent degradation in the final limit after a 9 day run.

For the 50-300 MHz run, a ≈ 131 cm biconical antenna (bicon) was chosen. The selected model is manufactured by COMPOWER, model AB-900A [45]. In a phone call with the manufacturer as well as testing of the isolated balun, it was determined that the balun used in the antenna was 1:1. This allows for simple simulation of a free-space aperture which

1160 agrees remarkably well with manufacturer data, Fig. 2.39. In COMSOL [46], the lumped
1161 port option allows for a balanced drive of an antenna. A match to a 50Ω transmission line
1162 through a 1:1 balun is simply modeled as a lumped port, a very simple object in COMSOL
1163 featured in nearly all of the antenna tutorials²⁵. Additionally, there is good agreement
1164 between simulated and measured antenna impedance. See the Smith Chart in Fig. 2.40.

²⁵See for example the dipole antenna tutorial, available at <https://www.comsol.com/model/dipole-antenna-8715>

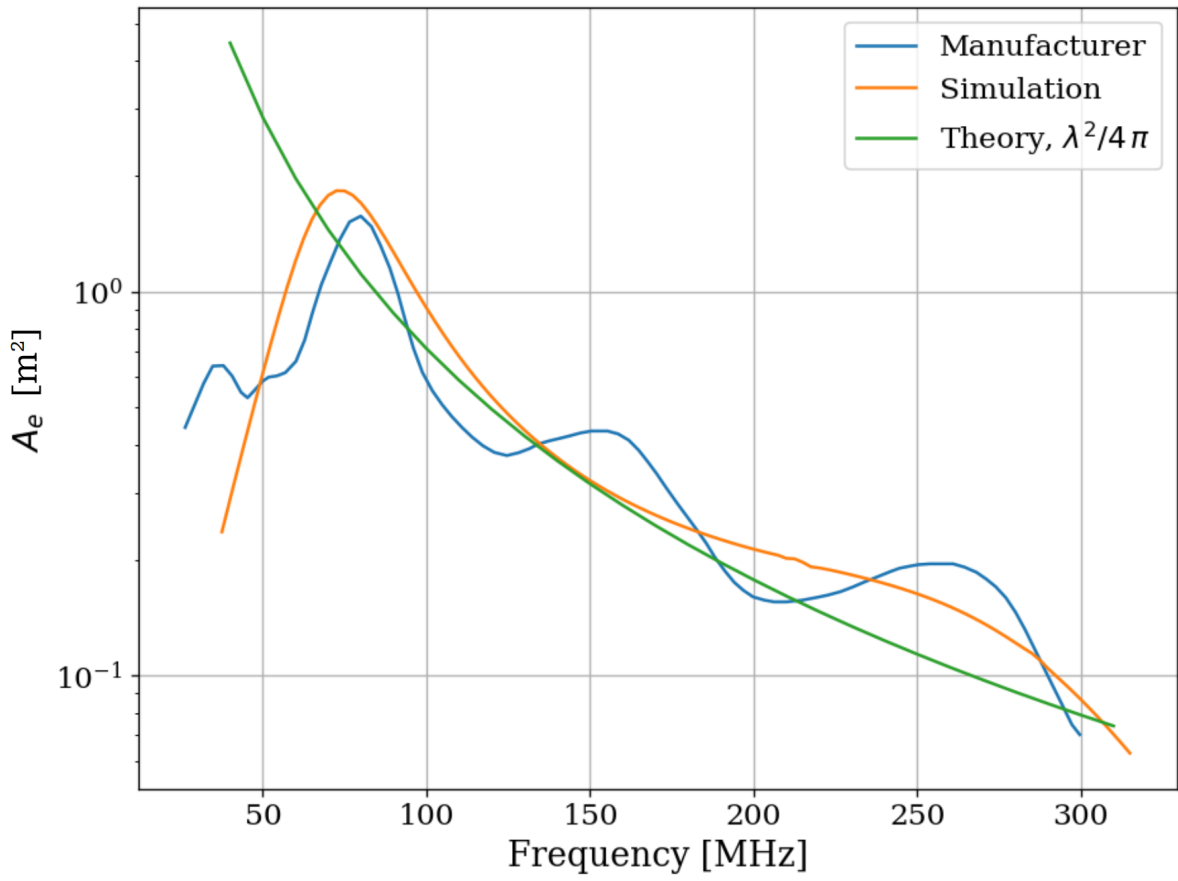


Figure 2.39: AB-900A biconical antenna effective aperture, simulated, measured and theoretical in free space. Simulation performed in COMSOL [46]. The measurement was provided by manufacture [45] as an antenna factor and was converted to aperture. Variations observed in the manufacturer's measured data are the result of testing over a ground plane and are a known discrepancy between simulations and measurements of “free space” antenna factor. See for example [47]

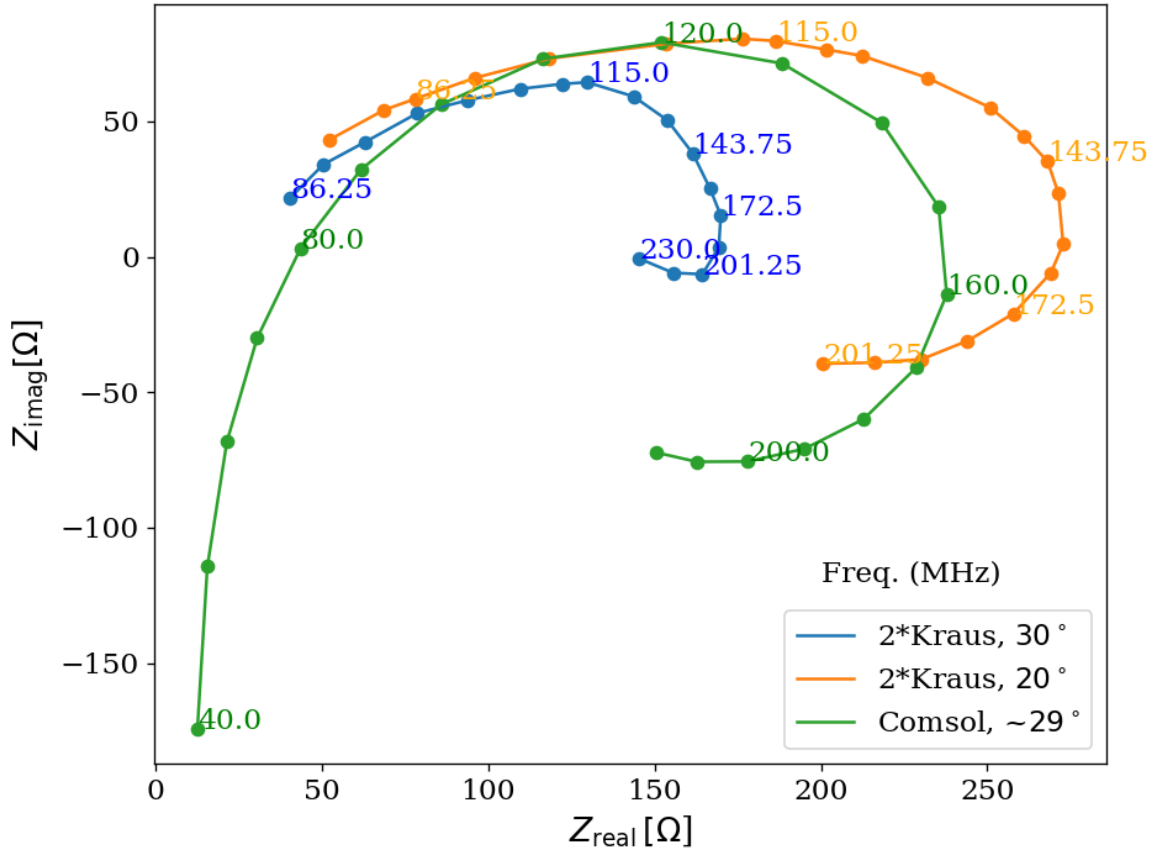


Figure 2.40: Simulated AB-900A biconical antenna free space complex input impedance shown in blue. The simulation was performed in COMSOL. The measurement is from Kraus' Antennas, second edition, Fig 8-13 [48]. Measured data is for a monoconical antenna and must be multiplied by 2 to compare to a biconical antenna, as discussed in Kraus. Numbers along the curve indicate the frequency in MHz.

1165 **2.5.3 Terminator and fiber-optic switch control**

1166 Experience has shown that it is advantageous to have a stable noise reference at the begin-
1167 ning of the signal chain to monitor system performance. One may think the antenna can
1168 provide this following Sec. 2.1.1.2, but in practice, the antenna is not that stable, Sec. 2.3.
1169 Furthermore, while RFI was not significant in the actual run, it very well could have been,
1170 introducing some uncontrolled, coherent power into the spectrum, which would have had
1171 an unknown origin. A terminator will give a very constant noise power density $S_{\text{term}} = kT$
1172 regardless of RFI and antenna position. For this reason, one is included. It is at the same
1173 temperature as the walls and is a nice passive solution. The RF switch shown in Fig. 2.37
1174 is actuated periodically during the run to measure the terminator's noise power through the
1175 same amplifier chain as the antenna. The terminator is connected to the switch via a 21-foot
1176 cable (LMR 400) that is identical to the antenna's cable. The switch is controlled via a
1177 fiber-optic link in order to reduce RFI. The fiber optic is an extremely important feature
1178 that was overlooked for several years at the beginning of the experiment, leading to lots of
1179 RFI.

1180 **2.5.4 Signal conditioning**

1181 As discussed in Sec. 2.1.5, the ADC has internal signals that are mitigated by introducing
1182 gain before the ADC. The amount of gain must be carefully chosen since too much will
1183 cause the ADC to clip. Additionally, high frequencies must be limited before digitizing to
1184 prevent aliasing. To accomplish this, several RF components must be selected to condition

1185 the analog signal: an LNA, a secondary amplifier, band-pass filter and several attenuators.

1186 **2.5.4.1 Low noise amplifier**

1187 The important concepts of the LNA have been introduced in Sec. 2.1.4. The key takeaway

1188 is that low noise gain helps to mitigate signal-to-noise degradation that occurs later in the

1189 signal path. As long as the LNA introduces minimal noise, the overall signal-to-noise ratio

1190 improves. The relevant specifications for the Pasternack PE15A1012 [22] are summarized in

1191 table 2.3.

Specification	Value	Uncertainty (50-300MHz)	Units
Frequency Range	50-1,000	-	MHz
Gain	40	± 1	dB
Noise Temperature	110	± 10	K
Input Return Loss	< -15	-	dB
Output Return Loss	< -15	-	dB
Price	500	-	USD
Voltage	9-15		V
Current	100	10	mA

Table 2.3: Specifications for the Pasternack PE15A1012-E low noise amplifier. The voltage is regulated internally, so the exact voltage supplied is not critical, though there is a slight gain dependence on voltage since a higher voltage causes the amp to run warmer, see Fig 3.8.

1192 We have several identical amplifiers which are labeled with letters. At the time of writing,

1193 amplifiers A-D are out of commission. Amplifier E was used for Run 1A.4.

1194 **2.5.4.2 Secondary amplifier**

1195 As discussed in 2.1.4, the noise temperature of a secondary amplifier has negligible impact
1196 on the total system noise temperature. For this reason, a cheaper secondary amplifier is
1197 used. The specifications for the Mini-Circuits ZKL-1R5+ [49] are outlined in Table 2.4.
1198 This amplifier has no internal regulator, so gain and noise temperature depend strongly on
1199 the bias voltage. Voltage was set to 9.05 V for Run 1A.4 using an external regulator (built
1200 around a TI LM317 [50]).

Specification	Value	Uncertainty (50-300MHz)	Units
Frequency Range	50-1,000	-	MHz
Gain	40.5	.3	dB
Noise Temperature	275	15	K
Input VSWR	<1.14	-	dB
Output VSWR	<1.37	-	dB
Price	235	-	USD
Voltage	9-15	-	V

Table 2.4: Specifications for the Mini-Circuits ZKL-1R5+ as measured with 9.05 V bias. This amplifier contains no internal regulator, so the voltage is set using an external regulator (built around a TI LM317 [50]).

1201 **2.5.4.3 Band pass filter**

1202 The band-pass filter has two purposes. The first purpose is to minimize the bandwidth
1203 entering the ADC. This allows for introducing as much gain as possible without wasting
1204 power amplifying frequencies where the antenna doesn't offer a good match. This will be
1205 computed below in Sec. 2.5.4.4. The second purpose is to prevent aliasing²⁶. Aliasing occurs

²⁶Aliasing is a rather complex topic that is greatly simplified here. Wikipedia's aliasing page is an excellent reference. For a more rigorous treatment, see Ch. 7 Sec. 3 of the second edition of Signals and Systems by

1206 when the analog signal contains frequency components at frequencies greater than half the
1207 sample rate, in other words, when the signal and ADC don't obey a condition called the
1208 Nyquist criterion, $\nu_s/2 \geq \nu$, where ν_s is the sampling frequency and ν is the frequency of
1209 the analog signal.

1210 When this criterion is not met, higher frequencies are mapped back down to a lower
1211 frequency, described by the aliasing formula:

$$\nu_{\text{alias}} = |\nu_{\text{signal}} - n \times \nu_s|, \quad (2.47)$$

1212 where ν_{alias} is the aliased frequency, ν_{signal} is the original signal frequency, ν_s is the
1213 sampling rate, and n is an integer which specifies the Nyquist zone. In the simple case
1214 with bandpass filters that roll off well within the first Nyquist zone, only $n = 1$ must be
1215 considered.

1216 As an example, a $\nu_{\text{signal}} = 500$ MHz signal sampled at $\nu_s = 800$ MHz (the Run 1A sample
1217 rate), it would alias to $\nu_{\text{alias}} = 300$ MHz. This also means that 1,300 MHz (residing in the
1218 second Nyquist zone) would alias down to 300 MHz, but again this and higher frequencies
1219 won't be considered. This means that by choosing only to analyze frequencies less than 300
1220 MHz, only frequencies greater than 500 MHz will alias into this analysis span.

1221 The Mini-Circuits ZX75LP-288-S+ low pass filter[52] serves as the anti-aliasing filter in
1222 Run 1A. It has an insertion loss of 68 dB at 500 MHz, while being flat to within 2dB from
1223 50 to 300 MHz. Additionally, the Mini-Circuits SHP-50+ [53] is used as the high pass filter.
1224 When connected in series, these two filters constitute the band-pass filter shown in Fig. 2.37.

Oppenheim et. al [51]

1225 **2.5.4.4 Assembling a signal conditioning chain**

1226 The total gain required can be estimated by setting the output referred power of bandlimited,
1227 400 K noise source times the gain equal to the maximum power the ADC can handle,
1228 $V_{\text{RMS}}^2/Z = 0.63 \text{ mW}$ for $Z = 50 \Omega$. Assuming a perfect filter from 50-300MHz (a 250 MHz
1229 bandwidth), the gain required is

$$G = \frac{0.63 \text{ mW}}{k 400 \text{ K} 250 \text{ MHz}} = 4.5 \times 10^8 = 87 \text{ dB.} \quad (2.48)$$

1230 Noise is a Gaussian random process, however. This much gain ensures 1σ of the time-
1231 domain samples are below clipping. Since many samples are collected ($2^{24} \approx 1.6 \times 10^7$ in
1232 Run 1A), and each has a probability of about 16% of clipping, many samples will clip with
1233 87 dB of gain. However, it gives a good estimation for what to expect.

1234 The band-pass filter is not a brick wall from 50 - 300 MHz as was assumed in 2.48. The
1235 effective bandwidth of a filter is defined here as the integral of the square magnitude of its
1236 through gain,

$$B_{\text{eff}} \equiv \int_{-\infty}^{\infty} d\nu 10^{S_{21}/10}. \quad (2.49)$$

1237 Where S_{21} is measured in dB, and we are interested in integrating a quantity that is
1238 proportional to linear power, so it is divided by 10 rather than 20. The linear S-parameters of
1239 components connected in series multiply [29], but since dB are logarithmic, this is equivalent
1240 to adding their S-parameters (in dB). Also note that $|S_{21}| \equiv \text{IL}$, the insertion loss. Insertion
1241 loss is frequently given on data sheets.

1242 With all this in mind, we can compute $B_{\text{eff}} = 237.06$ Hz for the actual filters (Mini-
 1243 Circuits SLP-50+ high pass filter and Mini-Circutis ZX75LP-288-S+ low pass filter) from
 1244 their data sheets. Curves of S_{21} for the real band-pass filter and an ideal brick wall filter are
 1245 shown in Fig. 2.41. Note that it is actually slightly less than the ideal 250 MHz bandwidth
 1246 since there is some loss in-band.

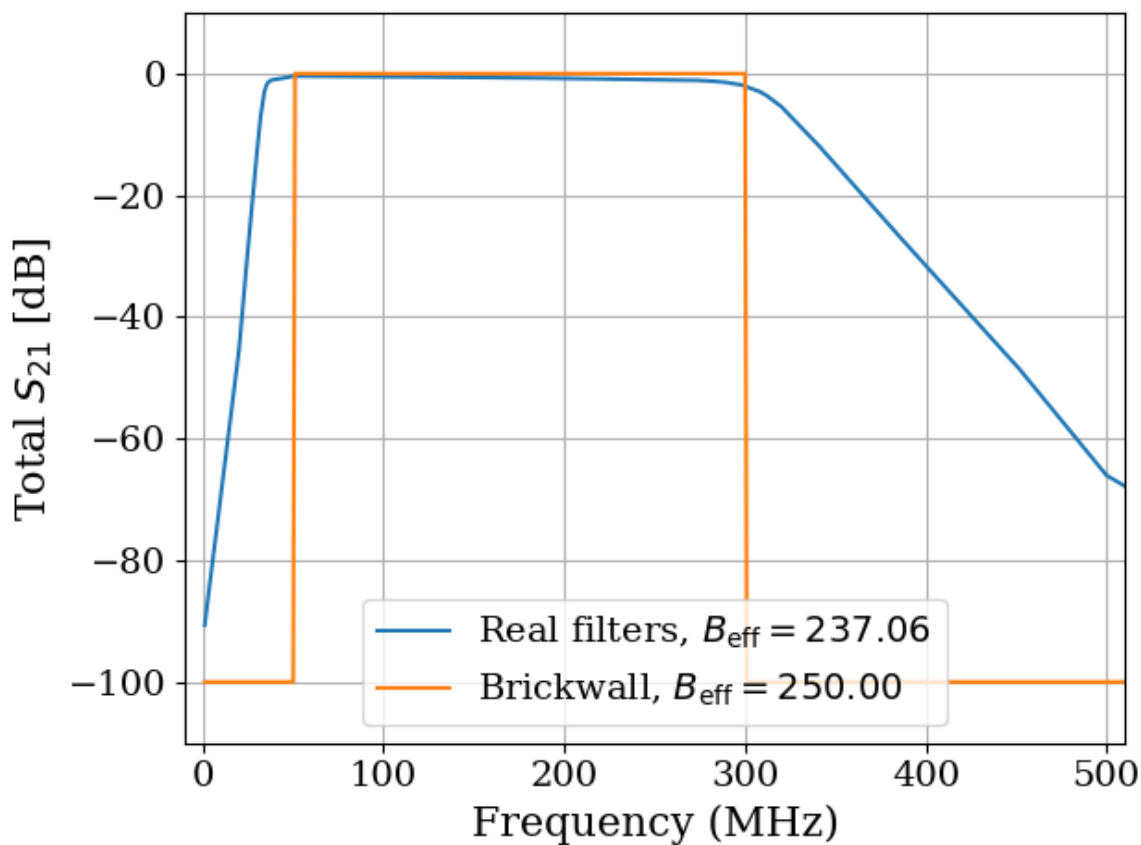


Figure 2.41: Measured through gain (S_{21}) of the Run 1A band-pass filter. Shown in dB, however B_{eff} is computed with linear S_{21} as in Eq. 2.49. The response of an ideal brickwall filter is shown for reference. **comment: Add Hz in legend**

1247 Setting the gain is ultimately done by trial and error; taking a scan, adding some attenu-
 1248 ation if it clips, taking a scan, etc. Experience and preliminary simulations have shown

1249 that a few dB of clipping for a noise-dominated signal actually doesn't matter much, but
 1250 this was not fully explored. If future runs are to scan for longer, they may have significant
 1251 contamination from ADC spurs (see Sec. 2.1.5.1), so additional gain driving into clipping
 1252 may be fruitfully explored. Every dB of gain added allows for $10^{1dB/5} \approx 44\%$ more averaging
 1253 before ADC effects are at the same relative level²⁷, so a little extra gain goes a long way.

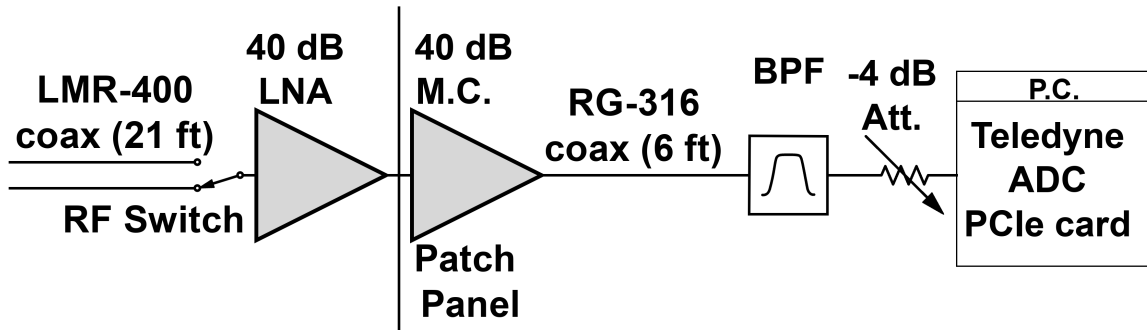


Figure 2.42: Schematic of Run 1A amplifier chain. Antenna (Sec. 2.5.2) and terminator (Sec. 2.5.3) are not part of the amplifier chain and, therefore, are not shown, but they would be at the far left of the schematic. All RF connectors are SMA, except the connection between the bicon antenna and its cable which is N type (though that cable has SMA on the switch-side). RF switch is Teledyne CR-33S8D-T. 40 dB LNA is Pasternack PE15A1012-E (Table 2.3). The patch panel uses an SMA bulkhead connector labeled "A" (far left-hand side when standing outside the shielding room, as shown in Fig. 2.38). 40 dB Mini-Circuits (M.C.) is Mini-Circuits ZKL-1R5+ (Table 2.4). Band-pass filter (BPF) is made up of Mini-Circuits SLP-50+ high pass filter and Mini-Circutis ZX75LP-288-S+ low pass filter. Note that filters and attenuator are directly connected to the SMA port of the Teledyne ADC (Sec. 2.5.7) to mitigate RFI received in the RG-316 cable run.

²⁷Calculations in dB like this are handy once they are understood, but can seemingly come out of nowhere. This can be worked out by a careful reading of section 2.2, using properties of logarithms and definition of the dB.

1254 **2.5.5 Veto antenna**

1255 The veto antenna is an identical Compower AB900 bicon antenna [54] as is used in the
1256 shielded room. It is connected to channel A of the ADC with no amplification. However, it
1257 has a Mini-Circuits ZX75LP-288-S+ low pass filter [52] to prevent aliasing. This is the same
1258 model low pass filter that is used for the main channel. The antenna is hung a few feet in
1259 front of the door from some pipes on the ceiling. The proximity to these pipes likely gives
1260 the antenna a strange response, but its purpose is simply to look for large RFI signals, so
1261 this isn't that important.

1262 **2.5.6 12 V power system**

1263 The LNA and switch are active components that require power to operate. The experiment
1264 is incredibly sensitive to RFI, so while there is 120 VAC in the room, it is simpler to provide
1265 the power from a 12 V battery than to use an AC/DC regulator. Originally a 12 V lithium-
1266 ion (LiFePO4) battery was used. Lithium-ion batteries contain several cells and a controller
1267 to regulate charge/discharge between the cells. In order to remove the possibility of this
1268 controller emitting RFI in the room (which would create candidates that would be extremely
1269 difficult to veto), the lithium-ion was replaced with a 12 V lead acid golf cart battery ²⁸.

1270 The LNA is interlocked to the door such that power is cut when the door is opened.
1271 This prevents the large radio signals from being amplified once they enter the room and

²⁸This was done between run 1.2 and 1.3 due to interference resulting in many candidate detections. Most of these were likely external RFI, which were eliminated by cleaning the door (discussed in Sec. 3.2. Two variables were changed (cleaning of the door and replacement of the battery) so it's unclear if a lead acid is necessary. It works, however, and if it ain't broke, don't fix it.

1272 protects the ADC. The circuit that controls this is shown in Fig. 2.43. Note that it takes a
 1273 few seconds for the slow turn on circuit to discharge, so the door should be opened slowly

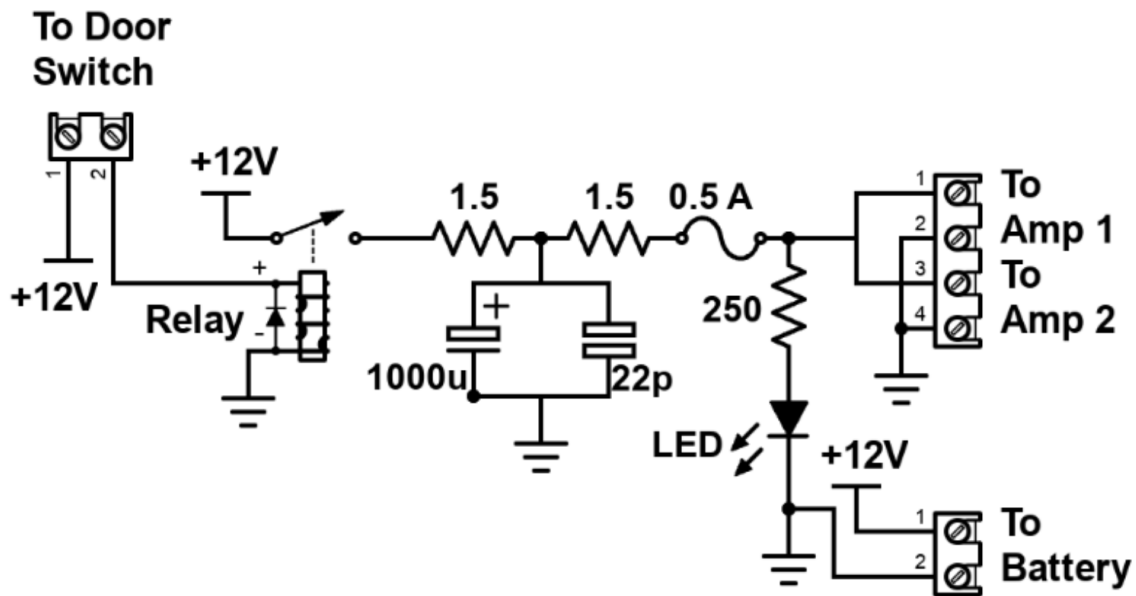


Figure 2.43: Schematic of Interlock board. No voltage regulation is provided because it is designed to work with amplifiers containing internal regulation (Pasternack PE15A1012 [22]). Not shown is a simple “slow turn on circuit” consisting of a 0.68 F capacitor and an 8Ω , 10 W resistor (time constant = 5.4 seconds) which was installed to protect the amplifier from transient voltages when the door is closed. This circuit can be seen in Fig. 2.44. Experience has shown the liberal use of fuses to be prudent when working with car batteries in a metal room.

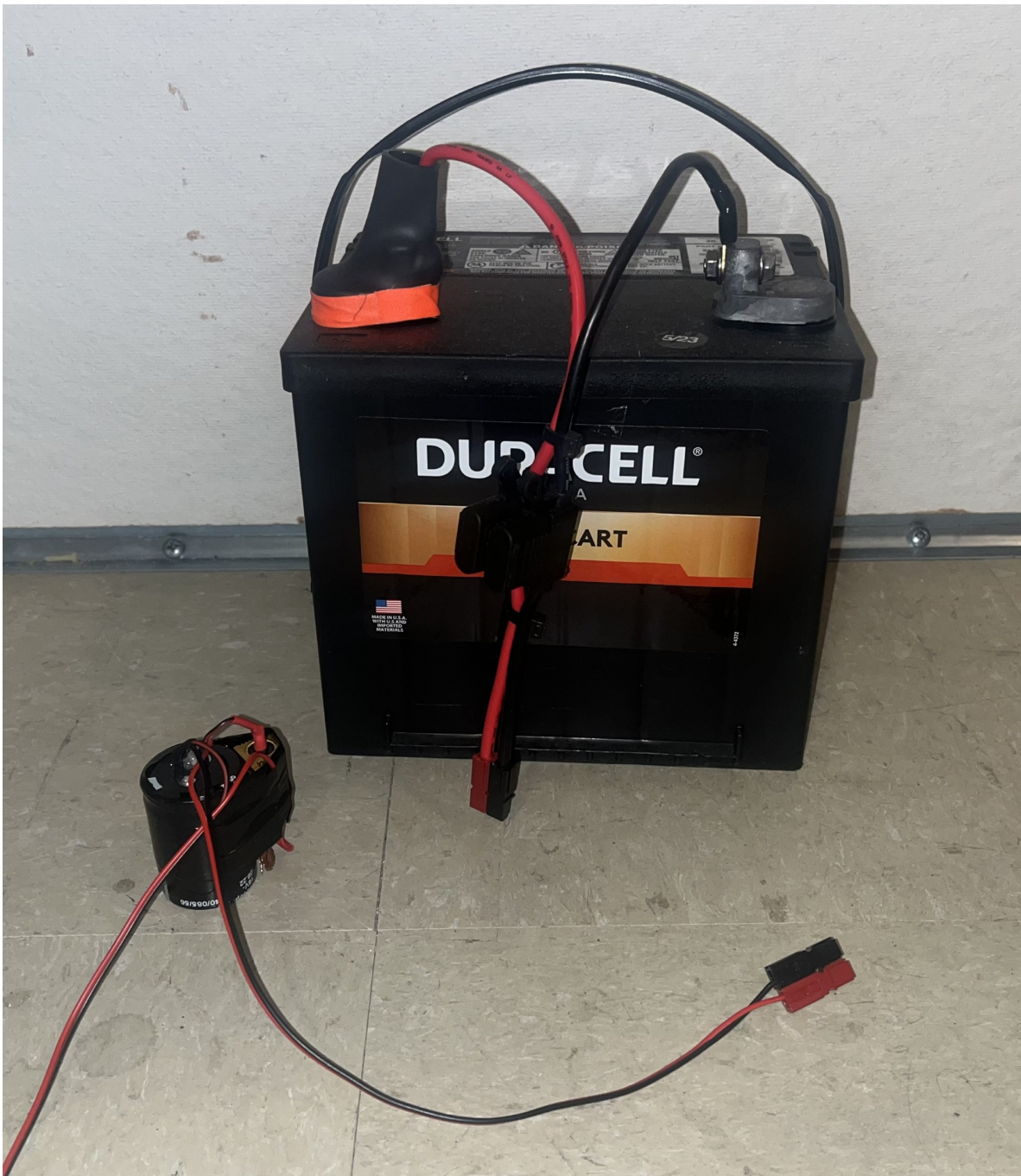


Figure 2.44: Photo of 12 V lead-acid battery and slow turn-on circuit. Both connect directly to the interlock board shown in Fig. 2.43. The slow turn-on circuit is connected between the interlock board and amplifier. The battery includes a 2A fast fuse installed in a commercial Anderson power pole assembly.

1274 **2.5.7 GPU-Based Real-Time Spectrum Analyzer**²⁹

1275 The use of commercial Spectrum Analyzers (SAs) that feature so-called real-time spectrum
1276 analyzer (RTSA) mode comes with several restrictions that limit the efficiency with which
1277 they are able to perform wide-band scans with narrow frequency resolution, as pointed out
1278 the dark radio pilot run [4]. The number of frequency bins output by a real discrete Fourier
1279 transform (DFT) is equal to half of the number of time domain samples, while the bandwidth
1280 is given by half of the sample rate. Furthermore, the ability to acquire data in real-time
1281 requires a DFT algorithm (generally implemented as a fast Fourier transform, FFT) and
1282 computational resources that can operate on time domain data at least as fast as it is
1283 acquired. In practice, real-time DFTs with high-frequency resolution and wide bandwidth
1284 require modest memory, transfer rates and processing resources. Commercial “real-time
1285 spectrum analyzers” tend to cheat a bit to reduce hardware requirements. Frequency mixers
1286 reduce the required sample rate (and therefore span), limits on FFT lengths reduce either
1287 span or resolution, and limits on the rate of scans make it so that these SAs aren’t real-time
1288 (at least in the sense that we require them to be).

1289 For this reason, I have constructed a custom SA based on the Teledyne ADQ32 PCIE
1290 digitizer[23], which is wide-bandwidth (up to 1.25 GHz frequency span), high resolution
1291 (2^{24} point FFT), and nearly 100% real-time (see Fig. 3.16). I have been unable to find a
1292 commercial SA with comparable capabilities. Specifications are shown in table 2.5.

²⁹Code for this section can be found at: <https://github.com/josephmlev/darkRadio/tree/master/daqAnalysisAndExperiments/teledyne>

Bit depth	12 bits
Sample rate	800MHz
DFT input length	2^{24} samples
FFT compute time	2 ms
Channel count	2
Efficiency	99.765%

Table 2.5: Specifications for the custom, real-time spectrum analyzer used for Run 1A.

1293 After passing through an amplifier and filter chain outlined in Sec. 2.5.4, both the main
 1294 and veto antenna's RF signals are digitized by the ADQ32's two independent ADCs. This
 1295 raw, digitized time series is sampled at the digitizer's clock rate. Since the discrete Fourier
 1296 transform (DFT) of a perfect sinusoid sampled by an unstable clock will have a finite spectral
 1297 width, clock stability must be better than the expected spectral width of candidate signals,
 1298 which in our case is set by the expected $Q_{DP} \approx 10^6$. To achieve the required stability, we
 1299 synchronize the sample clock (Valon 5009 RF synthesizer) of our ADC to a 10 MHz rubidium
 1300 frequency standard (Stanford Research Systems FS725), which is further steered by the
 1301 one pulse-per-second (PPS) signal from a GPS receiver. Clock performance is discussed in
 1302 Sec. 3.3.3.

1303 This system utilizes a GPU direct write in order to minimize CPU-GPU copies tends to
 1304 be significantly slower than the FFT itself. This GPU direct write is implemented by the digi-
 1305 tizer's C++ API which is called from python. This happens in the `teledyneTemplate/drDaq.py`
 1306 script (within the directory linked as a footnote at the beginning of this subsection). The
 1307 GPU is a Nvidia A5000. The process is shown graphically in Fig. 2.45

1308 First, several buffers are allocated in GPU memory. A record is acquired (2^{24} time domain

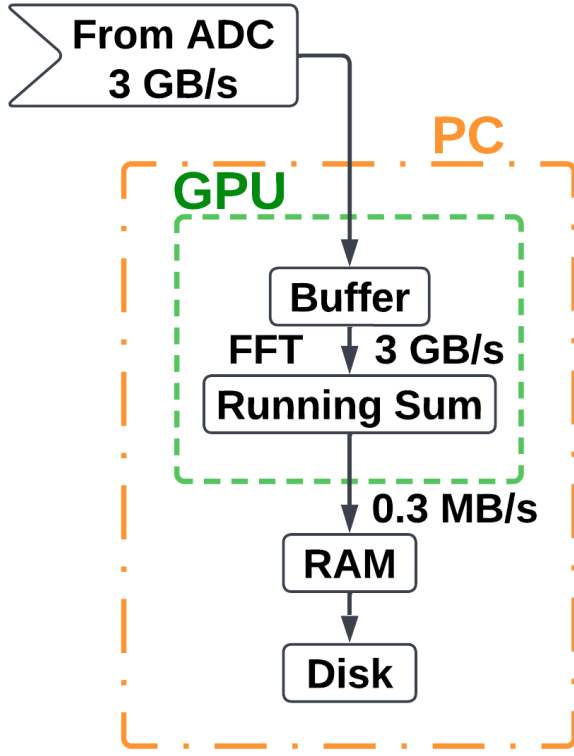


Figure 2.45: Real time DAQ data stream. Approximately 10^4 time series records (about 3 minutes of real-time data) are written from the ADC directly to GPU buffers. FFTs are performed on these records, resulting in a pre-averaged spectrum that can be saved to disk. This setup is duplicated for channels A and B, though the data rates indicate the sum of both channels.

1309 samples for Run 1A). This record is written to a pre-allocated, time-domain buffer in the
 1310 GPU's memory. Next, an FFT is performed using Pytorch, which I found to be the fastest
 1311 algorithm, at least on a Nvidia GPU. 8,600 FFTs are performed and added to a cumulative
 1312 sum on the GPU (representing about 3 minutes of real-time data). Dividing by the number of
 1313 FFTs provides an averaged spectrum that is saved for offline processing. This *pre-averaging*
 1314 reduces the raw $\approx 1.5 \text{ GB/s}/\text{channel}$ data stream to $\approx 0.15 \text{ MB/s}/\text{channel}$, which greatly
 1315 reduces storage requirements. However, this comes at the cost of temporal resolution of

1316 transient candidates. Since we are interested in constant (or at least very slowly varying)
1317 signals, this is not a problem, but in other radio astronomy applications, this step should be
1318 avoided. Pre-averaging is set using the NOF_BUFFERS_TO_RECEIVE variable, see Appendix A .

¹³¹⁹ **Chapter 3**

¹³²⁰ **System Characterization and Data**

¹³²¹ **Acquisition System**

¹³²²

“When you can measure what you are speaking about and express it in numbers you know something about it; but when you cannot measure it, when you cannot express it in numbers your knowledge is of meagre and unsatisfactory kind; it may be the beginning of knowledge but you have scarcely progressed in your thoughts to the stage of science whatever the matter may be.”

Lord Kelvin

1323 This chapter covers the characterization of the system as a whole, including the shielded
1324 room (Introduced in Sec. 2.5.1), amplifier chain (Sec. 2.5.4) and real-time spectrum analyzer
1325 system (RTSA, Sec. 2.5.7). This section provides data and information about how they
1326 were collected from tests that were performed, but that distract from the narratives of the
1327 preceding and following chapters. This chapter can be skimmed and referenced with further
1328 care during the reading of Ch. 4.

1329 **3.1 Measurement of Amplifier Chain Performance**

1330 The amplifier chain conditions the analog signal (described in Sec. 2.5.4). The following data
1331 show some measurements that are useful in confirming the system is operating as expected.
1332 Similar data should be collected and inspected before, during and after a new data run so
1333 that any performance degradation can be monitored. At the very least, one should take
1334 note of the power spectrum from a room temperature terminator (Fig. 3.10) and monitor it
1335 throughout the run for any changes. The heads-up display (Fig. A.1) makes this very easy.

1336 **3.1.1 Y-factor method¹**

1337 The Y-factor method [55] [56] is a common technique for measuring the gain and noise
1338 temperature of an amplifier chain (details in Sec. 2.1.4). A matched terminator is placed at
1339 the end of a transmission line, which is connected to the input of an amplifier chain under
1340 test. The output of the amplifier chain is measured with the terminator at two different

¹Code for this section can be found at: <https://github.com/josephmlev/darkRadio/tree/master/daqAnalysisAndExperiments/run1p4/yFactorTest/yFactorTest.ipynb>

1341 temperatures². These temperatures must be known, and the larger the difference the better
1342 the measurement because it is easier to extrapolate the slope and intercept from these data
1343 (see Fig. 3.1).

1344 There are a few different ways to handle the algebra, but the simplest is to fit a line of
1345 the form

$$T_{\text{out}}(\nu) = G T_{\text{term}} + B, \quad (3.1)$$

1346 where all terms are dependent on frequency. The x-intercept (and therefore the negative
1347 amplifier temperature) is simply G/B . This is shown as a cartoon for a single frequency in
1348 Fig. 3.1.

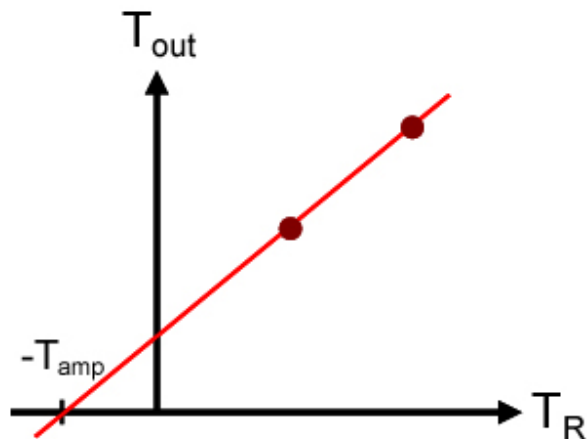


Figure 3.1: Cartoon showing Y-factor data. The (negative of) amplifier temperature is read off of the x-intercept. The gain is given by the slope. Figure from Wikipedia [57].

1349 To make this measurement, I wanted to use liquid nitrogen for the cold temperature

²Alternatively, a calibrated noise source can be used to simulate a very hot terminator, usually thousands of degrees Kelvin.

1350 (77 K) and a calibrated noise source for the hot temperature (\sim 12,000 K). The test was
1351 conducted using the noise source and a 30 dB attenuator placed directly before the ADC.
1352 This attenuation was later accounted for, yielding a calibrated measurement. However,
1353 while the test was set up to use this noise source, it gave unreliable results. I was able
1354 to confirm it became uncalibrated using a spectrum analyzer, so I did not use that data
1355 point. Additionally, I made the measurements with a much wider band-pass filter (0-1 GHz)
1356 compared to the span of Run 1A (0-0.3 GHz) so that the same data would also give the gain
1357 and noise temperature up to 1 GHz (though this is not shown in this thesis). Both the 30 dB
1358 attenuator and the 0-1 GHz band-pass filter will be calibrated out. As a check, this is done
1359 correctly, the gain was measured again using a tracking generator with the actual setup,
1360 avoiding corrections. This is shown in Fig 3.7. The two gain curves agree quite well.

1361 The test setup is nearly identical to the Run 1A amplifier chain (see Fig. 2.42). The
1362 differences are the 30 dB attenuator and band-pass filter (discussed above) and the short,
1363 semi-rigid, cryogenic-capable cable between the terminator and LMR 400 cable. The cryo-
1364 genic setup is the same as shown in the right panel of Fig. 2.28. The raw data (including
1365 only liquid nitrogen and room temperature) are shown in Fig. 3.2.

1366 The spectra of Fig. 3.2 contain hot and cold measurements at 2^{18} frequency points. At
1367 each point, a fit is performed according to Eq. 3.1. To demonstrate, this is shown for a single
1368 frequency (625 MHz) in Fig. 3.3.

1369 Finally, fitting the raw spectra shown in Fig. 3.2 with Eq. 3.1 at each of the frequency
1370 points, the frequency-dependent gain and noise temperature of the amplifier chain is ex-
1371 tracted. These are shown (after correcting for the 30 dB attenuator) in Figs. 3.4 and 3.5.

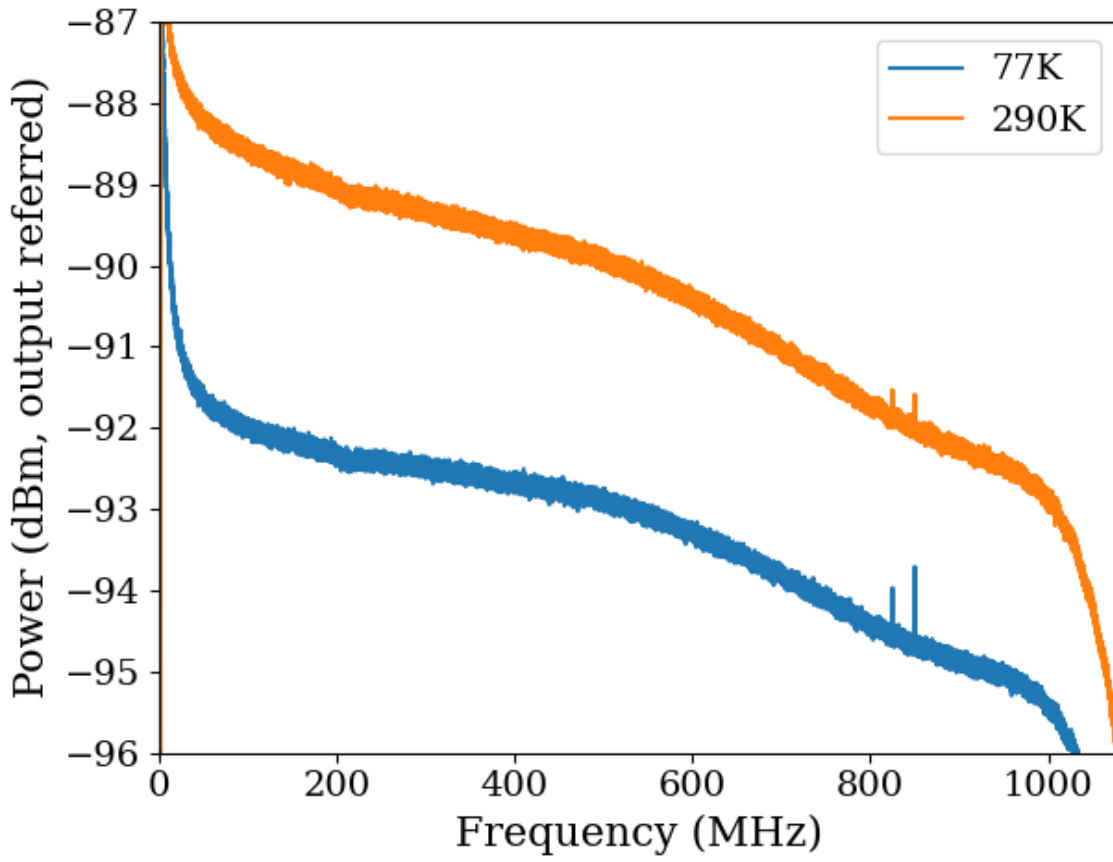


Figure 3.2: Raw output power spectra used to compute the gain and noise temperature for the Run 1A amplifier chain using the Y-factor method. $\Delta\nu_{\text{RF}} \approx 9.5 \text{ kHz}$, and 10,000 averages were taken. These data are only used to characterize the system between 50 and 300 MHz, so the low frequency ADC effects and RFI around 800 MHz do not affect the calculation. Note that the amplifier chain under test has a 30 dB attenuator directly before the ADC which is discussed in the text. This had an impact on the measured gain, and it is corrected for in the following analysis. It has negligible impact on the noise figure however, as shown in Eq. 2.29.

1372 As a final check, I took the Run 1A terminator data and corrected it for the gain and noise
 1373 figure found using the Y-factor method of this section, expecting to recover the -174 dBm/Hz
 1374 as predicted by Johnson's formula for a terminator at room temperature. The agreement is
 1375 excellent, as shown in Fig. 3.6.

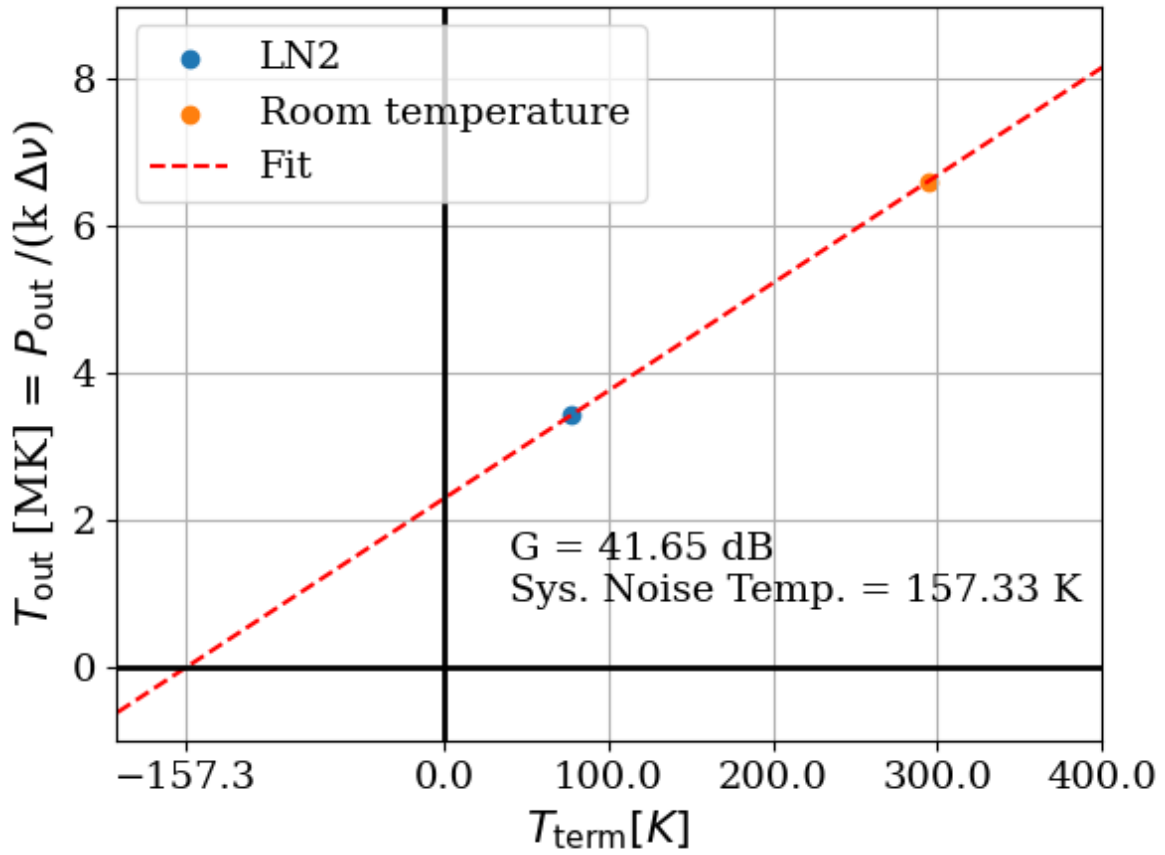


Figure 3.3: Y-factor data from the Run 1A amplifier chain at a single frequency (625 MHz). Note that T_{out} is in MK or millions of degrees Kelvin. This is expected since there is approximately 41 dB of gain on an input temperature of a few hundred Kelvin. Reminder, there is a 30 dB attenuator which has not yet been corrected for.

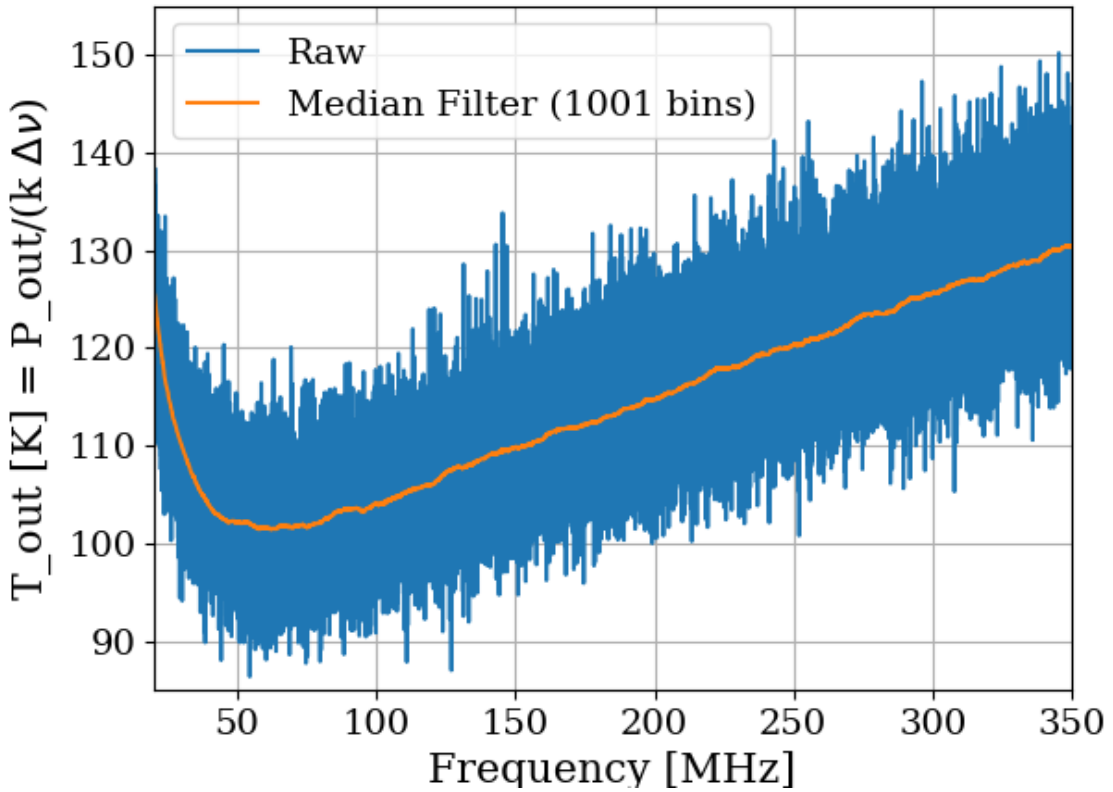


Figure 3.4: Frequency-dependent noise temperature of the Run 1A amplifier chain, measured using the Y-factor method. Low-frequency behavior is consistent with the data sheet of the LNA [22]. The increase at high frequency is due to the attenuation of the cable before the LNA. Future runs may place the LNA directly on the antenna to minimize this issue, though other complications will be introduced. The median filter is a simple rolling median to smooth out the noisy measurements.

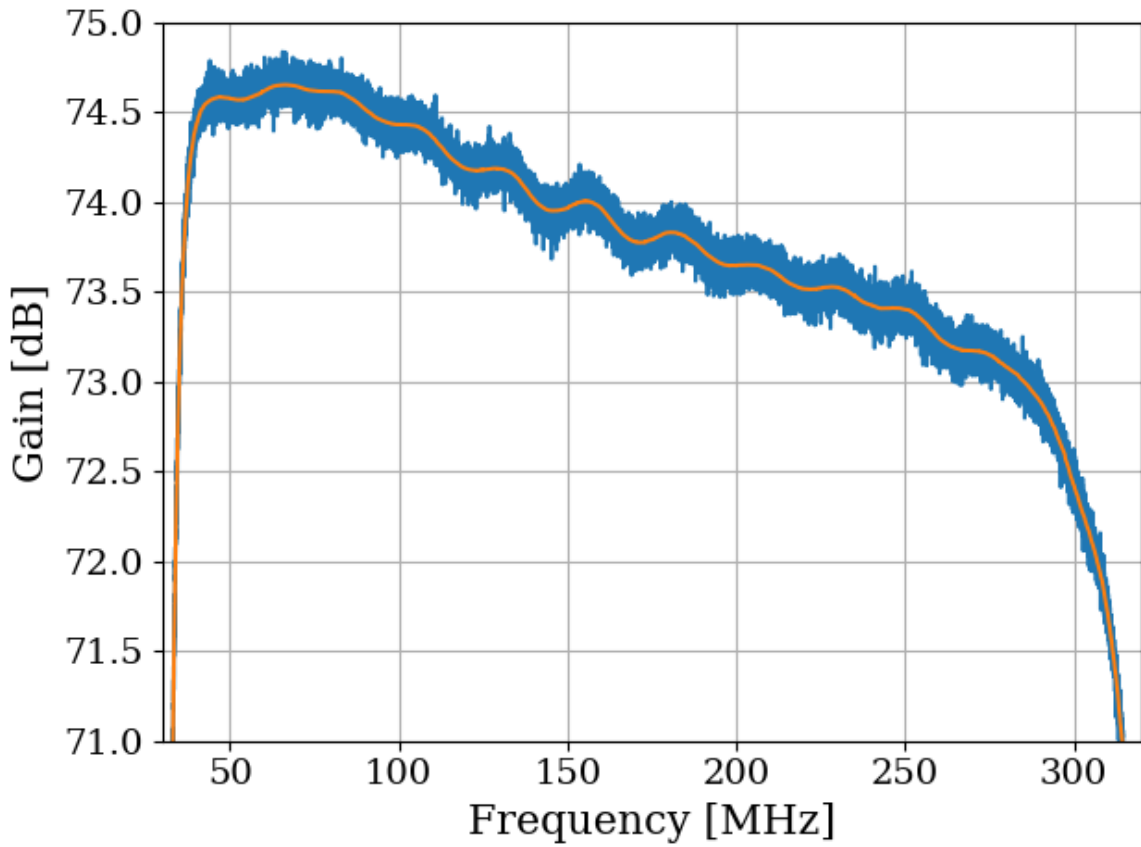


Figure 3.5: Frequency-dependant gain of the Run 1A amplifier chain, measured using the Y-factor method. The 30 dB attenuator and band-pass filter have been corrected for in this plot. The slow decrease of gain with frequency is consistent with the datasheets for the LNA [22] and secondary amplifier [49]. Roll-off at high and low frequencies is due to the band-pass filter (see 2.5.4.3). Bumpy behavior is due to the small impedance mismatch of the terminator to the 50Ω system.

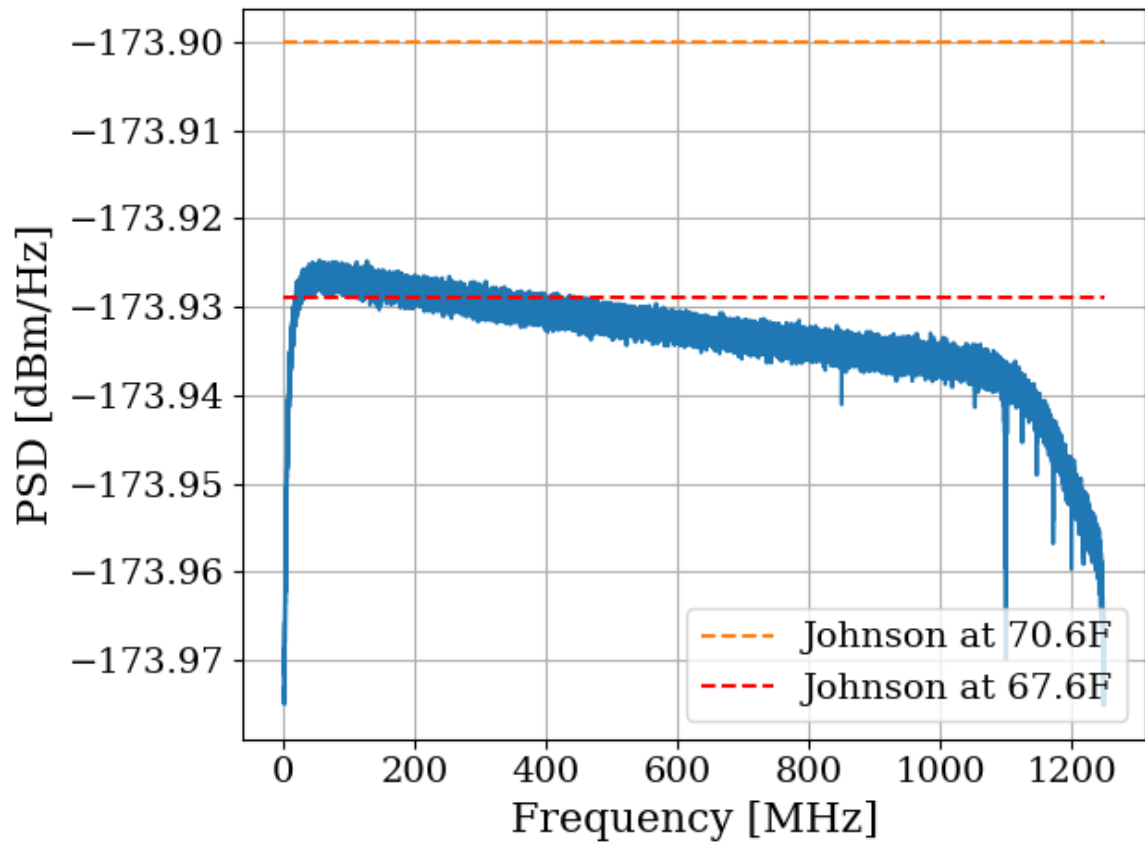


Figure 3.6: Run 1A terminator, input-referred power spectral density. Excellent agreement with the predicted value from the formula for Johnson noise at room temperature. Two reference temperatures are given with the dashed lines.

1376 **3.1.2 Confirming gain with tracking generator measurement**

1377 As a sanity check for the Y-factor method, the system gain was measured again using the
1378 tracking generator on the Rigol RSA-5065-TG [58], with good agreement. This measurement
1379 was useful since there were some corrections involved in the Y-factor measurement (the 30 dB
1380 attenuator and band-pass filter).

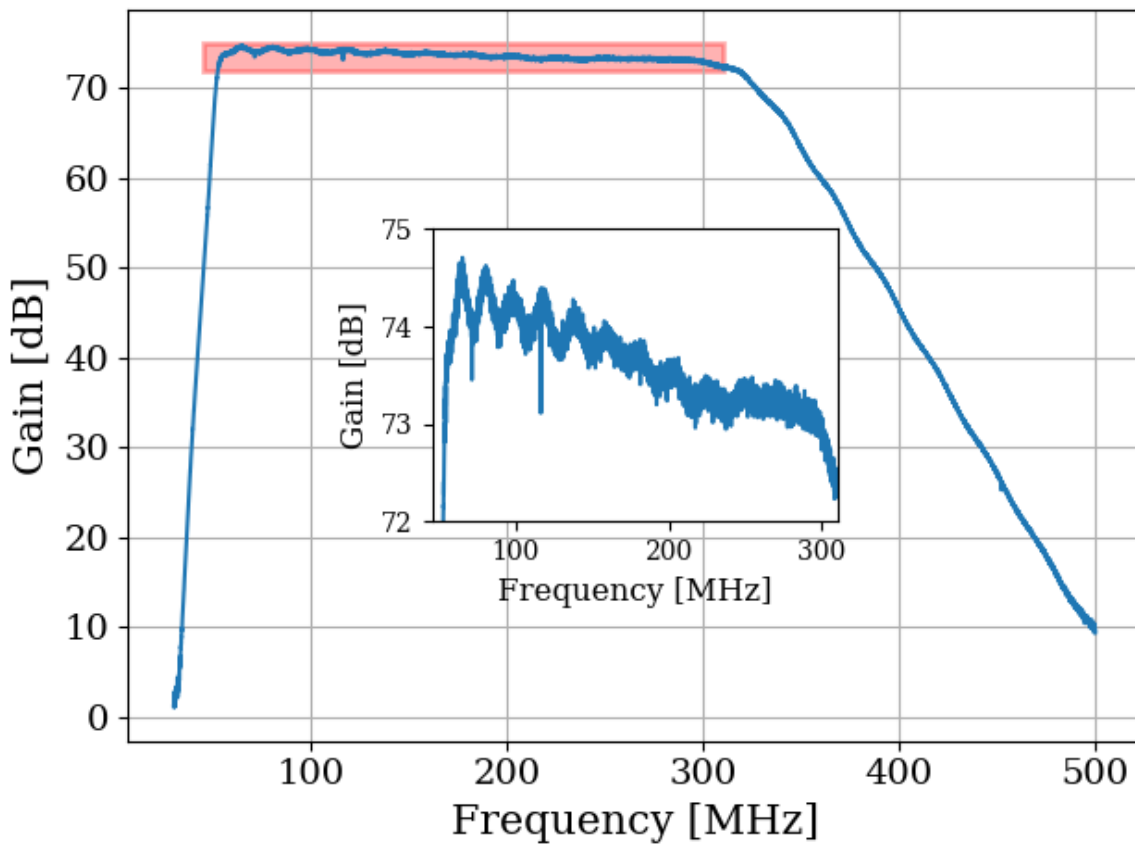


Figure 3.7: Gain vs. frequency of the Run 1A amplifier chain, including LNA, secondary amplifier, band-pass filter and attenuators. The inset shows the zoom of the region enclosed in the red box. This was measured using the tracking generator on Rigol RSA-5065-TG [58]. Wiggles visible in the inset are a known artifact due to an impedance mismatch between the Rigol's tracking generator and the system under test. The gain was confirmed by comparing it to the gain found with the Y-factor method (Sec. 3.1.1)

1381 **3.1.3 System stability over a run period** ³

1382 The system's gain will vary slightly over the course of a run. An obvious culprit is the
1383 battery voltage decreasing with time⁴. At first glance, one may conclude that since the LNA
1384 is equipped with an internal voltage regulator, it is insensitive to the battery voltage as long
1385 as it is above some minimum value. However, at higher voltage, the regulator must dissipate
1386 more power which will make the LNA warmer. Temperature does have an effect on the gain
1387 of the LNA. Tests of gain vs. LNA voltage show that this is a minor issue. This is shown in
1388 Fig. 3.8.

1389 Knowing the gain vs. voltage is only useful if it is understood how the battery voltage
1390 will behave over the course of the run. These data are shown in Fig. 3.9.

1391 As a final check of system performance during the run, Fig. 3.10 shows the output-referred
1392 power (averaged from 50-300 MHz) over the course of the 9-day Run 1A. The gain varies by
1393 about 0.7%, an insignificant amount given the other uncertainties involved (especially that
1394 of simulation and calibration, Sec. 4.3).

³Code for this section can be found at: [https://github.com/josephmlev/darkRadio/tree/master/daqAnalysisAndExperiments/run1p4/run1p4_timeDependence.ipynb](https://github.com/josephmlev/darkRadio/tree/master/daqAnalysisAndExperiments/run1p4/run1p4_analysis/run1p4_timeDependence.ipynb)
https://github.com/josephmlev/darkRadio/tree/master/daqAnalysisAndExperiments/run1p4/gainAndNF/gainAndNF_analysis.ipynb

⁴The LNA is powered by a battery. The secondary amplifier is outside of the room and powered with a voltage regulator.

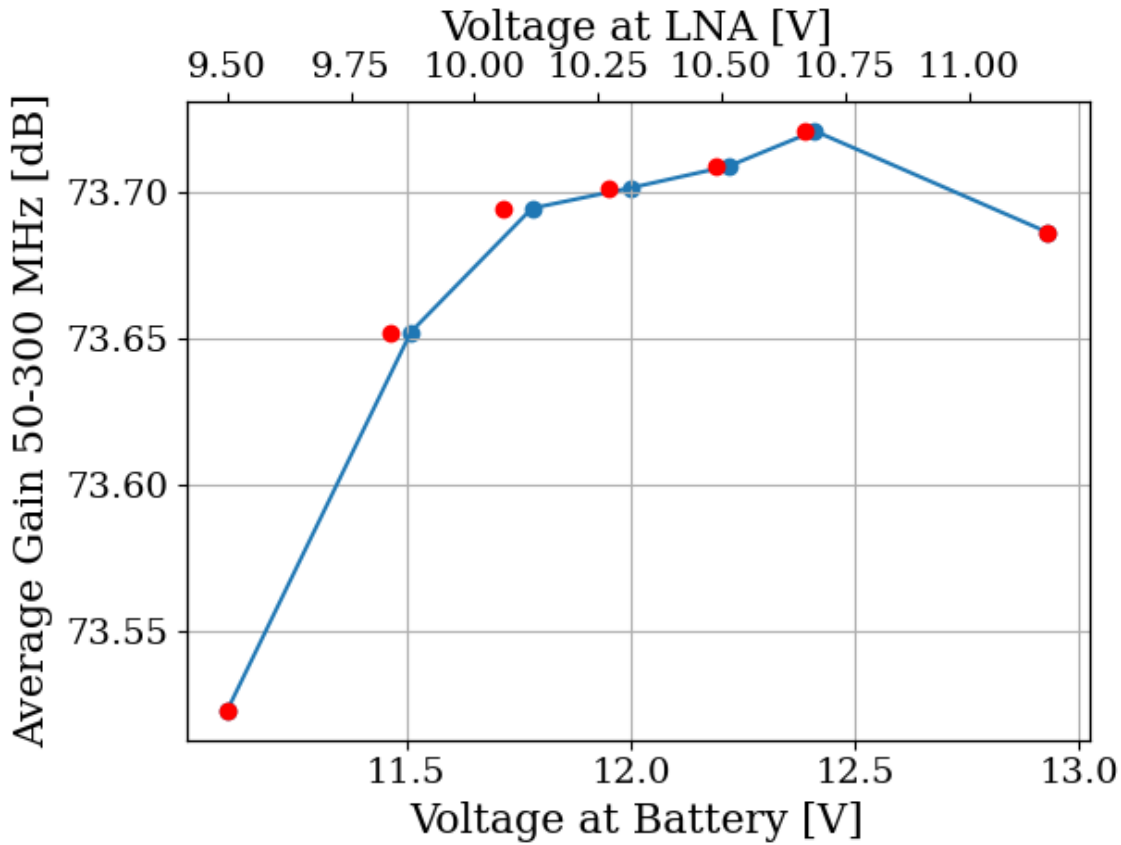


Figure 3.8: Gain vs. LNA voltage of the Run 1A amplifier chain, including LNA, secondary amplifier, band-pass filter and attenuators. This was measured using the tracking generator on Rigol RSA 5065TG [58]. Gain is frequency dependent; its average value is between 50 and 300 MHz is shown here. The voltage at the amplifier was measured directly at its terminals after a significant voltage drop due to interlock and slow turn-on circuits (described in Sec. 2.5.6). Gain is in good agreement with the previous two subsections, 3.1.1 and 3.1.2. The operating voltage range specified on LNA data sheet [22] is 10-15 V. The voltage at the LNA (red) does not exactly line up with voltage at battery (blue), so there is a slight offset. The scale of the x-axes scale has been set so that the maximum and minimum voltages line up.

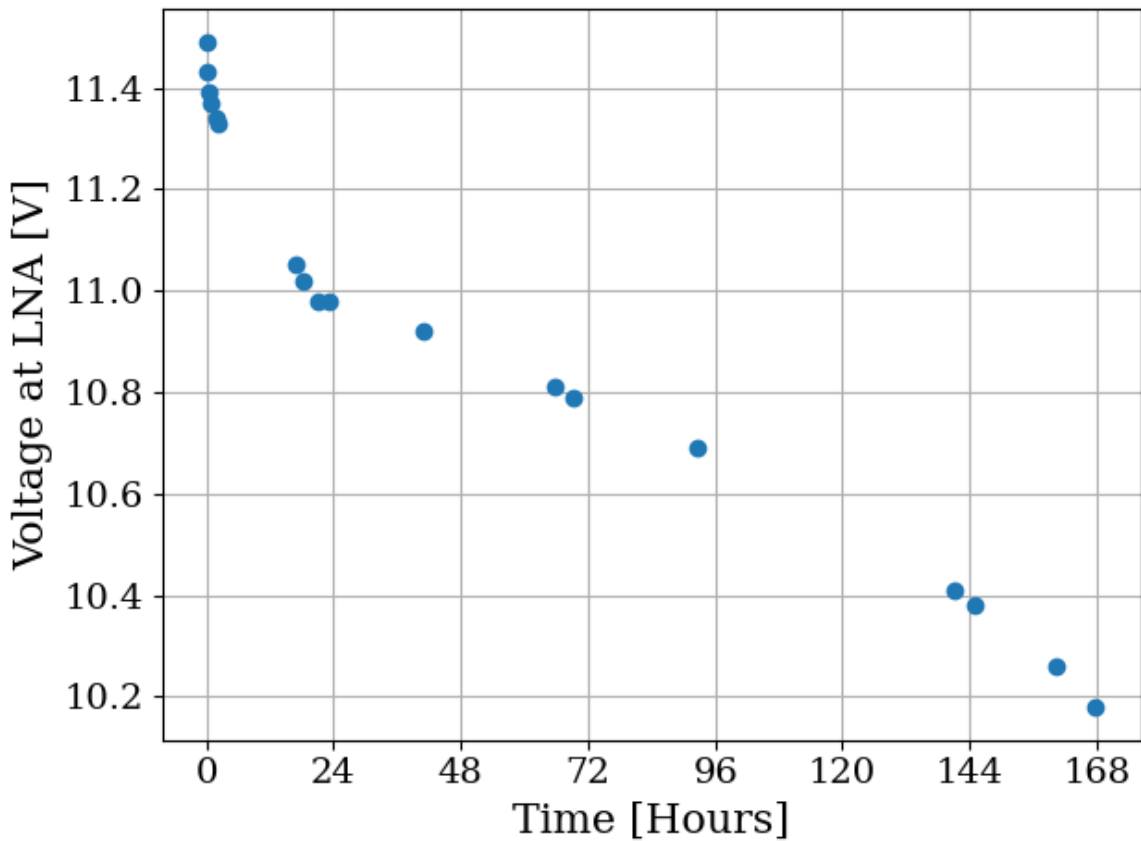


Figure 3.9: Voltage at LNA vs. time with Run 1A setup. These data were acquired 7/15/2024 through 7/22/2024 using battery number 2 immediately after being charged. The system was set up as it was for Run 1A, including the switching cycle (on for 3 minutes, off for 45 minutes). The battery supplies 177 mA when the switch is off and 370 mA when the switch is on. There is an additional data point (not shown) around 196 hours where the voltage has dropped to 6.2 V, well below the minimum required voltage. The battery had approximately 20 charge/recharge cycles at the time of this test and was about 14 months old. A repeat of this test may be required to use the battery for longer periods between charges.

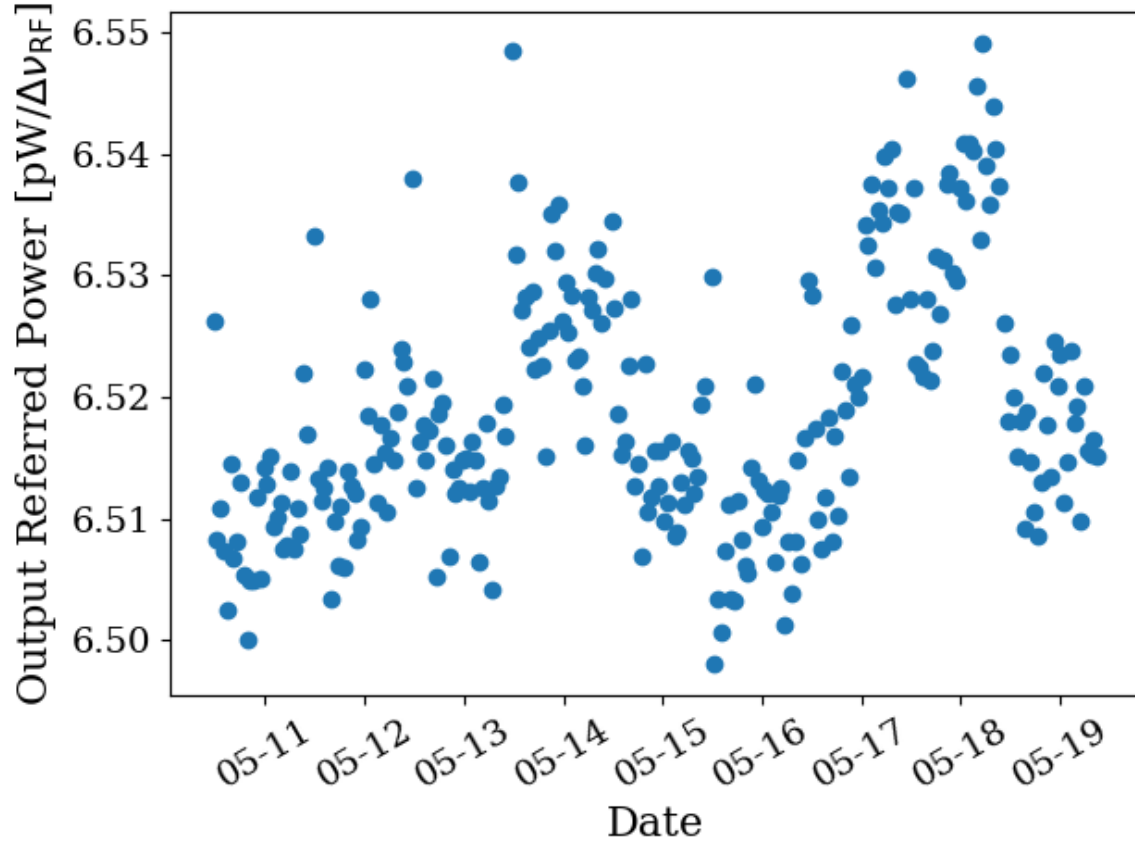


Figure 3.10: Frequency-averaged power spectral density vs. time of the terminator from Run 1A (schematically shown in Fig. 2.37). Each data point represents the mean power between 50 and 300 MHz of the terminator. In Run 1A, a \sim 3 minute long scan of the terminator took place after \sim 45 minutes of antenna scans. The dates shown are all May 2023 (month-day format, year suppressed), and the x-axis ticks are placed at midnight.

1395 **3.2 Measurement of shielding effectiveness and radio**
1396 **frequency interference**

1397 Shielding effectiveness (SE) and radio frequency interference (RFI) were introduced in Secs.
1398 2.1.3 and 2.5.1. Their measurement is introduced here.

1399 Similar to the warning given in the previous section, SE should be measured before
1400 starting a data run or after entering a new frequency range/modifying anything on the
1401 patch panel. In addition, it is best practice to clean the door's RF seal before beginning a
1402 run (the procedure is described in the text of this section).

1403 Due to reciprocity between antennas, measuring the shielded room's ability to keep radi-
1404 ation *out* is equivalent to measuring how well the room can keep it *in*. The latter method is
1405 simpler and was performed. The IEEE standard prescribing a very detailed SE measurement
1406 procedure [59] was used as a rough guideline, but the simple results presented here should
1407 be viewed as an estimate. While simplified, the results do tend to agree with predictions of
1408 when RFI should become detectable, based on comparisons to the veto antenna spectrum ⁵.

1409 The SE was measured by placing a Rigol DSG830 signal generator and 25 Watt RF power
1410 amplifier inside the room, both powered by the filtered 120 VAC Edison outlets inside the
1411 room, shown in Fig. 3.11. An antenna was connected to the signal generator. Outside of
1412 the room, an identical antenna was connected to a Rigol RSA-5065-TG spectrum analyzer
1413 [58]. The spectrum is scanned to find a frequency without local interference which would

⁵Or at least they did agree before cleaning the door. With the excellent isolation values, no RFI was detected in Run 1A.

1414 confuse the results. The spectrum analyzer was set to attenuate its input to prevent clipping
1415⁶, and the signal generator was set to output a sine wave near the maximum power of the
1416 RF amplifier ($20\text{ W} = 43\text{ dBm}$). The power measured on the spectrum analyzer is P_{open} in
1417 Eq. 2.46. The door was closed, attenuation removed and P_{closed} was measured. In some
1418 cases the SE was so high a signal was buried below the noise floor of the spectrum analyzer.
1419 These data are shown in red in Figs. 3.12 3.13 and should be interpreted as an upper limit
1420 on isolation, since the true value is lower (better).

1421 SE can drop off to less than 80 dB if the RF gasket around the door is not clean. Previous
1422 day-long test runs detected several hundred signals that originated from RFI emitted from
1423 the PC and several local radio stations. Cleaning was performed by scrubbing the copper
1424 finger stock and steel mating surfaces with red Scotch-Brite using denatured alcohol as a
1425 lubricant⁷. After two passes of polishing were complete, a layer of DeoxIT D100L liquid
1426 was added. Maintenance cleanings were performed using only DeoxIT D5 spray. These
1427 signals were not detected after the gasket was cleaned, which is consistent with calculations
1428 of Sec. 2.1.3

1429 The primary RFI in the 50-300 MHz span are from local radio broadcasts. The electric
1430 field of the strongest signals is $\sim 100\text{ }\mu\text{V/m}$ when measured in the lab. There are also many
1431 lower level peaks which span the entire frequency range, though are more pronounced in a
1432 few frequency bands (60-75 MHz, 130-140 MHz, and 270-290 MHz). These peaks come from

⁶The spectrum analyzer automatically calibrates the displayed spectrum to its internal attenuator and pre-amplifier. If external gain/attenuation are used, they must be accounted for manually. Since this is a relative measurement (i.e., a ratio of $P_{\text{open}}/P_{\text{closed}}$), this calibration does not matter much.

⁷Alcohol fumes are nasty. Be careful to open the hallway door and use a fan to blow in air from the hall. Take frequent breaks. Don't get dizzy while standing on a chair!



Figure 3.11: Photo showing setup to measure SE of 314. Photo taken using Vivaldi antennas for data shown in Fig. 3.13. The same setup was used with bicon antennas for the 50-300 MHz data shown in Fig. 3.12. The bicon antenna shown in the background of this photo was not used for this test.

1433 the PC which is an integral part of the spectrum analyzer system, housing the ADC, so it
1434 can not be removed. Before the door was cleaned, many of these signals were detectable
1435 after a few hours of integration, but cleaning the door resulted in a clean spectrum for the
1436 9-day data Run 1A. The spectrum from the veto antenna (discussed in Sec. 2.5.5) is shown
1437 in Fig. 3.14

314 Shielding Effectiveness

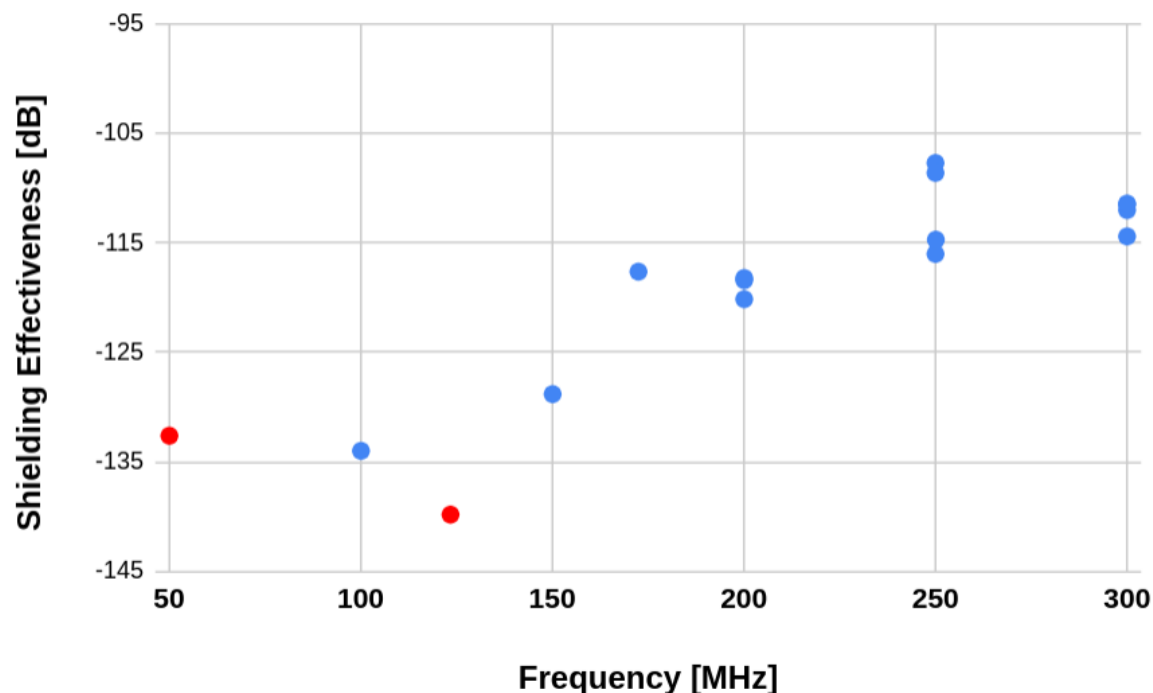


Figure 3.12: Shielding effectiveness of shielded room measured with bicon antenna. Red points indicate measurements limited by the noise floor of the spectrum analyzer located outside the shielded room and are an upper limit. The true SE is lower (better). To get the true SE for these points, measurement would require a higher gain amplifier inside the room. SE measurements are all better than required for Run 1A, and no RFI candidates were detected. At a few frequencies, the antenna inside the room was moved to get a sense of the uncertainty of the measurement.

314 Shielding Effectiveness

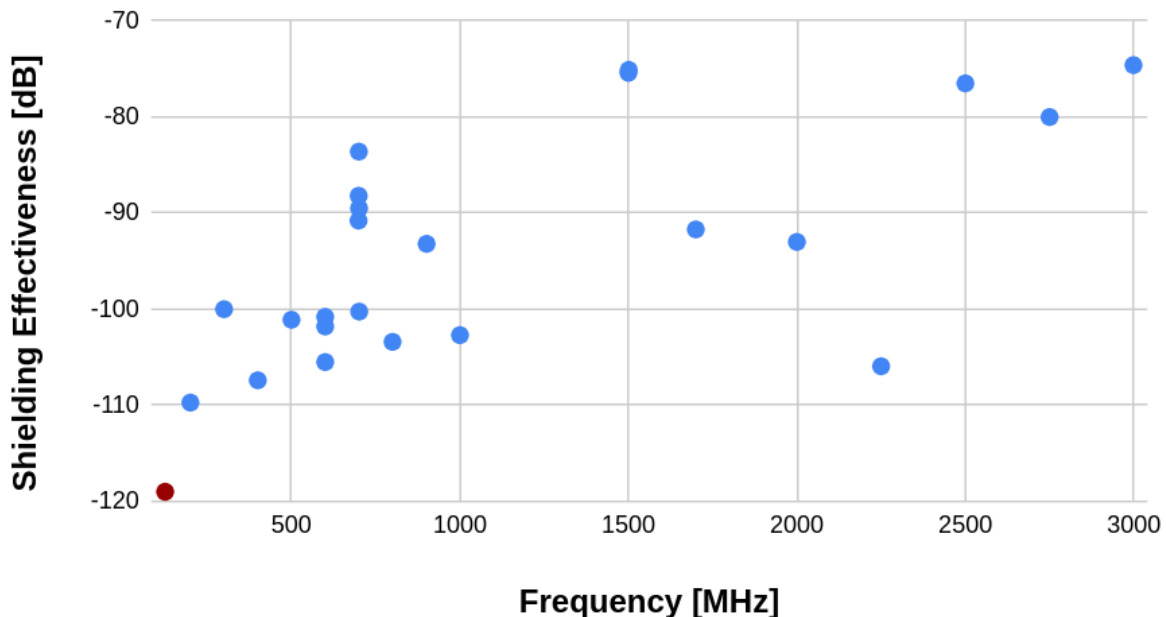


Figure 3.13: Shielding effectiveness of shielded room measured with Vivaldi antenna. Red points indicate measurements limited by the noise floor of the spectrum analyzer located outside and are an upper limit; true SE is lower (better). Measurement would require a higher gain amplifier inside the room. At a few frequencies, the antenna inside the room was moved to get a sense of the uncertainty of the measurement.

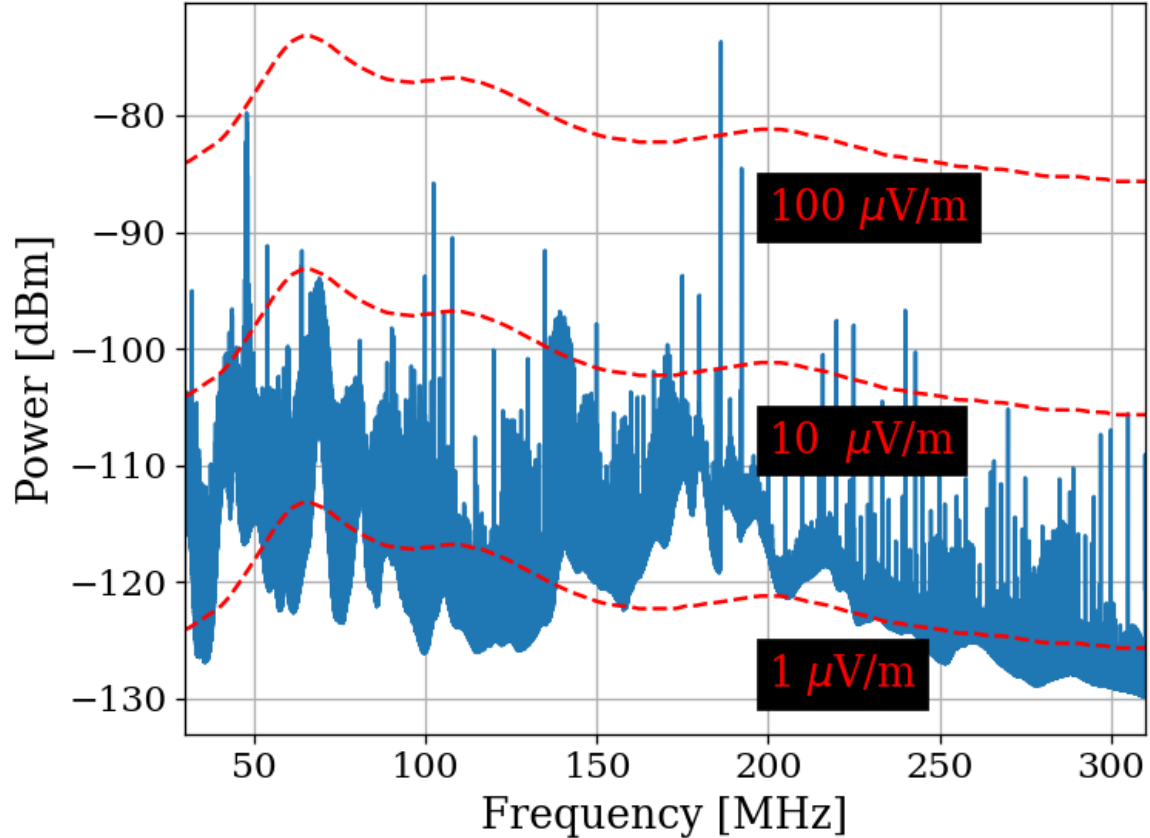


Figure 3.14: Spectrum from veto antenna during the 300 MHz data run. Spectrum plotted as measured power in dBm. Red curves indicate the equivalent field strength. These curves track the free-space antenna factor with frequency for the Com-Power AB900 [45] bicon. Two identical AB900-A antennas are used, one to search for dark photons in the shielded room, and a second to monitor the local RFI background.

1438 3.3 Spectrum Analyzer Characterization

1439 This section outlines several tests performed to ensure the GPU-based real-time spectrum
1440 analyzer (RTSA) system performs as expected. Background information that relates to
1441 this system is described in Sec. 2.5.7.

1442 3.3.1 Spectrum analyzer calibration

1443 The first step in determining if the RTSA system is working adequately is to make sure
1444 it is able to correctly identify known, injected signals and noise. This calibration step is
1445 important since the FFT is normalized manually (see Eq. 2.15), and it is rather easy to
1446 mess up. The test signals were generated with a Rigol DSG830 signal generator. The time-
1447 domain peak-to-peak voltage measured by the RTSA system agreed with the injected voltage
1448 to about 2 %. The signal generator's output frequency and power were verified in both the
1449 frequency and time domain using a separate oscilloscope and spectrum analyzer. This is an
1450 important step since cable losses are significant at this level of precision. They can be taken
1451 into account by consulting the data sheet for the cable⁸.

1452 Next, it is important to understand how the system handles noise spectra, since this is the
1453 primary use of the system. This is tested by amplifying the Johnson noise of a terminator (see
1454 Sec. 2.1.1.2) and measuring the power spectral density. Knowing the gain and noise figure
1455 of the amplifier chain allows for calibration using the procedure outlined in detail earlier in
1456 this chapter, see Sec. 3.1, specifically Fig. 3.6. These results were confirmed several times

⁸There are several cheap black SMA cables which are great for testing, but not for calibration. They have more than 5 dB of loss above 1 GHz. Use a nice cable for these tests, and blow out the SMA connector with compressed air while you are at it.

1457 preceding the data run. Note that due to windowing, other spectrum analyzers will disagree
1458 with the theoretical calculation by a few dB if the equivalent noise bandwith (ENBW) of
1459 the window function is not included. Also remember to take cable effects into account, as
1460 discussed in the previous paragraph.

1461 One final test on a system that integrates noise is to confirm the standard deviation σ of
1462 the noise averages down as predicted by Eq. 2.16. This was confirmed, and the results are
1463 shown in Figs. 4.16 and 4.17.

1464 **3.3.2 Spurious signal performance of the ADC**

1465 Any practical spectrum analyzer will have small, coherent signals that sneak into the analog
1466 signal path and, after being digitized and Fourier transformed, manifesting as spurious signals
1467 or *spurs* (see Sec. 2.1.5.1). These spurs likely come from clock signals within the same
1468 enclosure as the ADC. They can also come from local oscillators bleeding through mixers in
1469 a mixed, high-frequency system such as the Rigol RSA 5065TG [58] or the future, upgraded
1470 dark radio system discussed in Ch. 6.

1471 Regardless of their origin, the spurs must be characterized such that if a known spur is
1472 detected, it can be classified as such and rejected quickly. Ideally, the system has enough
1473 gain that any spurs are subdominant to the amplified thermal noise, as discussed in Eq. 2.1.
1474 However, since there is a maximum amount of gain that can be added before clipping the
1475 ADC (see Sec. 2.5.4.3), this is not always possible.

1476 Experience with the Teledyne RTSA system has shown that spurs are rather simple to

1477 classify because they do not change much with time in either frequency or amplitude. Their
1478 frequency drifts by ~ 1 kHz and their amplitude changes by a few dB.

1479 To classify them, the input of the Teledyne is terminated and a scan is performed few
1480 minutes using the exact same system configuration as for the run (with the possible exception
1481 of the number of averages). See Appendix A for details. The averaged spectra of the
1482 terminated inputs are shown in Fig. 3.15.

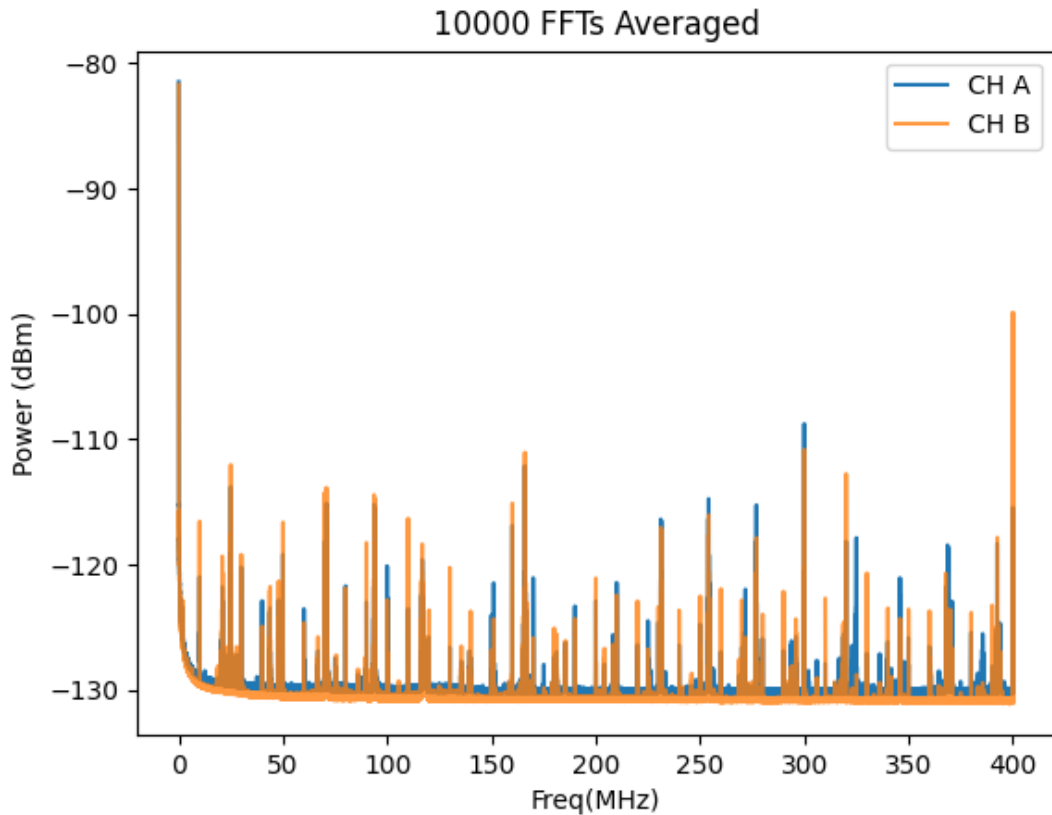


Figure 3.15: Scan of terminated input of Teledyne spectrum analyzer system to measure spur performance. The spectra were acquired with run 1A parameters ($\Delta\nu_{RF} = 47.7$ Hz) with 10,000 averages (~ 3.5 minutes). This plot is taken directly from test mode of the system (not post-processed in any way). The largest spur in the 50-300 MHz range is at 299.97 MHz and is also the single significant signal in Run 1A (see Sec. 4.2.5).

1483 Once a test scan is acquired, comparing the largest spurs (≈ -110 dB) to the expected
1484 output-referred background ([Johnson noise + LNA noise] * Gain ≈ -81 dBm/ $\Delta\nu_{\text{RF}}$) allows
1485 the calculation of the number of averages which are required before the spurs are significant.
1486 Working this out is a good test of understanding of Sec. 2.2. This spur should be detectable
1487 with 95% confidence after about 4 days, which is exactly what happened in Run 1A. The
1488 false positive candidate is described in Sec. 4.2.5.

1489 3.3.3 ADC clock performance

1490 Any ADC requires a clock that dictates the precise time at which a sample should be ac-
1491 quired. This subsection deals with the evaluation of the performance of that clock.

1492 Determining the performance of a clock generally relies on having a better (read: more
1493 expensive) clock known as a *standard* and measuring the clock under test against the stan-
1494 dard. The Valon 5009a[60] RF synthesizer was tested against a rubidium frequency standard
1495 and was found to be just on the threshold of stable enough to work (this threshold is ex-
1496 plained in Sec. 2.5.7). To ensure the measurement is not limited by clock instability, the
1497 sample clock of the ADC is synchronized to a 10 MHz rubidium frequency standard (Stanford
1498 Research Systems FS725) which is further steered by the one pulse-per-second (pps) signal
1499 from a GPS receiver. This system has medium and long term fractional frequency stability
1500 (Allan deviation [61, 62]) of $\sigma_y(\tau) < 3 \times 10^{-12}$ (where τ is the averaging time) and phase
1501 noise of less than -65 dBc/Hz at offset frequencies > 50 Hz from the carrier [63]. This means
1502 that over the course of a single acquisition, the power contained in a bin will spread to an

1503 adjacent bin by less than 1 part in 10^6 which is more than sufficient for our experiment.

1504 This is a rare example of something in this experiment where we trust the datasheet[63].

1505 We do not have access to a clock which is better than this, so confirming its performance

1506 is difficult. Furthermore, even if the specifications are an order of magnitude worse than

1507 advertised there is still more than enough stability for the experiment. This statement holds

1508 at higher frequencies. Since the Q of the signal is fixed, higher frequencies have wider bins so

1509 the relevant offset frequency at which the phase noise is measured increases with frequency.

1510 The dimensionless Allan deviation is also not affected.

1511 **3.3.4 Real-time data collection efficiency**

1512 As a final test, one would like to know how efficiently data scans can be acquired and

1513 averaged. We call a 100 % efficient system *real-time* as described in Sec. 2.5.7. Figure 3.16

1514 illustrates this efficiency. For Run 1A, it is $\sim 99.765\%$. However, in practice run logistics

1515 such as moving the antenna prevent the full efficiency of the system from being realized.

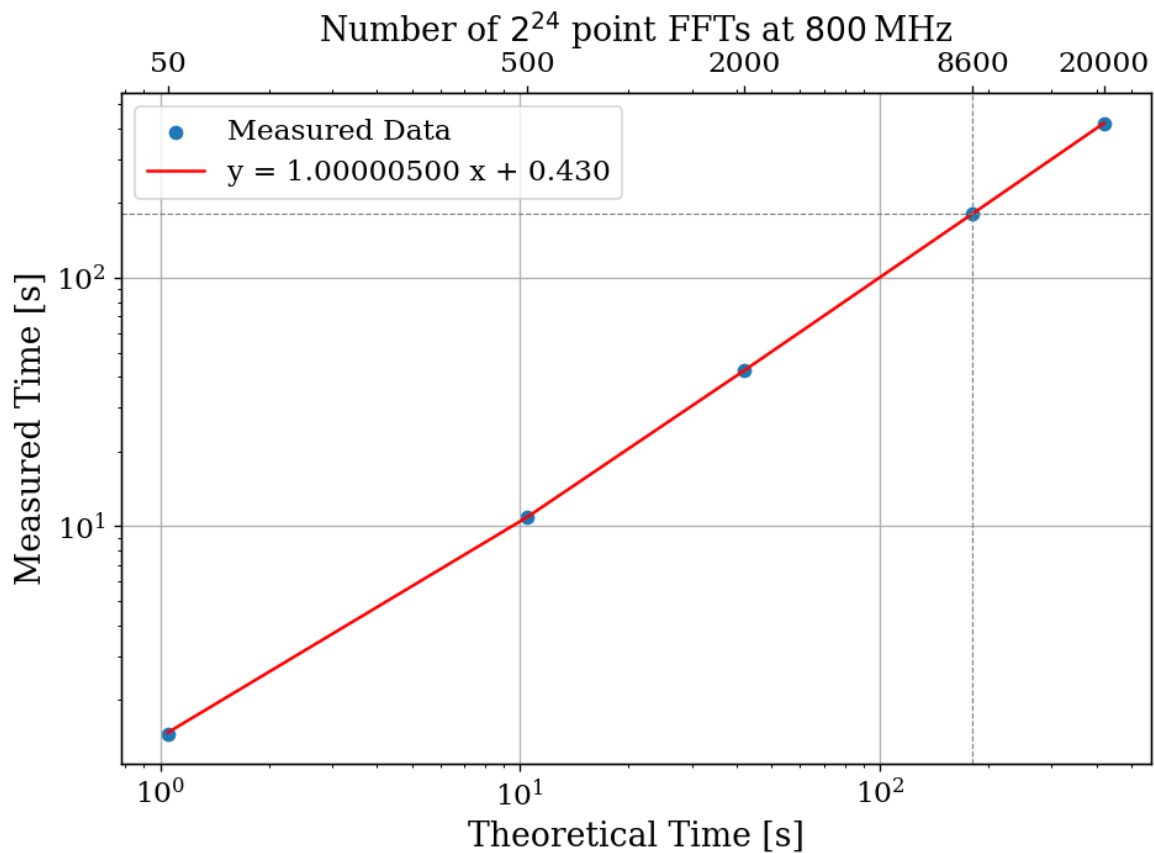


Figure 3.16: Acquisition efficiency for GPU-based real-time spectrum analyzer computed from measured vs. theoretical times. The constant offset of 0.43 s corresponds to a small set-up period when starting an acquisition containing, in the case of run 1A, 8600 FFTs. In the limit of an infinite length acquisition, the system's efficiency may be read off from the slope and is 99.9995%. The more realistic efficiency is a function of the number of FFTs per acquisition and for Run 1A = $180.3551 \text{ [s]} / 180.7782 \text{ [s]} = 99.765\%$.

₁₅₁₆ Chapter 4

₁₅₁₇ Data Acquisition, Data Analysis and
₁₅₁₈ Calibration

1519 Thus far, this thesis has built a foundation for the dark radio technique as well as the
1520 design and testing of the experiment and its sub-systems. This chapter outlines the process
1521 of acquiring actual data, analyzing that data to search for a small power excess, and, in the
1522 absence of that excess, converting the null result into an exclusion limit on the dark photon
1523 mass/ ϵ parameter space. Section 4.4 describes an injection test that detects a realistic,
1524 hardware-injected, dark photon proxy-signal. This chapter borrows heavily from my paper,
1525 *New Limit on Dark Photon Kinetic Mixing in the 0.2-1.2 μeV Mass Range From the Dark*
1526 *E-Field Radio Experiment*[25], which was published in August 2024.

1527 The cleanest way to model the contents of this chapter is by compartmentalizing the
1528 steps outlined above. For this reason, the chapter is organized as follows. In Sec. 4.1, the
1529 procedure for a 9-day data run is outlined. Where appropriate, references to previous sections
1530 are provided which are helpful in understanding how different procedures were developed.
1531 This section concludes with the frequency-dependent, output-referred power spectral density
1532 S_o , which must be searched for a power excess. We call this search *analysis*, and it is covered
1533 in Sec. 4.2. The task of analysis is to extract a dark photon signal from this spectrum if
1534 it is present. Otherwise, in its absence, we set a limit on the amount of output-referred
1535 power that would have been detectable *most of the time* were a narrow signal to be present
1536 in this averaged dataset. We quantify the meaning of “most of the time” by conducting a
1537 series of Monte Carlo *pseudo-experiments* on artificial signal-containing spectra for synthetic
1538 signals of varying powers and frequencies. With a limit on dark photon power extracted,
1539 Sec. 4.3 works back through the system to determine a limit on ϵ above which we have some
1540 confidence we would have observed a signal. This produces the exclusion limit, which is

1541 ultimately the deliverable of this experiment. This limit is shown in Ch. 5.

1542 4.1 Data Acquisition

1543 Data were collected during a 9-day run from May 10 to May 19, 2023. As discussed in the
1544 introduction to Ch. 2, this data run is referred to Run 1.4 in the code base since it was the
1545 fourth attempt at taking this data. It was used for to publish the limit of Run 1A, so it is
1546 referred to as Run 1A throughout this thesis or as Run 1A.4 if it is necessary to distinguish
1547 between previous attempts. The details of this run are shown in Tab. 4.1.

Specification	Value
Analysis span	50 - 300 MHz
-3 dB span of analog filters	34 - 208 MHz
Antenna	AB-900A biconical antenna
RTSA	Teledyne GPU system (Sec. 2.5.7)
Frequency resolution ($\Delta\nu_{RF}$)	47.7 Hz
Length of record	2^{24} samples
Sample rate	800 MHz
Window type	None (rectangular)
Acquisition time per spectrum	20.96 ms
Run start time	2023-05-10 11:29:48
Total time of run	8 days, 21.13 hours
Efficiency (Time spent scanning antenna/total time)	92.03%

Table 4.1: Run 1A details. Many specifications are related and can be computed from each other but are listed for reference. The efficiency differs from that calculated in Fig. 3.16 mainly because of switching to a terminator and brief daily pauses to move the antenna.

1548 Each day was subdivided into data-collection (23 hours 15 minutes) and setup (45 min-
1549 utes) periods. The setup period includes moving the antenna, changing a 12 V battery for

1550 the LNA (Sec. 2.5.6), file management and documentation. In order to reduce the data
1551 rate and storage requirements, all data were pre-averaged into 3-minute chunks and then
1552 saved. This pre-averaging is shown in Fig. 2.45. Additionally, an RF switch (see Fig. 2.37)
1553 is actuated for a 3-minute scan for every 15 antenna scans in order to monitor the status
1554 of the amplifier chain. For the data analysis, all 9 days of data were averaged together to
1555 create a single spectrum S_o (Fig. 4.1). If candidates are found, their time dependence are
1556 observed by looking at the 3-minute pre-averages. All further analysis is performed on the
1557 full 9-day S_o spectrum and is described below (Sec. 4.2).

1558 4.1.1 Raw data, S_o

1559 All 9 days of pre-averaged data from the run are averaged together. The stability of the
1560 sample clock (Sec. 3.3.3) ensures that this is a simple process. Frequency bins ($\Delta\nu_{RF} =$
1561 47.7 Hz) corresponding to a given frequency are added and normalized by the total number
1562 of pre-averaged spectra. This process produces the raw spectrum, S_o (Fig. 4.1), on which
1563 we will perform a search for power excess.

1564 Inspection of S_o reveals small power variations over spans of tens of kHz. The origin of
1565 these variations is explored in Sec. 2.3, but it is summarized here. Given an antenna in a
1566 cavity in thermal equilibrium with the input of an amplifier, whose input is assumed to be real
1567 and matched, one would expect an output PSD which is constant with respect to frequency
1568 up to small variations in system gain. The theory for this is outlined by Dicke in [64]. These
1569 variations are not noise; for a given antenna position, we repeatedly measure the same shape

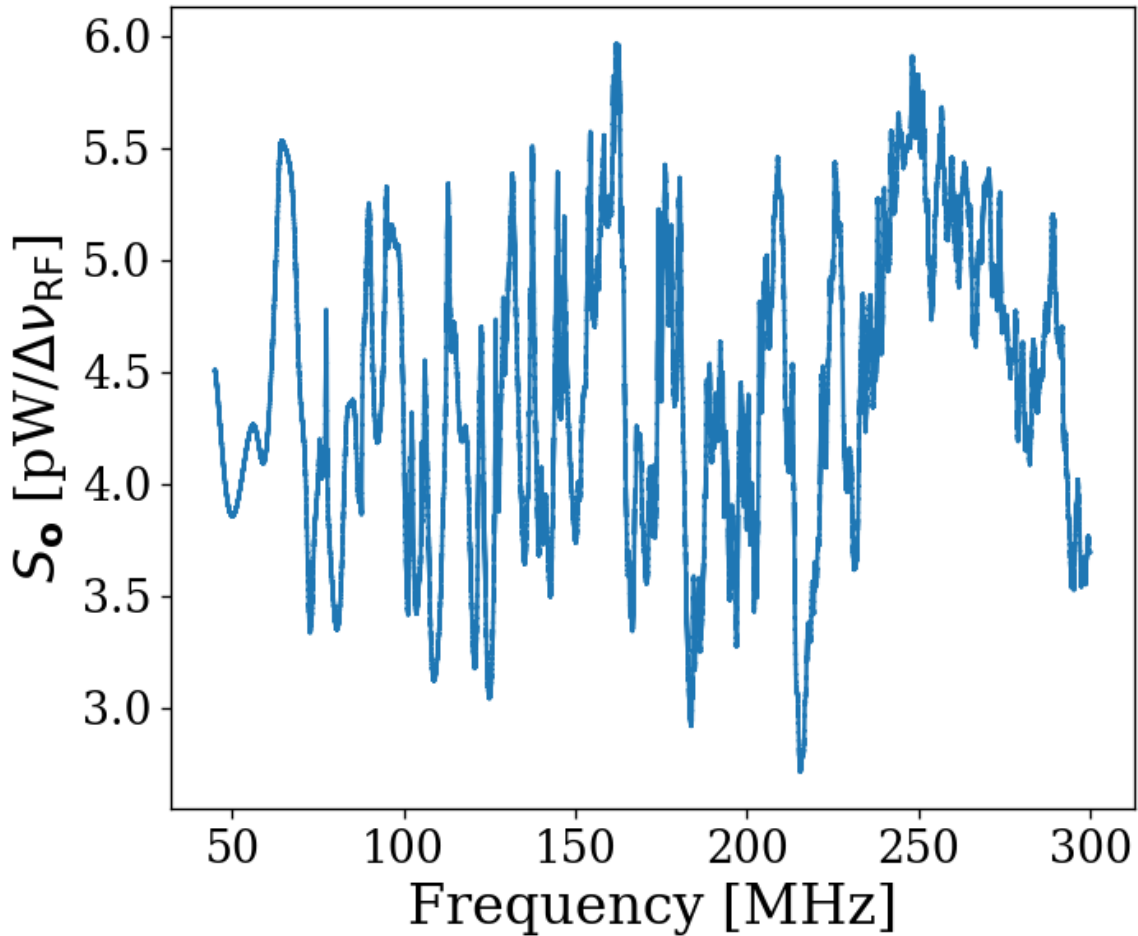


Figure 4.1: Run 1A averaged, output-referred antenna power spectrum S_o . Data were taken over a 9-day period at 9 antenna positions. For context, Fig. 4.2 shows these data plotted alongside the power spectrum of the terminator. The narrow variations are mainly due to the effective temperature difference between the room and LNA (Sec. 2.3), though there is a small contribution due to amplifier gain and noise temperature variations (Sec. 4.1.1). The variations seen here are not noise; their shape is repeatable for a given antenna position. The noise on this background is not visible at this level of zoom, but is seen in Fig. 4.4, which shows a zoomed-in view of the spectrum at 240 MHz. The noise is also seen nicely in Fig. 4.18

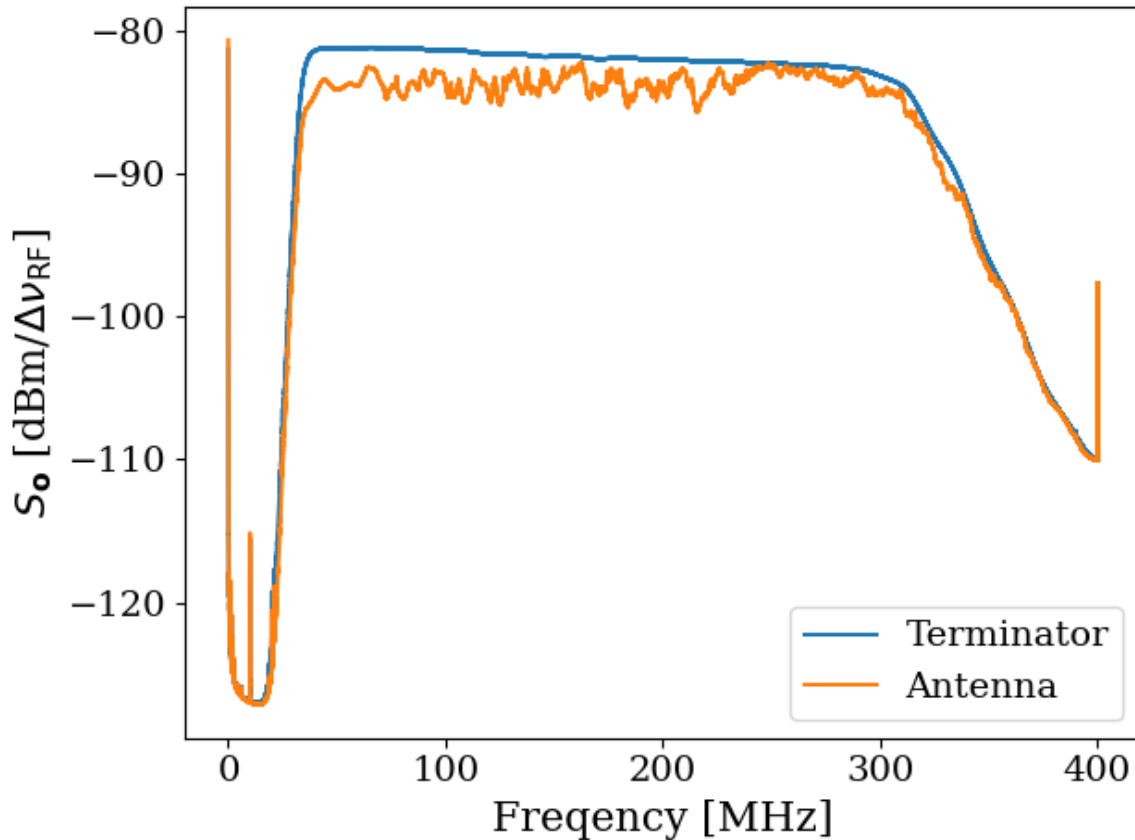


Figure 4.2: Logarithmic scaled Run 1A averaged, output-referred, antenna and terminator power spectra. Bandwidth is defined by hardware band-pass filters (Fig. 2.37). Spurious signals at 10 MHz, as well as low and high-frequency behavior, are ADC effects and are visible in Fig. 3.15.

1570 (though the noise riding on these variations *is* random). The origin of the observed small
 1571 variations lies in the effective temperature difference between the room and LNA causing
 1572 a net power flow from the antenna into the LNA. This effective temperature difference
 1573 partially excites modes of the antenna/cavity system, causing the observed variations. We
 1574 suspect this effect originates from a small reactive component of the LNA's input causing
 1575 the electronic cooling described originally by Radeka [5]. This effect can be eliminated by

1576 adding an isolator between the antenna and LNA [18, 65] though for our experiment, it
1577 is impractical to get an isolator that covers such a wide band at relatively low frequency.
1578 Furthermore, the relatively wide (tens of kHz) variations are handled by fitting to them,
1579 which is discussed in Sec. 4.1.

1580 4.2 Data Analysis

1581 At this point, we have compiled a single, averaged, output-referred power spectrum, S_o
1582 (Fig. 4.1). The task of *analysis* is to extract a dark photon signal from this spectrum if
1583 it is present. Otherwise, in its absence, we would like to set a limit on the amount of
1584 output-referred power we would be able to detect *most of the time* were a narrow signal
1585 to be present in this averaged dataset. We quantify the meaning of “most of the time”
1586 by conducting a series of Monte Carlo “pseudo-experiments” on artificial, signal-containing
1587 spectra for synthetic signals of varying powers and frequencies. The following subsections
1588 are organized as follows:

1589 4.2.1: Fit S_o to extract an estimate of the background B (which we call \hat{B}) whose origin was
1590 discussed in Sec. 4.1.1. See Fig. 4.4.

1591 4.2.2 Divide the spectrum by \hat{B} to generate the *normalized spectrum*, which very nearly
1592 follows a Gaussian distribution. Discuss statistics of the normalized spectrum and
1593 choose a global significance level and its associated *significance threshold*. See Fig. 4.5.
1594 Also note this was derived in Sec. 2.2.

1595 4.2.3 Apply a matched filter to the normalized spectrum and establish a significance thresh-

1596 old on its output using the same method defined in the previous section. See Fig. 4.6.

1597 The previous three steps comprise our *detection algorithm* which is shown in Fig. 4.3.

1598 4.2.4 Perform a Monte Carlo analysis to simulate the required power of a signal that can be

1599 detected above the significance threshold 95% of the time. We use this to recover a

1600 95% exclusion limit on the output referred power spectrum.

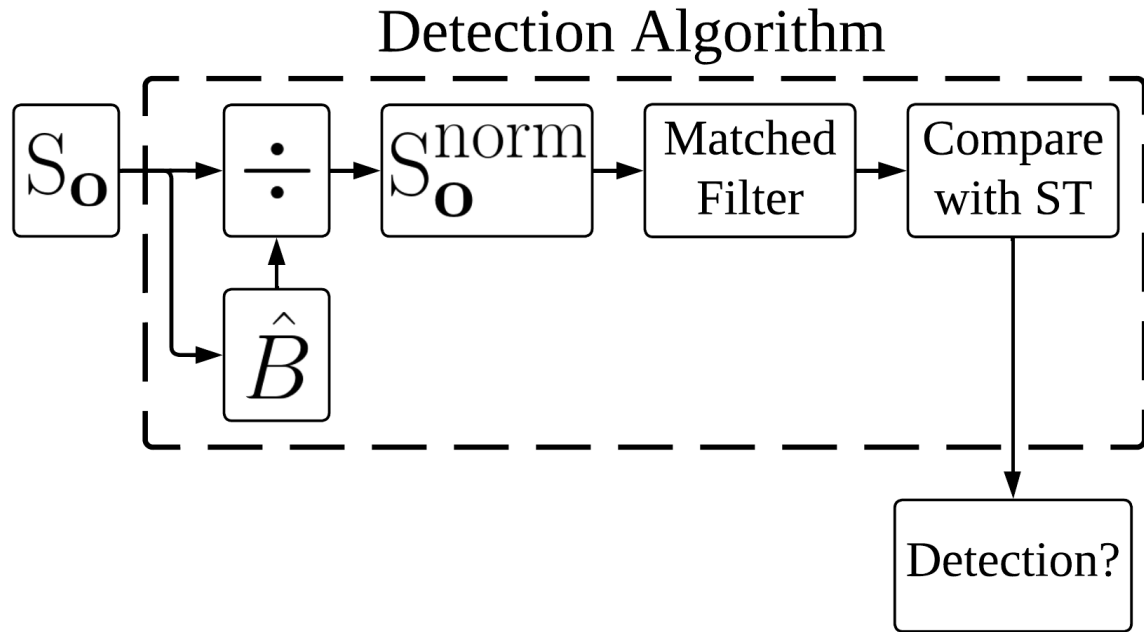


Figure 4.3: Flow chart outlining the logic of signal processing in the detection algorithm of sections 4.2.1 through 4.2.3. \hat{B} is the smoothed fit to S_o generated by low pass filtering. The output, *Detection?*, is a Boolean array which signifies a detection or lack thereof at each frequency bin. We detect a candidate if a bin contains more power than a significance threshold (ST) (Sec. 4.2.2).

1601 In Sec. 4.3 we convert this threshold on S_o into an actual limit on ϵ .

1602 Throughout the figures of this section, we will follow a relatively large (40 fW, output-
1603 referred) software-injected, synthetic dark photon signal at 240 MHz to illustrate what a
1604 candidate would look like as it passes through the analysis procedure. This signal is added
1605 to S_o . For clarity, a single interfering candidate has been removed. This is discussed in
1606 Sec. 4.2.5.

1607 As a final note, at this point if you are unfamiliar with the data analysis, it would be
1608 advantageous to spend a few minutes looking through Figs. 4.18 through 4.20 to get a sense
1609 of the task at hand. It can be disorienting to deal with a spectrum that contains 8 million
1610 frequency points. Zooming in on a signal is very informative.

1611 **4.2.1 Fit background, $\hat{B}(\nu)$** ¹

1612 As shown in Fig. 4.1, the measured power spectrum looks like flat thermal noise *multiplied*
1613 by some frequency-dependent background, $B(\nu)$ ². However, for this section, we will not
1614 concern ourselves with the origin of B or any details of the experiment aside from two
1615 assumptions:

- 1616 1. The measured background is the product of a normally distributed spectrum and some
1617 background. This is enforced by the central limit theorem due to the large number of
1618 averaged spectra, independent of any experimental specifics.

¹Code for this section can be found at: https://github.com/josephmlev/darkRadio/tree/master/daqAnalysisAndExperiments/run1p4/run1p4_analysis/analysisClass.ipynb

²When I was first working on this, I used $H(\nu)$ to represent this background. This naming convention persists in the analysis code.

1619 2. The line shape of the signal is known and the width of this signal is much narrower
1620 than the width of features on the background, viz. $\Delta\nu_{\text{DP}} \ll \Delta\nu_{\text{B}}$

1621 The first assumption (1) implies that if we were able to extract the background, dividing
1622 S_o by this extracted background would yield a *dimensionless*, normally distributed power
1623 spectral density on which a search for a dimensionless signal is performed. The second
1624 assumption (2) will be critical in both performing the fit to the background (this section),
1625 and performing matched filtering (Sec. 4.2.3).

1626 In light of these assumptions, we attempt to fit the background power spectrum. Since
1627 this fit estimates B , we use the symbol \hat{B} to refer to it. As discussed in [6], a particularly
1628 effective fitting technique that can discriminate between the wide bumps of S_o and a narrow
1629 signal is to use a low pass filter. We implement this filter in two stages:

1630 1. A median pre-filter (51 bins or about 2.4 kHz wide) attenuates any very narrow, very
1631 large excursions which would interfere with any following filters, causing them to
1632 “ring”³

1633 2. A 6th-order Butterworth low pass filter (corner frequency of 210 bins or 10 kHz)

1634 These bin widths/frequencies should be interpreted as the width of spectral features on
1635 S_o that are attenuated and will, therefore, not show up in the background fit. A narrow
1636 zoom of this fit with a synthetic signal is shown in orange in Fig. 4.4.

³I recommend that this pre-filtering step is omitted if the spectrum analyzer in use does not produce large spurs. It is the slowest part of the analysis chain. It also causes the filtered spectrum to deviate slightly from Gaussian.

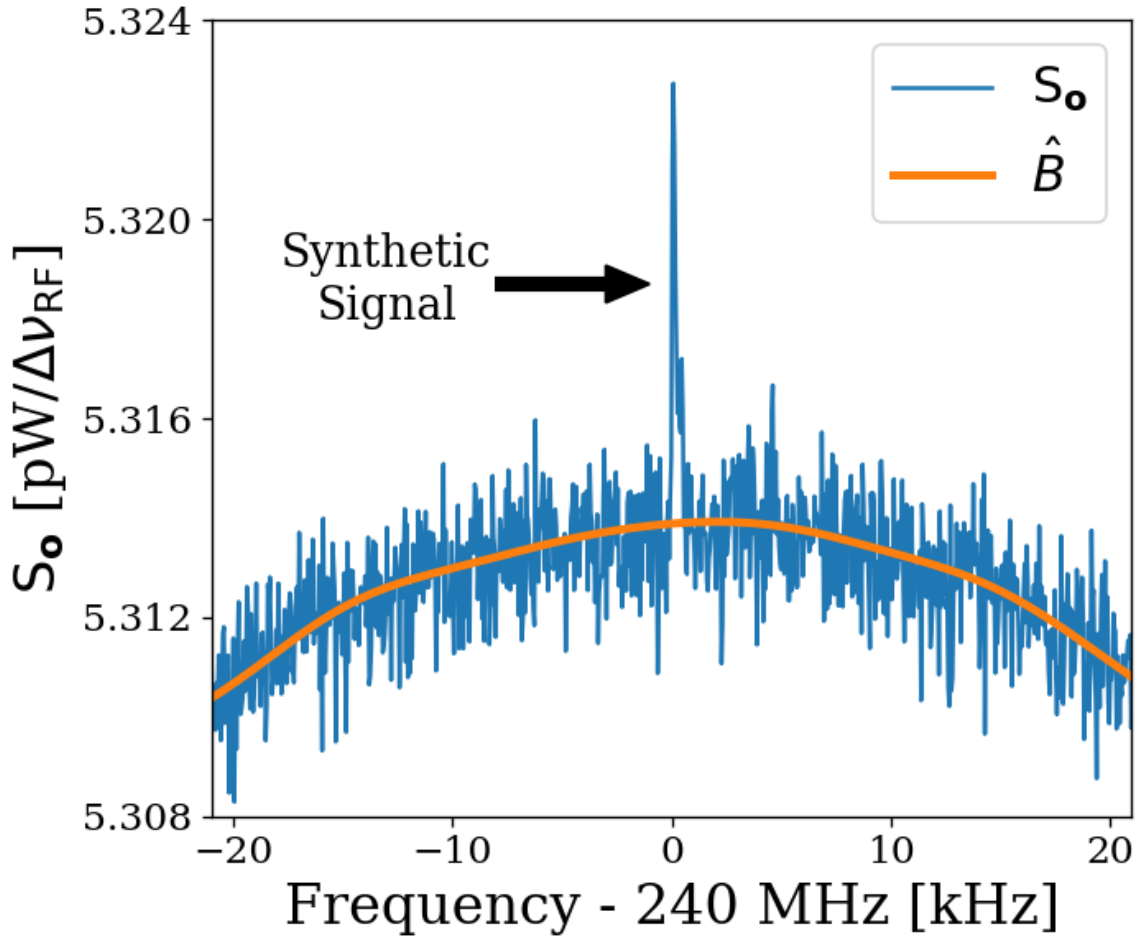


Figure 4.4: Fitting background \hat{B} in the presence of a synthetic signal injected at 240 MHz. Starting from the averaged, output-referred spectrum (S_o), we fit the background using a series of filters (section 4.2.1, and Fig. 4.3). This figure is a highly zoomed-in view (240 MHz \pm 20 kHz) in order to show the noisy Rayleigh signal shape.

¹⁶³⁷ **4.2.2 Normalized spectrum, S_o^{norm}**

¹⁶³⁸ Once we have a fit to the background, \hat{B} , division of S_o by this fit yields a dimensionless,

¹⁶³⁹ Gaussian distributed spectrum

$$S_o^{\text{norm}} \equiv \frac{S_o}{\hat{B}}. \quad (4.1)$$

1640 As discussed in Sec. 2.1.1.3, this normalized spectrum (Fig. 4.5) should have a mean $\mu_{\text{norm}} = 1$
 1641 and a standard deviation given by the Dicke radiometer equation $\sigma_{\text{norm}} = (\tau \Delta\nu_{\text{RF}})^{-1/2}$ where
 1642 τ is the total integration time (≈ 9 days) and $\Delta\nu_{\text{RF}}$ is the width of a bin (47.7 Hz). This
 1643 works out to a predicted σ_{norm} of 1.727×10^{-4} . μ_{norm} and σ_{norm} calculated from the data
 1644 are $1 - 1.2 \times 10^{-5}$ and 1.741×10^{-4} respectively, which agree with the predicted values
 1645 to better than 1%. Knowing the statistics of the background allow us to set a threshold
 1646 above which we have some confidence that a candidate is not a random fluctuation. This
 1647 significance threshold was derived in Sec. 2.2.1. As a reminder, the probability that all N
 1648 bins are less than z standard deviations, $z\sigma$, for a standard normal distribution is given
 1649 by $\left\{ \frac{1}{2} [1 + \text{erf}(z/\sqrt{2})] \right\}^N$, where $\text{erf}(z)$ is the standard error function and z is real. A 5%
 1650 ST for 5.2×10^6 bins (our 50-300 MHz analysis span) works out to 5.6σ . This is shown in
 1651 Fig. 4.5.

1652 It is possible to set a simple limit using this significance threshold on the normalized
 1653 spectrum, which was our method in [4]. However, knowing the line shape of the dark photon
 1654 signal provides additional information that improves sensitivity (up to a factor of ≈ 2) at
 1655 the higher frequency end of the spectrum, as shown in Fig. 4.8.

1656 4.2.3 Signal-matched filter

1657 As discussed in 4.2.2, one simple method to set a limit is to look for single-bin excursions
 1658 above some threshold. However, galactic dynamics impart a dark photon candidate with
 1659 a Rayleigh-distributed, spectral signature, which has a dimensionless width $Q_{\text{DP}} \approx 10^6$

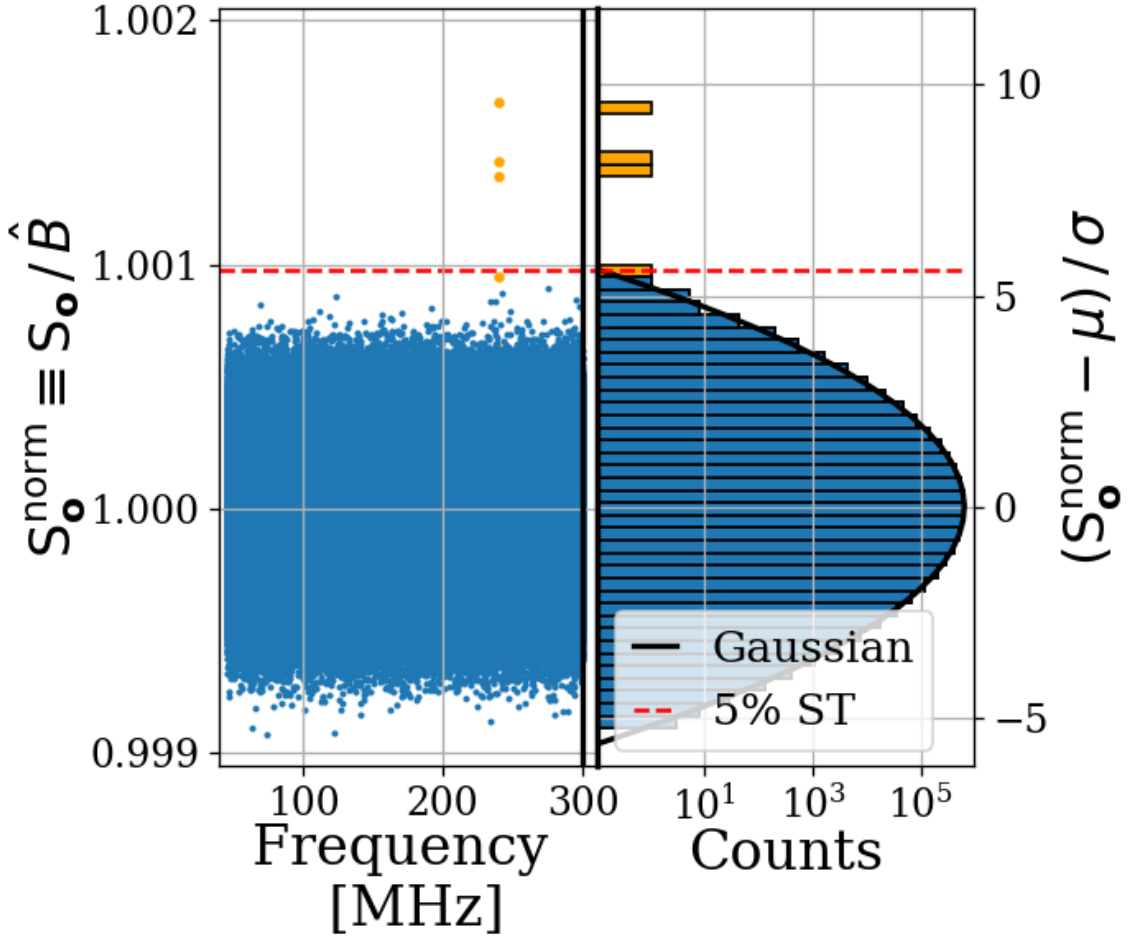


Figure 4.5: Dividing S_o by \hat{B} yields a dimensionless, normally distributed power spectrum that we define as S_o^{norm} . We show S_o^{norm} in two ways: a normalized power/frequency spectrum (*left*) and rescaled into Z-score units and collapsed into a histogram (*right*). The histogram shows power excess and Gaussian fit, but frequency information is lost. We compute a 5% significance threshold ST (*dashed red*), above which we will detect a candidate by chance 5% of the time. Bins adjacent to the 240 MHz synthetic signal show up in orange on both plots. A single interfering signal has been removed for clarity. We discuss this further in Sec. 4.2.5

1660 [19]. This means that the expected width of a candidate signal over our analysis span (50-
 1661 300 MHz) varies between 50-300 Hz. We set $\Delta\nu_{\text{RF}} = 47.7$ Hz to maximize SNR for the lowest
 1662 expected signal width. However, this divides signal power between adjacent bins, an effect

1663 that becomes more pronounced at higher frequencies, leading to a decrease in sensitivity.
1664 By using a signal processing technique known as *signal-matched filtering* [66, 67], we restore
1665 some of the sensitivity lost due to the splitting of signal between the fixed-width frequency
1666 bins of the FFT. A similar “optimal weighting” procedure has been well established in axion
1667 haloscope experiments, notably by [6, 68]. Below, the signal-matched filter is referred to
1668 simply as a *matched filter*.

1669 For a known signal shape, the detection technique that optimizes SNR is the matched
1670 filter. This is implemented on the normalized power spectrum using the Rayleigh-distributed
1671 spectral line shape of [19] as a template. Since we have a constant $\Delta\nu_{\text{RF}}$ and expect the
1672 width of the signal to vary across our span, we must calculate several templates of varying
1673 width to match the expected line shape. Every 10% of fractional frequency change, a new
1674 template is generated and used to search that small subspan of the normalized spectrum,
1675 each of which is also normally distributed though with its own standard deviation. This
1676 results in 20 subspans (50-55 MHz, 55-60.5 MHz etc.). The normalized spectra of all 20
1677 subspans and the histogram of the 227-250 MHz subspan are shown in Fig. 4.6.

1678 As the width of the templates increase, the standard deviation of the output decreases,
1679 resulting in the $\nu^{-1/2}$ shape of the 5% significance threshold shown in Fig. 4.6. It should be
1680 noted that since the total number of bins remains 5.2 million, the 5% significance threshold
1681 still corresponds to 5.6σ ; the shaping in Fig. 4.6 is due to the variation in σ for different
1682 templates, not a change in the $z = 5.6$ pre-factor.

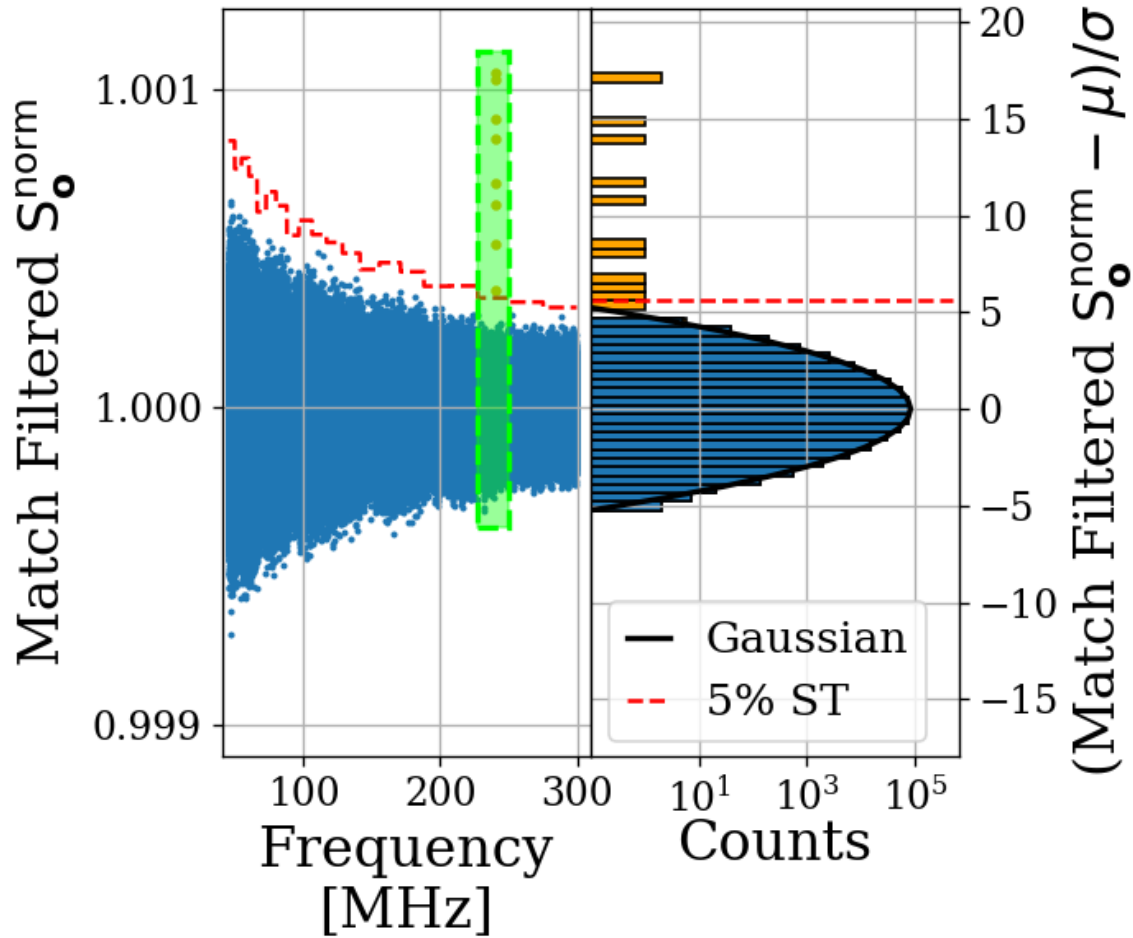


Figure 4.6: S_o^{norm} after it has been passed through a matched filter. The template varies in width throughout the frequency span resulting in 20 subspans, each with a constant 5% significance threshold ST (*dashed red*). This is discussed in the text of this section. The histogram only includes 227-250 MHz subspan (enclosed in the green box). The signal-to-threshold ratio of the synthetic signal (orange) improves by a factor of about 1.8 as compared to Fig. 4.5 without a matched filter. The frequency dependence of this effect is shown in Fig. 4.8. A single interfering signal has been removed for clarity.

1683 4.2.4 Monte Carlo: pseudo experiments

1684 The previous three sub-sections outline the procedure for detecting the presence of a signal

1685 of known spectral line shape embedded in wide-band noise. We refer to this procedure as a

1686 *detection algorithm* (see Fig. 4.3), which we now calibrate through a Monte Carlo method.
1687 Synthetic background spectra are generated, and known signals are added to this background
1688 to create a *test spectrum*. This test spectrum is passed to the detection algorithm, which
1689 attempts to detect the signal. This process is repeated many thousands of times, and the
1690 statistics of the detectability of a signal (as a function of its frequency and power) provide
1691 insight into how much power could have been detected in the experiment.

1692 A synthetic, background spectrum is constructed by multiplying some background $B(\nu)$
1693 by randomly generated Gaussian white noise characterized by μ_{norm} and σ_{norm} , as discussed
1694 in section 4.2.2. A Rayleigh-distributed signal of known, total integrated, output-referred
1695 power and frequency, $\lambda(p, \nu)$, can now be added to this spectrum to create a *test spectrum*
1696 that can be passed through the detection algorithm (see Sec. 2.1.2 for a discussion of signal
1697 line-shape). The frequencies of the synthetic signals are evenly spaced (approximately every
1698 10 MHz). However, because the signal spans a small number of bins (one to six), the shape
1699 of the discretized signal is very sensitive to the frequency at which its peak lands relative to
1700 the bins. To compensate for the unknown dark photon frequency relative to a given bin, the
1701 frequency of the synthetic signal is randomly jittered by $\pm\Delta\nu_{\text{RF}}/2$, which is drawn from a
1702 uniform probability distribution at each iteration of the Monte Carlo. By repeatedly running
1703 these synthetic, signal-containing, test spectra through the detection algorithm, statistics are
1704 built up about how much total integrated power is required to detect a signal as a function
1705 of frequency *most of the time*. We quantify this as the statistical power of the detection
1706 algorithm and denote it $100\% - Y = 95\%$ following the standard convention of hypothesis
1707 testing.

	Only Noise	Noise + Signal
Detection	X	100% – Y
No Detection	100% – X	Y

Table 4.2: Threshold parameters that are part of the detection algorithm and Monte Carlo. X is the significance of the analysis. It is a parameter passed to the detection algorithm which specifies the significance threshold. The quantity 100% – Y is the statistical power of the analysis. It is a parameter in the MC, which specifies a threshold on signal power where a given signal is detected in 100% – Y of the MC iterations. We choose both X and Y = 5%.

1708 This Monte Carlo allows us to treat the detection algorithm as a black box that can
 1709 be calibrated by passing it a known input (a test spectrum, i.e. a synthetic S_o containing
 1710 a synthetic signal, both software-generated) and looking at its output; a Boolean array of
 1711 frequency bins representing signal detection. These data, along with a simple linear fit to
 1712 the 95% confidence interval, are shown in Fig. 4.7.

1713 The Monte Carlo's output $MC_{lim}(\nu, Y)$, is a normalized limit on signal power required
 1714 for detection. It is a function of frequency ν and statistical power $1-Y$. MC_{lim} can simply be
 1715 converted back to the limit on the total output-referred power contained in injected signals
 1716 which can be detected 95% of the time,

$$P_o^{lim} = MC_{lim}\sigma_{norm}\hat{B}. \quad (4.2)$$

1717 P_o^{lim} is shown in Fig. 4.8 in blue. Also shown in Fig. 4.8 is a limit that does not include
 1718 any matched filtering (orange) to highlight the frequency-dependent improvement of the
 1719 matched filter. This limit is only for illustration and not used in the following sections.

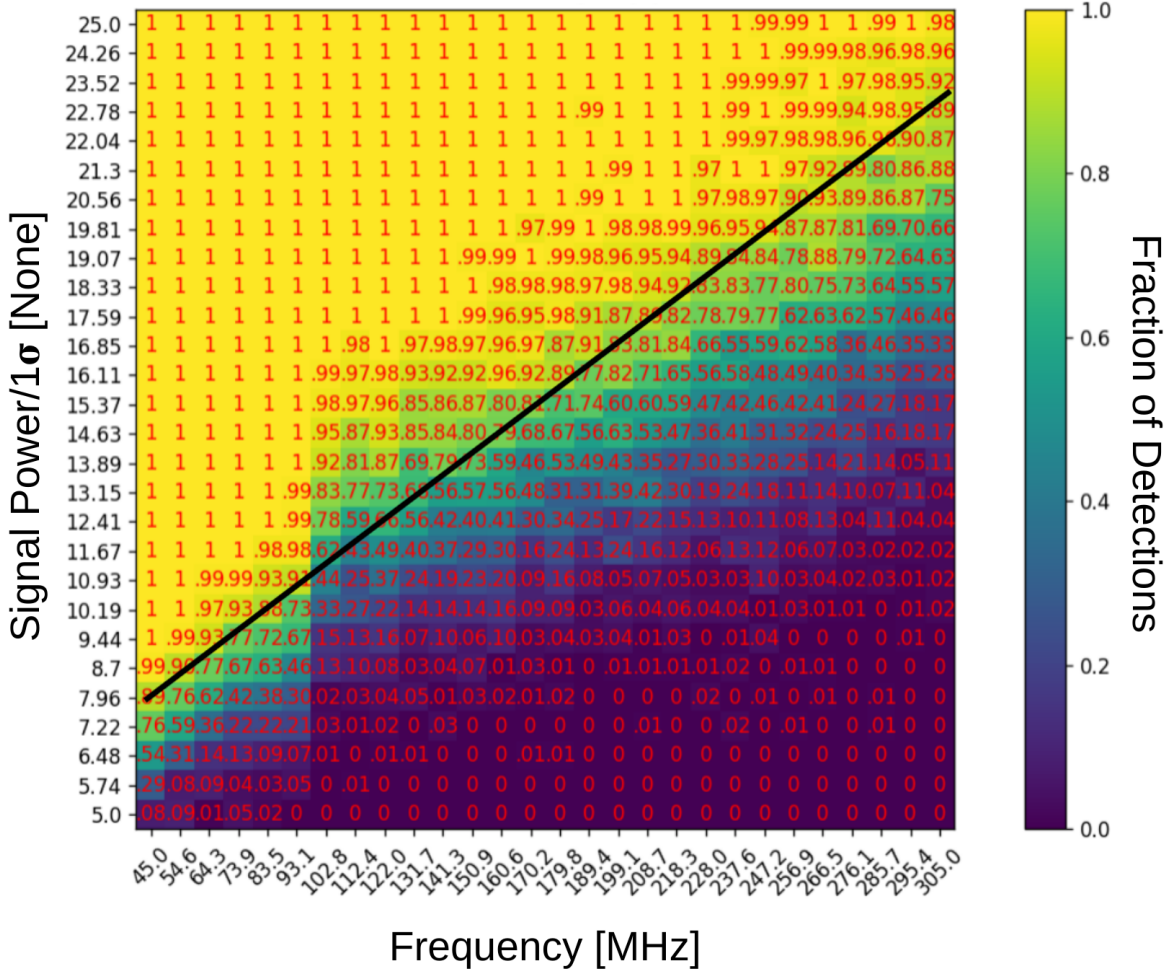


Figure 4.7: Result of Monte Carlo pseudo experiments on signal detection. Color and red numbering show the fraction of detections for each frequency/injected signal power of the 784 combinations tested. The signal power is shown in units of noise standard deviation σ . MC_{lim} is shown as a black line. This line was inserted by eye and gives an approximate fit to the frequency vs. injected signal power which results in a detection 95% of the time. The approximate form of this line is MC_{lim}(ν , Y = 5%) = 0.0686[P_{norm}/MHz] + 2.411[P_{norm}] where P_{norm} is the normalized injected signal power shown on the Y-axis.

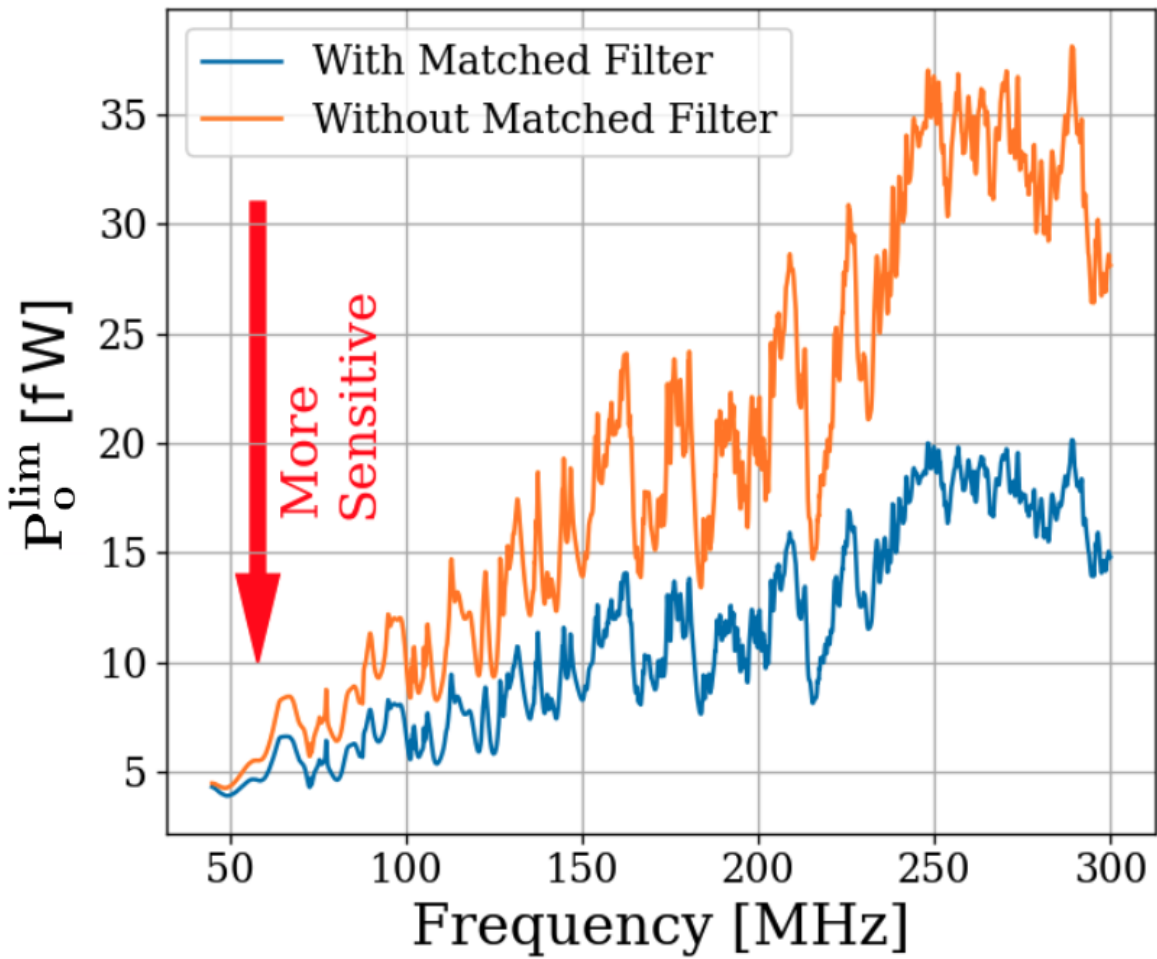


Figure 4.8: Limit on output-referred total integrated signal power, P_o^{lim} . Limits computed with (blue) and without (orange) a matched filter (Sec. 4.2.3). The limits are similar at lower frequencies, but the matched filter improves sensitivity at higher frequencies where the signal power is split among more bins. The blue curve is used in the following sections.

1720 **4.2.5 Rejection of a single candidate**

1721 Passing S_o through the detection algorithm diagrammed in Fig. 4.3 yields a single candidate
1722 at 299.97 MHz which is approximately 1 kHz wide. This candidate first became detectable
1723 above the noise after about 4 days of averaging, indicating it is just on the threshold of
1724 detectability. Four factors allow for the conclusion that the candidate is an interfering signal
1725 originating from within the PC or ADC, and not a signal in the shielded room (either a dark
1726 photon or RFI):

- 1727 • The candidate is present not only in the main spectrum, but also in the veto and
1728 terminator spectrum.
- 1729 • Inspection of the time evolution of this signal shows a narrow signal (about two bins,
1730 or \sim 100 Hz wide) which seems to wander in frequency periodically over the course of a
1731 day and, therefore, with temperature. This is expected behavior for a quartz oscillator.
- 1732 • Reducing the gain of the system causes the SNR of the candidate to *increase*, indicating
1733 it enters the signal path after the gain stages.
- 1734 • Changing the clock rate causes the frequency of the candidate to change.

1735 The limit set in this section is referred to the output of the amplifier chain. A single
1736 significant candidate was found, but the method of determining that it was not due to a
1737 dark photon was outlined above. The topic of the next section will be to work back through
1738 the amplifier chain, to an E-field limit in the cavity and ultimately to a limit on ϵ .

1739 4.3 Calibration

1740 In this section, we describe the calibration of the experiment and estimate its uncertainty.

1741 The previous section concluded with a frequency-dependent limit on the output-referred

1742 power P_o^{\lim} (Fig. 4.8), which we now must convert into a frequency-dependent limit on ϵ .

1743 We begin by inverting Eq. 1.1,

$$\epsilon(\nu) < \sqrt{\frac{|\mathbf{E}_{\text{ant}}^{\lim}|^2 \varepsilon_0}{2 \rho_{DM}}}, \quad (4.3)$$

1744 where the *lim* superscript indicates a limit, below which a detectable electric field may be

1745 hiding. The $<$ should be taken to mean that in setting a limit on $|\mathbf{E}_{\text{ant}}^{\lim}|$, ϵ is constrained to

1746 be less than the right-hand side (if it exists at all).

1747 The first step of calibration is to convert from output-referred power to *antenna-referred*

1748 *power*. This represents the signal power presented to the LNA by the antenna via a matched

1749 transmission line and is given by

$$P_{\text{ant}}(\nu) = \frac{P_o}{G} - T_{\text{amp}} k_B \Delta\nu_{\text{RF}}, \quad (4.4)$$

1750 where G and T_{amp} are the frequency-dependent system gain and noise temperature (74–75 dB

1751 and 100–120 K respectively, measured via the Y-factor method, see Sec. 3.1.1) and k_B is

1752 Boltzmann’s constant.

1753 Ultimately, the exclusion limit is set by fluctuations on this baseline described by

$$\begin{aligned}
P_{\text{ant}}^{\lim}(\nu) &= \frac{P_{\text{o}}^{\lim}}{G} - \left(\frac{2}{n} \right)^{1/2} T_{\text{amp}} k_B \Delta\nu_{\text{RF}} \\
&= \frac{P_{\text{o}}^{\lim}}{G} - \left(\frac{2 \Delta\nu_{\text{RF}}}{\tau} \right)^{1/2} T_{\text{amp}} k_B,
\end{aligned} \tag{4.5}$$

1754 where the *lim* superscript indicates an exclusion limit, n is the total number of spectra
 1755 averaged together, and τ is the total integration time. In the second line, we have used
 1756 $n = \Delta\nu_{\text{RF}} \tau$. In practice, the LNA correction is small; the first term divided by the second
 1757 varies with frequency between 7 and 50. The $\tau^{-1/2}$ dependence of P_{o}^{\lim} is implicit because it
 1758 was calculated from S_{o} which is itself an averaged spectrum. As mentioned above, this $\tau^{-1/2}$
 1759 dependence implies that the limit on ϵ scales as $\tau^{-1/4}$.

1760 In the remainder of this section we explore the relationship between P_{ant}^{\lim} and $|\mathbf{E}_{\text{ant}}^{\lim}|$ so
 1761 that we can use our experimental data to set a constraining limit on ϵ by employing Eq. 4.3.

1762 4.3.1 Average effective aperture, $\langle A_e(\nu) \rangle$

1763 An antenna's effective aperture, A_e [m^2], represents the effective area that it has to collect
 1764 power density or irradiance [W/m^2] from an incident Poynting vector. It was defined in
 1765 Eq. 2.9. Notably, it assumes a polarization match between the wave and the antenna (see
 1766 Sec 2.1.1.2).

1767 A_e is useful for an antenna in free space, however some modifications must be made to
 1768 construct an analogous quantity for an antenna in a cavity.

1769 The first modification is to average over many configurations of the system. The back-
 1770 ground for this is given in Sec. 2.4. As discussed, we denote this averaging with $\langle \rangle$ so that the

1771 average, effective aperture is denoted $\langle A_e \rangle$. It is interesting to note that by averaging over
1772 configurations (namely antenna direction), $\langle A_e \rangle$ simplifies since $\langle D(\Omega) \rangle = 1$ by construction
1773 [9].

1774 The second modification is to introduce a resonant enhancement factor that corresponds
1775 to the system's tendency to "ring up" in the same way any resonator will. We refer to
1776 this as *composite Q* and represent it as \tilde{Q} . It is analogous to the standard quality factor
1777 of a resonator with one important modification; we operate our experiment across a wide
1778 frequency range so we define \tilde{Q} across the continuum of these resonances, not only on classical
1779 eigenmodes of the system.

1780 These modifications provide a relationship between an observable E-field (\mathbf{E}_{ant} in Eq.
1781 4.3) and the power available at the port of an antenna for a given aperture

$$\langle P_{\text{ant}} \rangle = \frac{|\mathbf{E}_{\text{ant}}|^2}{\eta_0} \langle \tilde{Q} A_e \rangle, \quad (4.6)$$

1782 where η_0 is the impedance of free space. With this in mind, we perform an RF simulation
1783 to compute $\langle \tilde{Q} A_e \rangle$.

1784 4.3.2 Simulation of $\langle \tilde{Q} A_e \rangle$

1785 It is difficult to make claims about statistical uniformity in the "undermoded" regime where
1786 modes are not sufficiently mixed [69], so we have employed a commercial, electromagnetic,
1787 finite-element modeling software package (COMSOL Multiphysics RF module [46]). Within
1788 the simulation, a model of the antenna (with a 50Ω feed) is placed in a simplified room with

1789 wall features removed. Spot testing at various frequencies has shown that averaging results
1790 from various antenna positions using this simplified simulation behaves very similarly to one
1791 with the room features included at a fraction of computational complexity.

1792 Two similar simulations are run; driving an E-field while measuring the antenna's re-
1793 sponse and driving a second small monopole antenna and measuring the response of the
1794 primary antenna.

1795 In the first simulation, we drive currents on the walls which correspond to a surface E-
1796 field magnitude of 1 V/m (made up of equal components in the x, y and z directions) using
1797 COMSOL's source electric field option. This field takes the place of \mathbf{E}_{ant} in Eq. 4.6. The
1798 antenna/cavity system resonates and causes an enhancement by \tilde{Q} . The power received at
1799 the antenna's port is measured, allowing the calculation of $\tilde{Q} A_e$, again from Eq. 4.6. By
1800 repeating this simulation for several positions, averaging allows us to compute $\langle \tilde{Q} A_e \rangle$.

1801 The second simulation shares the same geometry, but is used to compute a correction
1802 factor to account for differences between simulation and measurement and to estimate un-
1803 certainty on the first simulation through comparison to physical measurement. Rather than
1804 driving the system through currents on the walls, power is injected into the system with a
1805 40 cm monopole. From this simulation, two-port scattering parameters (S-parameters, de-
1806 fined in 4.3.3) are computed. A similar test is performed on the physical system using a
1807 vector network analyzer (VNA) which provides a physical measurement of the S-parameters
1808 to compare with the simulation. The processing of the simulated and measured S-parameter
1809 datasets is discussed in the following sub-section. A screenshot of the COMSOL model GUI
1810 is shown in Fig. 4.9. The resulting S-parameters from the simulation are plotted against the

1811 measured S-parameters in Fig. 4.10

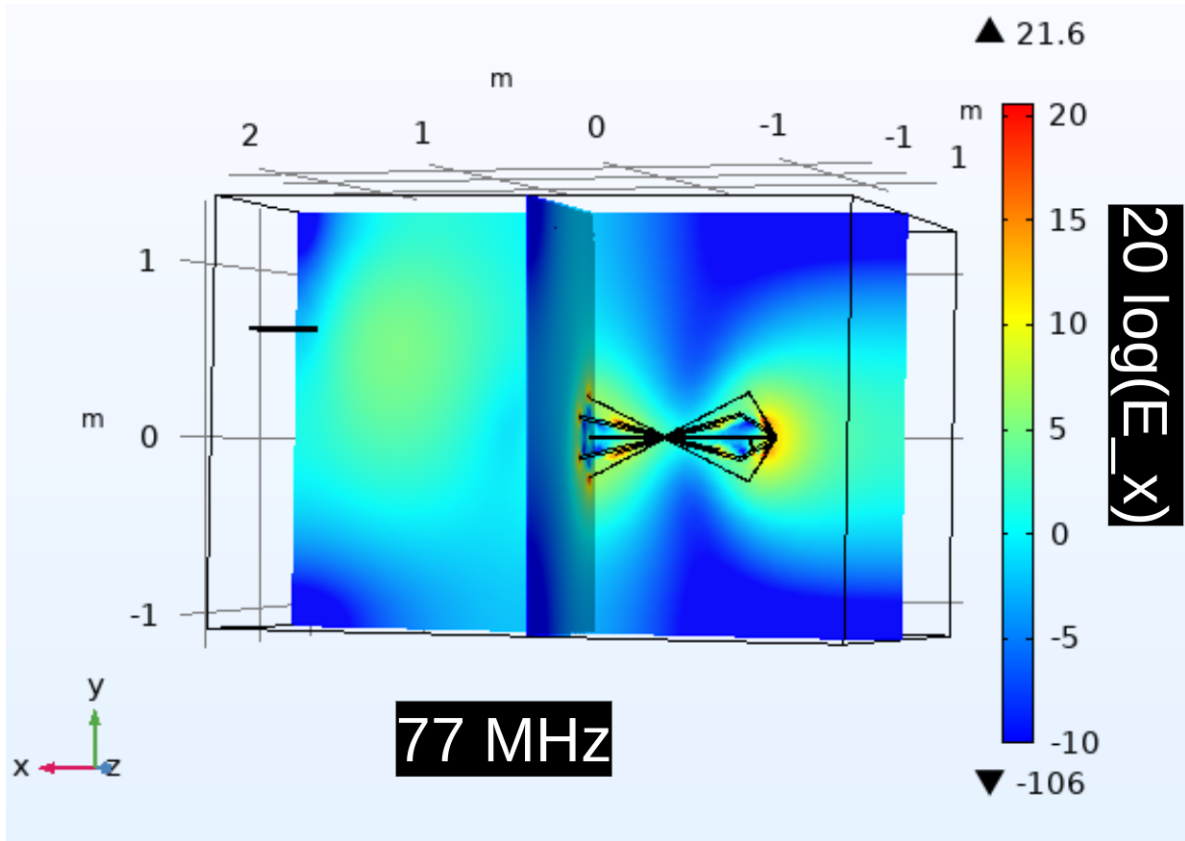


Figure 4.9: Screenshot of COMSOL simulation GUI for two-antenna validation. Shown only at a single position and single frequency (77 MHz). There are 18 antenna positions, 3 E-field components, and ~ 1000 frequency points, so there are many similar figures to this one. The x-component of the electric field is shown in color compared to 1 V/m.

1812 Both simulations are run at the same 18 positions; 9 of which are approximately equiva-
1813 lent to the physical antenna positions while the other 9 are different in order to estimate how
1814 many positions are required for decent convergence of $\langle \tilde{Q} A_e \rangle$. Repeatedly averaging 9 differ-
1815 ent, random positions (with replacement) results in about 20% variation on their averaged
1816 $\langle S_{21} \rangle$ coefficients at each frequency, allowing us to conclude 9 positions and polarizations
1817 provide acceptable convergence. This is a bootstrap method[70].

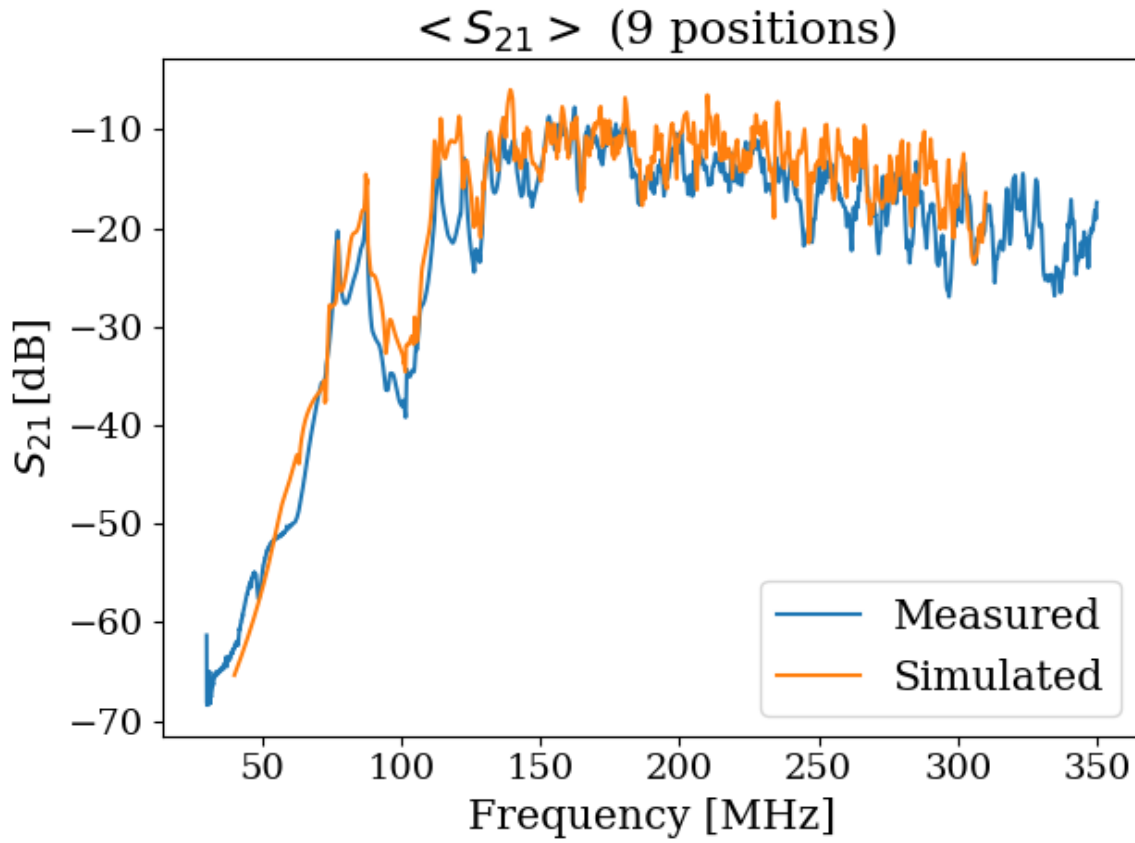


Figure 4.10: Simulated vs. measured $\langle S_{21} \rangle$. Averaged over 9 antenna positions. The procedures for generating these data are described in the text of this section.

1818 **4.3.3 Correction and uncertainty of $\langle \tilde{Q} A_e \rangle$**

1819 As outlined above, we approximate the uncertainty of the simulation by injecting power into

1820 the system via a second antenna and comparing the results to simulation.

1821 For a two-port microwave device, the ratio between the voltage presented at port one and

1822 the voltage measured at port two is known as S_{21} [29, 30]. For our system, S_{21} is a measurable

1823 quantity that is similar to a dark photon detection in that it requires the antenna to convert

1824 an electric field (which has interacted with the room) into a port voltage. Having frequency-

1825 dependent measurements of S_{21} for simulation and measurement gives us a correction to
1826 the simulation (to account for discrepancies in geometry) and estimate the uncertainty on
1827 $\langle \tilde{Q} A_e \rangle$.

1828 The difference between the measured and simulated values of $\langle |S_{21}| \rangle$ is described by

$$\langle |S_{21}^{\text{meas}}|^2 \rangle = \alpha \langle |S_{21}^{\text{sim}}|^2 \rangle, \quad (4.7)$$

1829 where meas/sim indicates measured/simulated and the average is over all 18 measured/sim-
1830 ulated positions and orientations of the antenna. We have taken the square since we are
1831 interested in the aperture, which is proportional to the square of the voltage. This equa-
1832 tion implies α is a frequency-dependent, multiplicative correction factor which results in a
1833 corrected $\langle |S_{21}^{\text{sim}}|^2 \rangle$. We find α to have a mean of 0.6, a minimum of 0.1 and a maximum of
1834 2.

1835 To determine uncertainty on effective aperture, we define the following test statistic

$$\Delta = \frac{\langle |S_{21,n}^{\text{meas}}|^2 \rangle - \alpha \langle |S_{21,n}^{\text{sim}}|^2 \rangle}{\langle |S_{21}^{\text{meas}}|^2 \rangle}, \quad (4.8)$$

1836 where n refers to the subset of n measured/simulated positions sampled randomly with re-
1837 placement. Δ defines the fractional difference between corrected, simulated S_{21} and measured
1838 S_{21} . The test statistic, Δ , is calculated 1000 times, providing a distribution of frequency
1839 dependent Δ s. The curves bounding 63% of these curves are taken to be the uncertainty
1840 on Δ . Thus we calculate the corrected $\langle \tilde{Q} A_e \rangle$ as well as its uncertainty. This is shown as a
1841 function of frequency in Fig. 4.11. The uncertainty on it is shown in gray and is simply

$$\delta \langle \tilde{Q} A_e \rangle = \langle \tilde{Q} A_e \rangle \delta \Delta. \quad (4.9)$$

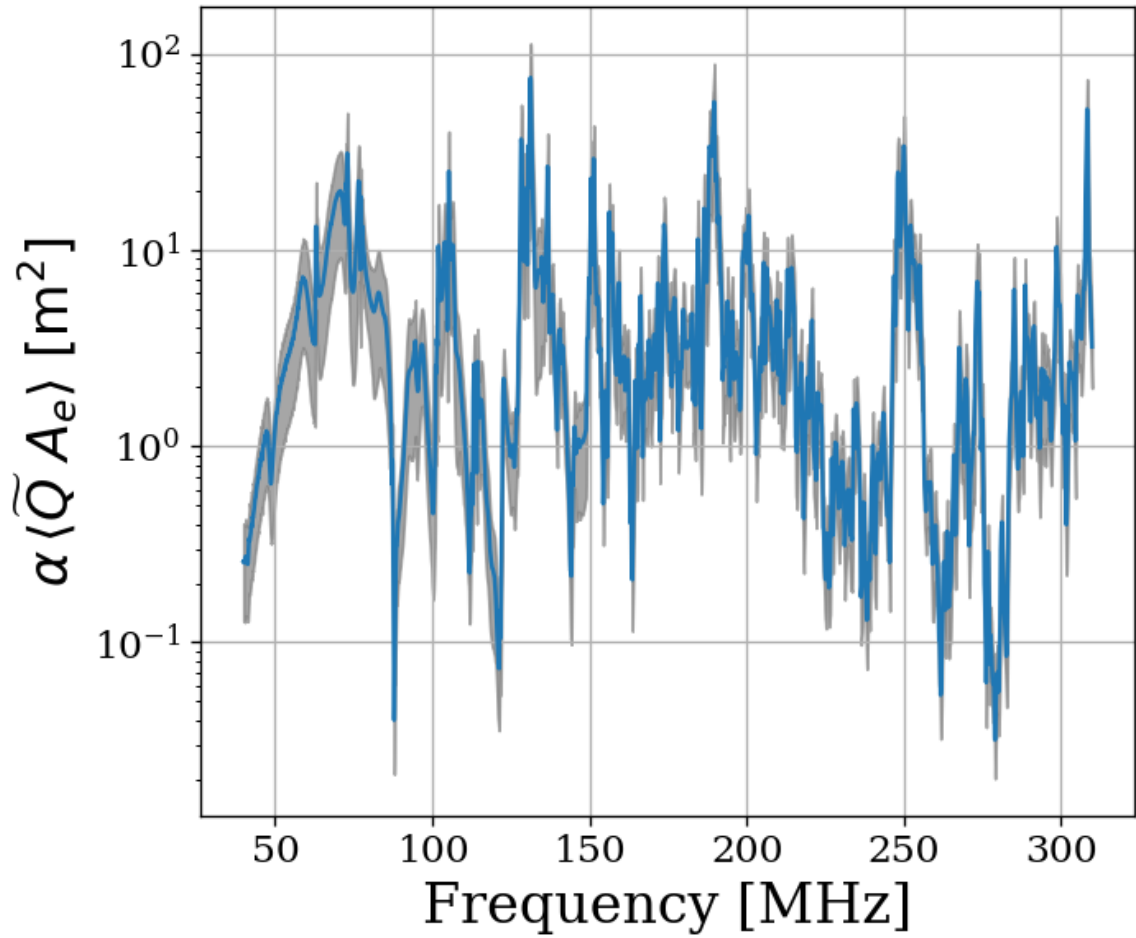


Figure 4.11: Corrected average effective aperture. Calculated with COMSOL RF. The aperture correction α (Eq. 4.7) and its uncertainty (gray) are estimated by comparing simulations to measured S parameters.

1842 A brief summary of the system's aperture is in order. In free space an antenna's ability
 1843 to couple an incoming wave's power density into a transmission line is given by its effective
 1844 aperture, Eq. 2.9. An antenna in a cavity acts as a coupled oscillator that exhibits very

1845 complex resonances above the first few modes (~ 100 MHz for our system). Attempts to
 1846 simulate an aperture for the antenna-cavity system are difficult because of the system's
 1847 extreme dependence on the placement of any conductor in the room, especially the antenna.
 1848 Averaging over system configurations (antenna positions and polarizations in our case) allows
 1849 for a significantly more repeatable *statistical* treatment of the aperture/quality factor, which
 1850 we call $\langle \tilde{Q} A_e \rangle$. Comparison of simulated and measured S_{21} gives a small, dimensionless
 1851 correction factor α , Eq. 4.7.

1852 Armed with $\alpha \langle \tilde{Q} A_e \rangle$ we now compute a limit on ϵ using the measured and simulated
 1853 quantities via Eqs. 4.5 and 4.6,

$$\epsilon(\nu) < \sqrt{\frac{1}{2c\rho_{\text{DM}}} \frac{P_{\text{ant}}^{\text{lim}}}{\alpha \langle \tilde{Q} A_e \rangle}}, \quad (4.10)$$

1854 where c is the speed of light, ρ_{DM} is the local dark matter density and $P_{\text{ant}}^{\text{lim}}$ is defined in
 1855 Eq. 4.5. We have separated the equation into constants (or, in the case of ρ_{DM} , values that
 1856 we fix) and values that we measure or simulate.

1857 In order to validate our entire detection system, we inject sub-threshold signals into the
 1858 shielded room to verify we are able to detect them.

1859 **4.4 Hardware Injection Test**⁴

1860 To validate the detection methodology, a separate proof-of-concept run with a proxy dark
 1861 photon signal injected into the shielded room was performed. Apart from the injection

⁴Code for this section can be found at: <https://github.com/josephmlev/darkRadio/tree/master/daqAnalysisAndExperiments/run1p4/injectionTesting/injectionTesting.ipynb>

1862 antenna (a 40 cm monopole, see Sec. 4.3.2), the setup was equivalent to Run 1A, including
1863 the data analysis. The proxy dark photon signal (detailed in Sec. 4.4.1.2) was injected at a
1864 frequency set by a colleague and was unknown to me at the time of analysis, constituting a
1865 blind analysis.

1866 4.4.1 Injection test prerequisites

1867 4.4.1.1 Determination of required injected power

1868 To accomplish the test, a minimum detectable power required for injection P_{inject} must be
1869 computed. P_{inject} should correspond to a signal that can be detected in a predictable amount
1870 of time (with some uncertainty, discussed in detail in Sec. 2.2.2). A simple way to begin
1871 is to read off the detectable, total integrated, power from Fig. 4.8. In other words the
1872 power contained in a dark photon line, integrated over the few bins spanned by the line
1873 ($Q_{\text{DP}} \approx 10^6$, discussed in Sec. 2.1.2). This gives the amount of output-referred power that
1874 would be detectable 95% of the time after 9 days of integration. Since we do not want to
1875 wait 9 days for this test, it is simple to convert this detection limit into one that would be
1876 produced in a shorter time using the Dicke radiometer equation, Eq. 2.16. Namely, the limit
1877 on power scales like the square root of time⁵, so a one-hour integration will require a factor
1878 $\sqrt{9 \text{ days}/1 \text{ hour}} = 14.7$ more power than is shown in Fig. 4.8.

1879 At this point, the simplest way to proceed is to measure the average through-power of the

⁵It is important to point out that one needs to test whether or not the system in question actually behaves as predicted by the Dicke equation for the amount of averaging in question. After lots of averaging, one may encounter non-thermal backgrounds that do not scale properly. It is shown in Fig. 4.17 that the dark radio system follows the Dicke radiometer equation at least for 9 days.

1880 monopole to the bicon in several antenna positions. This power is proportional to $\langle |S_{21}|^2 \rangle$.

1881 This is the same as the set up described in Sec. 4.3.2. The bicon was moved to 9 positions

1882 and the resulting S-parameters were measured at the reference planes shown in Fig. 4.12.

1883 They are shown in Fig. 4.13 after being averaged together.

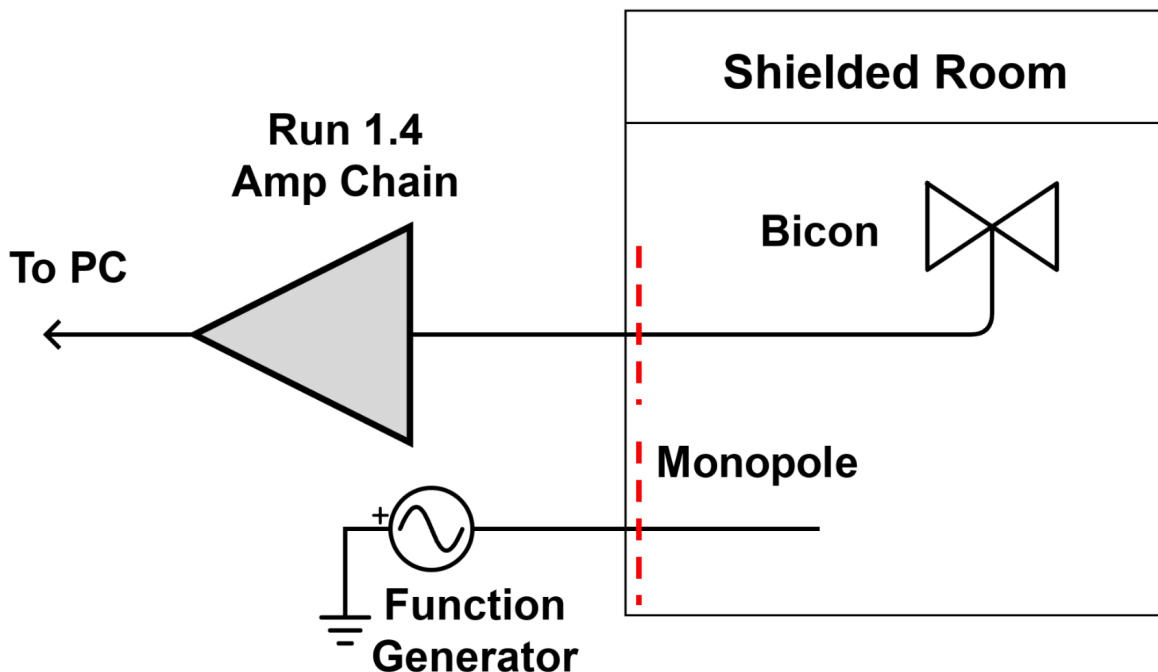


Figure 4.12: Schematic of hardware injection test. Dashed red lines indicate reference planes used to measure S-parameters, shown in Fig. 4.13. “Amp Chain” includes amplifiers, attenuators and filters as described in Sec. 2.5.4.

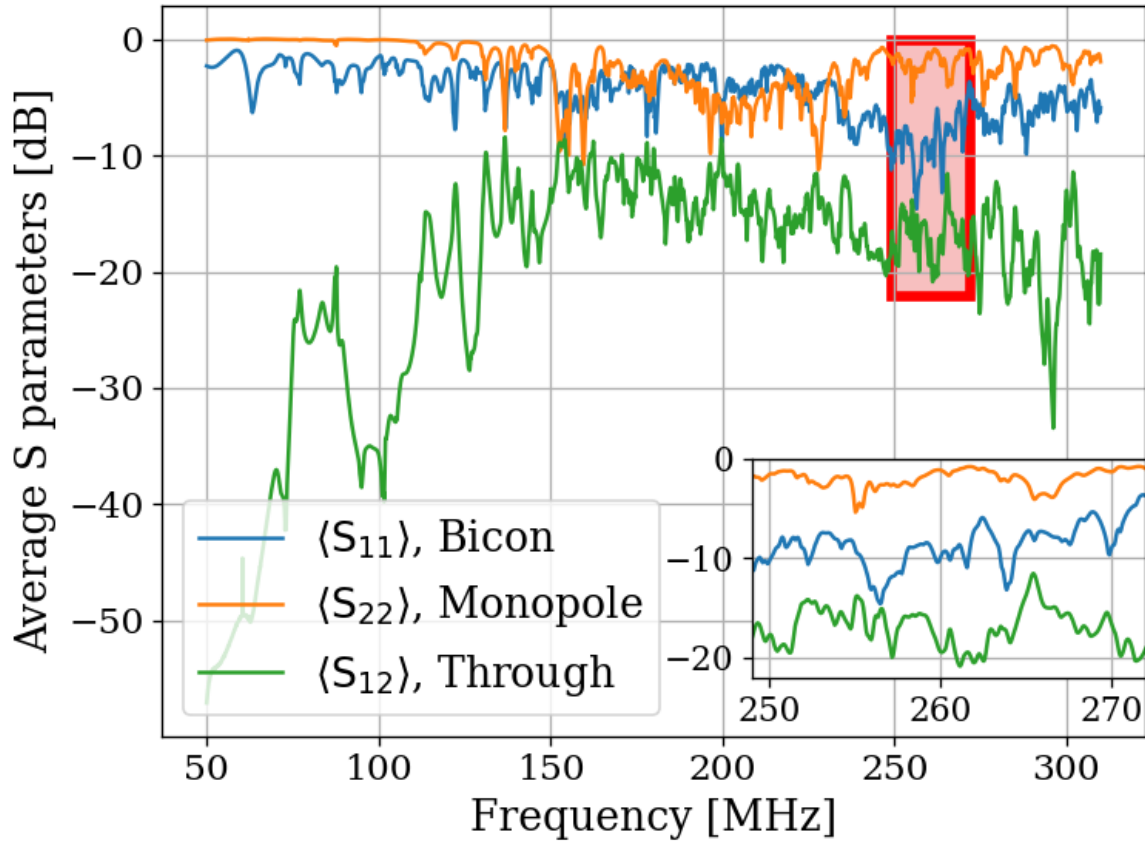


Figure 4.13: Average S-parameters of hardware injection test. Taken at 9 positions of the bicon antenna and averaged together (linearly). Ports 1 and 2 are defined to be for the bicon and monopole respectively. Note that $\langle S_{12} \rangle = \langle S_{21} \rangle$ so only $\langle S_{12} \rangle$ is shown. The inset shows a zoom-in of the area enclosed by the red box. Also note that dB is implicitly proportional to power.

1884 Knowing the output-referred power limit, the system's average $\langle |S_{21}|^2 \rangle$, and the gain G,
 1885 allows for a calculation of the required signal strength (as a function of frequency) which
 1886 will become detectable after a known amount of time. In order to simplify the test, a
 1887 smaller 1 MHz band is chosen between 268 and 269 MHz for the blind injection, where
 1888 $\langle |S_{21}|^2 \rangle$ is constant to about 1 dB. At first glance, this seems like cheating. However, there
 1889 are still $\sim 21,000$ frequency bins in this span, so a detection is very unlikely to be random.

1890 Furthermore, the entire 50-300 MHz span is sent to the detection algorithm (Discussed in
1891 Sec. 4.2 and illustrated in Fig. 4.3), which produces an output without knowing about this
1892 frequency restriction.

With all this in mind, the signal power required is simply

$$P_{\text{inject}} = \frac{P_{\text{o}}^{\text{lim}}}{G \langle |S_{21}|^2 \rangle},$$

1893 where each term is a function of frequency. For the parameters described in this section
1894 (including the increase in the power limit $\sqrt{9 \text{ days}/1 \text{ hour}} = 14.7$), this works out to
1895 $\approx 6 \times 10^{-19} \text{ W}$ or -152.5 dBm. The Rigol DSG830 signal generator is not calibrated
1896 to such low levels, so this was achieved through attenuation⁶.

1897 4.4.1.2 Proxy dark photon signal injection

1898 Now that the power for signal injection has been established, the finite-width proxy-signal
1899 ($Q_{\text{DP}} \approx 10^6$) is generated. The signal's line-shape is discussed in Sec. 2.1.2. An intuitive way
1900 to accomplish this would be with an arbitrary waveform generator injecting a time domain
1901 signal which is the Fourier transform of the the expected Rayleigh line shape, Eq. 2.24. This
1902 is the method employed by the ADMX experiment (see, for example, [71]). Another option
1903 would be to frequency-modulate a sine wave such that it slowly sweeps out the line shape,
1904 spending an amount of time at each frequency weighted by Eq. 2.24. While intuitive, I was
1905 unable to get this to work. Zhu et al.'s method of frequency hopping [72] is the discretized
1906 version of this, and it was very simple to implement. The signal generator is set to change

⁶Experience with this signal generator has shown it exhibits the best performance is when it is set around -30 dBm. Higher than this, large non-harmonic distortions appear, contaminating the run. Smaller, and the signal-to-spurious-noise-floor of the generator is poor, also contaminating the run.

1907 frequencies at some interval (discussed below). The frequency is randomly drawn from the
1908 PDF of Eq. 2.24.

1909 There are three considerations that determine the frequency hop period τ_{FH} that the
1910 frequency is changed⁷. First, τ_{FH} should be much longer than the acquisition time of a single
1911 buffer τ_{FFT} ⁸. On the Rigol signal generator, the power is briefly shut off while the frequency
1912 is changed. $\tau_{\text{FFT}} \ll \tau_{\text{FH}}$ ensures that most FFTs of data do not contain a frequency-hop.
1913 Second, τ_{FH} should be small compared to the total time of integration τ , so that there are
1914 many frequencies represented in the entire run. In the limiting case, $\tau_{\text{FH}} = \tau$ will yield an
1915 averaged spectrum containing a single injected frequency. In this case, the proxy-signal will
1916 be a delta function in the frequency domain. Third, τ_{FFT} should be longer than the ring-up
1917 time of the room, $\tau_{\text{FFT}} \gg Q/\nu$. For $Q = 100$ and $\nu = 260$ MHz, the right-hand side of this
1918 inequality is ≈ 0.3 μ s.

1919 Testing has shown that $\tau_{\text{FH}}/\tau_{\text{FFT}} \approx 10$ is more than adequate to address the first con-
1920 sideration. For Run 1A (and therefore, this test, which shares settings with Run 1A),
1921 $\tau_{\text{FFT}} = 2^{24}/800$ MHz = 21 ms, so τ_{FH} was set to 250 ms. This means that over 1 hour, the
1922 frequency will be set to $\approx 1.4 \times 10^4$ values, which addresses the second and third concerns.
1923 A histogram of this signal is shown in Fig. 4.14.

⁷Zhu et al. randomized this period to prevent any unintentional periodic signals entering. I did not find this to be necessary.

⁸One can likely bypass this restriction by coordinating the signal generator and ADC such that there is some dead time between collection of buffers, in which the frequency is set. Testing has shown that this restriction is adequate to avoid this extra programming step

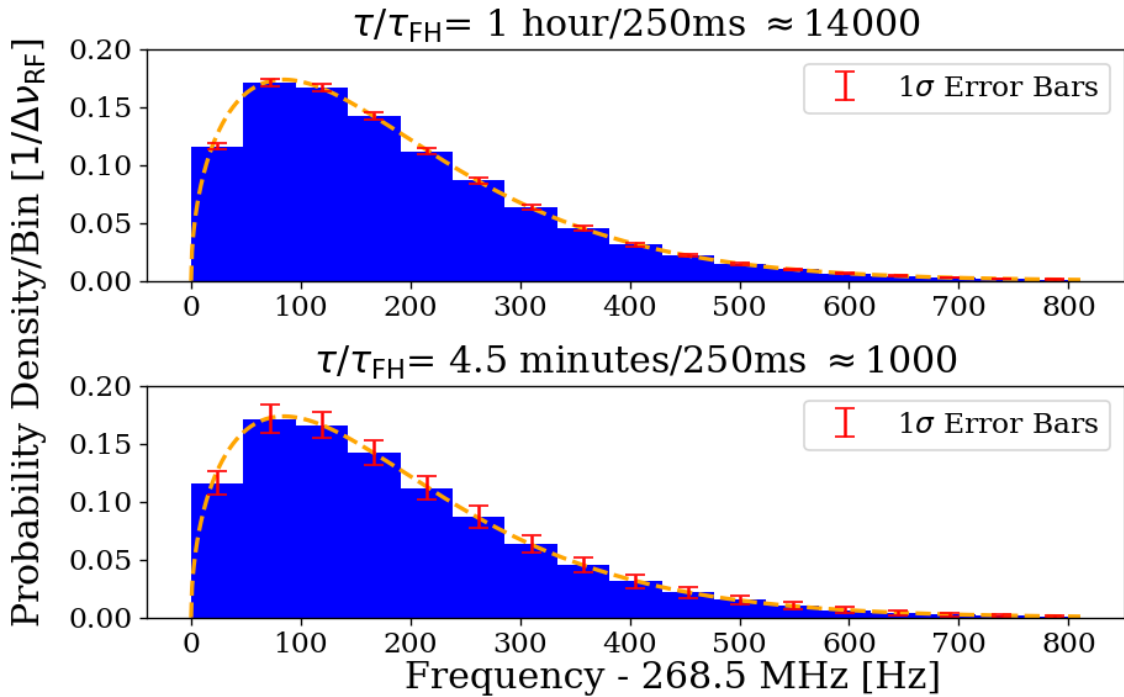


Figure 4.14: Histogram of frequencies used for hardware injection test, with realistic $\Delta\nu_{\text{RF}} = 47.7 \text{ Hz}$. The Orange dashed curve is the expected line shape from 2.24, and is the PDF frequencies are drawn from. The blue histogram and error bars are generated from the Monte Carlo simulation. They show the mean value per bin, with 1σ error bars in red. This involves generating 1000 lists of random frequencies (each of length τ/τ_{FH}), binning the data and calculating the standard deviation of each bin. τ is the total acquisition time and τ_{FH} is the amount of time spent on each frequency before “hopping” to the next. Their ratio, τ/τ_{FH} , is the number of frequencies that are injected in a given injection test, and was approximately 1.4×10^4 for the one-hour test outlined in this section. Two plots give an idea of how error scales with τ/τ_{FH} .

¹⁹²⁴ 4.4.2 Performing the injection test

¹⁹²⁵ Due to the uncertainties involved, more data were taken than the required 1 hour. This also
¹⁹²⁶ helped produce the pretty plot in Fig. 4 of Levine et al. [25]. 3.6 hr of data were collected
¹⁹²⁷ and saved in 30 s pre-averages so that progressively more data could be averaged if the signal
¹⁹²⁸ was not detected at the predicted time. As mentioned above, the signal was injected at a

1929 relatively high frequency within the span so that it would be split up into 5 or 6 bins, testing
1930 the matched filter's effectiveness. The bicon was moved to 9 positions. Spectra resulting from
1931 9 antenna positions and 30 seconds of pre-averaging at each position were averaged together
1932 giving 4.5 m time resolution. Three of these spectra are shown in Fig. 4.15. The standard
1933 deviation of these spectra average down with the square root of time, closely following the
1934 Dicke radiometer equation (discussed in Sec. 2.1.1.3). This scaling is shown in Fig. 4.17.

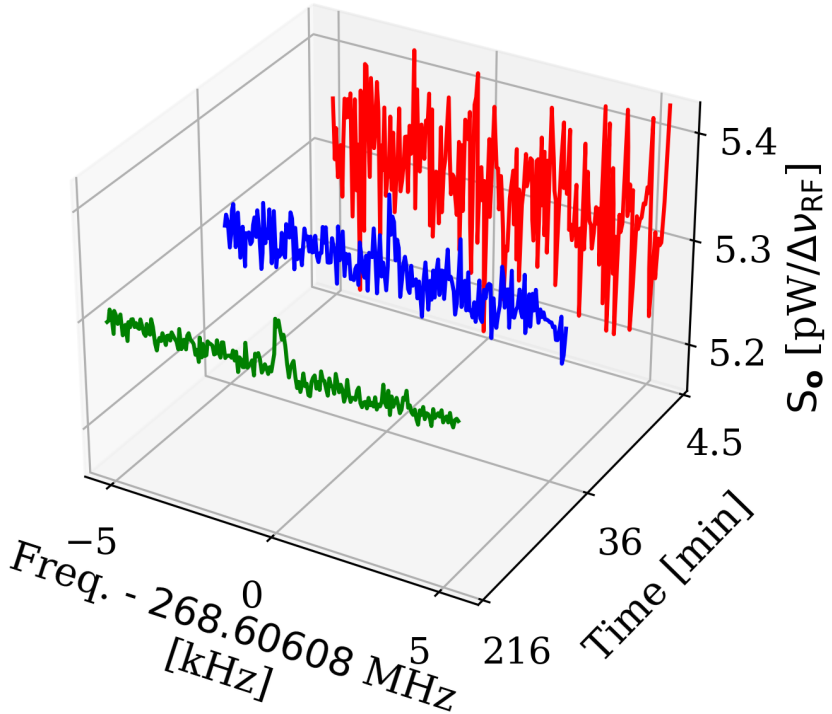


Figure 4.15: Output-referred power spectral density from the hardware injection test illustrating noise averaging down to reveal a persistent, hardware-injected, dark photon proxy signal. Spectra shown are highly zoomed around the injected frequency, 268.60608 MHz. The red, blue and green spectra represent 4.5, 36 and 216 minutes of integration time, respectively. The standard deviation of these spectra (excluding the bins containing the injected signal) averages down with the square root of time as expected. The blue spectrum shows the amount of averaging required for the signal to be detected by the detection algorithm (including the matched filter) at 5% significance. The tight zoom shown here is less than 1 part in 10^4 of the full 50-300 MHz spectrum analyzed.

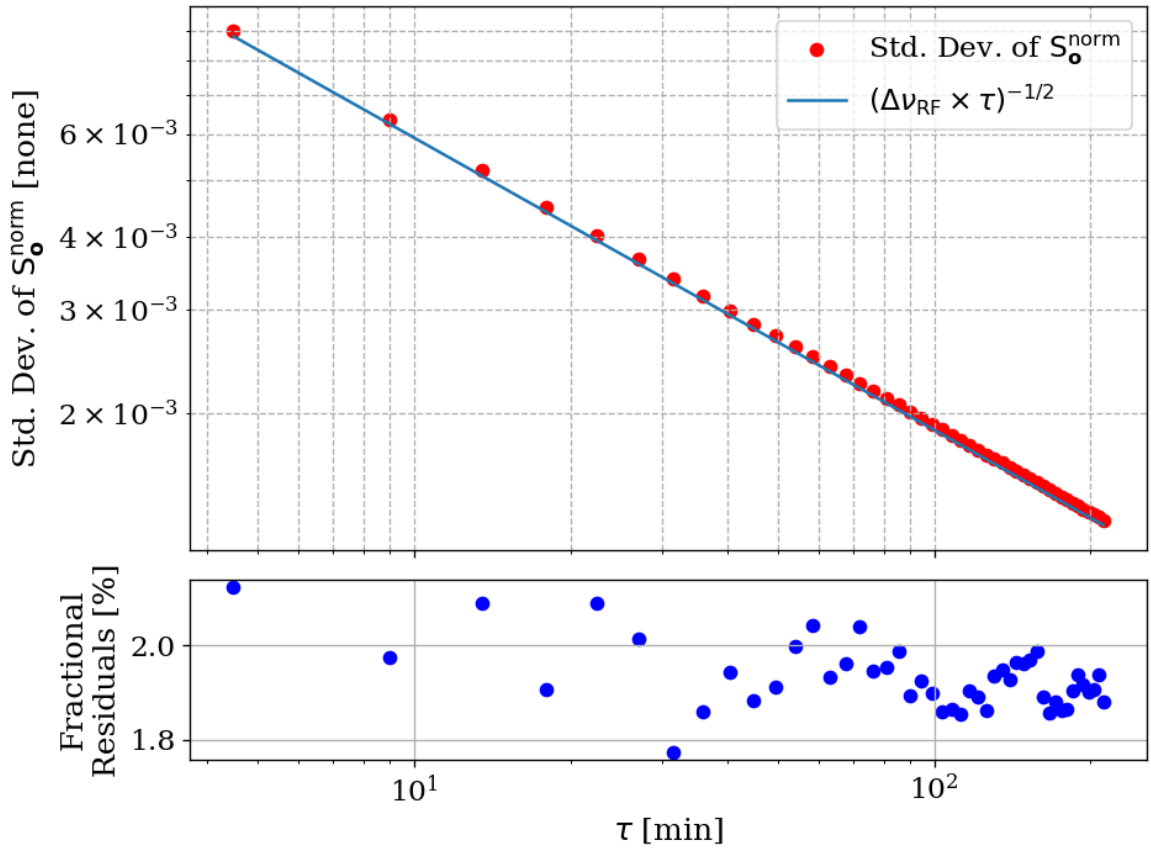


Figure 4.16: Standard deviation of normalized, output-referred power spectral density from the hardware injection test. The blue curve is the predicted standard deviation from the Dicke radiometer equation, Eq. 2.16. Each point represents the 9 antenna positions with an additional 4.5 minutes of data averaged (see Sec. 4.4.2). Correlation in residuals are observed when computing the standard deviation directly on S_o^{norm} as an artifact of fitting \hat{B} , as described in Sec. 4.2.1. A better fit is achieved through the median average deviation, Shown in Fig. 4.17.

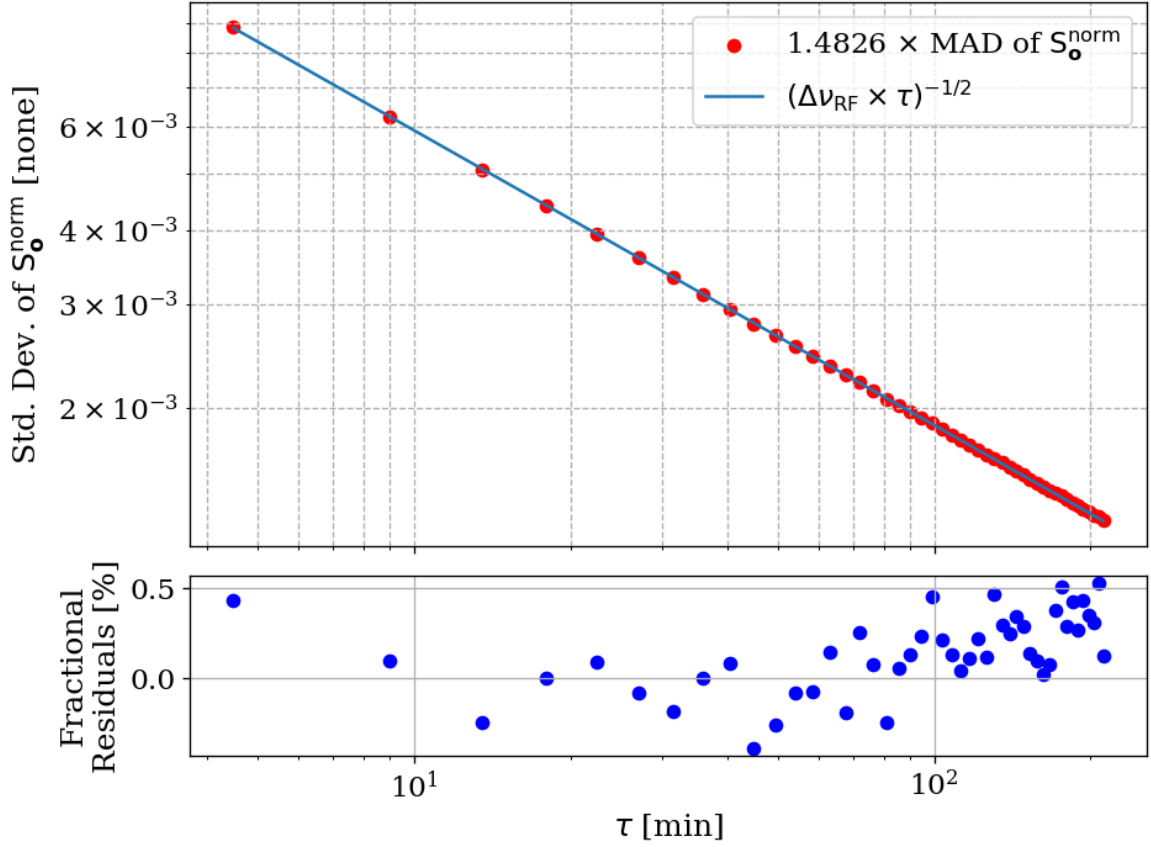


Figure 4.17: Standard deviation of normalized, output-referred power spectral density from the hardware injection test, computed with median absolute deviation (MAD). The blue curve represents the predicted standard deviation from the Dicke radiometer equation, Eq. 2.16. Each point corresponds to 9 antenna positions with an additional 4.5 minutes of data averaged (see Sec. 4.4.2). MAD provides a more robust measure of variability, reducing the influence of outliers and offering a better fit to the normalized spectra than direct standard deviation calculations. Note that the factor of 1.4826 is required to convert between MAD and standard deviation and assumes normally distributed data. It is derived in Sec. 2.3 of [73].

- 1935 These spectra were generated one at a time and passed through the detection algorithm.
- 1936 The first spectrum where a signal was detected was at 36 minutes, shown in blue in Fig. 4.15.
- 1937 Although hardly detectable to the eye, the matched filter detects the signal with 5% signifi-

1938 cance. At the point the signal was detected (i.e. before all data were averaged together), the
1939 injection frequency was confirmed to have been correctly identified, resulting in a success-
1940 ful, blind, hardware injection test. Only after this confirmation were all the data averaged
1941 together to make Fig. 4.15.

1942 **4.4.3 Inspection of Data**

1943 This final subsection simply contains some full-page figures which show data from the injec-
1944 tion test. They are all from the same 34 minutes of data but at different stages of processing,
1945 closely following the three main steps of Analysis, Sec. 4.2. They are meant to simulate the
1946 experience of inspecting a 2^{24} -point FFT's power spectrum in a matplotlib widget window.
1947 The zoom is seemingly unending, a feature that is difficult to appreciate in a printed docu-
1948 ment. These figures should provide some context for how futile a manual search of unfiltered
1949 data would be. Try and pick out the signal in the top left panel of Fig. 4.18!

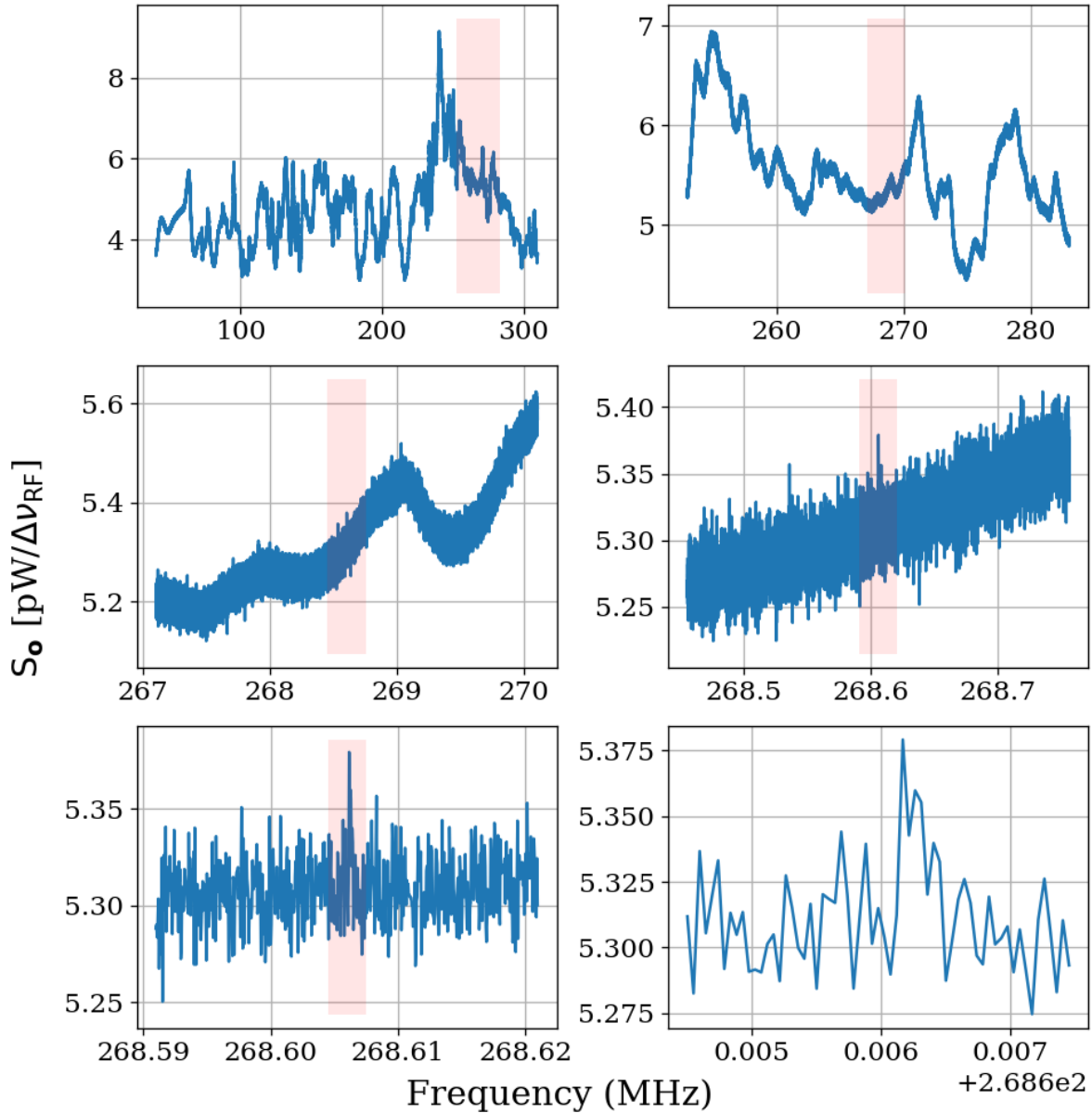


Figure 4.18: Output-referred power spectrum from hardware injection test. Injected signal at 268.60608 MHz. All spectra correspond to a total of 36 minutes of averaging, split evenly between 9 antenna positions. The full 50-300 MHz span contains $\approx 5.2 \times 10^6$ bins. Light pink boxes show the zoom level on the following plot.

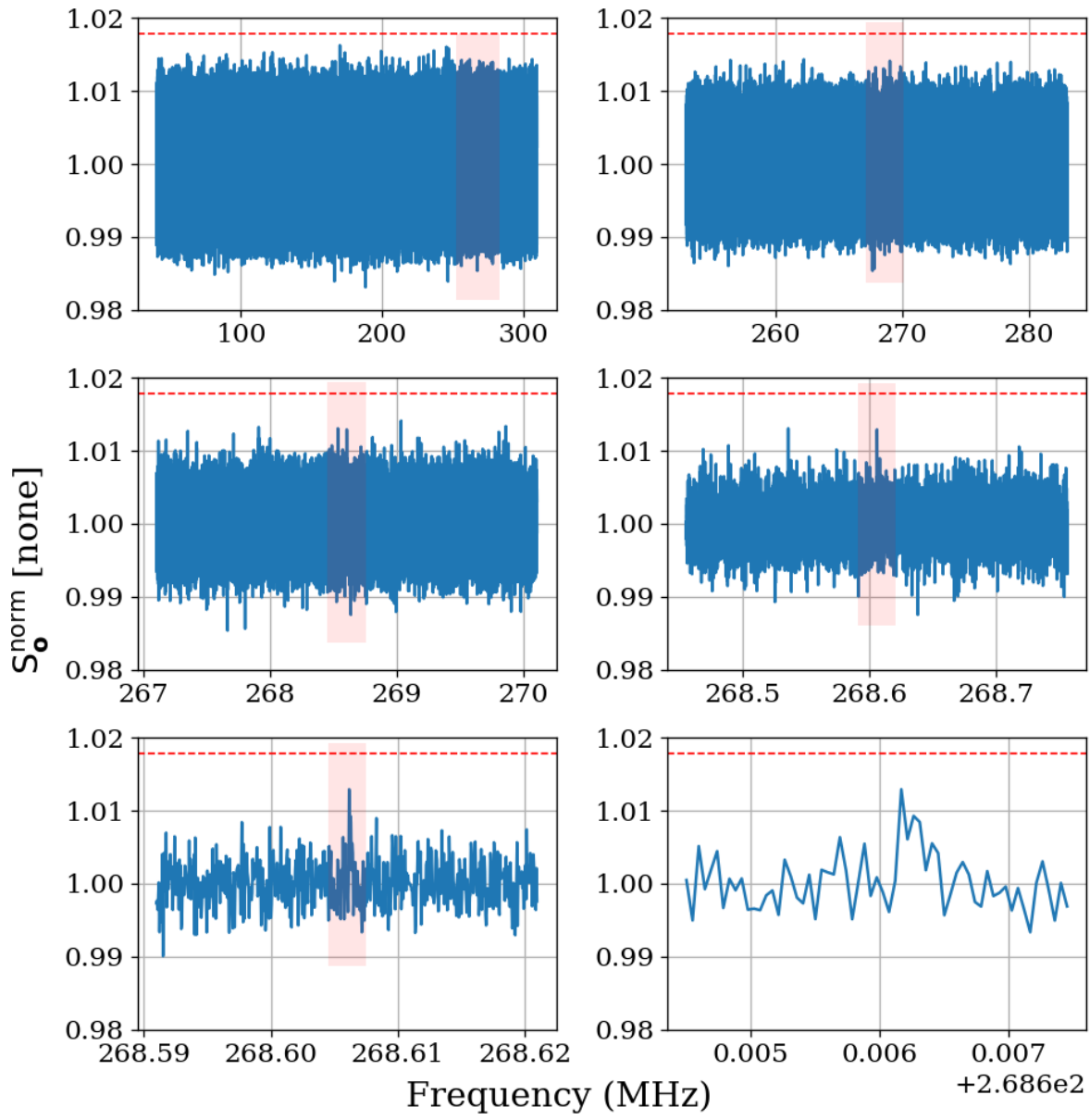


Figure 4.19: Normalized, output-referred power spectrum from hardware injection test. Injected signal at 268.60608MHz. Light pink boxes show the zoom level on the following plot. The red dashed line indicates the 5% significance threshold, derived in Sec. 2.2.1. A signal was not detectable above this threshold.

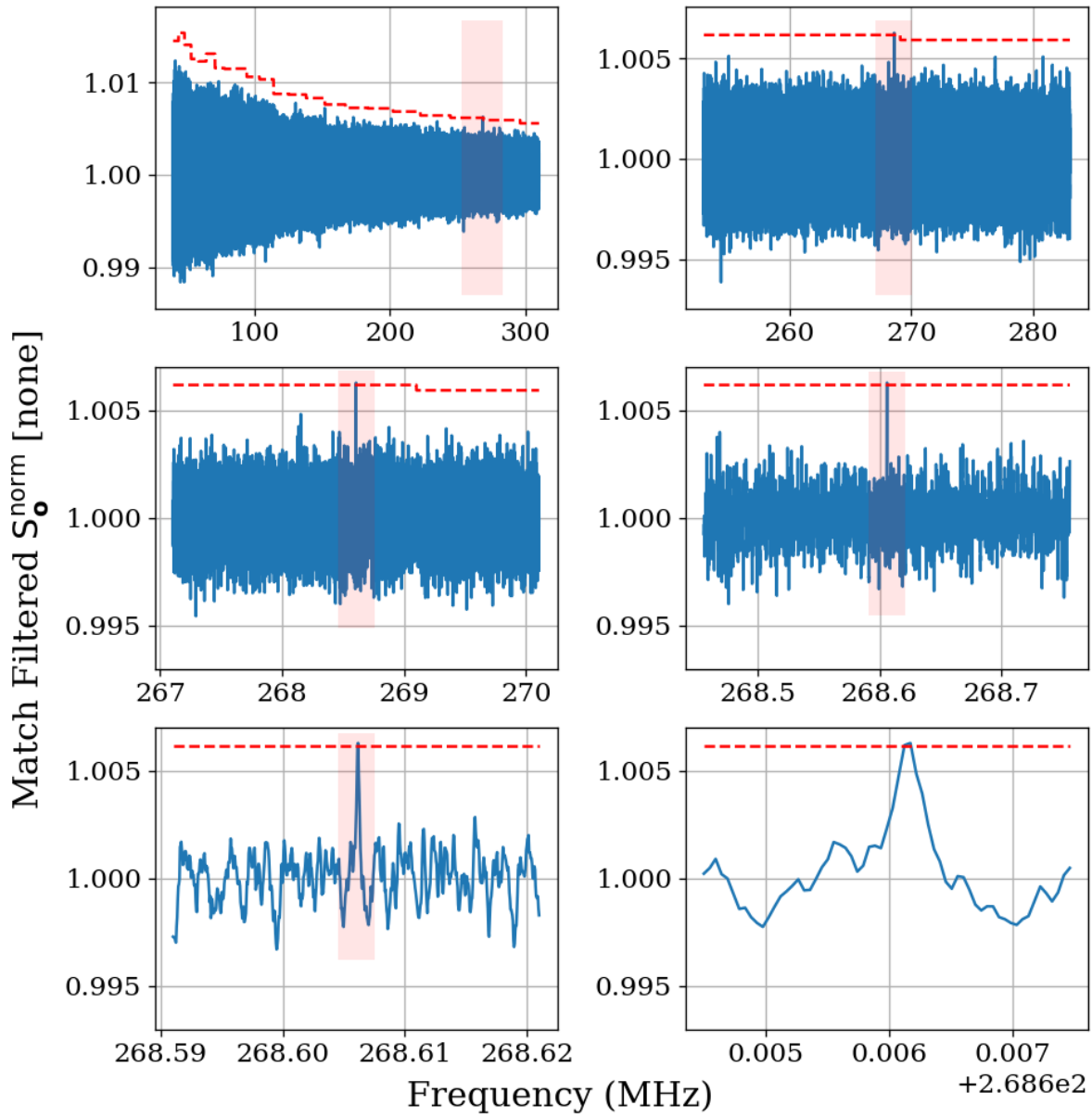


Figure 4.20: Matched filtered, output-referred power spectrum from hardware injection test. Injected signal at 268.60608MHz. Light pink boxes show zoom level on following plot. Red dashed line indicates the 5% significance threshold, derived in Sec. 2.2.1. Introducing the matched filter pushed signal above detectable above threshold compared to Fig. 4.19.

₁₉₅₀ Chapter 5

₁₉₅₁ Results

A quote will go here

₁₉₅₂

Bob Lob's Law Blog

1953 In this chapter, we report a 95%, frequency-dependent, exclusion limit on the kinetic
1954 mixing strength ϵ of the dark photon (Fig. 5.1). We discuss the uncertainties of the measured
1955 data. Finally, we display our results in context by plotting these new limits on top of
1956 an aggregation of existing limits in Fig. 5.2. Future runs of this experiment from 0.3-
1957 14 GHz in similar room-temperature RF enclosures and using 100 K noise temperature LNAs
1958 are indicated (the foundation for such a system is outlined in Sec. 6.2). We have only
1959 indicated planned runs, however at microwave frequencies, highly resonant cryogenic cavities
1960 and cryogenic LNAs as well as sub-THz instrumentation are feasible and could result in an
1961 order of magnitude improvement in the limit over the indicated frequency range and beyond.
1962 The design principles of such a system are outlined in Sec. 6.3.

1963 5.1 Discussion of Uncertainties

1964 The systematic uncertainty in this experiment comes primarily from three sources, listed in
1965 order of their contribution from greatest to least:

- 1966 1. Fractional uncertainty on the simulated antenna aperture, which is discussed in Sec. 4.3.3,
1967 $\approx 60\%$
- 1968 2. Fractional uncertainty on the first-stage amplifier noise temperature, $\approx 10\%$
- 1969 3. Fractional uncertainty on the gain of the amplifier chain, $\approx 5\%$

1970 The uncertainty on the simulated antenna aperture is significantly larger than the other
1971 two, and so we neglect them in the reported uncertainty on the ϵ limit.

1972 We follow the convention of similar experiments where we fix the value of ρ_{DM} and
1973 solve for an ϵ limit given this value. Therefore, we treat ρ_{DM} as a known constant with no
1974 uncertainty.

1975 **5.2 Exclusion Limit¹**

1976 This section incorporates the exclusion limit on output-referred power (Fig. 4.8) and Eq. 4.10
1977 to report a 95%, frequency-dependent, exclusion limit on the kinetic mixing strength ϵ of
1978 the dark photon. This limit is presented in Fig. 5.1, as well as in context by plotting it with
1979 other, similar experiments in Fig. 5.2.

¹Code for this section can be found at: <https://github.com/josephmlev/darkRadio/tree/master/Computelimit>

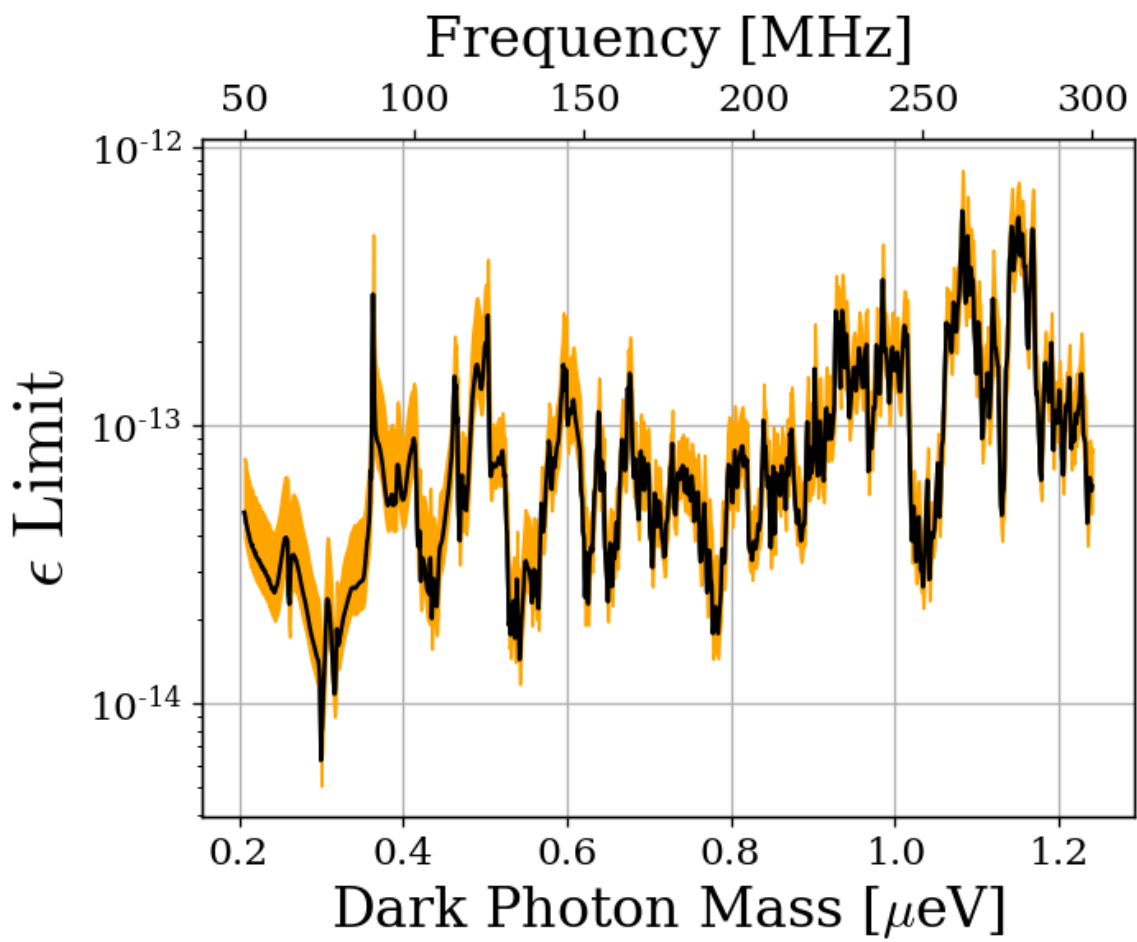


Figure 5.1: 95% exclusion limit on ϵ with uncertainty shown in the orange shaded region. This is based on a local dark matter density of $\rho_{\text{DM}} = 0.45 \text{ GeV/cm}^3$. The error estimate does not take the comparatively small gain and amplifier noise temperature errors into account.

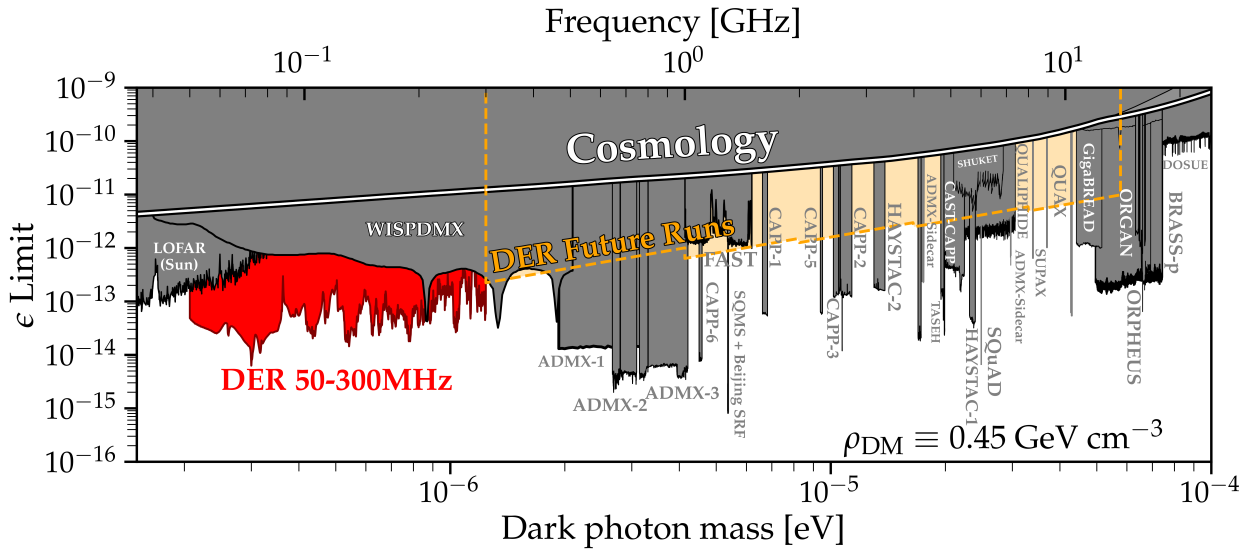


Figure 5.2: Dark photon limits of various experiments circa August 2024, with this work shown in red. The ragged lower bound is due to the complex structure of the resonant modes of the shielded room. Plot adapted by Ben Godfrey from [74] using code found at [75] and includes limit projections of various axion experiments. Astrophysical limits such as CMB interactions with the dark photon are in the region labeled *Cosmology*. Planned wideband extensions of our experiment searching from 0.3-14 GHz in similar room temperature RF enclosures are indicated (*orange*). These planned runs are summarized in Table 6.1.

₁₉₈₀ Chapter 6

₁₉₈₁ Beyond 300 MHz

To infinity and beyond!

1982

Buzz Lightyear

1983 As discussed in previous chapters, there is a wide mass/ ϵ parameter space available for
1984 exploration. This chapter details how the Dark E-Field Radio Experiment (DER) is poised
1985 to clear out additional parameter space.

1986 Since the parameter space consists of two variables (namely mass, AKA frequency ν and
1987 kinetic mixing ϵ), the “area” of this space must be considered. The advantage of this exper-
1988 iment is not absolute sensitivity; many experiments are orders of magnitude more sensitive
1989 due to extremely high Q superconducting cavities or lumped-element circuits. Rather, the
1990 advantage lies in the ability to clear out large frequency spans efficiently. The aforemen-
1991 tioned high-Q experiments are only capable of searching a single, narrow frequency span at
1992 a given time and must slowly step through the total required frequency span, waiting for a
1993 period of time $\approx Q/\nu$ at each step for the system to ring up. Limitations on tuning require
1994 swapping out hardware throughout the run, slowing down the process. See, for example,
1995 DMRadio m³[76].

1996 The four completed or planned phases of DER are outlined in Table 6.1. These phases
1997 are projected to exclude the orange-shaded region shown in Fig. 5.2. This region spans from
1998 0.3-14 GHz, though Run 2B may push slightly higher (16 GHz without much trouble).

1999 Section 6.1 covers progress made toward Run 1B. Section 6.2 covers the technique of
2000 frequency mixing, which extends the frequency range of the existing 1 GHz spectrum analyzer
2001 (Sec. 2.5.7) up to \sim 14 GHz.

2002 Beyond this, the experiment becomes more difficult. The topic of Sec. 6.3 is this frequency
2003 range. This section is less detailed than the previous sections, providing more general guid-
2004 ance as opposed to specific designs and testing procedures.

2005 Finally, Sec. 6.4 introduces a few considerations for axion experiments that would improve
2006 their sensitivity to dark photons. Axion experiments represent a significant investment of
2007 resources and are extremely sensitive, so this avenue is an extremely efficient one to clear
2008 dark photon parameter space.

Run Name	Frequency Range	Antenna	LNA	Mixer	Status	Statistical Uniformity	Comments
1A	50-300 MHz	Compower Bicon, 50-300 MHz	Pasternack PE15A-1012	N/A	Complete, published	N/A. Below lowest usable frequency. Move antenna and simulate aperture	N/A
1B	300-1000 MHz	RF Space UWB-5 Vivaldi, 0.3-6 GHz	Pasternack PE15A-1012	N/A	Preliminary run complete by moving antenna. 21 candidates detected.	Mode stirrer	50% dead time to allow for 2GHz sampling rate on Teledyne
2A	1-8 GHz	Small Vivaldi, model TBD	Low noise factory LNC0.3_14B	Miteq TB0440LW1	Waiting on mode stirrer and mixer system commissioning	Mode stirrer	N/A
2B	8-14 GHz (possibly ending at 16 GHz)	TBD	Low noise factory LNC0.3_14B	Miteq TB0440LW1	Waiting on mode stirrer and mixer system commissioning	Mode stirrer	N/A

Table 6.1: Overview of planned future runs including hardware (antenna, low noise amplifier (LNA), mixer), status, how/if statistical uniformity will be ensured, and any comments

2009 **6.1 A First Attempt at Run 1B¹**

2010 A preliminary attempt at Run 1B (300-1000 MHz) has been completed. This attempt had
2011 a few issues, which are discussed here and will be addressed in the future, but are beyond
2012 the scope of this thesis. In this section, upgrades and data acquisition are discussed. The
2013 projected ϵ limit from this run (along with Runs 2A and 2B) is shown in Yellow in Fig. 5.2.
2014 However, this projection is independent of the data shown here.

2015 **6.1.1 Run 1B upgrades**

2016 There are four main upgrades to consider before beginning Run 1B: software upgrades of the
2017 GPU-based spectrum analyzer, modifying the analog signal conditioning chain, modifying
2018 the current antenna stand to accept a Vivaldi antenna, and building a mode stirrer to ensure
2019 statistical uniformity. The remainder of this subsection will detail these upgrades.

2020 **6.1.1.1 Run 1B spectrum analyzer**

2021 The GPU-based spectrum analyzer (Sec. 2.5.7) is capable of sampling at up to 2.5 GHz,
2022 easily allowing for a run up to 1 GHz. However, the PCIe-based ADC has a maximum data
2023 transfer rate of 7GB/s. To accommodate two channels (main experiment and veto), the
2024 system was set up with 50% dead time to allow for data to transfer. The limit on ϵ scales
2025 with the quarter root of time, so this is only a 16% reduction in sensitivity. This is purely a
2026 software upgrade and has been completed.

¹Code for this section can be found at: <https://github.com/josephmlev/darkRadio/tree/master/daqAnalysisAndExperiments/run1B/analysis>

2027 **6.1.1.2 Run 1B signal conditioning**

2028 The signal conditioning chain (defined in Sec. 2.5.4) of Run 1B is very similar to that of Run
2029 1A, Fig. 2.42. The amplifiers are the same as defined in Tabs. 2.3 and 2.4. The band-pass
2030 filter was changed from that of Run 1A to allow for the required 300-1000 MHz span of Run
2031 1B. The Run 1B band-pass filter was constructed from a Mini-Circuits ZX75LP-1050-S+,
2032 1090 MHz low-pass filter² and a Mini-Circuits ZX75HP-250-S+, 250 MHz high pass filter.
2033 An additional 1 dB attenuator was added to account for the larger integrated noise power of
2034 the wider frequency span.

2035 **6.1.1.3 Vivalid antenna stand**

2036 The COMPOWER bicon antenna stand was modified to accommodate the RFSpace UWB-5
2037 Vivaldi antenna. This was completed and pictures of the modifications are shown in Figs. 6.1
2038 and 6.2.

2039 **6.1.1.4 Mode stirrer and statistical uniformity**

2040 Run 1A relied on moving the antenna to improve the statistical uniformity (Sec.2.4) but still
2041 required simulation to calibrate it (Sec.4.3.2). Run 1B, however, benefits from its frequency
2042 range beginning above the lowest usable frequency of the shielded room (~ 200 MHz, see
2043 Sec. 2.34). To take advantage of this, a proper mode stirrer (Sec. 2.4) must be employed. A
2044 lack of mode stirrer is the main limitation of this attempt at Run 1B. At the time of writing,

²The attenuation of this filter is greater than 50 dB above 1400 MHz. This is relevant aliasing frequency for a 1 GHz analysis span and 2.4 GHz sample rate.



Figure 6.1: Picture of modified COMPOWER antenna stand holding Vivaldi antenna for Run 1B.

2045 work is ongoing to construct a mode stirrer. **comment:** Since this is ongoing, I will circle

2046 back and add photos with current progress right before submitting a final draft

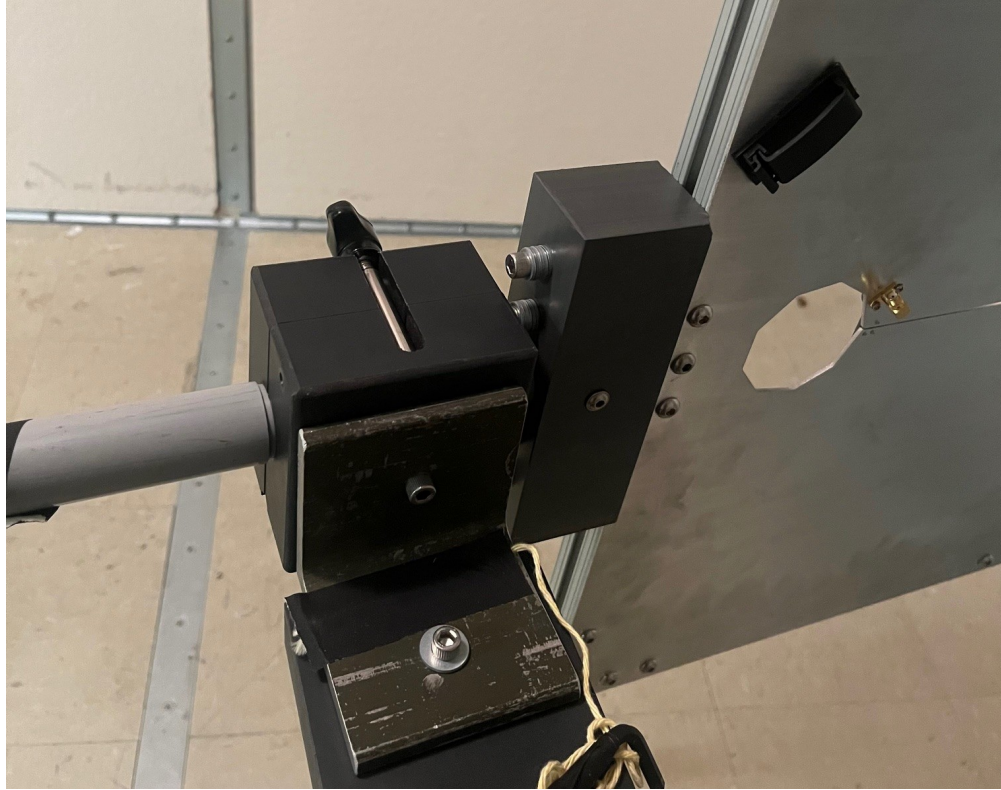


Figure 6.2: Closeup of modified COMPOWER antenna stand holding Vivaldi antenna for Run 1B

2047 6.1.2 Run 1B: data run and analysis

2048 The first attempt at Run 1B, (Run 1B.1) was taken between September 13 and 22, 2023.

2049 Run details are shown in Tab. 6.2.

2050 At the time of writing, Run 1B.1 has been the only attempt at this run. The raw data

2051 are shown in Fig. 6.3. The normalized standard deviation σ_{norm} (defined in Sec. 4.2.2 from

2052 the Dicke radiometer equation) is predicted to be 0.9885×10^{-3} , and is calculated from the

2053 data to be 1.001×10^{-3} . The sample rate of this run was set at 2.4 GHz. This is slightly

2054 higher than the required 2 GHz to prevent aliasing (described in Sec. 2.5.4.3).

Specification	Value
Analysis span	300-1000 MHz
-3 dB span of analog filters	250-1090 MHz
Antenna	RFSpace UWB-5 Vivaldi antenna
RTSA	Teledyne GPU system (Sec. 2.5.7)
Frequency resolution ($\Delta\nu_{RF}$)	286 Hz
Length of record	2^{23} samples
Sample rate	2.4 GHz
Window type	None (rectangular)
Acquisition time per spectrum	3.5 ms
Run start time	2023-09-13 16:32:41.33
Total time of run	8 days, 23.52 hours
Efficiency (Time spent scanning antenna/total time)	44.90%

Table 6.2: Run 1B details. Many specifications are related and can be computed from each other but are listed for reference. The efficiency differs from that calculated in Fig. 3.16 mostly because of the required dead time to allow for data transfer from the ADC to the GPU. There is a further, smaller, degradation to the efficiency due to the switching to a terminator and brief daily pauses to move the antenna.

2055 Processing this data through the detection algorithm (Fig. 4.3) of Run 1A, yields the
 2056 normalized, signal-matched-filtered spectrum and 5% significance threshold which are shown
 2057 in Fig. 6.4.

2058 Comparison of the spectrum and threshold pictured in Fig. 6.4 reveal 21 candidates³.
 2059 Furthermore, 13 of these are clustered between 758 and 768 MHz. This frequency span is
 2060 reserved for the First Responder Network Authority (FirstNet) and is likely in use locally
 2061 by emergency services.

2062 All of these candidates are almost certainly RFI with enough energy (i.e. signal power
 2063 integrated over the 9-day run) to overcome the isolation of the shielded room (Fig. 3.13).

³There are a total of 60 bins over the threshold, but many bins are adjacent. Combining adjacent bins results in 21 independent candidates

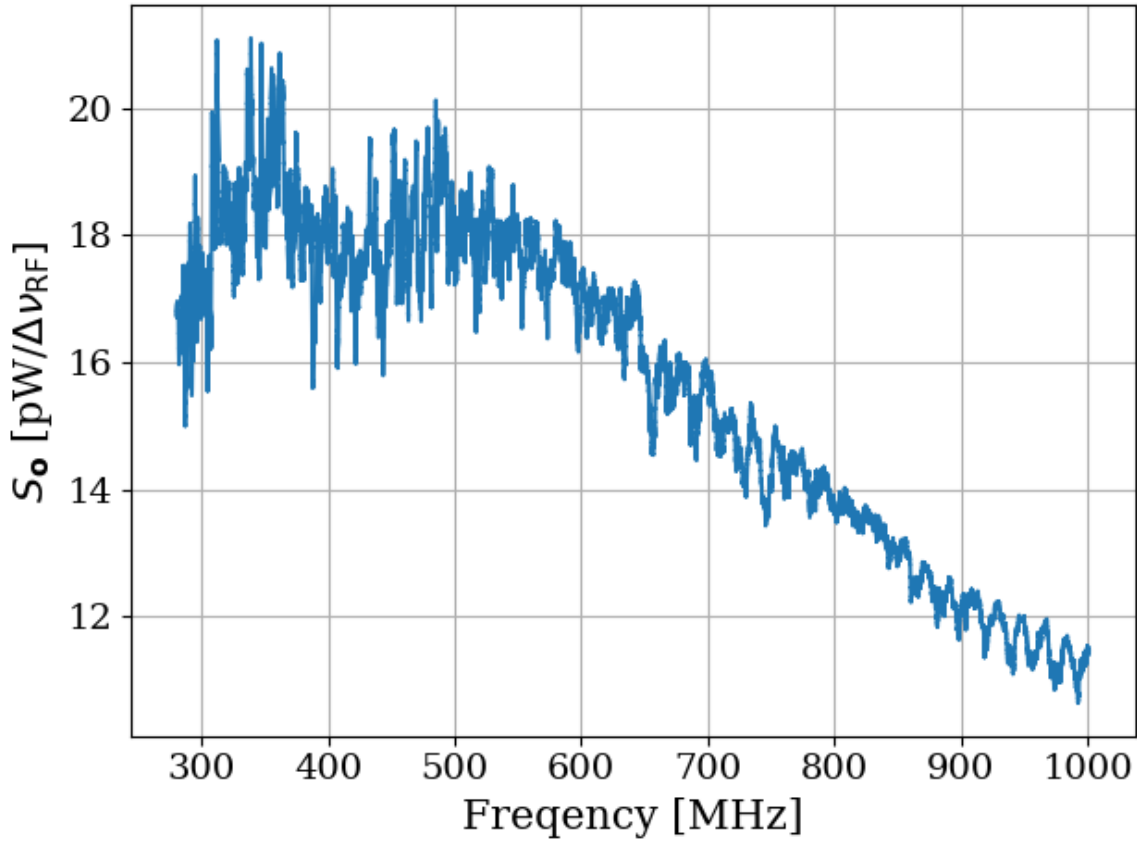


Figure 6.3: Run 1B averaged, output-referred antenna power spectrum S_o . Data were taken over a 9-day period at 9 antenna positions. The narrow variations are mainly due to the effective temperature difference between the room and low noise amplifier (LNA) (Sec. 2.3), though there is a contribution due to amplifier gain and noise temperature variations (Sec. 4.1.1). The variations seen here are not noise; their shape is repeatable for a given antenna position. The noise on this background is not visible at this level of zoom.

2064 These signals are visible in the veto spectrum (Fig. 6.5), but further investigation is required

2065 to conclusively exclude them as dark photons.

2066 Since simulations of this run are extremely difficult to calculate (wavelength at 1GHz <<

2067 room dimensions), it will have to be revisited when statistical uniformity can be established,

2068 i.e. with a mode stirrer. For this reason, further time domain analysis of these candidates is

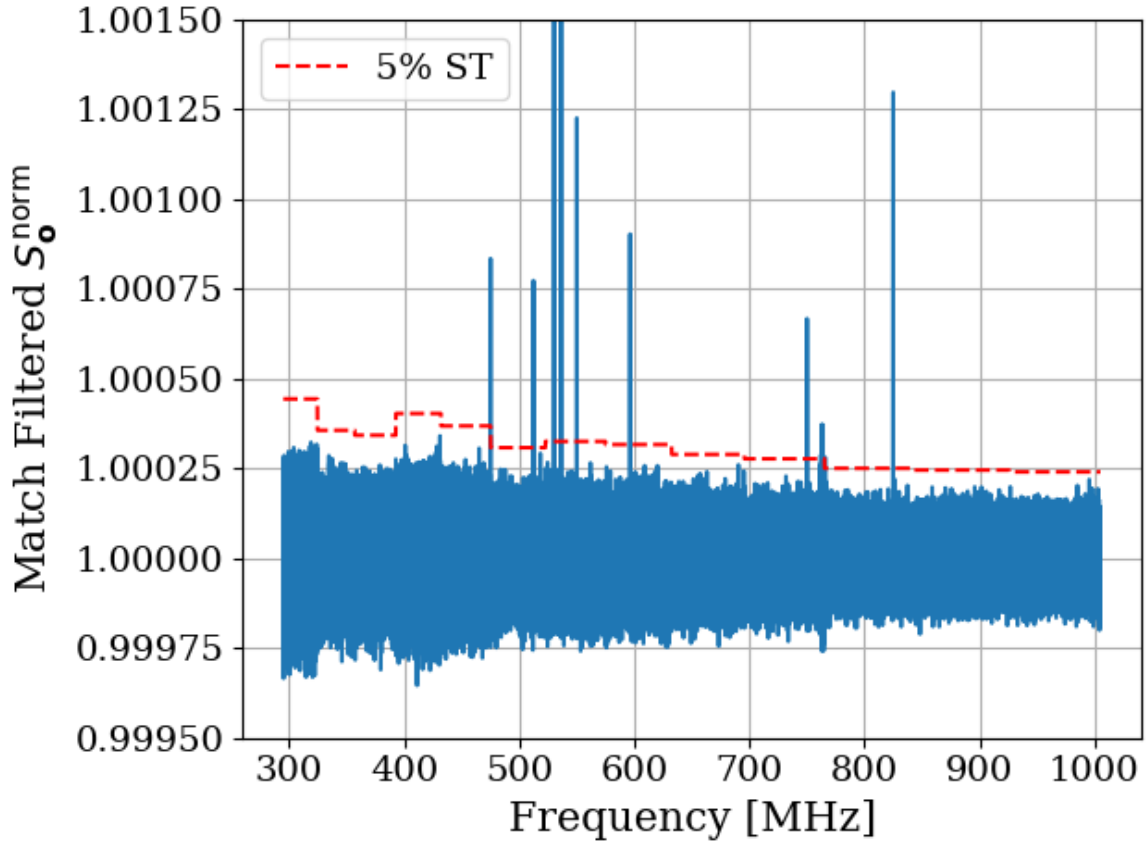


Figure 6.4: Run 1B S_o^{norm} after it has been passed through a matched filter. The template varies in width throughout the frequency span resulting in 13 subspans, each with a constant 5% significance threshold ST (*dashed red*), see Secs. 2.2.1 and 4.2.3. This plot is to Run 1B as Fig. 4.6 was to Run 1A. In contrast to Fig. 4.6, however, the narrow signals are not injected. They are almost certainly RFI with enough power to overcome the isolation of the shielded room (Fig. 3.13). These signals are visible in the veto spectrum, but further investigation is required to conclusively exclude them as dark photons. The vertical scale has been set such that the tops of two of the signals are cut off.

2069 not explored here.

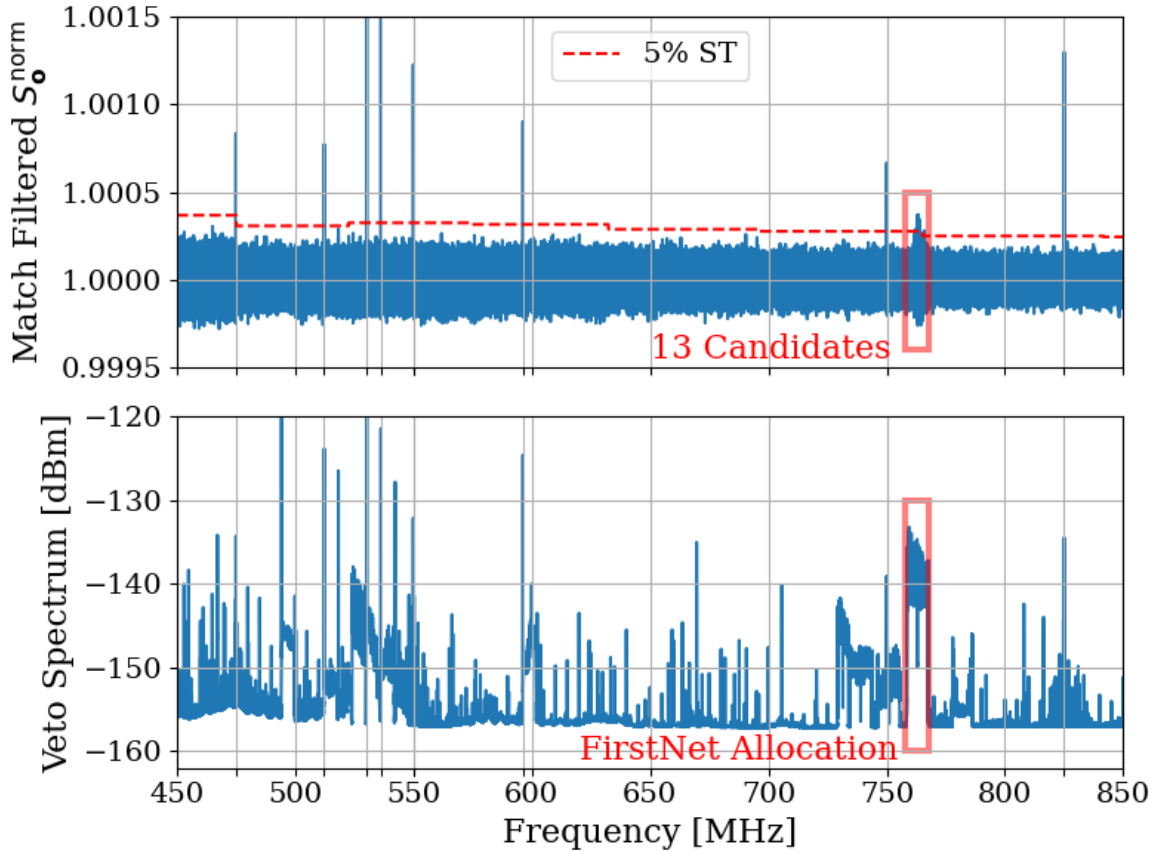


Figure 6.5: 9-day averaged veto spectrum and Run 1B $S_{\bullet}^{\text{norm}}$ after it has been passed through a matched filter. The 5% significance threshold ST (Secs. 2.2.1 and 4.2.3) is shown as a dashed red line. There are 21 independent candidates, however 13 of them are found in the FirstNet frequency span (758-768 MHz) which is discussed in the text of this subsection. This frequency span is shown in both the veto and experimental spectra with a red box. The remaining 8 candidates have ticks added to the x-axis to guide the eye between candidates in the upper panel and RFI in the lower panel. The vertical scale has been set such that the tops of two of the signals are cut off.

2070 6.2 Mixer System: Run 2

2071 Run 1 relied on an ADC with a sample rate of up to 2.5 GHz, allowing for direct RF sampling
 2072 of Run 1A/B. This system is a flexible platform, allowing for future upgrades to extend its
 2073 maximum frequency through the use of a mixer system which is described in this chapter.

2074 **6.2.1 Frequency mixing**

2075 Frequency mixing is a technique in RF and microwave systems used to shift the frequency
2076 of a signal to another frequency range which is more useful for a given task. For example,
2077 electronics are simpler to design at kHz frequencies, but antennas operate at MHz. After
2078 processing a kHz signal for transmission, it can be mixed up (“upconverted”) to MHz for
2079 transmission over the air. Once it is received, it can be mixed back down (“downconverted”)
2080 to kHz. Mixer engineering is a rather complex topic, and many details will be omitted here.
2081 The reader is encouraged to reference the Marki Microwave mixer primer [77] for a tutorial
2082 on mixers and Ch. 13 Pozar’s *Microwave Engineering* [78] for a more thorough treatment.

2083 In a mixer system, an input signal (RF) is combined with another signal, typically from
2084 a local oscillator (LO), such that the two frequencies multiply or “mix”, producing an inter-
2085 mediate frequency (IF). In other words, the RF signal $\cos(2\pi f_{\text{signal}}t)$ is multiplied by a local
2086 oscillator signal $\cos(2\pi f_{\text{LO}}t)$ ⁴. Using the trigonometric identity

$$\cos(A)\cos(B) = \frac{1}{2}(\cos(A+B) + \cos(A-B)), \quad (6.1)$$

2087 it can be seen that this multiplication produces two new components: one at the sum
2088 frequency $f_{\text{signal}} + f_{\text{LO}}$ and one at the difference frequency $|f_{\text{signal}} - f_{\text{LO}}|$.

2089 A mixer is a 3-port device that has two inputs and one output. The LO port is almost
2090 always an input, while the RF and IF ports can be used as either an input or an output (as

⁴The multiplication of CW signals outlined here is a simplification. In reality, the LO should have higher harmonics and approximate a square wave to overcome the transition region of the voltage-current curve of a real diode. See the Marki Microwave mixer primer for more details [77].

2091 long as they are opposite)⁵. Such a system can be used for upconversion (downconversion),
2092 where the RF is shifted to a higher (lower) frequency, as shown in Fig. 6.6. The situation
2093 when the signal above (below) the LO is desired, and the signal below (above) the LO is the
2094 image is known as low-(high-)side injection downconversion. In other words,

$$\text{Low-Side Injection: } f_{LO} < f_{RF} \text{ (desired signal is above the LO)} \quad (6.2)$$

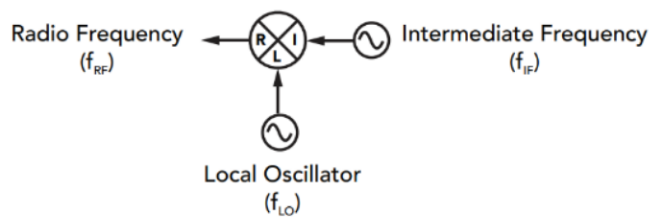
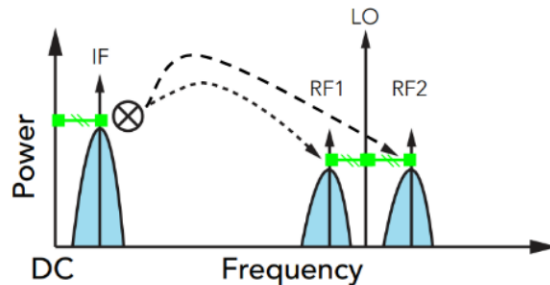
$$\text{High-Side Injection: } f_{LO} > f_{RF} \text{ (desired signal is below the LO).}$$

2095 The remainder of this subsection will focus on downconversion, but both downconversion
2096 and upconversion are important in the system, which is presented later in this section.

⁵Again, this is simplified. All three ports actually behave as both a load and a source. See the first footnote of the Marki Microwave mixer primer [77].

UPCONVERSION

$$f_{RF1} = f_{LO} - f_{IF} \quad f_{RF2} = f_{LO} + f_{IF}$$



DOWNCONVERSION

$$f_{IF} = |f_{LO} - f_{RF}|$$

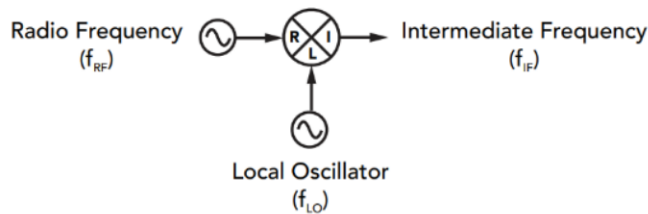
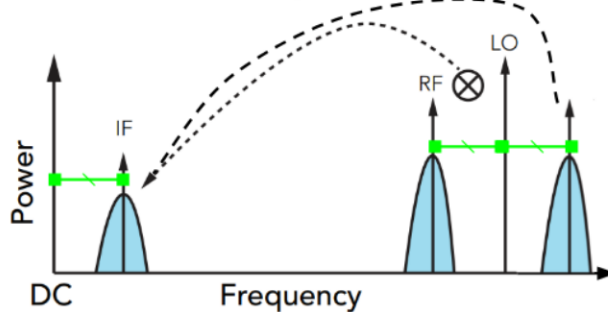


Figure 6.6: Overview of basic mixer operation in both upconversion and downconversion mode. The green lines with hash marks represent the IF frequency. Image modified from Marki Microwave's mixer primer [77].

2097 6.2.1.1 The superheterodyne receiver

2098 The presence of both a sum and difference frequency in Eq. 6.1 creates a challenge when
2099 employing mixers. A mixer performing downconversion will present both the sum-frequency
2100 and difference-frequency at its IF port (see Eq. 6.1). Usually, one of these signals will be
2101 desirable and will not. The latter is known as an image. Two power spectra illustrating this
2102 situation are shown in Fig. 6.7.

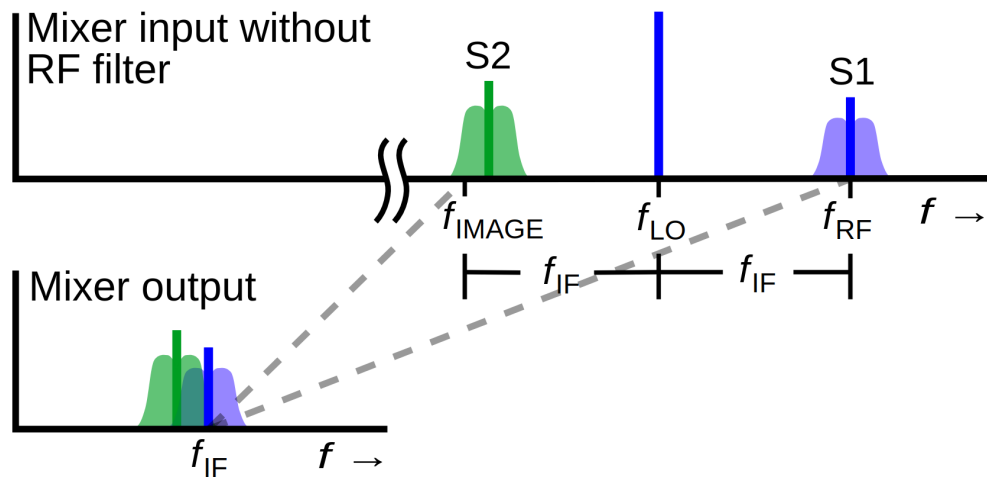


Figure 6.7: Illustration of the problem of images in frequency mixing. Both signals, S_1 and S_2 , are overlapping at the mixer's output as predicted by Eq. 6.1. The image must be filtered *before* mixing to avoid this problem. Figure from Wikipedia[79, 80]

2103 The solution to this image problem is to filter the image out of the RF before mixing.
2104 Furthermore, in a realistic mixer, the LO will bleed through to the IF port and will also
2105 need to be filtered. These points motivate including both an RF and IF filter in the design
2106 of a mixer-based receiver system (sometimes known as a superheterodyne receiver). The
2107 schematic of this type of system is shown in Fig. 6.8. Figure 6.9 shows the spectra after
2108 filtering the RF and IF; the signal S_1 is available for further processing at the desired

2109 frequency.

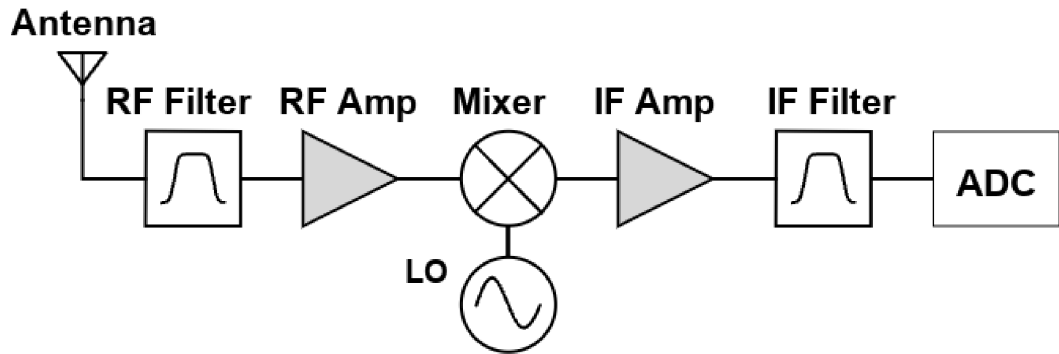


Figure 6.8: Schematic of a basic superheterodyne receiver system. The introduction of the RF filter before the mixer removes the image. Power spectra at various points are shown in Fig. 6.9. This figure is based on one from Wikipedia[79]

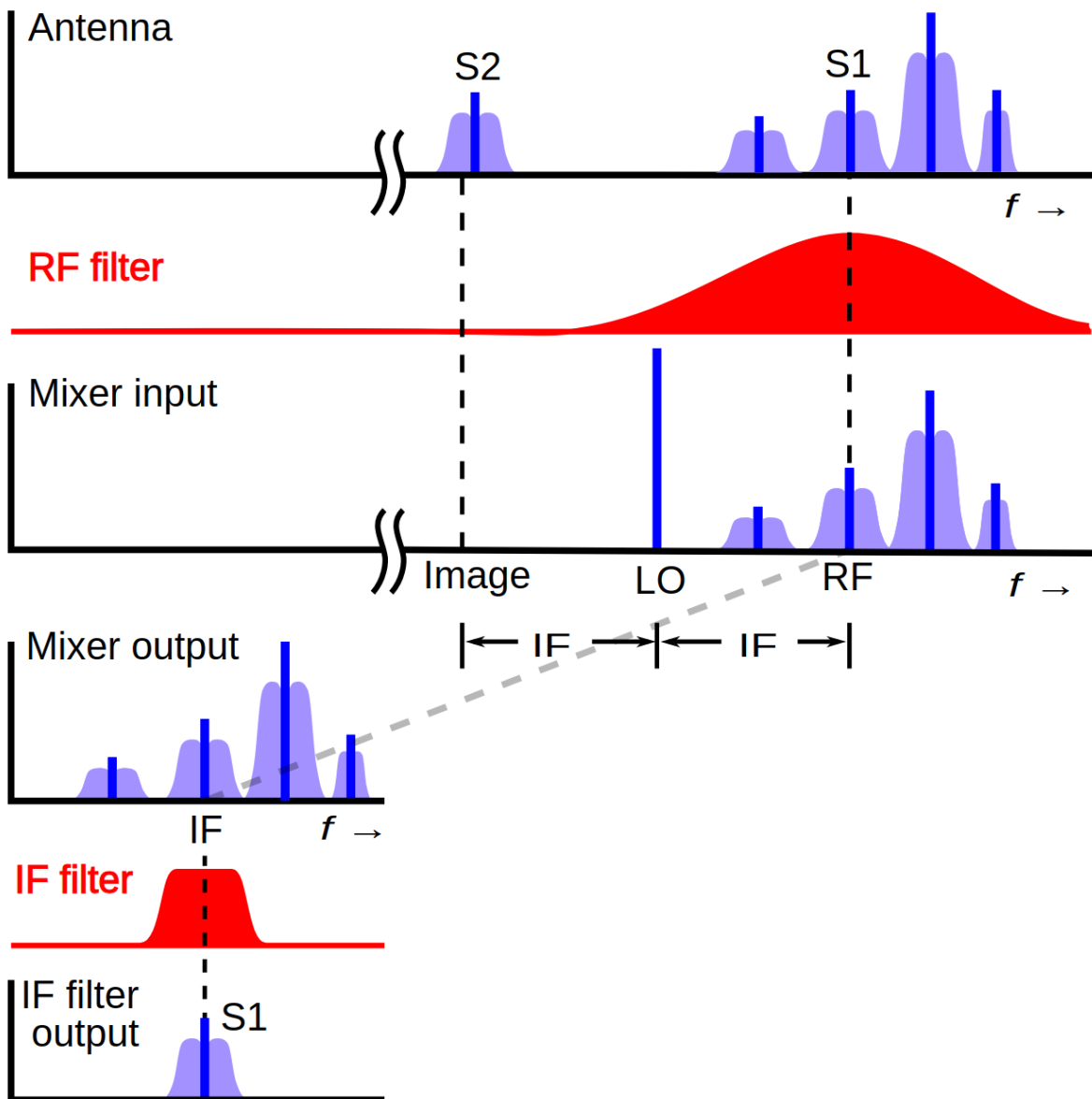


Figure 6.9: Power spectra along various points of a superheterodyne receiver, shown schematically in Fig. 6.8. The introduction of the RF filter before the mixer removes the image. The IF filter separates interfering signals that were near S_1 . This is an example of low-side injection down conversion, as described in the text of this subsection. Image from Wikipedia[79, 81]

2110 6.2.2 Design requirements

2111 The maximum sampling rate of the ADC (2.5 GHz) sets a limit as to how high of frequencies
2112 it can directly sample. Introducing a mixer system between the front end of the experiment
2113 (antenna/low noise amplifier) and the DAQ (ADC/GPU/PC) allows for previously inacces-
2114 sible frequencies to be mixed down into the so-called *baseband* of the ADC, $\lesssim 1$ GHz. The
2115 block diagram of such a system is shown in Fig. 6.10.

2116 The ability to control the mixer system via software greatly boosts efficiency since it
2117 means the experiment can be set up and stepped through a large frequency span (several
2118 GHz) without human intervention. The span of the wideband RF spectrum will be limited by
2119 the hardware of the front end, e.g. antenna and low noise amplifier (LNA). The bandwidth of
2120 the baseband (1.25 GHz) sets the maximum span that may be scanned at each step, though
2121 to reduce the data transfer rate, a smaller span closer to 500 MHz will likely be used for Run
2122 2.

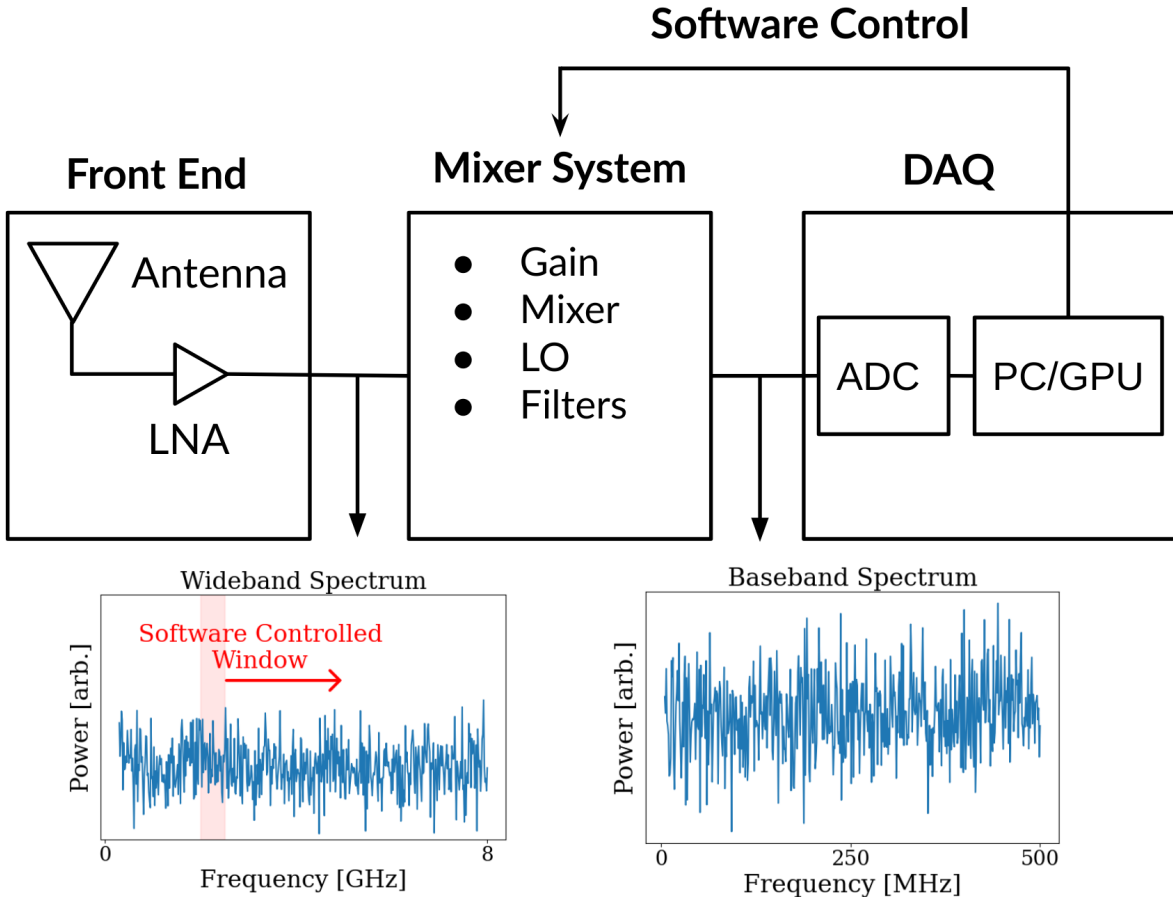


Figure 6.10: Block diagram of the mixer system to be used in Run 2. The PC provides control of the mixer system to sweep the frequency span (shown as a red box on the wideband spectrum) that is mixed down to the baseband and digitized. Frequencies are based on Run 2A, but are nominal and shown only for illustration. The two plots in this figure are only for illustration, but are analogous to the first and sixth subplots respectively in Figs. 6.13 and 6.14.

2123 6.2.3 The Dual-conversion superheterodyne receiver ⁶

2124 Allowing wideband (~ 8 GHz) RF into the mixer means the IF will be a sum of two frequency
 2125 bands (see Eq. 6.1 and Fig. 6.7). This could be avoided with the use of a narrow RF filter.

⁶Code for this section can be found at: <https://github.com/josephmlev/darkRadio/tree/master/daqAnalysisAndExperiments/mixerSystem/simFreqResponse/simFreqResponse.ipynb>

2126 However, this filter would need to be changed at each ~ 500 MHz span. The requirement
2127 that the system be software-controlled is non-trivial in light of the image problem.

2128 One simple solution that was explored is to use a bank of RF filters and a pair of coax RF
2129 switches. Assuming a 500 MHz baseband, a 1-8 GHz run would require 14 RF filters. This is
2130 impractical due to the high cost of high channel-count switches (two would be required) and
2131 the limited frequency span of these switches. A 16-channel switch is $\sim \$3,000$, and has a
2132 maximum frequency of 8 GHz, limiting the utility of this setup. Additionally, many of these
2133 filters would need to be custom, further adding to the cost.

2134 An elegant solution⁷ is the dual conversion superheterodyne receiver (DCSHR). In this
2135 configuration, the RF frequency band is mixed twice before being output as a final inter-
2136 mediate frequency to be digitized (IF2). The first mixer (M1) mixes the RF to a fixed IF
2137 frequency span (IF1), set by a fixed IF1 filter⁸. This mixer is controlled by an LO (LO1)
2138 with a software-controllable frequency. LO1 is set such that the desired RF frequency span
2139 will be mixed to the pass band of the IF1 filter. After this, the rest of the system looks
2140 just like the superheterodyne receiver of Sec. 6.2.1.1. The fixed, band-limited IF1 is simply
2141 mixed to IF2 (also known as baseband). In this case, $\sim 100\text{-}600$ MHz, set by the ADC. This
2142 second conversion step can be either low-side or high-side injection.

2143 A schematic of a simple DCSHR is shown in Fig. 6.11. A cartoon illustrating the operation
2144 of the first mixer stage of a DCSHR is shown in Fig. ?? Simulations⁹ of the system response

⁷Thank you to Greg Wright for suggesting this.

⁸This first mixing stage can be either an upconverter, a downconverter, or even a nonconverter. The only requirement is to mix RF such it lands in the span of the IF1 band-pass filter. A simple way to conceptualize the first mixer stage is that it simply moves where the IF1 filter's span lands on RF.

⁹Code for this section can be found at: <https://github.com/josephmlev/darkRadio/tree/master/daqAnalysisAndExperiments/mixerSystem/simFreqResponse/simFreqResponse.ipynb>

2145 at various points along the signal path are shown in Figs. 6.13 and 6.14. These simulations
2146 assume the filters specified for Run 2A. This system will be specified in more detail in
2147 Sec. 6.2.3.1 and in Tab. 6.3.

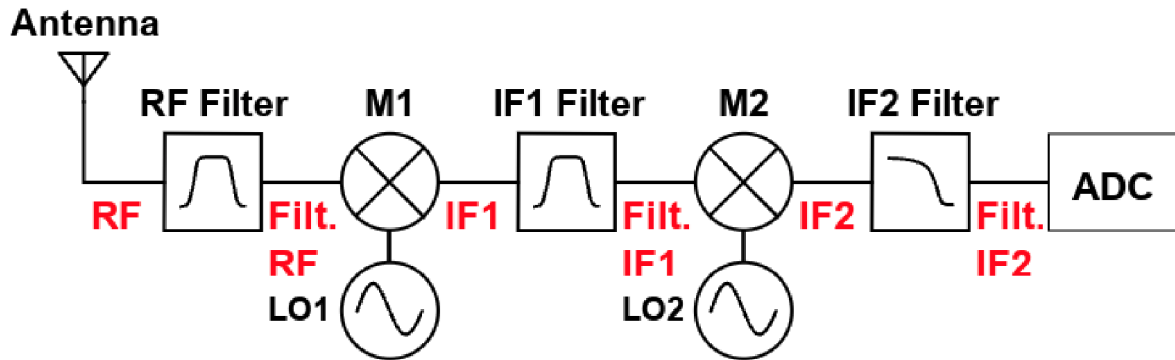


Figure 6.11: Schematic of a simple dual conversion superheterodyne receiver (DCSHR).
Text in red indicates the location of each subplot in Figs. 6.13 and 6.14.

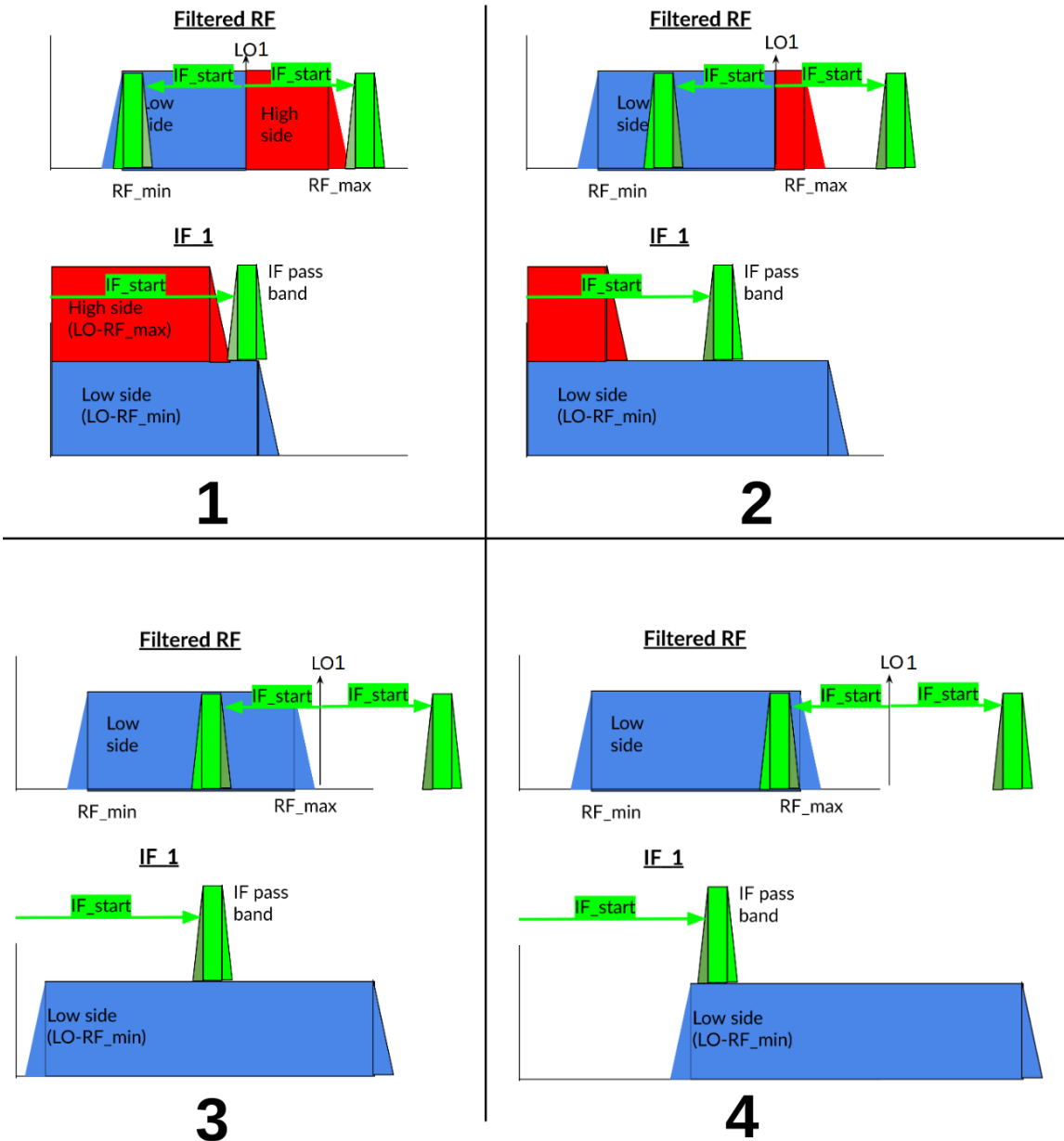


Figure 6.12: Cartoon illustrating the first mixer stage of dual conversion superheterodyne receiver system. Figures 6.13 and 6.14 are more detailed simulations than the cartoon shown here. The four panels represent four different frequency steps of LO1. Panel 1 corresponds to the first step of this LO1 (Fig. 6.13) and panel 3 to the last step (Fig. 6.14). Similar to Figs. 6.13 and 6.14, the low and high side RF are shown separately in the IF1 band (red and blue, respectively). Since Run 2A operates in high-side injection mode, the RF below the LO is useful. Note the dark green on the low-frequency side of the IF filter response. This is not a physical effect and is shown only to illustrate how frequencies appear to mirror when using low-side injection.

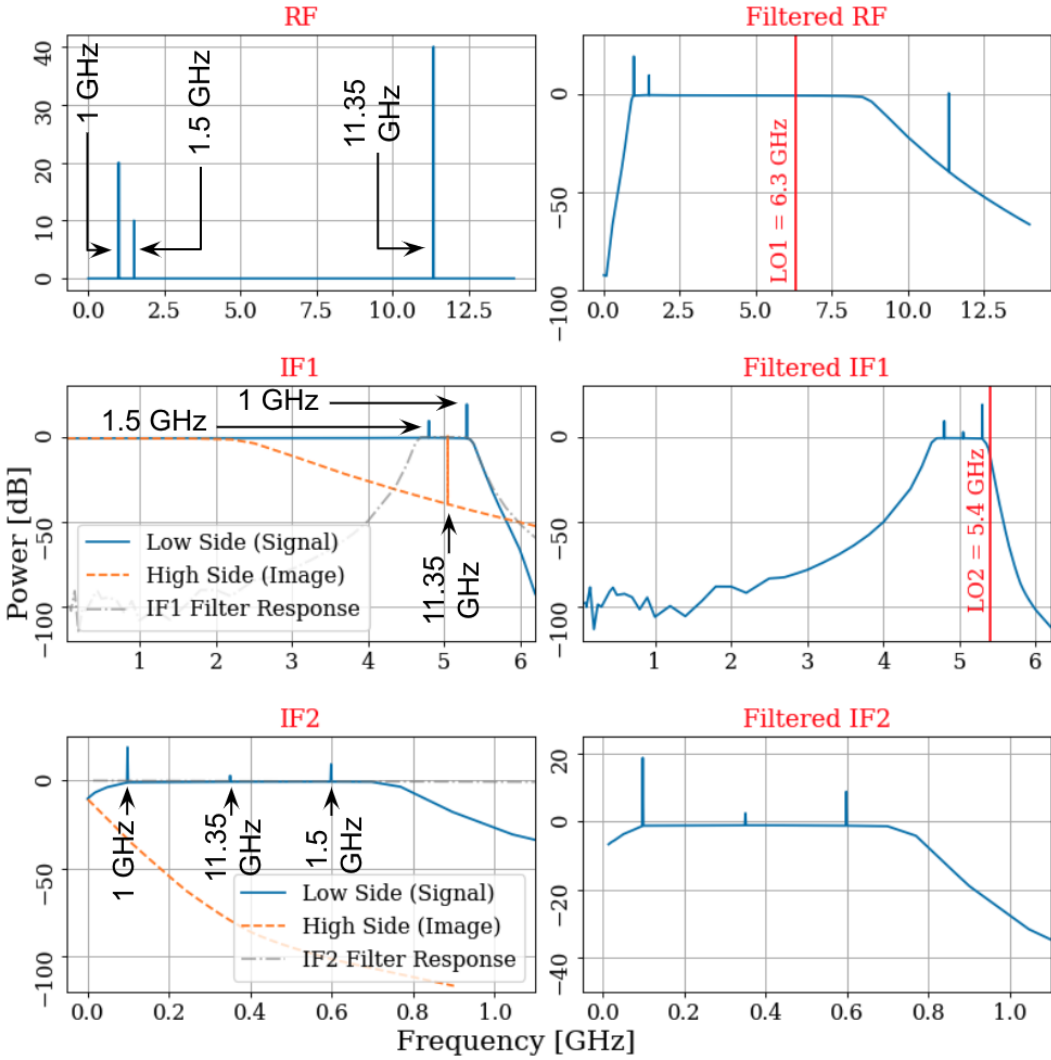


Figure 6.13: Simulated frequency response of dual conversion superheterodyne receiver (DCSHR) with signals around 1 GHz, the lowest frequencies of Run 2A. The input RF is the mean of broadband noise (truncated at 14 GHz), plus three coherent signals; two signals at 1 and 1.5 GHz simulate real signals, while one at 11.35 GHz simulates an image. All three of these signals will mix to the 4.7–5.3 GHz pass band of the IF1 filter in the Run 2A DCSHR. Each panel shows the spectrum at the points indicated in the red text along Fig. 6.11. LO1 is set to 6.3 GHz, the approximate lowest setting that will be used in Run 2A. The labels and arrows indicate the original frequency of the signal before mixing. The RF and IF1 filter response functions are taken from manufacturer data sheets from the filters in the Run 2A system described in Tab. 6.3. For other frequency steps in this run, LO2 remains fixed at 5.4 GHz while LO1 steps in frequency.

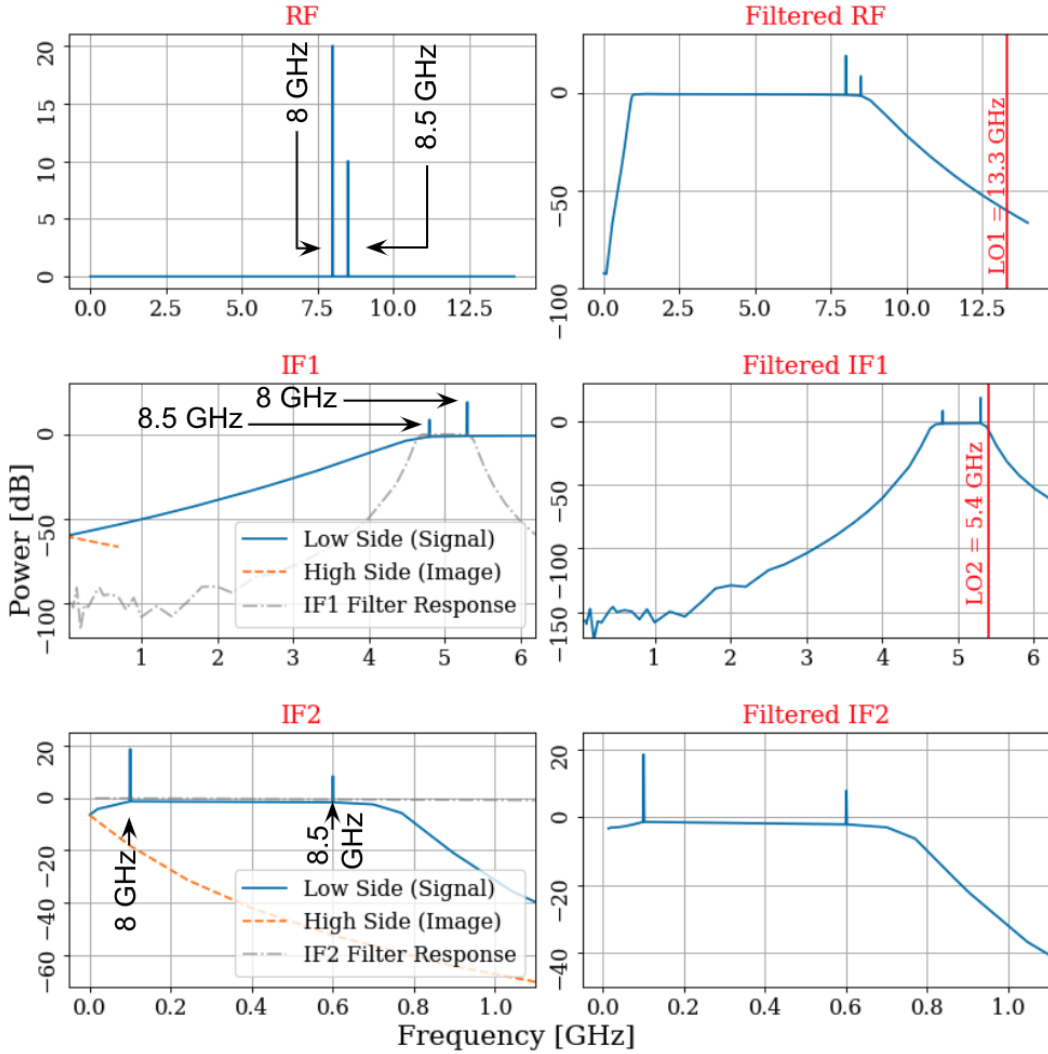


Figure 6.14: Simulated frequency response of dual conversion superheterodyne receiver (DCSHR) with signals around 8 GHz, the highest frequencies of Run 2A. The input RF is the mean of broadband noise (truncated at 14 GHz), plus two coherent signals at 8 and 8.5 GHz. The image signal would have been around 21.5 GHz, but is not shown here since it is so far out of band of the RF filter and LNA. Both of these signals will mix to the 4.7-5.3 GHz pass band of the IF1 filter in the Run 2A DCSHR. Each panel shows the spectrum at the points indicated in the red text along Fig. 6.11. LO1 is set to 13.3 GHz, the approximate highest setting that will be used in Run 2A. The labels and arrows indicate the original frequency of each signal before mixing. The RF and IF1 filter response functions are taken from manufacturer data sheets from the filters in the Run 2A system described in Tab. 6.3. For other frequency steps in this run, LO2 remains fixed at 5.4 GHz while LO1 steps in frequency.

2148 **6.2.3.1 Run 2A mixer system design**

2149 The Run 2A DCSHR was constructed and tested using the schematic shown in Fig. 6.15.
2150 The testing demonstrated proof of concept but was not comprehensive. An 18 GHz spectrum
2151 analyzer was used to monitor the signal path as various signals progressed through the
2152 system¹⁰. LO bleed (after both mixers) and inter-modulation products (after M2) were
2153 measured at expected frequencies and amplitudes. Further testing is required before using
2154 the system for a science run. An important test will be to terminate the input of the
2155 system in order to integrate several days of noise using the Teledyne GPU-based spectrum
2156 analyzer (see Sec. 2.5.7). In this test, LO1 should step through the list of frequencies that
2157 it will use for Run 2A. This will confirm that the standard deviation of the thermal noise
2158 averages down following the Dicke radiometer equation, Eq. 2.16. This is the test depicted
2159 in Fig. 4.16. In addition, these spectra should be searched for candidates using the Run 2A
2160 analysis pipeline. Furthermore, by adding some attenuation with loss L (in dB) before M1,
2161 any signals introduced after this attenuation will have a higher signal-to-noise ratio and will
2162 be detected in less real-time than would be required otherwise.

¹⁰Both the spectrum analyzer and signal generator were loaned from Paul Stucky

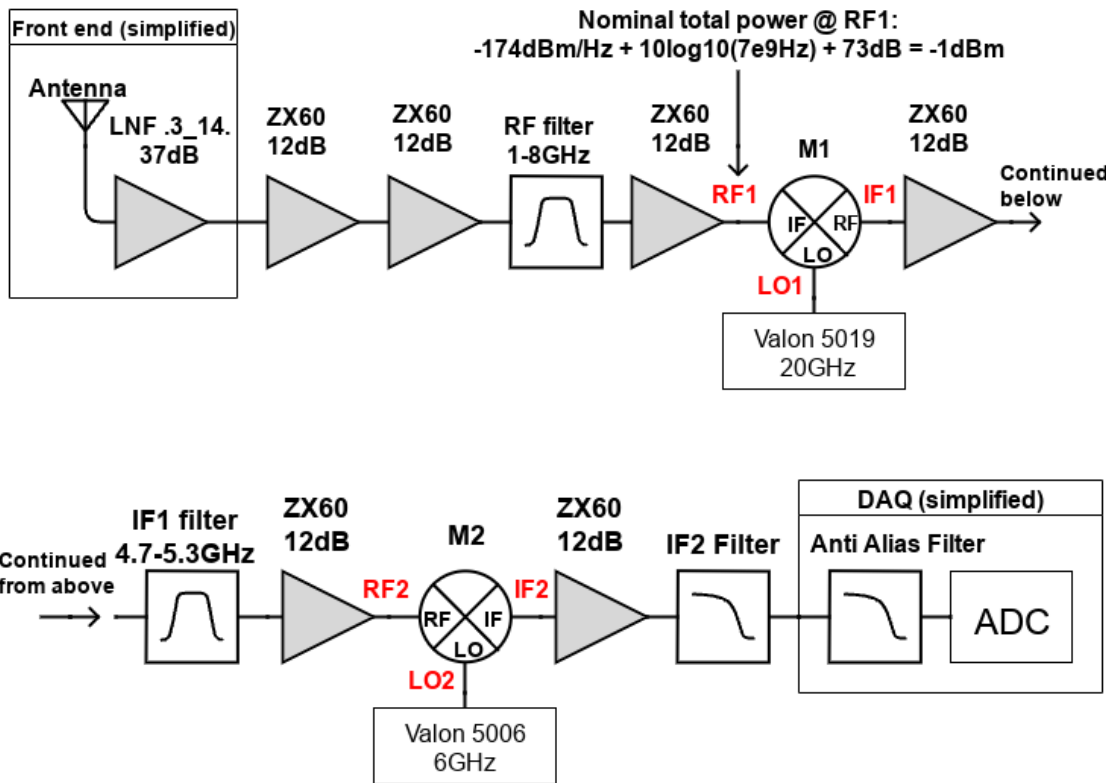


Figure 6.15: Schematic of Run 2A dual conversion superheterodyne receiver. See Tab. 6.3 for specific part numbers. The system was tested as shown here, but additional tweaks (such as adding a few small attenuators) may be necessary. The text in red labels the signal at each point so it can be related to other figures in this section. Note, however that M1 is intentionally connected “backwards”, where RF1 enters the IF port.

Function	Part name	Passband [GHz]	Comments
General amp, 12dB	MC ZX60-14012L+	0.003 – 14.0	
RF filter, LPF	MC ZLSS-8G-S+	< 8.0	
RF filter, HPF	MC SHP-1000+	> 1.0	Only rated up to 3 GHz. Tested up to 6 GHz. Requires test at 8 GHz.
Amp before M1, 17-23dB	ZX60-83LN12+	0.5 – 8.0	Not used, but we have one. Could replace two ZX60-14012L+.
Mixer 1	Miteq TB0440LW1	0.5 – 20.0	RF1 signal enters IF port. See schematic 6.15. Borrow from Paul Stucky.
LO 1	Valon 5019	0 – 20.0	
IF1 filter	MC ZVBP-5G-S+	4.7 – 5.3	
IF1 isolator	Teledyne T-5S83T-1C	4.7 – 12.3	Not used, but we have one. It would go directly before M2.
Mixer 2	Marki M1-0218LP	2.0 – 18.0	We have an extra.
LO 1	Valon 5009A		
IF2 filter	MC VLFX-1350+	< 1.35	
Digital step attenuator	ZSAT-31R5+	0.01–1.0	Optional. Compensate for gain variations upstream of DAQ.
Limiter	MC VLM-52-S+	0.01 – 0.5	Optional. Protection for the ADC. Untested.
Antialias filter	MC ZX75LP-470-S+	DC – 0.510	Extra rejection of high frequencies.
Power split	MC ZFRSC-183-S+	DC – 18	Used only for test setup.
Noise source	NoiseCom NC4563	0.01 – 12.4	Used only for test setup.

Table 6.3: Dual Conversion Mixer System Components, as shown in schematic, Fig. 6.15. Mini-Circuits is abbreviated “MC”.

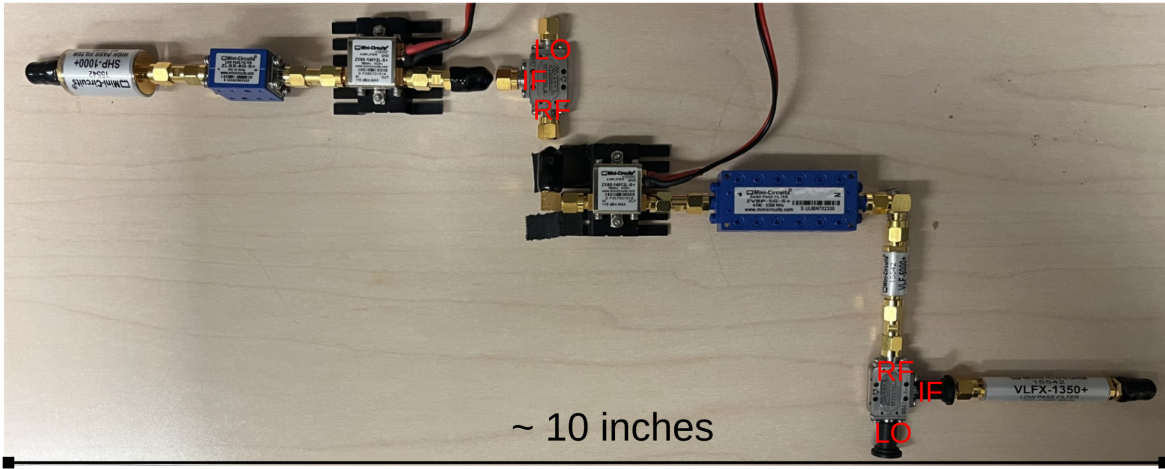


Figure 6.16: Picture of the (partially assembled) dual-conversion mixer system. Mixer 1 (M1) is a Miteq TB0440LW1, but is on loan from Paul Stucky in the UCD Chemistry department, so an extra Marki M1-0218LP is used as a placeholder. Note that M1 is connected “backwards”; the RF goes into the IF port and the IF emerges from the RF port. This configuration allows for M1 to accept frequencies as low as 500 MHz for the first conversion step.

2163 6.2.3.2 Additional considerations

2164 This sub-subsection lists a few design points considered during the design phase of the mixer

2165 system. Hopefully, it clarifies some design choices.

2166 **RF port as a source of the $2L \times 1R$ image spur** The Marki mixer primer [77] raises

2167 the point that the RF port of a real mixer will source a $2L \times 1R$ image spur. If this spur

2168 is out of the pass band of the RF filter, it will reflect off the filer, mix with the LO and

2169 downconvert to the desired difference frequency. To mitigate this, amplifiers were placed

2170 on either side of M1 and an isolator was selected for the input of M2. This spur was not

2171 measured without using the isolator, so it is labeled “optional” in Tab. 6.3.

2172 **Integrated noise power** When dealing with wideband noise, the total power in a given
2173 bandwidth must be considered to prevent clipping at each stage of a signal chain (see
2174 Sec. 2.5.4.4). On the other hand, the $\sim 13 \text{ dBm}$ LO power, along with the finite LO-
2175 IF¹¹ isolation of M1 means that a healthy signal level is required to keep the signal-to-noise
2176 ratio high.¹² This motivates adding gain throughout the system.¹³ The amount of re-
2177 quired gain changes drastically when going through the IF1 filter since the bandwidth is
2178 reduced from $\sim 7 \text{ GHz}$ to $\sim 0.6 \text{ GHz}$. Assuming a flat power spectral density, this requires
2179 $10\log_{10}(7 \text{ GHz}/0.6 \text{ GHz}) \sim 10.7 \text{ dB}$ of make-up gain to achieve the same total-integrated
2180 power as before the filter.

2181 **Extra IF1 filter** A secondary low-pass filter in the IF1 filer section may be required
2182 because the IF1 band-pass filter is not rated above 12GHz, and testing it requires borrowed
2183 gear. Testing did not show this to be an issue.

2184 **RF filter** The RF low-pass filter (SHP-1000) is only rated to 3 GHz. It was unit-tested up
2185 to 6 GHz, and 8 GHz signals made it through the assembled DCSHR with minimal attenua-
2186 tion, but this filter should be unit-tested up to 8 GHz when high-frequency test equipment
2187 is available.

¹¹Remember, M1 is “backward”, so the relevant specification here is labeled LO-RF isolation, listed as between 20 and 30 dB between 6 and 13 GHz on the data sheet[82].

¹²If we are being literal, we actually want a high noise-to-signal ratio. The experiment gives noise (which may contain a small, burred signal), and it is the coherent LO that is contaminating this noise. One person’s noise is another’s signal.

¹³In practice, gain comes quantized in 12 dB amplifiers, so attenuators may be needed to get precisely the correct amount.

2188 **Intermodulation spurs** Intermodulation spurs occur because of the non-linear behavior
2189 of the mixer[77]. They can be either single-tone or multi-tone. In the case of the former,
2190 a single tone enters the mixer and the spurs are computed using the power and frequencies
2191 of this tone along with that of the LO. In the case of the latter, multiple signals enter and
2192 all of them, along with the LO, are used to compute the spurs. Balanced mixers attempt
2193 to reduce the impacts of these effects, but they still occur to some degree. In the case of
2194 the Run 2 DCSHR, both single- and multi-tone intermodulation spurs must be considered.
2195 Neither appears to pose a major issue as will be discussed in the following paragraphs.

2196 The spectrum that the system is expected to process is mostly broadband noise. This
2197 noise can be viewed at many tones, all of which will cause multi-tone intermodulation spurs
2198 with each other. Since there is a dense sea of tones, the spurs will be equally dense, creating
2199 a new broadband noise floor. However, all of these tones are of random amplitude and
2200 phase, so their spurs are as well. This noise floor will average down in the same way that
2201 the amplified thermal noise of the experiment will. The effect is another noise floor, which is
2202 10s of dB below the primary thermal noise and is irrelevant. This is a similar consideration
2203 to the ADC noise of Sec. 2.1.5.2.

2204 Single-tone intermodulation distortion must be considered with a bit more care. LO1
2205 will be present in IF1. In the first frequency step of Run 2A, LO1 will be set to 6.3 GHz.
2206 The IF1 filter has a response of -60 dB at 6.3 GHz. M1 has a LO-RF isolation of -20 dB
2207 and requires an LO power around +10 dBm. After including the two 12 dB amplifiers, LO1
2208 will be present in the filtered IF1 at about -46dBm at the input of M2 (see Fig. 6.15).
2209 This signal will create single-tone intermodulation spurs in M2 with LO2. These spurs can

2210 easily be computed. Marki Microwave has a very nice graphic calculator, which was used to
 2211 generate the figure shown in Fig. 6.17. It turns out the only “intermodulation spur” that is
 2212 significant is the -1×1 spur; in other words, the normal image! At the first frequency step
 2213 (LO1 = 6.3 GHz), this image will appear at 1GHz in IF2¹⁴.

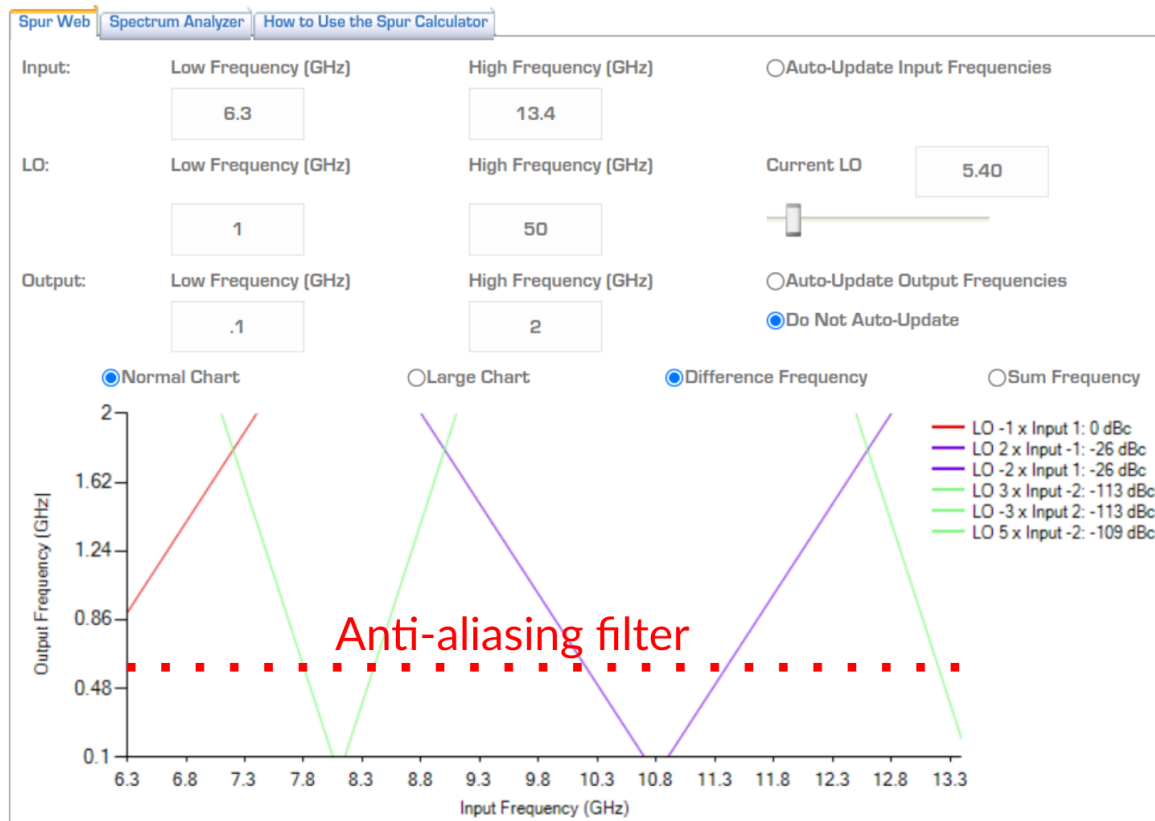


Figure 6.17: Spur web, calculated using Marki Microwave’s online calculator[83]. This shows that the only

2214 As previously calculated, LO1 will be about -46 dBm at the input of M2. The total
 2215 integrated noise power at this point (excluding the LO1 bleed) will be about -18 dBm¹⁵,
 2216 or about -66 dBm per 150 Hz (set by the ADC; 1.25 GHz sample rate and 2^{23} point FFT).

¹⁴Remember, LO2 is always 5.3 GHz.

¹⁵taking into account the 10 dB of IF-RF loss from M1

2217 While the LO1 image will be significant and immediately detectable (without averaging) on
2218 this background, it is still a small fraction of the total integrated power and won't cause any
2219 amplifiers or mixers to clip.

2220 Assuming the ADC samples at 1250 MHz, this 1 GHz image will alias to 375 MHz; right
2221 in the analysis span. An anti-aliasing filter will be required to reduce the 1 GHz image. The
2222 anti-aliasing filter specified in Tab. 6.3 attenuates 1 GHz by 65 dB. Therefore, after filtering,
2223 the aliased image will be about 45 dB below the background power density (again, assuming
2224 150 Hz bins). According to Eq. 2.16, this will be detectable in $\sim 10^9$ averages, or about
2225 77 days (for 1.25 GHz sample rate and a 2^{23} point FFT). Again, reducing the noise power
2226 introduced into the DCSHR through attenuation will cause this signal to become detectable
2227 by averaging for less real-time, and will be a useful troubleshooting step. In this test, the
2228 image should appear as predicted without waiting two months.

2229 The image introduced here is the most prevalent. Other spurs are both lower in amplitude
2230 (see Fig. 6.17) and will be reduced by nearly 100 dB by the IF1 filter.

2231 **DCSHR for veto channel** If the use of a veto system is required going forward, it will
2232 require a similar DCSHR system. Ideally, it should be an identical system to the main
2233 channel. This may not be possible due to budget, or the unavailability of sourcing a second
2234 Miteq TB0440LW1 mixer. One possible workaround is to use a coax switch and alternate
2235 between scans of the veto and experiment. This has the obvious disadvantage of loss of
2236 ability to correlate the experiment to possible RFI on the veto channel. However, RFI tends
2237 to be persistent, and this is likely not a major issue. Another solution is choosing another

2238 mixer. Marki T3H-20G mixers are a good choice. However, they have large unit-to-unit
2239 variation and may not offer enough LO-RF isolation.

2240 **6.2.3.3 Comments on Run 2B**

2241 While the exact system for the 8-14 GHz Run 2B will not be specified here, a careful reading
2242 of Sec.6.2 should be adequate preparation for the design of this system.

2243 **Selection of RF filter** A new RF filter will be required with a pass band of 8-14 GHz.
2244 Note that this 14 GHz restriction is set by the low noise amplifier (LNA)[84]. This LNA is
2245 rated up to 16 GHz, though the gain drops by 6 dB between 14 and 16 GHz. In other words,
2246 this 14 GHz limit is soft, and Run 2B could push up to 16 GHz with some care.

2247 **Change first mixer to low-side injection** The LO1 source is a Valon 5019 synthesizer[85], with a maximum output frequency of 20 GHz. The final LO1 setting of Run 2A
2249 will be around 13.3 GHz. By continuing with high-side injection (defined in Eq. 6.2), the
2250 highest RF frequency that can be mixed to the IF1 filter's passband (4.7-5.3 GHz) by a
2251 20 GHz LO1 is 15.3 GHz. If Run 2B (or a run beyond this that uses a similar DCSHR)
2252 pushes beyond an RF frequency of 15.3 GHz, M1 will need to operate in low-side injection
2253 mode.

2254 **Send RF to the RF port of M1** Run 2A sends the RF to the IF port of M1 (see
2255 Fig. 6.15). M1[82] has about 5 dB better LO-IF isolation than LO-RF isolation. Run 2B

2256 begins around 8 GHz, which will allow the RF to enter the RF port of M1. This configuration
2257 will offer better isolation between LO1 and the following signal path stages.

2258 **6.3 Possible Future Upgrades**

2259 The previous sections in this chapter addressed the progress towards the planned Run 1B
2260 (Sec. 6.1) and Runs 2A/B (Sec. 6.2). This section gives an outline for experiments beyond
2261 this. This section will be rather vague compared to the previous sections of this chapter. If
2262 those sections were a road map, this section is verbal instructions providing general direc-
2263 tions.

2264 **6.3.1 Detector design principles to maximize the signal-to-noise**

2265 **ratio**

2266 Chapter 2 began with a quote by Veljko Radeka [5] that claimed an optimal detector must
2267 have three components:

- 2268 1. The detector design must maximize the signal
- 2269 2. Noise must be reduced at its physical source
- 2270 3. The signal and noise must be optimally filtered

2271 The common thread is the improvement of the signal-to-noise ratio. The considerations
2272 are as true today as they were in 1974.

2273 **6.3.1.1 Maximize the signal**

2274 There are a few ways to ensure that the signal emerging from the detector is maximized. The
2275 traditional approach has been to use a highly resonant cavity. See, for example ADMX [7]
2276 or HAYSTAC [33]. To push to lower masses with wavelengths larger than practical cavities,
2277 lumped element detectors use electronic resonant circuits in place of resonant cavities to
2278 achieve a similar effect. See DMRadio [8, 76, 86] and ABRACADABRA [87].

2279 While these experiments have very high Q, they are only sensitive at a single frequency
2280 which must be scanned. The dark E-field radio (DER) technique differs in that it is broad-
2281 band; many frequencies are scanned simultaneously by taking a Fourier transform. At higher
2282 mass, a smaller reverb chamber can be employed, as long as the frequency of interest remains
2283 above the lowest usable frequency (defined in Sec. 2.4.2).

2284 A careful analysis of scan rates to reach a given sensitivity of ϵ for the DER technique
2285 compared to single-resonance experiments should be performed before attempting to over-
2286 come the difficulties of a DER-like experiment above ~ 20 GHz.

2287 **6.3.1.2 Reduce noise**

2288 The DER experiment operates at room temperature, using a low noise amplifier (LNA).
2289 Compared to cryogenic experiments, this represents an advantage in terms of reduced ex-
2290 perimental complexity, but it means the dominant background is classical thermal noise
2291 (~ 300 K, Sec. 2.1.1), followed closely by amplifier noise (~ 100 K, Sec. 2.1.4). These noises
2292 add to form the total system temperature $T_s \approx 400$ K. However, the limit in sensitivity scales

2293 with $T_s^{-1/2}$ (at least in the classical regime, $h\nu \ll k_b T$). For this reason, most haloscope
2294 experiments choose to forgo experimental simplicity and operate at extremely cold temper-
2295 atures (100s of mK, sometimes lower). At these temperatures, quantum effects begin to
2296 dominate the noise budget and simple linear amplifiers must be replaced by read-out tech-
2297 nologies such as superconducting quantum interference devices (SQUIDs) or single photon
2298 counting. If a cold detector is used, more complex amplification must also be employed or
2299 the noise budget will be dominated by the readout.

2300 **6.3.1.3 Filtering**

2301 Section 4.2.3 introduced signal-matched filtering as the optimal filtering for a dark photon
2302 of known lineshape, discussed in Sec. 2.1.2. This will be an important consideration going
2303 forward, but will not change much.

2304 However, there is an additional filter that has the potential to improve the sensitivity
2305 of Run 1A as well as any future runs. Assuming that the dark photons are uniformly
2306 polarized, the power received by a linearly polarized antenna will be modulated by the
2307 rotation of the earth. The time series¹⁶ of each frequency bin can be searched for modulation
2308 by $\alpha \cos^2(12\text{hr} \times t)$, where α is a dimensionless parameter that depends on the geometry of
2309 the antenna relative to the rotation of the earth. Many useful ideas for this calculation
2310 are presented in [74], however, the idea in this paper is simply to set up the experiment to
2311 maximize the signal, not search for modulations on existing data. As far as I know, this

¹⁶The time series will have temporal resolution set by the pre-averaging defined in Sec. 2.5.7; several minutes. Remember, the RF time series samples are not saved.

2312 analysis idea is original and was independently arrived at by both myself and Brian Kolner
2313 (a co-author on [25]).

2314 **6.4 Leveraging Axion experiments for Dark Photon**
2315 **searches**

2316 Axions (introduced in Sec. 1.3.1.1), are an ultra-light dark matter candidate similar to dark
2317 photons. They require a magnetic field to convert into standard photons, but they are
2318 detected using techniques very similar to dark photons. Axion experiments represent a sig-
2319 nificant investment of resources and frequently do not take full advantage of their sensitivity
2320 to dark photons. This section lists a few methods that can leverage this investment to probe
2321 the dark photon parameter space.

2322 **6.4.1 Reanalysis of axion haloscope data**

2323 A highly efficient dark photon search can be conducted by recognizing that many axion
2324 searches would have been sensitive to dark photons if not for vetos which rely on the state of
2325 an applied magnetic field. SHAFT[88], for example, has two toroids that can generate fields
2326 in opposite directions¹⁷. While the magnetic flux through the pick-up coil from an axion
2327 would flip polarity as the magnetic fields are reversed, the flux from a dark photon would not
2328 (see Fig. 1 of [88]). This differential technique gives a convenient way to veto radio frequency

¹⁷Actually, the field directions flip to all four possible combinations and they have a clever analysis chain to maximize sensitivity.

2329 interference. However, careful inspection of the time dependence of candidates may allow
2330 these signals to be reduced without relying on the magnetic field veto and ruling out dark
2331 photons¹⁸.

2332 This analysis was performed in 2021 [89], but should be revisited.

2333 **6.4.2 Design and operation of axion experiments for dark
2334 photons**

2335 By recognizing that an axion experiment is almost a dark photon experiment, the experiment
2336 can be designed from the beginning to maximize its sensitivity to dark photons. The main
2337 modification is to not veto based on the state of the magnetic field, as pointed out in
2338 Sec. 6.4.1. This comes with the caveat that interfering signals must be mitigated in a different
2339 way. This is likely harder than it sounds. One possible solution is to simply conduct the
2340 experiment in a shielded room, similar to the Dark E-Field Radio Experiment.

¹⁸This is just an example, as DMRadio will not rely on a veto and have much better sensitivity to dark photons in the SHAFT frequency range.

2341 Appendix A

2342 Overview of RTSA code base

2343 A basic overview of the code which are used to acquire and process data are outlined here.

2344 The version control is very simple and each experiment has it's own directory containing

2345 several key files. The general usage template from which other experiments can be developed

2346 is in the `teledyneTemplate` directory. The important files, in order of importance, are

2347 • `settings.py`: Settings are controlled from this file. If the DAQ code isn't to be

2348 modified, this is all the user must interact with in normal usage. While it is a python

2349 script, it functions more like a text file. Descriptions and notes about allowed values

2350 are included as comments. Read them carefully, settings can conflict.

2351 • `drDaq*.py`: Main script which calls all the helper functions. To take data, run this

2352 script after modifying (and saving) `settings.py`. There is usually a suffix indicating

2353 the date and information about version.

2354 • `avgFftModule.py`: This is modified code from teledyne. It handles all the heavy

2355 lifting: Interfacing with the C++ API, pinning GPU memory, transfer of data from
2356 PCIE card to the GPU, computation of the FFT on the GPU. This is all wrapped in
2357 a class called `avgFft`. An instance of this class is called `avgSpec` and is the workhorse
2358 of `drDaq.py`

2359 • `daqHelpers.py`: Lots of helper functions which are separated here to keep other code
2360 clean. It is imported as a module in other files. Lots of useful code lives in here,
2361 including the code that converts time series to power spectra (normalization is non-
2362 trivial, see Eq. 2.15), writes info to `database.txt`, saves the pre-averaged spectra
2363 including metadata in an HDF5 file.

2364 • `plotTesting.py`: This uses `dash` to host a web app which allows interactive `plotly`
2365 graphs for simple visualisation of run data. This is extremely useful as it can tell you
2366 if amplifiers die. Without this, all data would have to be averaged and more fully
2367 analyzed, but this is a good light-weight option. There is some creative use of data
2368 down sampling so it runs quickly while not removing any candidates. An example
2369 window is shown in Fig. A.1.

2370 • `backup.sh`: Simple shell script which backs up run data to locations of your choosing.
2371 In the `teledyneTemplate` directory, it is set up to back up to the secondary hard disk
2372 drive in the DR2 machine, and to peloton, but this can be easily modified. When taking
2373 real data, this script should not be run at the same time as `drDaq.py`. `backup.sh`
2374 should be run first, so it completes while the antenna is moved and batteries changed.
2375 This ensures there is not a heavy load on the hard drive due to back ups while data

2376 acquisition is ongoing. `valonInit.py`: sets up the valon signal generator to work as a
2377 clock. This should probably be a function inside of `daqHelpers.py`, but there may have
2378 been a reason I kept it separate.

2379 • `gdrapi.py` Comes from Teledyne. Defines functions for the api. I have not modified
2380 it at all.

2381 • `helperCupy.py` Comes from Teledyne. Defines functions for the GPU. I have not
2382 modified it at all.

2383 • `streamingHelpers.py` comes from Teledyne. Defines functions for streaming from
2384 PCIE card to GPU. I have not modified it at all.

2385 A Tips for using the RTSA system

2386 • As of September 2024, you must boot into kernel version 5.15.

2387 • Make sure to run `insmod.sh` in the `teledyneInstall/gdrcopy` directory after restart-
2388 ing the machine.

2389 – look at `teledyneInstall/installGuide.txt` on how to handle common errors
2390 involving this process.

2391 • Read through the `settings.txt` file carefully! Some settings will conflict with others,
2392 but they are mostly noted. There are also some notes about possible upgrades which
2393 could be made, some of which without much effort.

2394 **B Data structure and processing**

2395 Figure 2.45 shows the handling of data as it comes in as an RF time series and is converted
2396 to pre-averaged spectra. While significantly less cumbersome than the raw data, processing
2397 these spectra still represents a challenge. This subsection outlines how I have attempted to
2398 handle it. While it is a little convoluted, this is the third iteration of how to handle this
2399 data processing and is likely simpler than it seems on first blush. In other words, there is
2400 probably a better way to do this, but don't knock it til you try it.

2401 **B.1 Writing data**

2402 Once a pre-averaged spectrum is computed by dividing the running sum by `NOF_BUFFERS_TO_RECEIVE`,
2403 this can be written to an HDF5 file. Whether or not it is, can be controlled by the `SAVE_H5`
2404 boolean variable¹. Each pre-averaged spectrum is uniquely specified by `ACQ_NUM` in a given
2405 data run. In order to simplify backups and avoid placing all our eggs in one HDF5 basket,
2406 `NUM_SPEC_PER_FILE`² pre-averaged spectra are saved into a single HDF5 file, before starting
2407 a new file. These files are simply named as a zero-indexed number followed by their `.hdf5`
2408 extension. These files are saved in `SAVE_DIRECTORY`³. I usually make this save directory in
2409 a secondary SSD named `drBiggerBoy` in order to preserve the main drive. I think the stress

¹This variable exists because when testing things or taking miscellaneous measurements, you will frequently want to acquire a single spectrum without engaging the complex machinery of the HDF5 saving procedure.

²I have kept this around 16 and not experimented much outside of this range, but it's probably fine. This keeps the files around 1 GB. For run 1.4, this is about 45 minutes of antenna data and 3 minutes of terminator data per file, so if a file is corrupted it's not a big deal. I have never had a problem, this is paranoia inherited from Ben.

³A reminder that this is specified, like all other variables, in `settings.py`. Note you must create this directory ahead of time and include a sub-directory called `data`. It says this in the comments of `settings.py` which you are reading, right?

2410 of continuous reads and writes will probably kill this drive, so I prefer to keep it separate
2411 from the main boot drive, drBigBoy.

2412 When `SAVE_H5 == 1`, a `database.txt` file is created in `SAVE_DIRECTORY`, shown in Table
2413 A.1.

Attribute	Pre-averaged spectrum 0	Pre-averaged spectrum 1
ACQ_NUM	0	1
DATETIME	2023-05-10 11:32:48.365	2023-05-10 11:35:49.193
SWITCH POS	0	1
ANT POS IDX	0	0
TEMP	295.64	295.54
LEN FFT LOG2	24	24
SAMPLE RATE MHZ	800.0	800.0
NOF BUFFERS	8600	8600
AMP1	1012_E_PbAcid	1012_E_PbAcid
AMP2	ZKL_9p05VReg	ZKL_9p05VReg
LPF	HSP50+	HSP50+
HPF	288S+	288S+
ATTENUATOR	4dB_FIXED	4dB_FIXED
ADC	ADQ32	ADQ32
CLOCK	SRS_VIA_VALON	SRS_VIA_VALON
File Number	0	0

Table A.1: Example database file from run 1.4. In this run, `ACQ_NUM` counts up to 4175, and these spectra are saved between 261 HDF5 files. Some of the values are auto-generated (`temp`, `DATETIME`, etc.) while others are manually entered into `settings.txt` (`AMP1`, `LPF`, etc.) Note that this table has been transposed in order to fit on the page.

2414 When setting up a data run, you must test that the data are saved how you expect. I have
2415 had success by reducing `NOF_BUFFERS_TO_RECEIVE` to a small number⁴, and taking a simu-
2416 lated data run. The process of switching is hacked together and can give you unpredictable

⁴`NOF_BUFFERS_TO_RECEIVE` times the time per buffer must be larger than around 2 seconds or it will crash

2417 results. Did I mention to read the comments in `settings.py`?

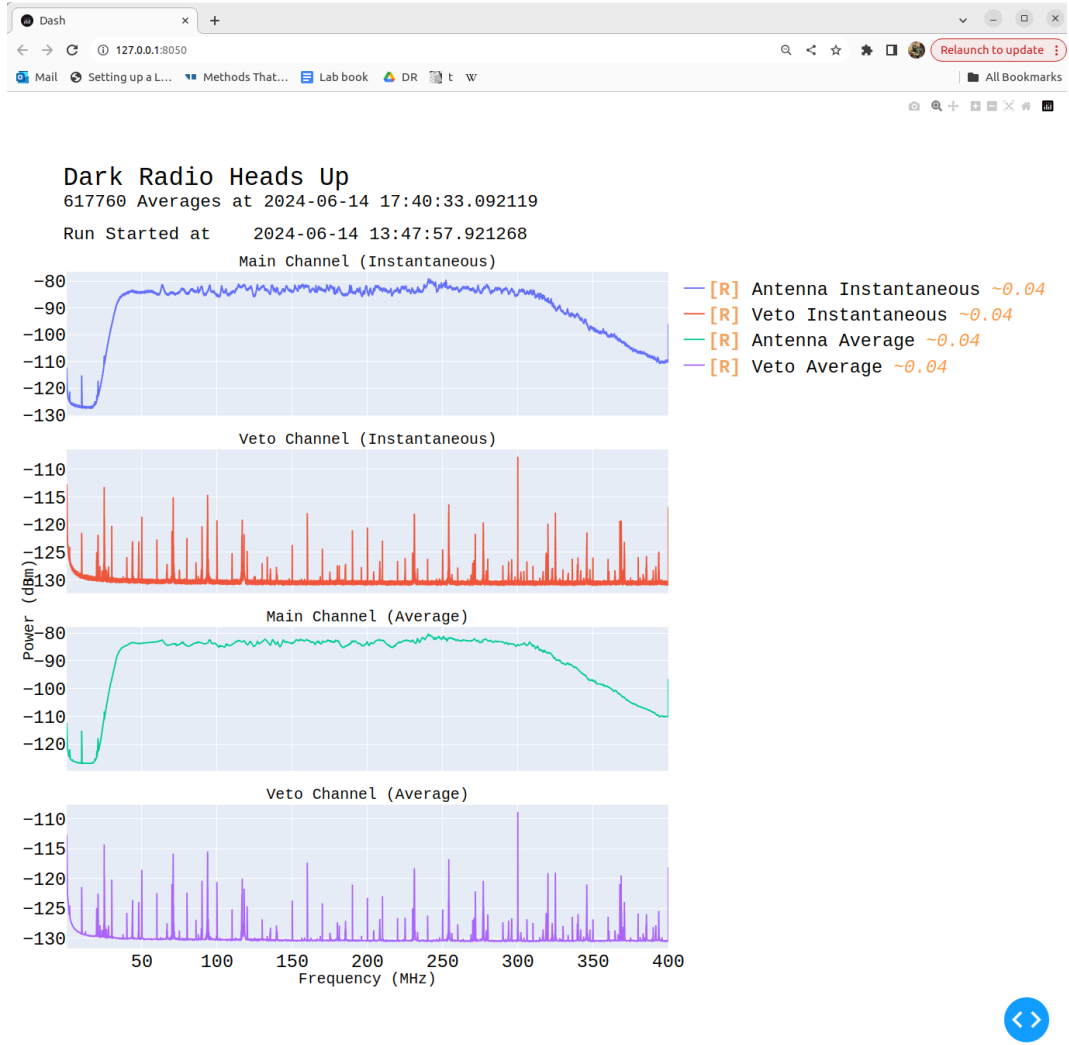


Figure A.1: Real time heads up window for data acquisition. Built with Plotly and Dash, and displays in web browser, in this case Google Chrome. Spectra contain 2^{23} frequency bins, so are down-sampled so as to display 10^4 bins at any given level of zoom. This allows for interaction with the plot in real time with very little lag. The resolution currently displayed (in MHz) is shown in yellow next to the legend (right of first plot). This down-sampling is "smart" in that it will show any excursions, and is implemented with the `plotlyResampler` package in `MinMaxAggregator` mode. Mousing over a curve causes a "Tooltip" to appear, indicating the frequency and power at that point in the curve. The frequency axes are all linked, so zooming on one plot will cause all plots to display the same frequency range. Icons on upper right allow for navigation of plot. Frustratingly there is no back button, so be careful when zooming on a very narrow feature; a wrong move means you have to go all the way back out and start over.

2418 **B.2 Reading and averaging data**⁵

2419 After taking a data run, you should have a `SAVE_DIRECTORY` containing a directory full of
2420 many HDF5 files and a `database.txt` file (and possibly a directory of plotting spectra if
2421 that is chosen in `settings.txt`. The basic idea is to “pre-process” the HDF5 files into a
2422 single, large HDF5 file which can be more quickly accessed to compute a single, averaged
2423 S_o spectrum for further analysis (see next chapter). The `database.txt` file is loaded into
2424 python as a pandas dataframe in order to find specific spectra in this large data structure.

2425 I tried (for a while) to keep the files separate to allow for multi-processing to speed up
2426 the averaging, but I ran into issues. The most serious issue is that all the files live on the
2427 same drive, so you can’t get much of a speed up since the drive is read-limited to around
2428 500 MB/s. I found multiprocessing is more effort than it’s worth. It takes about 20 minutes
2429 to pre-average run 1.4 (9 days of data, 3 minute pre-averages yields 4175 spectra which take
2430 about 280 GB), and you only have to do this once after a run.

2431 Following the example of `run1p4_packAvgAllAnalysis.ipynb`, the first step is to load
2432 `database.txt` as a pandas dataframe which can be used to index the pre-processed file.
2433 Next, a list of which ACQ_NUMs correspond to an antenna and terminator must be computed,
2434 after removing any which are known to be contaminated⁶. The list of indices which are
2435 to be averaged together is called either `antIdx` or `termIdx`. Note that you can devise any
2436 number of ways to generate these lists, or even hard code them. The code given is just an

⁵Code for this section can be found at: https://github.com/josephmlev/darkRadio/tree/master/daqAnalysisAndExperiments/run1p4/run1p4_analysis/run1p4_packAvgAllAnalysis.ipynb

⁶In run 1.4, the first antenna and terminator spectra are thrown out, since the computer monitor was on to verify the run started successfully. This was out of paranoia and probably didn’t do anything.

2437 example.

2438 Next, info in the dataframe (no power spectra data yet) are analyzed as a sanity check.

2439 These are not super important but a good check.

2440 The cell beginning with the comment `#pack pre proc dataset` is where the heavy lifting

2441 happens. A large HDF5 file is initialized. It contains two datasets, one for each channel

2442 (main experiment and veto in run 1.4). Note that in this example, it is hard coded to expect

2443 8388609 frequency bins ($2^{23} + 1$), and this must be changed if doing something other than a

2444 2^{24} -point FFT. The HDF5 sub-files are iterated over, their data is read, and written into the

2445 pre-processed HDF5 file. Make sure not to remove the error handling for closing the HDF5

2446 file, or you will corrupt it and have to rerun the pre-processing.

2447 Now that the pre-processed HDF5 file has been packed with data and a list of indices

2448 to be averaged has been generated, averaging is trivial (though still takes a few minutes, so

2449 maybe test it with a sub set of `antIdx`. The code is provided below:

```
2450
2451 def avgSpecFromPacked(avgIdxs, specStr):
2452     sum = np.zeros(2**23+1)
2453     for i in avgIdxs:
2454         sum += f[specStr][:,i]
2455     avgSpec = sum/(len(avgIdxs))
2456     return avgSpec
2457
```

Listing A.1: Python function for averaging spectra from pre-processed data

2458 Note that this assumes a single HDF5 file, `f`, is in scope. `specStr` is a string which

2459 specifies which channel to average, for example `spec_W_chA`.

2460 The output of this function is S_o which can be passed to following functions for further
2461 analysis.

²⁴⁶² Bibliography

- ²⁴⁶³ [1] Fritz Zwicky. “The Redshift of Extragalactic Nebulae”. In: (1933).
- ²⁴⁶⁴ [2] Vera C. Rubin and Jr. Ford W. Kent. “Rotation of the Andromeda Nebula from a
²⁴⁶⁵ Spectroscopic Survey of Emission Regions”. In: (1970).
- ²⁴⁶⁶ [3] Marco Battaglieri *et al.* *US Cosmic Visions: New Ideas in Dark Matter 2017: Com-*
²⁴⁶⁷ *munity Report*. 2017. DOI: 10.48550/ARXIV.1707.04591. URL: <https://arxiv.org/abs/1707.04591>.
- ²⁴⁶⁸
- ²⁴⁶⁹ [4] Benjamin Godfrey *et al.* “Search for dark photon dark matter: Dark E field radio pilot
²⁴⁷⁰ experiment”. In: *Phys. Rev. D* 104 (1 July 2021), p. 012013. DOI: 10.1103/PhysRevD.
²⁴⁷¹ 104.012013. URL: <https://link.aps.org/doi/10.1103/PhysRevD.104.012013>.
- ²⁴⁷² [5] V. Radeka. “Signal, Noise and Resolution in Position-Sensitive Detectors”. In: *IEEE*
²⁴⁷³ *Transactions on Nuclear Science* 21.1 (1974), pp. 51–64. DOI: 10.1109/TNS.1974.
²⁴⁷⁴ 4327444.
- ²⁴⁷⁵ [6] B. M. Brubaker *et al.* “HAYSTAC axion search analysis procedure”. In: *Physical Re-*
²⁴⁷⁶ *view D* 96.12 (Dec. 2017). DOI: 10.1103/physrevd.96.123008. URL: <https://doi.org/10.1103%2Fphysrevd.96.123008>.
- ²⁴⁷⁷

- 2478 [7] C. Boutan et al. *Axion Dark Matter eXperiment: Run 1A Analysis Details*. 2023. arXiv:
2479 2312.16668.
- 2480 [8] Maximiliano Silva-Feaver et al. “Design Overview of DM Radio Pathfinder Experi-
2481 ment”. In: *IEEE Transactions on Applied Superconductivity* 27.4, 2631425 (June 2017),
2482 p. 2631425. DOI: 10.1109/TASC.2016.2631425.
- 2483 [9] David Hill. “Plane Wave Integral Representation for Fields in Reverberation Cham-
2484 bers”. en. In: 40 (1998-08-01 00:08:00 1998).
- 2485 [10] W. L. Stutzman and G. A. Thiele. *Antenna Theory and Design*. John Wiley Sons,
2486 1998.
- 2487 [11] J.D. Kraus. *Antennas*. McGraw-Hill, 1950. ISBN: 07-035410-3.
- 2488 [12] H. Nyquist. “Thermal Agitation of Electric Charge in Conductors”. In: *Phys. Rev.* 32
2489 (1 July 1928), pp. 110–113. DOI: 10.1103/PhysRev.32.110. URL: <https://link.aps.org/doi/10.1103/PhysRev.32.110>.
- 2491 [13] J. B. Johnson. “Thermal Agitation of Electricity in Conductors”. In: *Phys. Rev.* 32 (1
2492 July 1928), pp. 97–109. DOI: 10.1103/PhysRev.32.97. URL: <https://link.aps.org/doi/10.1103/PhysRev.32.97>.
- 2494 [14] Robert H Dicke. “The measurement of thermal radiation at microwave frequencies”.
2495 In: *Review of Scientific Instruments* 17.7 (1946), pp. 268–275.

- 2496 [15] Albert Einstein. “Über die von der molekularkinetischen Theorie der Wärme geforderte
2497 Bewegung von in ruhenden Flüssigkeiten suspendierten Teilchen”. In: *Annalen der*
2498 *Physik* 322.8 (1905), pp. 549–560.
- 2499 [16] Herbert B. Callen and Theodore A. Welton. “Irreversibility and Generalized Noise”.
2500 In: *Phys. Rev.* 83 (1 July 1951), pp. 34–40. DOI: 10.1103/PhysRev.83.34. URL:
2501 <https://link.aps.org/doi/10.1103/PhysRev.83.34>.
- 2502 [17] C. L. Mehta. “Coherence-time and effective bandwidth of blackbody radiation”. In:
2503 *Il Nuovo Cimento (1955-1965)* 28.2 (1963), pp. 401–408. DOI: 10.1007/BF02828589.
2504 URL: <https://doi.org/10.1007/BF02828589>.
- 2505 [18] Raphael Cervantes et al. *Deepest Sensitivity to Wavelike Dark Photon Dark Matter*
2506 *with SRF Cavities*. 2022. arXiv: 2208.03183 [hep-ex].
- 2507 [19] Alexander V. Gramolin et al. “Spectral signatures of axionlike dark matter”. In: *Physi-*
2508 *cal Review D* 105.3 (Feb. 2022). ISSN: 2470-0029. DOI: 10.1103/physrevd.105.035029.
2509 URL: <http://dx.doi.org/10.1103/PhysRevD.105.035029>.
- 2510 [20] Michael S. Turner. “Periodic signatures for the detection of cosmic axions”. In: *Phys.*
2511 *Rev. D* 42 (10 Nov. 1990), pp. 3572–3575. DOI: 10.1103/PhysRevD.42.3572. URL:
2512 <https://link.aps.org/doi/10.1103/PhysRevD.42.3572>.
- 2513 [21] Greg Durgin. *Lecture on Noise Figure*. Accessed: 2024-06-23. 2017. URL: https://www.youtube.com/watch?v=M_SRUF4TQgA.

- 2515 [22] Pasternack Enterprises. *PE15A1012: 1 Watt Amplifier Operating From 0.01 GHz to*
2516 *6 GHz*. Accessed: 2024-05-17. 2024. URL: <https://www.pasternack.com/images/ProductPDF/PE15A1012.pdf>.
- 2518 [23] SP Devices. *ADQ32 Datasheet*. Accessed: 2024-06-23. 2024. URL: https://www.spdevices.com/en-us/Products_/Documents/ADQ32/20-2378%20ADQ32%20datasheet.pdf.
- 2521 [24] Benjamin Godfrey. “A Novel Search for Dark Photons”. Ph.D. dissertation. UC Davis,
2522 2022. URL: <https://escholarship.org/uc/item/72b776v4>.
- 2523 [25] Joseph Levine et al. *New Limit on Dark Photon Kinetic Mixing in the 0.2-1.2 μeV Mass Range From the Dark E-Field Radio Experiment*. 2024. arXiv: 2405.20444
2524 [hep-ex]. URL: <https://arxiv.org/abs/2405.20444>.
- 2526 [26] L.A. Wainstein and V.D. Zubakov. *Extraction of Signals from Noise*. Englewood Cliffs,
2527 NJ: Prentice-Hall, 1962. ISBN: 9780132981330.
- 2528 [27] Andy Marvin and Simon Jonathan Bale. “Thermal Noise Measurements in a Rever-
2529 beration Chamber”. English. In: *IEEE Transactions on Electromagnetic Compatibility*
2530 64.3 (June 2022). © 2022 IEEE. This is an author-produced version of the published
2531 paper. Uploaded in accordance with the publisher’s self-archiving policy. Further copy-
2532 ing may not be permitted; contact the publisher for details, pp. 893–896. ISSN: 0018-
2533 9375. DOI: [10.1109/TEMC.2022.3142937](https://doi.org/10.1109/TEMC.2022.3142937).
- 2534 [28] F. Reif. *Fundamentals of Statistical and Thermal Physics*. Long Grove, IL: Waveland
2535 Press, 2009. ISBN: 9781577666127.

- 2536 [29] R. H. Dicke. “A Computational Method Applicable to Microwave Networks”. In: *Jour-*
2537 *nal of Applied Physics* 18.10 (Oct. 1947), pp. 873–878. ISSN: 0021-8979. DOI: 10.1063/
2538 1.1697561. eprint: <https://pubs.aip.org/aip/jap/article-pdf/18/10/873/18307533/873\1\online.pdf>. URL: <https://doi.org/10.1063/1.1697561>.
- 2539
- 2540 [30] Hewlett-Packard. *S-Parameter Design*. Application Note 154. 1990. URL: https://www.hpmemoryproject.org/an/pdf/an_154.pdf.
- 2541
- 2542 [31] NoiseWave. *NoiseWave FAQ Document*. Accessed: 2024-06-23. 2024. URL: <https://noisewave.com/faq.pdf>.
- 2543
- 2544 [32] Whitham D. Reeve. *Noise Tutorial Part III: Attenuator and Amplifier Noise*. Revision
2545 0.1, Updated: July 7, 2014. Reeve Engineers. 2014. URL: https://www.reeve.com/Documents/Noise/Reeve_Noise_3_AttenAmpNoise.pdf.
- 2546
- 2547 [33] S. Al Kenany et al. “Design and operational experience of a microwave cavity axion
2548 detector for the 20-100 μ eV range”. In: *Nuclear Instruments and Methods in Physics*
2549 *Research Section A: Accelerators, Spectrometers, Detectors and Associated Equipment*
2550 854 (May 2017), pp. 11–24. ISSN: 0168-9002. DOI: 10.1016/j.nima.2017.02.012.
2551 URL: <http://dx.doi.org/10.1016/j.nima.2017.02.012>.
- 2552 [34] Raphael Cervantes et al. *Deepest Sensitivity to Wavelike Dark Photon Dark Matter
2553 with SRF Cavities*. 2022. arXiv: 2208.03183 [hep-ex].
- 2554 [35] Maurio B. Grando, Christian R. Boutan, and Jihee Yang. *A Multiport Approach to
2555 Thermal Noise and Scattering Parameter Simulation of Cryogenic Experiments*. 2022.
2556 arXiv: 2209.04008 [physics.ins-det]. URL: <https://arxiv.org/abs/2209.04008>.

- 2557 [36] G.H. Bryant. *Principles of Microwave Measurements*. London, United Kingdom: Pe-
2558 ter Peregrinus Ltd., on behalf of the Institution of Electrical Engineers, 1993. ISBN:
2559 0863412963.
- 2560 [37] David A. Hill. “Wall Losses and Cavity Q”. In: *Electromagnetic fields in cavities: De-*
2561 *terministic and statistical theories*. John Wiley & Sons Inc., 2009, pp. 31–33.
- 2562 [38] R.H. Price, H.T. Davis, and E.P. Wenaas. “Determination of the statistical distribution
2563 of electromagnetic-field amplitudes in complex cavities”. In: *Physical Review E* 48
2564 (1993), pp. 4716–4729. DOI: 10.1103/PhysRevE.48.4716.
- 2565 [39] John David Jackson. *Classical Electrodynamics*. 3rd. New York: Wiley, 1998. ISBN:
2566 9780471309321.
- 2567 [40] Bing-Hope Liu, David C. Chang, and Mark T. Ma. *Eigenmodes and the Composite Q*
2568 *Factor of a Reverberating Chamber*. Tech. rep. Aug. 1983.
- 2569 [41] *Series 83 RF Shielded Enclosure*. Lindgren R.F. Enclosures, Inc. 2021. URL: <https://www.ets-lindgren.com/datasheet/shielding/rf-shielding-and-accessories/11003/1100307>.
- 2572 [42] David A. Hill. *Electromagnetic Theory of Reverberation Chambers*. Technical Note
2573 1506. Gaithersburg, MD: National Institute of Standards and Technology, 1998. URL:
2574 https://tsapps.nist.gov/publication/get_pdf.cfm?pub_id=24427.
- 2575 [43] D.A. Hill. “A reflection coefficient derivation for the Q of a reverberation chamber”. In:
2576 *IEEE Transactions on Electromagnetic Compatibility* 38.4 (1996), pp. 591–592. DOI:
2577 10.1109/15.544314.

- 2578 [44] Lawrence Krauss et al. “Calculations for cosmic axion detection”. In: *Physical Review*
2579 *Letters* 55.17 (1985), pp. 1797–1800. DOI: 10.1103/PhysRevLett.55.1797. URL:
2580 <https://doi.org/10.1103/PhysRevLett.55.1797>.
- 2581 [45] *Biconical Antenna AB-900A*. Rev. D05.19. Com-Power Corporation. May 2019. URL:
2582 <https://documentation.com-power.com/pdf/AB-900A-1.pdf>.
- 2583 [46] *COMSOL Multiphysics*. 5.4. Available at <https://www.comsol.com/>. COMSOL, Inc.
2584 One First Street, Suite 4 Los Altos, CA 94022.
- 2585 [47] Zhong Chen and Michael D. Foegelle. “A numeric investigation of ground plane effects
2586 on biconical antenna factor”. In: *Electromagnetic Compatibility, 1998. 1998 IEEE In-*
2587 *ternational Symposium on*. Vol. 2. IEEE. IEEE, 1998, pp. 802–806. DOI: 10.1109/
2588 ISEMC.1998.750302. URL: <https://ieeexplore.ieee.org/document/750302>.
- 2589 [48] John D. Kraus. *Antennas*. 2nd. New York: McGraw-Hill, 1988, p. 892. ISBN: 9780070354227.
- 2590 [49] Mini-Circuits. *ZKL-1R5: 50 Ω Gain Block Amplifier*. Accessed: 2024-06-23. 2024. URL:
2591 <https://www.minicircuits.com/pdfs/ZKL-1R5.pdf>.
- 2592 [50] Texas Instruments. *LM317: 3-Terminal Adjustable Regulator*. Accessed: 2024-06-23.
2593 2024. URL: <https://www.ti.com/lit/ds/symlink/lm317.pdf?ts=1720749307506>.
- 2594 [51] Alan V. Oppenheim, Alan S. Willsky, and S. Hamid Nawab. *Signals and Systems*. 2nd.
2595 Upper Saddle River, NJ: Prentice Hall, 1996. ISBN: 978-0138147570.
- 2596 [52] Mini-Circuits. *ZX75LP-288-S+: Low Pass Filter*. Accessed: 2024-06-23. 2024. URL:
2597 <https://www.minicircuits.com/pdfs/ZX75LP-288-S+.pdf>.

- 2598 [53] Mini-Circuits. *SHP-50+: High Pass Filter*. Accessed: 2024-06-23. 2024. URL: <https://www.minicircuits.com/pdfs/SHP-50+.pdf>.
- 2600 [54] *Biconical Antenna*. AB-900A. Rev. D. Com-Power Corporation. May 2019.
- 2601 [55] *The Y Factor Technique For Noise Figure Measurements*. 1MA178. Version 5e. Rhode
2602 & Schwarz. Oct. 2021.
- 2603 [56] *Noise Figure Measurement Accuracy: The Y-Factor Method*. 1MA178. Version 5e.
2604 Keysight Technologies. Oct. 2021.
- 2605 [57] Wikipedia contributors. *Y-factor Sketch*. Accessed: 2024-06-23. 2024. URL: https://en.wikipedia.org/wiki/Y-factor#/media/File:Y-factor_sketch.jpg.
- 2607 [58] Rigol Technologies. *RSA5000 Series: Real-Time Spectrum Analyzer Datasheet*. Ac-
2608 cessed: 2024-06-23. 2024. URL: https://beyondmeasure.rigoltech.com/acton/attachment/1579/f-0816/1/-/-/-/RSA5_datasheet.pdf.
- 2610 [59] “IEEE Standard Method for Measuring the Effectiveness of Electromagnetic Shielding
2611 Enclosures”. In: *IEEE Std 299-1997* (1998), pp. 1–48. DOI: [10.1109/IEEESTD.1998.88115](https://doi.org/10.1109/IEEESTD.1998.88115).
- 2613 [60] Valon Technology, LLC. *5009a Dual Frequency Synthesizer Module Operations Man-
2614 ual*. Version 1.39. Updated September 8, 2023. Northern California, USA, 2023. URL:
2615 https://www.valontechnology.com/5009users/Valon_5009_opman.pdf.
- 2616 [61] David W. Allan. “Statistics of atomic frequency standards”. In: *Proceedings of the
2617 IEEE* 54.2 (1966), pp. 221–230.

- 2618 [62] Keysight Technologies. *Analyzing Frequency Stability in the Frequency and Time Do-*
2619 *mains*. Tech. rep. 5991-4797EN, August 11, 2014. USA: Keysight Technologies, 2014.
- 2620 [63] Stanford Research Systems. *FS725 Rubidium Frequency Standard Manual*. Accessed:
2621 2024-06-23. 2024. URL: <https://www.thinksrs.com/downloads/PDFs/Manuals/FS725m.pdf>.
- 2623 [64] R. H. Dicke. “The Measurement of Thermal Radiation at Microwave Frequencies”.
2624 In: *Rev. Sci. Instrum.* 17 (1946), p. 268. DOI: 10.1063/1.1770483. URL: <https://aip.scitation.org/doi/10.1063/1.1770483>.
- 2626 [65] S. Al Kenany et al. “Design and operational experience of a microwave cavity axion de-
2627 tector for the 20-100 micro-eV Range”. In: *Nuclear Instruments and Methods in Physics*
2628 *Research Section A: Accelerators, Spectrometers, Detectors and Associated Equipment*
2629 854 (May 2017), pp. 11–24. ISSN: 0168-9002. DOI: 10.1016/j.nima.2017.02.012.
2630 URL: <http://dx.doi.org/10.1016/j.nima.2017.02.012>.
- 2631 [66] G. Turin. “An introduction to matched filters”. In: *IRE Transactions on Information*
2632 *Theory* 6.3 (1960), pp. 311–329. DOI: 10.1109/TIT.1960.1057571.
- 2633 [67] Robert N McDonough and Anthony D Whalen. *Detection of signals in noise*. Academic
2634 Press, 1995.
- 2635 [68] S. Asztalos et al. “Large-scale microwave cavity search for dark-matter axions”. In:
2636 *Phys. Rev. D* 64 (9 Oct. 2001), p. 092003. DOI: 10.1103/PhysRevD.64.092003. URL:
2637 <https://link.aps.org/doi/10.1103/PhysRevD.64.092003>.

- 2638 [69] G. Orjubin et al. “Statistical model of an undermoded reverberation chamber”. In:
2639 *IEEE Transactions on Electromagnetic Compatibility* 48.1 (2006), pp. 248–251. DOI:
2640 10.1109/TEMC.2006.870705.
- 2641 [70] B. Efron. “Bootstrap Methods: Another Look at the Jackknife”. In: *The Annals of
2642 Statistics* 7.1 (1979), pp. 1–26. DOI: 10.1214/aos/1176344552. URL: <https://doi.org/10.1214/aos/1176344552>.
- 2643 [71] R. Khatiwada et al. “Axion Dark Matter Experiment: Detailed design and operations”.
2644 In: *Review of Scientific Instruments* 92.12 (Dec. 2021), p. 124502. ISSN: 0034-6748.
2645 DOI: 10.1063/5.0037857. eprint: https://pubs.aip.org/aip/rsi/article-pdf/doi/10.1063/5.0037857/16136265/124502\1_online.pdf. URL: <https://doi.org/10.1063/5.0037857>.
- 2646 [72] Yuqi Zhu et al. “An improved synthetic signal injection routine for the Haloscope
2647 At Yale Sensitive To Axion Cold dark matter (HAYSTAC)”. In: *Review of Scientific
2648 Instruments* 94.5 (May 2023). ISSN: 1089-7623. DOI: 10.1063/5.0137870. URL: <http://dx.doi.org/10.1063/5.0137870>.
- 2649 [73] Frank Hampel et al. *Robust Statistics: The Approach Based on Influence Functions*.
2650 John Wiley & Sons, Mar. 1986. ISBN: 9780471735779. DOI: 10.1002/9781118186435.
- 2651 [74] Andrea Caputo et al. “Dark photon limits: A handbook”. In: *Phys. Rev. D* 104 (9
2652 Nov. 2021), p. 095029. DOI: 10.1103/PhysRevD.104.095029. URL: <https://link.aps.org/doi/10.1103/PhysRevD.104.095029>.

- 2658 [75] Ciaran O'Hare. *cajohare/AxionLimits: AxionLimits*. <https://cajohare.github.io/AxionLimits/>. Version v1.0. July 2020. DOI: 10.5281/zenodo.3932430.
- 2659
- 2660 [76] DMRadio Collaboration et al. *Electromagnetic modeling and science reach of DMRadio-*
2661 *m³*. 2023. arXiv: 2302.14084 [hep-ex]. URL: <https://arxiv.org/abs/2302.14084>.
- 2662 [77] Ferenc Marki and Christopher Marki. *Mixer Basics Primer: A Tutorial for RF &*
- 2663 *Microwave Mixers*. Marki Microwave, Inc. Morgan Hill, CA, 2010. URL: https://markimicrowave.com/assets/c2c4688b-15c7-4421-a703-254cb238f9fb/Mixer_Basics_Primer.pdf.
- 2664
- 2665
- 2666 [78] David M. Pozar. *Microwave Engineering*. 4th ed. Hoboken, NJ: Wiley, 2011. ISBN:
2667 978-0470631553.
- 2668 [79] Wikipedia contributors. *Superheterodyne receiver*. Accessed: 2024-06-23. 2024. URL:
2669 https://en.wikipedia.org/wiki/Superheterodyne_receiver.
- 2670 [80] Chetvorno. *Superheterodyne image problem*. Accessed: 2024-11-14. 2024. URL: https://commons.wikimedia.org/wiki/File:Superheterodyne_image_problem.svg.
- 2671
- 2672 [81] Chetvorno. *How superheterodyne receiver works*. Accessed: 2024-11-14. 2024. URL:
2673 https://commons.wikimedia.org/wiki/File:How_superheterodyne_receiver_works.svg.
- 2674
- 2675 [82] Narda-MITEQ. *TB0440LW1 4 to 40 GHz Triple-Balanced Mixer*. Technical Bulletin
2676 TB-0440, Revised: April 24, 2012. 2012. URL: <https://nardamiteq.com/docs/MITEQ-TB0440.PDF>.
- 2677

- 2678 [83] Marki Microwave. *Spur Calculator*. Accessed: 2024-06-23. 2024. URL: <https://markimicrowave.com/technical-resources/tools/spur-calculator>.
- 2679
- 2680 [84] Low Noise Factory. *LNF-LNC0.3_14B: 0.3-14 GHz Cryogenic Low Noise Amplifier*.
2681 Datasheet, Revised: 2023-02-24. Low Noise Factory AB. Nelliekevägen 24, 412 63
2682 Göteborg, Sweden, 2023. URL: https://lownoisefactory.com/wp-content/uploads/2023/03/lnf-lnc0-3_14b.pdf.
- 2683
- 2684 [85] Valon Technology, LLC. *5015/5019 Frequency Synthesizer Module Operations Manual*.
2685 Version 1.21. Updated February 17, 2023. Redwood City, CA, USA, 2023. URL: https://valontechnology.com/5015users/Valon_5015-5019_opman.pdf.
- 2686
- 2687 [86] Arran Phipps et al. “Exclusion limits on hidden-photon dark matter near 2 nev from
2688 a fixed-frequency superconducting lumped-element resonator”. In: *Microwave Cavities
2689 and Detectors for Axion Research*. Springer, 2020, pp. 139–145.
- 2690 [87] Jonathan L. Ouellet et al. “Design and implementation of the ABRACADABRA-10
2691 cm axion dark matter search”. In: *Phys. Rev. D* 99 (5 Mar. 2019), p. 052012. doi:
2692 10.1103/PhysRevD.99.052012. URL: <https://link.aps.org/doi/10.1103/PhysRevD.99.052012>.
- 2693
- 2694 [88] Alexander V. Gramolin et al. “Search for axion-like dark matter with ferromagnets”.
2695 en. In: *Nature Physics* 17.1 (Jan. 2021), pp. 79–84. ISSN: 1745-2473, 1745-2481. doi:
2696 10.1038/s41567-020-1006-6.
- 2697 [89] Sumita Ghosh et al. “Searching for dark photons with existing haloscope data”. In:
2698 *Physical Review D* 104.9 (Nov. 2021), p. 092016. doi: 10.1103/PhysRevD.104.092016.